UNIVERSITY OF OKLAHOMA

GRADUATE COLLEGE

STRESS PATH AND PORE PRESSURE IN AND AROUND A PRODUCING FORMATION PIERCED BY A SALT DOME

A THESIS

SUBMITTED TO THE GRADUATE FACULTY

in partial fulfillment of the requirements for the

Degree of

MASTER OF SCIENCE

By

LAURA MARIA HERNANDEZ RIVEROS
Norman, Oklahoma
2018

Downloaded from SHAREOK. Persistent Handle URL: https://hdl.handle.net/11244/316312

STRESS PATH AND PORE PRESSURE IN AND AROUND A PRODUCING FORMATION PIERCED BY A SALT DOME

A THESIS APPROVED FOR THE
MEWBOURNE SCHOOL OF PETROLEUM AND GEOLOGICAL ENGINEERING

BY

Dr. Ahmad Ghassemi, Chair

Dr. Mashhad Fahes

Dr. Siddharth Misra

© Copyright by LAURA MARIA HERNANDEZ RIVEROS 2018
All Rights Reserved.

This thesis is dedicated to my parents Jorge and Liliana, who have been my inspiration and support through all my life. To my brother Jorge and my little nephew Jacob, who encourage me to pursue my dreams and teach me to enjoy the simple things. To my husband Ruben who has been by my side during this journey, lifting me up when I have fallen, giving me strength to keep going. To my beautiful family, specially to my grandfather Clareth, who will always hold a place in my heart and to my uncle Jorge, whose words and advice have made me a better person. I extend this dedication to my friends Yuliana and Andrea, who had made my days funnier and easier the last three years. And to all the friends I had the opportunity to meet during my time in Oklahoma.

Acknowledgements

I would like to express my deepest gratitude to my advisor Dr. Ahmad Ghassemi. Thank you for giving me the opportunity to learn under your guidance, for your support, wealth of knowledge, and valuable suggestions during my research. I am really grateful for pushing me to think critically to find the solution whenever I was stuck.

I also thank Yuliana Zapata for helping me with the edition of this work, I really enjoyed the time we spent together learning from each other work. To Ruben Gonzalez for sharing his knowledge of programming and passing it on to me. To Behzad Hemami and Ahmir Kamali for sharing their knowledge of FLAC-3D and rock mechanics. I appreciate your time and patience.

My appreciation also extends to my thesis committee members, Dr. Mashhad Fahes and Dr. Siddharth Misra for their time and expertise to review and feedback for this work. Thank you to the Mewbourne School of Petroleum and Geologial Engineering faculty and staff for your kind and constant work to help the students to fulfill their goals.

Table of Contents

List of Figures x

Abstract xxxiv

Chapter 1: Introduction 1

1.1 Problem statement 1

1.2 Objective 1

Chapter 2: Literature review 2

2.1 Salt domes 2

2.2 Mechanical behavior of salt 4

2.3 Two-component Norton Power Law 6

2.4 The Mohr Coulomb Model 7

2.5 The Power Law viscoplastic model 9

2.6 Stress path 12

2.7 Effects of stress path on compaction 17

Chapter 3: Geomechanical model 21

3.1 Model Geometry 21

3.2 Rock mechanical and fluid properties 24

3.3 Boundary and initial conditions 26

3.4 Initial conditions 26

Chapter 4: Simulation description 29

Chapter 5: Results 32

5.1 Pore pressure 34

5.2 Total and effective vertical stresses 40

5.3 Total and effective maximum horizontal stresses 53
5.4 Total and effective minimum horizontal stresses 65
5.5 The xy-component of total stress tensor 77
5.6 The yz-component of total stress tensor 82
5.7 The xz-component of the total stress tensor 87
5.8 Total and effective stress path 91
5.9 Total and effective vertical stress path 100
5.10 Total and effective maximum horizontal stress path 103
5.11 Total and effective minimum horizontal stress path 106
5.12 Volumetric strain 109
Chapter 6: Sensitivity analysis 113
6.1 Pore pressure 115
6.2 Total and effective vertical stresses 117
6.3 Total and effective maximum horizontal stress 120
6.4 Total and effective minimum horizontal stress 123
6.5 The xy-component of total stress tensor 126
6.6 The yz-component of total stress tensor 128
6.7 The xz-component of total stress tensor 131
6.8 Total and effective vertical stress path 134
6.9 Total and effective maximum horizontal stress path 137
6.10 Total and effective minimum horizontal stress path 139
6.11 Volumetric strain 142
Conclusions 145

References.....147

List of Tables

Table 1. Rock mechanical input properties..... 24

Table 2. Creep power law input properties from Napoleonville salt dome..... 25

Table 3. Rock permeability and porosity data. 25

Table 4. Rock saturation and fluid properties. 25

Table 5. Shale, Reservoir and Salt total stress gradients. The maximum principal stress is the vertical, the intermedium and the minimum are horizontal. 28

Table 6. Well schedule. 32

Table 7. Parameters studied during the sensitivity analysis. 114

List of Figures

Figure 1. Circular salt dome shaped that upturned pierced beds favoring the accumulation of hydrocarbon. 3

Figure 2. Hydrocarbon traps of an idealized section associated with salt domes: (1) simple domal anticline draped over salt; (2) graben fault trap over dome; (3) porous cap rock; (4) flank sand pinchout and sand lens; (5) trap beneath overhang; (6) trap uplifted and upholded against salt structure; (7) unconformity; (8) fault trap down-thrown away from dome; (9) fault trap downthrown toward dome (Halbouty, 1979). 4

Figure 3. Mohr Coulomb failure criterion implemented by Flac-3D, which combines the Mohr Coulomb criterion with a tension cutoff (Itasca, 2012). 9

Figure 4. Simple illustration of the possible total stress path (γ) followed by a reservoir that undergoes depletion, analyzing the same point that moves from the position A to A'. The initial state is represented by the small Mohr circle and the final state by the big Mohr circle. Which means that depletion induces the total stresses to decrease, in this case, $\sigma 3$ decreases more than $\sigma 1$ which makes the Mohr circle diameter to increase. 15

Figure 5. Simple illustration of the possible effective stress path (γ') followed by a reservoir that undergoes depletion, analyzing the same point that moves from the position A to A'. The initial state is represented by the small Mohr circle and the final state by the big Mohr circle. Which means that depletion induces the effective stresses to increase. The Mohr circle diameter changes because the total principal stresses $\sigma 3$ and $\sigma 1$ change in a different proportion. 16

Figure 6. Ekofisk seismic-derived compaction map with water injection wells displayed as black dots from 1989 to 1999 (Guilbot & Smith, 2002). 20

Figure 7. Reservoir dimensions. The size of the reservoir is 2590 m, 609 m and 38 m in x, y and z-direction. 21

Figure 8. Cross-section of the model geometry in Y. This plot shows the extension and thickness of the reservoir, shale and salt dome..... 22

Figure 9. Model Geometry. The Reservoir layer (yellow) dips 45 degrees toward the salt dome (blue). The shale is constituted for 2 groups: lower shale (brown) and upper shale (brown). 23

Figure 10. Model dimensions. The size of the model is 3657 m, 2133 m and 1524 m in x, y and z-direction. 23

Figure 11. Model boundary conditions. Fix in the bottom, and rollers on the sides. The top can move freely on z-direction. 26

Figure 12. Stress tensor that represents the initial orientation of the principal stresses at a point in the model..... 27

Figure 13. Von Mises shear stresses at mechanical equilibrium and after 100,000 years of creep. It is observed that the shear stresses in the salt decreased significantly because of plastic deformation of the salt, after 100,000 years of creep. 30

Figure 14. Orientation of the principal stresses around the salt dome before production. The arrows indicate the general trend of the stress vector orientation at that point..... 31

Figure 15. (a) Trajectory ABCD along the reservoir and salt dome. Point A is in the flat region of the reservoir located 182.4 m apart from the well, point B represents the position of the well, point C is located at the salt/sediment interface, and D is 38 m inside the salt. (b) Vertical subdivision of the segment ABC along the shale and reservoir, including an element inside the salt (point D). 33

Figure 16. Differential pore pressure as a function of distance from the salt/sediment interface, along the curve ABCD defined in Figure 15. (a), after 13 years of production. Reservoir elements are represented in green, while salt elements are represented in blue. The pressure drawdown and pressure build up at a certain location is controlled by its location relative to the well. The salt pore pressure remains zero after production. The pore pressure of the reservoir elements at the salt/sediment interface is altered by the salt creep. The salt elements at the salt/sediment interface present a pore pressure different than zero, because the contour of this element interpolates the values of the sediment gridpoint (different than zero) and salt gridpoint (zero). 35

Figure 17. Pore pressure drawdown along a xz-plane in the middle of the reservoir. (a) Initial state, (b) 6 years of production, (c) 13 years of production and (d) 3 years of steady state. The highest depletion occurred along the reservoir and extends in the shale above and below the producing formation. Three years after shut-in, the pore pressure increased in the reservoir and shale. 36

Figure 18. Pore pressure drawdown in the xy-plane through the middle of the reservoir. (a) Initial state, (b) 6 years of production, (c) 13 years of production and (d) 3 years of steady state. The depletion was higher at the salt/sediment interface than in the flat region. Three years after shut-in, the pore pressure in the reservoir stabilizes and distributes..... 37

Figure 19. Pore pressure as a function of distance from the salt/sediment interface along the trajectory ABCD, defined in Figure 15. (a). The pressure drawdown and pressure build up at a certain location is controlled by its location relative to the well. The salt pore pressure remains zero after 16 years of simulation. The pore pressure of the reservoir elements at the salt/sediment interface is altered by the salt creep. The salt elements at the salt/sediment interface present a

pore pressure different than zero, because the contour of this element interpolates the values of the sediment gridpoint (different than zero) and salt gridpoint (zero). 38
Figure 20. Pore pressure during production time of three upper shale elements (A1, B1 and C1), situated at different locations with respect to the dome, described in Figure 15(b). The element above the well, experienced the maximum pressure drawdown during the first year of production, followed by a change of the slope that decreases. The slope of the pressure at point C1 looks steeper than at point A1 39
Figure 21. Pore pressure during production time of three lower shale elements (A3, B3 and C3) situated at different locations with respect to the dome, described in Figure 15(b). The element below the well experienced more depletion..... 40
Figure 22. Change of total vertical stress as a function of distance from the salt/sediment interface, along the curve ABCD, after 13 years of production. Reservoir elements are represented in green, while salt elements are represented in blue. The total vertical stress decreased toward the dome and increases in the salt. The effect of a production well on the total stress resulted in higher reduction around higher depleted zone. The total vertical stress of the reservoir elements at the salt/sediment interface is altered by the salt creep. The salt elements at the salt/sediment interface present a total vertical stress different than the salt elements next to it, because the contour of this element interpolates the values of the sediment and salt gridpoints. 43
Figure 23. Total vertical stress changes along a xz-plane in the middle of the reservoir. (a) Initial state, (b) 6 years of production, (c) 13 years of production and (d) 3 years of steady state. The total vertical stress decreased in the reservoir, reaching the maximum reduction along the dipping layer. While it increased in the salt right next to the reservoir interface. Three years after shut-in, σzz increases in the reservoir and decreases in the salt, looking for a steady state. 44

Figure 24. Total vertical stress changes in the xy-plane through the middle of the reservoir. (a) Initial state, (b) 6 years of production, (c) 13 years of production and (d) 3 years of steady state. The total vertical stress decreased toward the dome and the well location impact the stress pattern along the dipping layer. While it increased in the salt right next to the reservoir interface. Three years after shut-in, σzz increases in the reservoir as the pore pressure in the reservoir stabilizes..... 45

Figure 25. Total vertical stress as a function of distance from the salt/sediment interface, along the trajectory ABCD. The total vertical stress during and after production is controlled by the dipping angle and the proximity to the salt dome. The vertical stresses in the salt increased after production and decreased after shut-in. The total vertical stress of the reservoir elements at the salt/sediment interface is altered by the salt creep. The salt elements at the salt/sediment interface present a total vertical stress different than the salt elements next to it, because the contour of this element interpolates the values of the sediment and salt gridpoints. 46

Figure 26. Change of effective vertical stress as a function of distance from the salt/sediment interface, along the curve ABCD, after 13 years of production. Reservoir elements are represented in green, while salt elements are represented in blue. The highest increment occurred at point B. The effective vertical stress increased more at point A that at the salt/sediment interface. The effective vertical stress of the reservoir elements at the salt/sediment interface is altered by the salt creep. The salt elements at the salt/sediment interface present an effective vertical stress different than the salt elements next to it, because the contour of this element interpolates the values of the sediment and salt gridpoints. 47

Figure 27. Effective vertical stress changes in the xz-plane through the middle of the reservoir. (a) Initial state, (b) 6 years of production, (c) 13 years of production and (d) 3 years of steady

state. The effective vertical stress is controlled by the well location and increased in the reservoir and shale. The value of the effective stress in the salt corresponds to the change of the total vertical stresses, according to Eq. (32), because the pore pressure in the salt remains zero during and after production. Three years after shut-in, the σzz′ decreases in the model. 48

Figure 28. Effective vertical stress changes in the xy-plane through the middle of the reservoir. (a) Initial state, (b) 6 years of production, (c) 13 years of production and (d) 3 years of steady state. The effective vertical stress is controlled by the well location and increased with depletion. The value of the effective stress in the salt corresponds to the change of the total vertical stresses, according to Eq. (32), because the pore pressure in the salt remains zero during and after production. Three years after shut-in, the σzz′ decreased in the model. 49

Figure 29. Effective vertical stress as a function of distance from the salt/sediment interface, along the trajectory ABCD defined in Figure 15(a). The major increment of σzz′ was 5.57 MPa around the well. After shut-in, the σzz′ decreased 0.97 MPa at point B. The effective vertical stress of the reservoir elements at the salt/sediment interface is altered by the salt creep. The salt elements at the salt/sediment interface present an effective vertical stress different than the salt elements next to it, because the contour of this element interpolates the values of the sediment and salt gridpoints. 50

Figure 30. Total vertical stress (A1, B1 and C1) and effective vertical stress (A'1, B'1 and C'1) during production time for three upper shale elements, situated at different locations with respect to the dome, described in Figure 15(b). The element at the salt/sediment interface experienced the maximum σzz reduction, while the element above the well experienced the highest σzz′ increment, with production. 51

Figure 31. Total vertical stress (A3, B3 and C3) and effective vertical stress (A’3, B’3 and C’3) during production time of three lower shale elements situated at different locations with respect to the dome, described in Figure 15(b). The element at the salt/sediment interface experienced the maximum σzz reduction, while the element below the well experienced the highest σzz′ increment, with production. 53
Figure 32. Change of total maximum horizontal stress as a function of distance from the salt/sediment interface, along the curve ABCD, after 13 years of production. Reservoir elements are represented in green, while salt elements are represented in blue. The highest reduction of the total maximum horizontal stress occurs 24 m away from the well, in the flat region. Lower reduction of the total maximum horizontal stress around the dome, compared to the flat zone. It decreased up to 0.68 MPa in the salt. The total maximum horizontal stress of the reservoir elements at the salt/sediment interface is altered by the salt creep. The salt elements at the salt/sediment interface present a total maximum horizontal stress different than the salt elements next to it, because the contour of this element interpolates the values of the sediment and salt gridpoints. 55
Figure 33. Total maximum horizontal stress changes in the xz-plane through in the middle of the reservoir. (a) Initial state, (b) 6 years of production, (c) 13 years of production and (d) 3 years of steady state. The reduction of σxx in the reservoir is function of the well location and, extends toward the flatten area. Three years after shut-in, σxx increases in the reservoir and the salt..... 56
Figure 34. Total maximum horizontal stress changes in the xy-plane through the middle of the reservoir. (a) Initial state, (b) 6 years of production, (c) 13 years of production and (d) 3 years of steady state. The reduction of σxx in the reservoir is function of the well location and, extends toward the flatten area. Three years after shut-in, σxx increases in the reservoir and the salt..... 57

Figure 35. Total maximum horizontal stress as a function of distance from the salt/sediment interface, along the trajectory ABCD. The σxx decreased after production and increased after shut-in, with the major change around the well (point B). The total maximum horizontal stress of the reservoir elements at the salt/sediment interface is altered by the salt creep. The salt elements at the salt/sediment interface present a total maximum horizontal stress different than the salt elements next to it, because the contour of this element interpolates the values of the sediment and salt gridpoints. 58

Figure 36. Change of effective maximum horizontal stress as a function of distance from the salt/sediment interface, along the curve ABCD, after 13 years of production. Reservoir elements are represented in green, while salt elements are represented in blue. The σxx′ increased along the reservoir and decreased in the salt, with a major increment at the salt/sediment interface, compared to the flat region. The effective maximum horizontal stress of the reservoir elements at the salt/sediment interface is altered by the salt creep. The salt elements at the salt/sediment interface present an effective maximum horizontal stress different than the salt elements next to it, because the contour of this element interpolates the values of the sediment and salt gridpoints. 59

Figure 37. Effective maximum horizontal stress changes in the xz-plane through the middle of the reservoir. (a) Initial state, (b) 6 years of production, (c) 13 years of production and (d) 3 years of steady state. The σxx′ is controlled by the well location and increases after production in the reservoir and shale. Three years after shut-in, the σxx′ decreases in the model. 60

Figure 38. Effective maximum horizontal stress changes in the xy-plane through the middle of the reservoir. (a) Initial state, (b) 6 years of production, (c) 13 years of production and (d) 3 years

of steady state. The σxx′ is controlled by the well location and the dipping angle and increases with depletion. Three years after shut-in, the σxx′ decreased in the model. 61

Figure 39. Effective maximum horizontal stress as a function of distance from the salt/sediment interface, along the trajectory ABCD. The increment of the effective maximum horizontal stresses caused by production goes up to 4.5 MPa at the well location. Once the well shuts in, the pressure in the reservoir builds up and stabilizes. During this period, the stress decreased up to 2.5 MPa in the reservoir. The effective maximum horizontal stress of the reservoir elements at the salt/sediment interface is altered by the salt creep. The salt elements at the salt/sediment interface present an effective maximum horizontal stress different than the salt elements next to it, because the contour of this element interpolates the values of the sediment and salt gridpoints. 62

Figure 40. Total maximum horizontal stress (A1, B1 and C1) and effective maximum horizontal stress (A'1, B'1 and C'1) during production time of three upper shale elements, situated at different locations with respect to the dome, described in Figure 15(b). The total maximum horizontal stress decreased in the upper shale and the effective maximum horizontal stress increased. The σxx decreased more above the well, while the σxx′ increased more at the salt/sediment interface. 63

Figure 41. Total maximum horizontal stress (A1, B1 and C1) and effective maximum horizontal stress (A'1, B'1 and C'1) during production time of three lower shale elements situated at different locations with respect to the dome, described in Figure 15(b). The element below the well, experienced the maximum σxx reduction and the highest σxx′ increment during production. 65

Figure 42. Change of total minimum horizontal stress as a function of distance from the salt/sediment interface, along the curve ABCD, after 13 years of production. Reservoir elements are represented in green, while salt elements are represented in blue. The σyy is controlled by the well location, where it presented the maximum decrease. The total minimum horizontal stress of the reservoir elements at the salt/sediment interface is altered by the salt creep. The salt elements at the salt/sediment interface present a total minimum horizontal stress different than the salt elements next to it, because the contour of this element interpolates the values of the sediment and salt gridpoints. 67

Figure 43. Total minimum horizontal stress changes along a xz-plane in the middle of the reservoir. (a) Initial state, (b) 6 years of production, (c) 13 years of production and (d) 3 years of steady state. The reduction of σyy in the reservoir is function of the well location and, extends toward the dipping layer. Three years after shut-in, σyy increases in the reservoir and the salt, reaching a steady state. 68

Figure 44. Total minimum horizontal stress changes in the xy-plane through the middle of the reservoir. (a) Initial state, (b) 6 years of production, (c) 13 years of production and (d) 3 years of steady state. The reduction of σyy in the reservoir is function of the well location and, extends toward the dipping layer. Three years after shut-in, σyy increases in the reservoir and the salt, reaching a steady state. 69

Figure 45. Total minimum horizontal stress along the trajectory ABCD. The σyy decreased after production and increased three years after shut-in. The minimum horizontal stress in the salt hardly change during the simulation. The total minimum horizontal stress of the reservoir elements at the salt/sediment interface is altered by the salt creep. The salt elements at the salt/sediment interface present a total minimum horizontal stress different than the salt elements

next to it, because the contour of this element interpolates the values of the sediment and salt gridpoints. 70
Figure 46. Change of effective minimum horizontal stress as a function of distance from the salt/sediment interface, along the curve ABCD, after 13 years of production. Reservoir elements are represented in green, while salt elements are represented in blue. The effective minimum horizontal stress increased along the reservoir and the salt. Where the major increment happened at point B2. The σyy′ change is greater at the salt/sediment interface, compared to the flat region. The effective minimum horizontal stress of the reservoir elements at the salt/sediment interface is altered by the salt creep. The salt elements at the salt/sediment interface present an effective minimum horizontal stress different than the salt elements next to it, because the contour of this element interpolates the values of the sediment and salt gridpoints. 71
Figure 47. Effective minimum horizontal stress changes along a xz-plane in the middle of the reservoir. (a) Initial state, (b) 6 years of production, (c) 13 years of production and (d) 3 years of steady state. The σyy′ is controlled by the well location and increases after production in the reservoir and shale. Three years after shut-in, the σyy′ decreases in the model..... 72
Figure 48. Effective minimum horizontal stress changes along a xy-plane in the middle of the reservoir. (a) Initial state, (b) 6 years of production, (c) 13 years of production and (d) 3 years of steady state. The $\sigma yy'$ is controlled by the well location and increases with depletion. Three years after shut-in, the $\sigma yy'$ decreased in the model. 73
Figure 49. Effective minimum horizontal stress along the trajectory ABCD. The increment of the σyy′ caused by production goes up to 3.91 MPa at the well location. Three years after shut-in, the σyy′ increased up to 1.4 MPa around the well. The effective and total stresses in the salt are the same. The effective minimum horizontal stress of the reservoir elements at the salt/sediment

interface is altered by the salt creep. The salt elements at the salt/sediment interface present an effective minimum horizontal stress different than the salt elements next to it, because the contour of this element interpolates the values of the sediment and salt gridpoints. 74
Figure 50. Total minimum horizontal stress (A1, B1 and C1) and effective maximum horizontal stress (A'1, B'1 and C'1) during production time of three upper shale elements, situated at different locations with respect to the dome, described in Figure 15(b). The element above the well experienced the maximum σyy reduction and the highest $\sigma' yy$ increment. 75
Figure 51. Total minimum horizontal stress (A1, B1 and C1) and effective maximum horizontal stress (A'1, B'1 and C'1) during production time of three lower shale elements situated at different locations with respect to the dome, described in Figure 15(b). The element above the well, experienced the maximum σyy reduction and the highest σ'yy increment. 77
Figure 52. Change of Sxy total stress as a function of distance from the salt/sediment interface, along the curve ABCD, after 13 years of production. Reservoir elements are represented in green, while salt elements are represented in blue. The stress perturbation magnitude increases slightly and concentrates toward the well location and toward the salt/sediment interface. However, the stress perturbation in the salt tend to dissipate as a result of the salt creep, because the salt cannot sustain shear stresses..... 78
Figure 53. Sxy total stress in the xy-plane through the middle of the reservoir. (a) Initial state, (b) 6 years of production, (c) 13 years of production and (d) 3 years of steady state. The shear stresses increase with production, which is a result of the vertical and horizontal stress changes. 79
Figure 54. Sxy total stress along the trajectory ABCD. The stress perturbation magnitude increases with depletion around the well and toward the salt/sediment interface. 80

Figure 55. Sxy total stress during production time of three upper shale elements (A1, B1 and C1), situated at different locations with respect to the dome, described in Figure 15(b). The stress perturbation magnitude in the upper shale increases at the salt/sediment interface, while it decreases above the well and in the flat area. 81
Figure 56. Sxy total stress during production time of three lower shale elements (A3, B3 and C3) situated at different locations with respect to the dome, described in Figure 15(b). The stress perturbation magnitude in the lower shale increases at the salt/sediment interface and below the well, while it decreases in the flat area. 81
Figure 57. Change of Syz total stress as a function of distance from the salt/sediment interface, along the curve ABCD, after 13 years of production. Reservoir elements are represented in green, while salt elements are represented in blue. The stress perturbation magnitude increases slightly and concentrates toward the well location and toward the salt/sediment interface. However, the stress perturbation decreased in the area with a steeper dipping angle (up to 0.012 MPa). The stress perturbation in the salt tend to dissipate as a result of the salt creep, because the salt cannot sustain shear stresses..... 83
Figure 58. Syz total stress in the yz-plane through the middle of the reservoir. (a) Initial state, (b) 6 years of production, (c) 13 years of production and (d) 3 years of steady state. The shear stresses decreased in the sides of the reservoir toward the well location during production, which is a result of the vertical and horizontal stress changes. 84
Figure 59. Syz total stress along the trajectory ABCD. The shear stresses tend to increase toward the salt dome, where the dipping angle is steeper. The stress perturbation magnitude increases with depletion around the well and toward the salt/sediment interface and decreases in the area with a steeper dipping angle. 85

Figure 60. Syz total stress during production time of three upper shale elements (A1, B1 and C1), situated at different locations with respect to the dome, described in Figure 15(b). The stress perturbation magnitude in the upper shale increases above the well and in the flat area, while it decreases at the salt/sediment interface. 86
Figure 61. Syz total stress during production time of three lower shale elements (A3, B3 and C3) situated at different locations with respect to the dome, described in Figure 15(b). The stress perturbation magnitude in the lower shale increases below the well, while it decreases at the salt/sediment interface and in the flat area. 86
Figure 62. Change of Sxz total stress as a function of distance from the salt/sediment interface, along the curve ABCD, after 13 years of production. Reservoir elements are represented in green, while salt elements are represented in blue. The stress perturbation magnitude increases slightly and concentrates toward the well location and toward the salt/sediment interface. However, the stress perturbation in the salt tend to dissipate as a result of the salt creep, because the salt cannot sustain shear stresses. 87
Figure 63. Sxz total stress along a xz-plane in the middle of the reservoir. (a) Initial state, (b) 6 years of production, (c) 13 years of production and (d) 3 years of shut in. The shear stresses increased with production around the well and extended toward the salt/sediment interface. 88
Figure 64. Sxz total stress along the trajectory ABCD. The stress perturbation magnitude increases with depletion around the well and decreases toward the salt/sediment interface. 89
Figure 65. Sxz total stress during production time of three upper shale elements (A1, B1 and C1), situated at different locations with respect to the dome, described in Figure 15(b). The stress perturbation magnitude in the upper shale decreases at the salt/sediment interface and above the well, while it slightly increases in the flat area. 90

Figure 66. Sxz total stress during production time of three lower shale elements (A3, B3 and C3) situated at different locations with respect to the dome, described in Figure 15(b). The stress perturbation magnitude in the lower shale decreases below the well, at the salt/sediment interface and flat area. 90
Figure 67. Mohr circles and total stress path during production at different locations in the reservoir: (a) flat area, (b) well location and (c) salt/reservoir interface. It is observed that depletion induces the total stresses to decrease, however, σ3 decreases more than σ1 which makes the Mohr circle diameter to increase. 92
Figure 68. Mohr circles and total stress path during production at different locations in the upper shale: (a) flat area, (b) above the well and (c) salt/upper shale interface. It is observed that depletion induces the total stresses to decrease, however, σ3 decreases more than σ1 which makes the Mohr circle diameter to increase. 94
Figure 69. Mohr circles and total stress path during production at different locations in the lower shale: (a) flat area, (b) below the well and (c) salt/lower shale interface. It is observed that depletion induces the total stresses to decrease, however, σ3 decreases more than σ1 which makes the Mohr circle diameter to increase. 95
Figure 70. Mohr circles and effective stress path during production at different locations in the reservoir: (a) flat area, (b) well location and (c) salt/reservoir interface. It is observed that depletion induces the effective stresses to increase. The Mohr circle diameter changes because the total principal stresses σ3 and σ1 change in a different proportion. 96
Figure 71. Mohr circles and effective stress path during production at different locations in the upper shale: (a) flat area, (b) above the well and (c) salt/upper shale interface. It is observed that

depletion induces the effective stresses to increase. The Mohr circle diameter changes because the total principal stresses σ3 and σ1 change in a different proportion. 98
Figure 72. Mohr circles and effective stress path during production at different locations in the lower shale: (a) flat area, (b) below the well and (c) salt/lower shale interface. It is observed that depletion induces the effective stresses to increase. The Mohr circle diameter changes because the total principal stresses σ3 and σ1 change in a different proportion. 99
Figure 73. Total and effective vertical stress path as a function of distance from the salt/sediment interface, along the curve ABCD, after 13 years of production. The vertical stress path may be controlled by the dipping angle and the distance from the salt dome. Where the maximum value of γv occurred at the salt/sediment interface (0.34) and the minor in the flatten area. The salt creep affects the element at the salt/sediment interface (point C2), which presents a lower magnitude of γv, compared to the green element next to it. The spatial distribution of γv′ is controlled by the dipping angle and the proximity to the salt. It decreased less at the salt/sediment interface, compared to point A. The resultant value of γv′ in element at point C is altered by the salt creep..... 101
Figure 74. Total vertical stress path contour along curve ABC in the reservoir. The vertical stress path seems to be controlled by the dipping angle, which increases toward the salt/sediment interface..... 102
Figure 75. Total vertical stress path contour along a xy-plane in the middle of the reservoir after 13 years of production. The γzz′ is controlled by the dipping angle, which increases toward the salt/sediment interface. However, the γzz′ seems to be affected by the boundaries of the reservoir. 102

Figure 76. Total and effective maximum horizontal stress path as a function of distance from the salt/sediment interface, along the curve ABCD, after 13 years of production. The maximum horizontal stress path is controlled by the dipping angle and proximity to the salt dome, where the minimum value of γH occurred at the salt/sediment interface (0.21) and the major in the flat area. The spatial distribution of γH′ is controlled by the dipping angle and the proximity to the salt. It decreased more at the salt/sediment interface, compared to point A. The resultant value of γH′ in element at point C is altered by the salt creep..... 104

Figure 77. Total maximum horizontal stress path contour along curve ABC. The γHmax is function of the dipping angle and the proximity to the salt. Which indicates major changes at point A2, compared to the salt/sediment interface..... 105

Figure 78. Total maximum horizontal stress path contour along a xy-plane in the middle of the reservoir after 13 years of production. The γxx′ is controlled by the dipping angle, which decreases toward the salt/sediment interface. 105

Figure 79. Total and effective minimum horizontal stress path as a function of distance from the salt/sediment interface, along the curve ABCD, after 13 years of production. The minimum horizontal stress path is controlled by the well location, the proximity to the salt and the dipping angle. Where the maximum value of γh happened at the salt/sediment interface (0.493) and the lowest where the well is located. The value of γh at point C2 is not considered into the analysis, because it is altered by the salt creep. Which gives a wrong idea about the impact of the dipping angle. The spatial distribution of γh′ is controlled by the well location, the dipping angle and the proximity to the salt. It decreased less at the salt/sediment interface, compared to point B. The resultant value of γh′ in element at point C is altered by the salt creep. 107

Figure 80 Total minimum horizontal stress path contour along curve ABC. The minimum horizontal stress path increases toward the dome. Where the salt creep has a strong impact on the elements at the salt/sediment interface, decreasing the magnitude of γhmin. 108
Figure 81. Total minimum horizontal stress path contour along a xy-plane in the middle of the reservoir after 13 years of production. The γyy′ is controlled by the dipping angle, which increases toward the salt/sediment interface. However, the well location affects the γyy′, which decreases around the borehole. 108
Figure 82. Volumetric strain as a function of distance from the salt/sediment interface, after 13 years of production. Reservoir elements are represented in green, while salt elements are represented in blue. The volumetric strain is controlled by the well location, where the reservoir experienced the major compaction (-3.9x10 − 4). In addition, the element at the salt/sediment interface is analyzed and noticed that it shrunk more than the element at point A. The salt exhibited expansion at the salt/sediment interface..... 110
Figure 83. Volumetric strain behavior after 6 and 13 years of production, and 3 years after shut-in on a xz-plane in the middle of the reservoir. The reservoir and shale exhibit compaction after 13 years of production, with a stronger impact around the well (-3.9x10 − 4). Three years after shut in the well, the pressure built up, increasing the volume of the reservoir and shale elements. 111
Figure 84. Volumetric strain behavior along a xy-plane in the middle of the reservoir. (a) Initial state, (b) 6 years of production, (c) 13 years of production and (d) 3 years of steady state. The reservoir exhibited compaction that increases with depletion, which is controlled by the well location. Three years after shut in the well, the pressure built up, increasing the volume of the reservoir elements. 112

Figure 85. Cross-section of the model geometry in Y of Case 4. This plot shows the extension and thickness of the reservoir, shale and salt dome. 113
Figure 86. Pore pressure drawdown behavior with respect to BC at different locations, after 13 years of production. The parameters that impacted more the depletion in the reservoir was the Biot's coefficient and the dipping angle. The former induced additional pressure drawdown (up to 0.5 MPa), while the dipping angle decreased the pressure drop up to 0.8 MPa. 116
Figure 87. Pore pressure drawdown in the reservoir along trajectory ABCD, as a function of distance from the salt/sediment interface, after 13 years of production. Case 6 and 7 increased depletion in the reservoir, while Case 3, 4 and 5 decreased the pressure drop. Besides this behavior, the depletion observed in Case 4 tends to increase around the steeper dipping area.. 117
Figure 88. Total vertical stress behavior with respect to BC at different locations, after 13 years of production. The total vertical stresses did not vary significantly in the reservoir or the salt. The parameters that attenuated the σzz changes in the reservoir were the pore compressibility and the dipping angle. The former caused less reduction of σzz, while the dipping angle decreased more 118
Figure 89. Change of total vertical stress in the reservoir along trajectory ABCD, as a function of distance from the salt/sediment interface after 13 years of production. Case 3 and 4 reduced more the total vertical stress in the reservoir, with a major impact along the steeper dipping area, while Case 5, 6 and 7 presented less reduction of the σzz..... 119
Figure 90. Change of effective vertical stress in the reservoir along trajectory ABC, as a function of distance from the salt/sediment interface, after 13 years of production. Case 3, 4 and 5 presented the lowest effective stress magnitude along the reservoir, while case 6 and 7 increased the σzz′..... 120

Figure 91. Total maximum horizontal stress behavior with respect to BC at different locations, after 13 years of production. The dipping angle and the pore compressibility were the parameters that altered more the total maximum stress changes in the reservoir and the salt. Where Case 4 experienced the major reduction of σxx around the well, and the lowest at the salt/sediment interface..... 121

Figure 92. Change of total maximum horizontal stress in the reservoir along trajectory ABCD, as a function of distance from the salt/sediment interface after production. Case 3 and 4 reduced more the σxx, with a major impact around the well, extending 107 m toward the dome; beyond this point σxx decreased less than the other cases. Case 5, 6 and 7 presented less reduction of the σxx. 122

Figure 93. Change of effective maximum stress in the reservoir along trajectory ABC, as a function of distance from the salt/sediment interface, after 13 years of production. Cases 3 and 5 presented lower effective stress magnitude along the reservoir, while Cases 6 and 7 reported highest σxx′. Case 4 presented the lowest σxx′ value from point A to 107 m from the well toward the salt dome, where the σxx′ increased above the BC. 123

Figure 94. Total minimum horizontal stress behavior with respect to BC at different locations, after 13 years of production. The dipping angle, the reservoir pore compressibility and porosity were the parameters that altered more the total maximum stress changes in the reservoir. However, Case 3 presented the maximum reduction of σyy where the well is located. 124

Figure 95. Change of total minimum horizontal stress in the reservoir along trajectory ABCD, as a function of distance from the salt/sediment interface, after 13 years of production. Case 3 reduced more the σyy in the reservoir, with a major impact around the well, while the σyy

decreased less in Cases 4, 5 and 6. The σyy is more affected at the salt/sediment interface, compared to flat area. 125
Figure 96. Change of effective minimum stress in the reservoir along trajectory ABC, as a function of distance from the salt/sediment interface, after 13 years of production. Case 3 and 5 presented the lowest effective stress value along the reservoir, while case 6 and 7 experienced the maximum effective stresses. The resultant σyy′ for Case 4 is altered around the steeper dipping area, where it increased. 126
Figure 97. The Sxy total stress behavior with respect to BC at different locations, after 13 years of production. The dipping angle, the reservoir Young's modulus and the pore compressibility were the parameters that affected more the shear stresses in the reservoir. However, Case 4 presented the highest value of Sxy inside the salt. 127
Figure 98. Change of Sxy in the reservoir along trajectory ABCD, as a function of distance from the salt/sediment interface, after 13 years of production. The effect of higher reservoir porosity is to increase the induced shear stresses and concentrate them close to the well, while the other cases have the opposite impact. However, the stress perturbation magnitude at the salt/sediment interface increases for reservoirs less stiff. 128
Figure 99. The Syz total stress behavior with respect to BC at different locations, after 13 years of production. The dipping angle, the reservoir Young's modulus and the pore compressibility were the parameters that affected more the shear stresses at points B, C and D. However, Case 4 presented the major reduction of Syz at the salt/sediment interface. 130
Figure 100. Change of Syz in the reservoir along trajectory ABCD, as a function of distance from the salt/sediment interface, after 13 years of production. The lower reservoir Biot's coefficient

caused the maximum Syz increment at the salt/sediment interface, and the highest Syz reduction in the steeper dipping area of the producing layer. The Syz tend to decrease inside the salt. 131
Figure 101. The Sxz total stress behavior with respect to BC at different locations, after 13 years of production. The highest induced shear stress values occurred at point B. The dipping angle, the reservoir Young's modulus and the pore compressibility were the parameters that affected more the Sxz at points B, C and D. However, Case 3 presented the largest increment of Sxz at point B and Case 6 caused the largest reduction in the same location. 133
Figure 102. Change of Sxz in the reservoir along trajectory ABC, as a function of distance from the salt/sediment interface, after 13 years of production. The lower reservoir Young's modulus induced the highest increment of shear stresses around the well which extended toward the steeper dipping area, while reducing the pore compressibility induced the maximum Sxz in the same zone. However, Case 4 originated the mayor reduction of Sxz at the salt/sediment interface. 134
Figure 103. Total vertical stress path in the reservoir along trajectory ABC, as a function of distance from the salt/sediment interface, after 13 years of production. Cases 3, 4 and 5 increased the resultant stress path along the reservoir, where Case 4 exhibited the maximum increment in the steeper dipping area toward the dome. In the contrary, cases 6 and 7 decreased the γz in the producing formation..... 136
Figure 104. Effective vertical stress path in the reservoir along trajectory ABC, as a function of distance from the salt/sediment interface, after 13 years of production. The γv′ decreased less for cases 3, 4 and 7, where Case 4 exhibited the minor reduction in the steeper dipping area toward the dome. In the contrary, case 6 decreased more the γ′z along the reservoir..... 136

Figure 105. Total maximum horizontal stress path in the reservoir along trajectory ABC, as a function of distance from the salt/sediment interface, after 13 years of production. Cases 3 and 4 increased the resultant stress path along the reservoir, but in the steeper dipping area Case 4 exhibited the minimum stress path value in the producing formation. In addition, cases 6 and 7 decreased the γH in the reservoir. 138
Figure 106. Effective maximum horizontal stress path in the reservoir along trajectory ABC, as a function of distance from the salt/sediment interface, after 13 years of production. The γH′ decreased less for cases 3, 4 and 7, where Case 4 exhibited the major reduction in the steeper dipping area toward the dome. In the contrary, case 6 decreased more the γ′H along the reservoir. 139
Figure 107. Total minimum horizontal stress path in the reservoir along trajectory ABC, as a function of distance from the salt/sediment interface, after 13 years of production. Cases 3 and 4 increased the resultant stress path along the reservoir, but in the steeper dipping area Case 4 decreased toward the salt dome. In addition, cases 6 and 7 decreased the γh in the reservoir, where case 6 induced the lowest minimum horizontal stress path along the curve ABC. 141
Figure 108. Effective minimum horizontal stress path in the reservoir along trajectory ABC, as a function of distance from the salt/sediment interface, after 13 years of production. The γh′ decreased less for cases 3, 4 and 7. In the contrary, case 6 decreased more the γ′h along the reservoir and case 4 decreased more in the steeper dipping area. 141
Figure 109. Vertical strain behavior with respect to BC at different locations, after 13 years of production. The major volumetric strain changes in order of magnitude occurred at point B, point C and point A. The dipping angle and the reservoir Young's modulus increased compaction during production, while cases 5, 6 and 7 experienced less compaction at points A, B and C.. 143

Figure 110. Volumetric strain in the reservoir along trajectory ABCD, as a function of distance from the salt/sediment interface, after 13 years of production. Lower Young's modulus and higher dipping angle, increased compaction in the reservoir, reaching the major value around the well. Moreover, compaction at the salt/sediment interface is greater compared to point A..... 144

Abstract

The pore pressure decrease due to production from a reservoir causes changes in the total and effective stresses, leading to compaction and deformation of the reservoir and the surrounding rocks, which can translate into surface subsidence, casing deformation, sand production, and increment of seismic events in the compacted region. Reservoirs pierced by salt domes are characterized by complex stress regime close to the salt/sediment interface.

This thesis presents coupled flow and deformation numerical simulations to analyze the behavior of pore pressure and stress path along a reservoir pierced by a dome, as well as the influence of rock properties, reservoir dipping angles and salt creep on these trends after 13 years of production. The total stress path γ_j is defined as the ratio of the change in total stress $(\Delta\sigma_j)$ to the pore pressure change (Δp_f), and the effective stress path γ'_j is defined as the ratio of the effective stress changes $(\Delta'\sigma_j)$ to the pore pressure change (Δp_f). After 13 years of production, the total vertical stress in the reservoir decreased. The degree of reduction is a function of function of the well location (up to 1.42 MPa) and the 45° dipping angle (up to 1.7 MPa). The effective vertical stress increased as a function of the well location, where it reached a maximum value of 5.57 MPa and the dipping angle (up to 3.26 MPa. In the reservoir, the reduction of the total vertical stress at the salt/sediment interface was 1.46 MPa higher than the reduction in the area where the dipping angle is 0° “Flat area” (0.24 MPa). While the increment of the effective vertical stress at the salt/sediment interface was 0.99 MPa lower than the increment in the flat area (4.25 MPa). In addition, the total maximum horizontal stress decreased, also as a function of the well location (up to 2.55 MPa) and the dipping angle (up to 1.04 MPa). The effective maximum horizontal stress increased as a function of the well location (up to 4.52 MPa) and the dipping angle (up to

3.92 MPa). In the reservoir, the reduction of the total maximum horizontal stress at the salt/sediment interface was 1.04 MPa lower than the reduction in the flat area (2.08 MPa). While the increment of the effective maximum horizontal stress at the salt/sediment interface was 1.51 MPa higher than the increment in the area where the dipping angle is 0° (2.41 MPa). The total minimum horizontal stress decreased also as a function of the well location (up to 3 MPa) and the 45° dipping angle (up to 2.45 MPa). The effective minimum horizontal stress increased as a function of the well location (up to 3.92 MPa), while the increment at the salt/sediment interface (up to 2.52 MPa) and in the flat area (up to 2.49 MPa) was relatively the same. In the reservoir, the reduction of the total minimum horizontal stress at the salt/sediment interface was 0.45 MPa higher than the reduction in the flat area (2 MPa). The total vertical (γ_v) and minimum horizontal (γ_h) stress paths increase more at the salt/sediment interface than the flat region, while the effective vertical (γ'_v) and minimum (γ'_h) stress paths decreased less close to the dome compared to the well location and the flat area. The total maximum horizontal stress path (γ_H) behaved different, it increased less at the salt/sediment interface than the flat region, whereas the effective stress path (γ'_H) decreased more toward the salt dome. The spatial distribution of the stress path is controlled by the proximity to the salt, the dipping angle and the well location. Moreover, the horizontal stress reductions are more significant than the vertical stress reductions, with the highest reduction of the vertical and minimum horizontal stresses close to the salt dome where gravity drainage enhances the pore pressure drawdown near the salt/reservoir interface, compared to the changes in the flat zone. The depletion and the stress changes induce compaction in the reservoir.

The outcome from the sensitivity analysis shows that the reduction of the Young's modulus and the steeper dip angles of the reservoir magnified the reduction of the total vertical stress up to 0.5 MPa, the maximum horizontal stress up to 0.2 MPa and the minimum horizontal stress up to 0.1 MPa, during production. However, the effective vertical stress increased 0.4 MPa less, the effective maximum horizontal stress increased 0.3 MPa less and the effective minimum horizontal stress increased 0.3 MPa less. Which is reflected as an increment of the total vertical and horizontal stress path values, that have a significant impact on compaction (the volumetric strain increased up to $2.97x10^{-4}$). Lower reservoir pore compressibility and lower reservoir Biot's coefficient results on lower vertical and horizontal stress paths along the producing formation, that resulted in $1.07x10^{-4}$ less volumetric strain of the reservoir.

Chapter 1: Introduction

1.1 Problem statement

Salt structures have been of special interest to the oil and gas industry for many years, since a significant fraction of the world's hydrocarbon reserves are related to salt structures, that not only seal the reservoirs, but create structural potential traps. Additionally, salt structures are widely used as storage of oil, natural gas, CO_2, and nuclear waste. Depending on the depositional environment and the growth stages of salt domes, sand bodies are characterized by high porosity and permeability, that favor the accumulation of hydrocarbons (Jackson and Galloway 1984).

The salt rock is impermeable and capable to deform under certain conditions. Because of these properties, the sediments around these structures are exposed to several stress changes compared to the far field, making the salt/sediment interface very complex and extremely perturbated (Heidari et al., 2016). Geological layers generally show increasing dips toward the salt dome, indicating that diapirism alters the sediments structure. The steep reservoir dipping angle and the proximity to the dome, represent a challenge for the development of the field and generate concerns about the geomechanical implications on subsidence, compaction and sediment failure.

1.2 Objective

Our goal is to study the behavior of pore pressure and stress path along a reservoir pierced by a salt dome, as a mean to understand its impact on sediments deformation (compaction or expansion) and tendency to failure (shear stress increment). Additionally, a sensitivity analysis to study the influence of rock properties is performed –Young's modulus, porosity, permeability, Biot's coefficient and pore compressibility– and the reservoir dipping angle.

Chapter 2: Literature review

2.1 Salt domes

Salt domes are formed by gravitational equilibrium between the salt and the surrounding rocks, because of the density difference (Trusheim, 1960). High temperature reduces the salt viscosity, facilitating the salt to flow to places of lower overburden load. Circular to elliptical salt domes are must common in the Gulf of Mexico region of United States (see Figure 1). In a vertical cross section, the salt structure often looks cylindrical, and its diameter increases downward, so the flanks may be inclined to vertical (Halbouty & Hardin, 1956). The salt composition is mainly halite (sodium chloride) with some anhydrite (calcium sulfate). It behaves plastically at a temperature of 100°C and a pressure above 600 Kg/cm^2 (Baar, 1977). Domes are classified according to the depth of the caprock or the salt itself, into shallow, intermediate, and deep (Teas, 1935). The accumulation of hydrocarbons controlled by salt uplifts depends on the geometry of the salt structures. Figure 2 shows the most common type of hydrocarbon traps associated to salt domes. Petroleum geologists define the domes as piercement structures if the layers pierced are potential reservoirs, otherwise they are considered non-piercement. Pierced beds tend to upturn or overturn.

The salt is a weak material that cannot sustain shear stresses acting on the interface between the salt and the surrounding formations. This means that the principal stresses reorient to become perpendicular and parallel to this plane of weakness. If differential stresses are present in the salt, it deforms until it reaches an isotropic stress state ($\sigma_1 = \sigma_2 = \sigma_3$). Fredrich et al. (2003) demonstrated that horizontal stresses in a salt body are not always equal to the lithostatic stress, as it has been commonly assumed. On the contrary, the surrounding rock, can sustain shear

stresses, and its brittle behavior generates fault structures (Heidari et al., 2017). The stress regime around a salt can be complex with normal, reverse, and strike-slip regimes occurring in different zones in the rocks around the dome (Dusseault et all., 2004). The extent of the stress regimes and their magnitudes are hard to determine, particularly at the shoulders and upper flanks of the dome, because of plastic deformation imposed on the surrounding rock, porosity loss (diagenesis), bedding plane dip and sedimentary accretion are difficult to determine (Dusseault et al., 2004). Faulting associated with salt structures is predominantly normal, but strike-slip and reverse is present in some cases as well. Offset, radial, graben or horst are the typical fault patterns present over or adjacent to salt domes (Weijermars et al., 1993). Radial faults emerge from a central point, if domes are circular shaped and shallow.

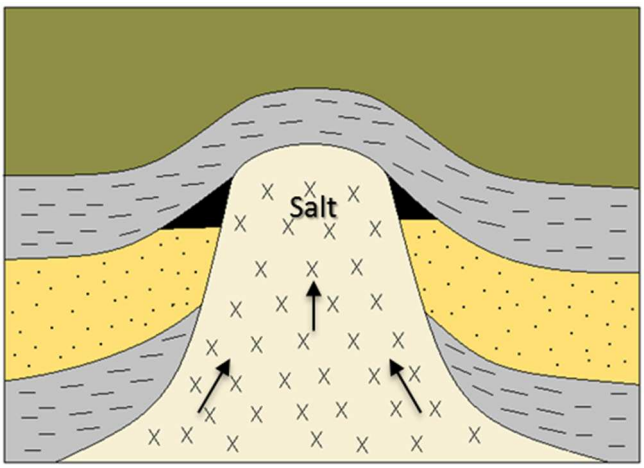


Figure 1. Circular salt dome shaped that upturned pierced beds favoring the accumulation of hydrocarbon.

Texas-Louisiana coastal basin is characterized by large salt intrusions (salt ridges or single salt domes, with numerous spike-like projections), some of them surrounded by a dry brittle shale.

Beds in direct contact with the salt will be more upturned than the ones in contact with the dried shale, as the shale absorbs most of the energy of the uplift (Halbouty 1979).

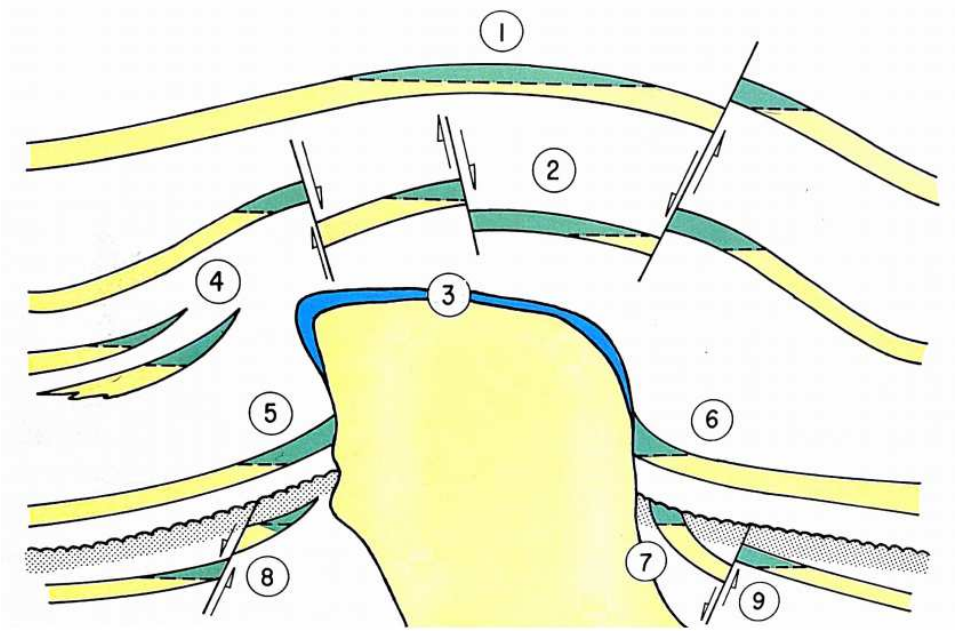


Figure 2. Hydrocarbon traps of an idealized section associated with salt domes: (1) simple domal anticline draped over salt; (2) graben fault trap over dome; (3) porous cap rock; (4) flank sand pinchout and sand lens; (5) trap beneath overhang; (6) trap uplifted and upholded against salt structure; (7) unconformity; (8) fault trap down-thrown away from dome; (9) fault trap downthrown toward dome (Halbouty, 1979).

2.2 Mechanical behavior of salt

The salt is a viscoplastic material that deforms over time, which alters the stresses of the surrounding sediments, making the salt/sediment interface complex and highly perturbated. The salt creep depends on many parameters including the temperature (Sriapai et al., 2012), the load rate (Zhang, 2006), the confining stresses (Hunsche & Hampel, 1999), and the salt properties themselves.

For many years, experiments have been done on salt to determine the creep mechanisms that affect the salt deformation. Climb-controlled dislocation mechanism (Harper & Dorn, 1957) occurs at lower stress levels, which is characterized by a linear relation at a constant temperature between the strain rate and an applied load, and an independent relationship between the strain rate and grain size at a given temperature and stress applied. Cross-slip dislocation mechanism happens when a screw dislocation moves from one plane to another (Heard, 1972; Skrotzki & Haasen, 1988; Wawersik & Zeuch, 1986). Pressure solution mechanism (Rutter, 1983), involves the dissolution of minerals at the contact between grains into a pore fluid in areas of high stress and deposit it into regions of the same rock of lower stress or removing it from the rock. Fluid-enhanced dynamic recrystallization (Urai, 1983), is a mechanism in which brine is present during the deformation of the rock, which first experiences dynamic recrystallization by grain boundary migration, followed by sub-grain development and equal boundary migration. Coble creep (Coble, 1963) is a mechanism of crystalline solids deformation, predominant at lower stress levels and higher temperatures.

Many scientists have developed constitutive models to predict the time-dependent behavior of salt. Norton (1929) formulated the viscoelastic Power Law, based on empirical tests. Herrmann et al., (1980) developed the empirical viscoelastic Waste Isolation Power Plant model (WIPP), which is commonly used for underground isolation of nuclear waste. Goodman (1989) defined the Burger model that combines the viscoelastic models of Maxwell and Kelvin, this law is frequently used for mining applications. Cristescu and Hunsche (1991) formulated an elastic/viscoplastic constitutive equation for salt rock. Hou and Lux (1998) proposed a new elastic/viscoplastic model for the salt, including damage and accelerated creep. Jin and Cristescu

(1998), developed a new elastic/viscoplastic model for transient creep. Itasca (2012) developed three constitutive viscoplastic models and implemented them in Fast Lagrangian Analysis of Continua in 3 Dimensions (FLAC-3D). The Burgers-creep (Cvisc), that combines the Burger and the Mohr Coulomb models. The Power Law viscoplastic model (Cpower), that combines the Norton Power Law and the Mohr Coulomb models. The WIPP-creep viscoplastic model that combines the WIPP model and the Drucker-Prager model (Pwipp).

Shahmorad et al., (2016) conducted a study to analyze the Burger, Power Law and WIPP model, which concluded that the Power Law and WIPP models are more capable of predicting underground salt behavior than Burger. It determined that the Norton Power Law offers a more conservative analysis. Another study was performed by Durup and Xu (1993) who compared 5 common salt constitutive models (Lemaitre, Norton-Hoff Power, Power, Transient Power, and Munson-Daw-son), which showed that the Norton power law and other combined laws describe accurately the salt creep deformation when the temperature effect is ignored. The two parameters power law has been commonly used to model the rock salt behavior for many years (Ehgartner & Sobolik, 2002; Munson, 1998; Park et al., 2005; Wawersik & Zeuch, 1984).

2.3 Two-component Norton Power Law

The Norton Power Law is a viscoelastic formulation developed by Norton (1929), which is commonly used to model the creep behavior of salt. The standard form of this viscoelastic model is given by

$$\dot{\epsilon_{cr}} = A\overline{\sigma}^{n} \quad (1)$$

Where $\dot{\epsilon}_{cr}$ is the creep rate, A and n are the material properties, and $\bar{\sigma}$ is the deviatoric stress, also known as von Mises stress. The latter is defined by $\bar{\sigma} = \sqrt{3J_2}$, where J_2 is the second invariant of the effective deviatoric stress tensor and is given by Eq. (2)

$$J_2 = \frac{((\sigma_1 - \sigma_2)^2 + (\sigma_1 - \sigma_3)^2 + (\sigma_2 - \sigma_3)^2)}{6} \quad (2)$$

In Eq. (2), $\sigma_1, \sigma_2 \; and \; \sigma_3$ are the principal stresses.

When the amount of data justifies adding more parameters to the creep law, we could use the two-component viscoelastic law, which is based on multiple creep mechanisms:

$$\dot{\epsilon}_{cr} = \dot{\epsilon}_1 + \dot{\epsilon}_2 \quad (3)$$

Where:

$$\dot{\epsilon}_1 = \begin{cases} A_1 \bar{\sigma}^{n_1} & \bar{\sigma} \geq \sigma_1^{ref} \\ 0 & \bar{\sigma} < \sigma_1^{ref} \end{cases}$$

$$\dot{\epsilon}_2 = \begin{cases} A_2 \bar{\sigma}^{n_2} & \bar{\sigma} \leq \sigma_2^{ref} \\ 0 & \bar{\sigma} > \sigma_2^{ref} \end{cases}$$

The σ_1^{ref} is a reference value. If $\sigma_1^{ref} = \sigma_{12}^{ref} = 0$, $\bar{\sigma}$ is always positive, which translates to a one-component law with

$$\dot{\epsilon}_{cr} = A\bar{\sigma}^{n_1} \qquad \bar{\sigma} \geq \sigma_1^{ref} \quad (4)$$

If both components are active: $\sigma_1^{ref} = 0$ and $\sigma_{12}^{ref} =$ "large",

$$\dot{\epsilon}_{cr} = A\bar{\sigma}^{n_1} + A\bar{\sigma}^{n_2} \qquad \sigma_1^{ref} < \bar{\sigma} < \sigma_2^{ref} \quad (5)$$

2.4 The Mohr Coulomb Model

The Mohr-Coulomb model received its name in honor to Coulomb (1776) and Mohr (1906). It is used to define the shear strength of rocks and soils at different effective stresses. The failure

envelope corresponds to a Mohr coulomb criterion (shear yield function) with a tension cutoff (tension yield function).

The Mohr Coulomb criterion implemented by Itasca (2012) is formulated in terms of the principal stresses (σ_1, σ_2 and σ_3). Figure 3 represents the failure criterion in the plane (σ_1, σ_3). Compressive stresses are negative, so $\sigma_1 \leq \sigma_2 \leq \sigma_3$. The failure envelope is defined from point A to B by the Mohr Coulomb failure criterion $f^s = 0$, where:

$$f^s = \sigma_1 - \sigma_3 \left(\frac{1+\sin\phi}{1-\sin\phi}\right) + 2C\sqrt{\left(\frac{1+\sin\phi}{1-\sin\phi}\right)} \tag{6}$$

And from point B to C by the tension failure criterion $f^t = 0$, where:

$$f^t = \sigma_3 - \sigma^t \tag{7}$$

Where ϕ is the friction angle, C is the cohesion, and σ^t is the tensile strength, which cannot exceed the value of σ_3 that corresponds to the intersection of the straight lines $f^s = 0$ and $\sigma_3 - \sigma_1 = 0$ in the plane mentioned before. The maximum value of σ^t is given by

$$\sigma^t_{max} = \frac{c}{\tan\phi} \tag{8}$$

The potential function is defined by two functions, the shear plastic flow (g^s) and tensile plastic flow (g^t). The shear plastic flow is given by

$$g^s = \sigma_1 - \sigma_3 \left(\frac{1+\sin\psi}{1-\sin\psi}\right) \tag{9}$$

Where ψ is the dilation angle and the tensile plastic flow is given by

$$g^t = -\sigma_3 \tag{10}$$

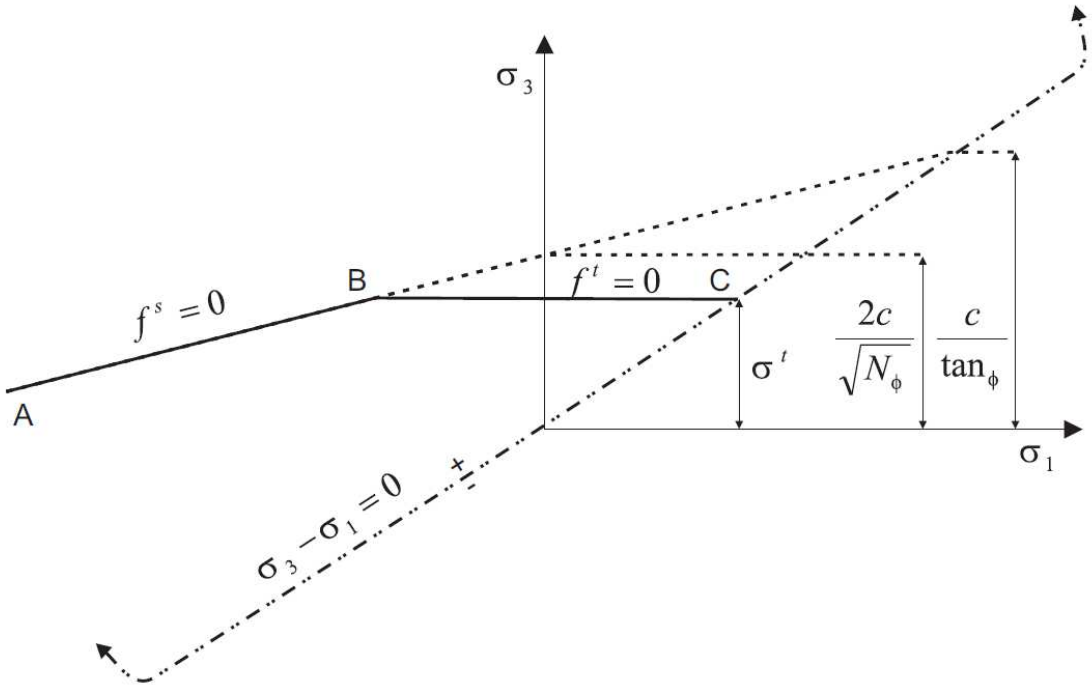


Figure 3. Mohr Coulomb failure criterion implemented by Flac-3D, which combines the Mohr Coulomb criterion with a tension cutoff (Itasca, 2012).

2.5 The Power Law viscoplastic model

The viscoplastic model (Cpower) generated by Itasca (2012), integrates the Two-component viscoelastic Power Law and the Mohr Coulomb elasto-plastic model. In the Cpower formulation, the total strain rate is decomposed into elastic ($\dot{\epsilon}^{e}_{ij}$), viscous ($\dot{\epsilon}^{c}_{ij}$) and plastic ($\dot{\epsilon}^{p}_{ij}$) components:

$$\dot{\epsilon}_{ij} = \dot{\epsilon}^{e}_{ij} + \dot{\epsilon}^{c}_{ij} + \dot{\epsilon}^{p}_{ij} \tag{11}$$

Where the elastic strain rate $\dot{\epsilon}^{e}_{ij}$ is the only component contributing to the stress rate Itasca (2012). The deviatoric behavior is visco-elasto-plastic is defined by Itasca (2012):

$$\dot{S}_{ij} = 2G\left(\dot{e}_{ij} - \dot{e}^{c}_{ij} - \dot{e}^{p}_{ij}\right) \tag{12}$$

Where G is the shear modulus. The deviatoric stress component ($\dot{S}_{ij}$) and the deviatoric strain component ($\dot{e}_{ij}$), are given by von Mises (1913):

$$\dot{S}_{ij} = \sigma_{ij} - \sigma_0 \delta_{ij} \tag{13}$$

$$\dot{e}_{ij} = \epsilon_{ij} - \frac{e_{vol}}{3}\delta_{ij} \tag{14}$$

Where δ_{ij} is the Kronecker delta, $\delta_{ij} = 0$ if $i \neq j$ and $\delta_{ij} = 1$ if $i = j$.

$$\sigma_0 = \frac{\sigma_{kk}}{3} \tag{15}$$

And

$$e_{vol} = \epsilon_{kk} \tag{16}$$

The volumetric behavior is elasto-plastic and is defined by Itasca (2012) as:

$$\dot{\sigma}_0 = K\left(\dot{e}^{e}_{vol} - \dot{e}^{p}_{vol}\right) \tag{17}$$

Where $\dot{\sigma}_0 = (\dot{\sigma}_{11} + \dot{\sigma}_{22} + \dot{\sigma}_{33})/3$, $\dot{e}_{vol} = \dot{e}_{11} + \dot{e}_{22} + \dot{e}_{33}$, and K is the bulk modulus.

According to Norton (1929), creep is activated as a consequence of the von Mises stress $q = \sqrt{3J_2}$. The creep rate is defined by Norton (1929) as:

$$\dot{e}^{c}_{ij} = \dot{e}_{cr}\frac{\partial q}{\partial S_{ij}} \tag{18}$$

Deriving the von Mises stress, we obtained the direction of creep flow:

$$\frac{\partial q}{\partial S_{ij}} = \frac{3}{2}\frac{S_{ij}}{q} \tag{19}$$

The creep intensity $\dot{e_{cr}}$ has two components, according to the two-component Norton Power Law

$$\dot{e_{cr}} = \dot{e^{1}_{cr}} + \dot{e^{2}_{cr}} \tag{20}$$

Where:

$$\dot{e^{1}_{cr}} = \begin{cases} A_1 q^{n_1} & q \geq \sigma_1^{ref} \\ 0 & q < \sigma_1^{ref} \end{cases}$$

$$\dot{e^{2}_{cr}} = \begin{cases} A_2 q^{n_2} & q \leq \sigma_2^{ref} \\ 0 & q > \sigma_2^{ref} \end{cases}$$

Mohr Coulomb flow rule define the plastic strain rate,

$$\dot{e}_{ij}^{p} = \dot{e}_{p} \frac{\partial g}{\partial \sigma_{ij}} - \frac{1}{3} \dot{e}_{vol}^{p} \delta_{ij} \tag{21}$$

Where

$$\dot{e}_{vol}^{p} = \dot{e}_{p} \left[\frac{\partial g}{\partial \sigma_{11}} + \frac{\partial g}{\partial \sigma_{22}} + \frac{\partial g}{\partial \sigma_{33}} \right] \tag{22}$$

The Mohr Coulomb potential function (g) is used to express the direction of plastic flow $\partial g / \partial \sigma_{ij}$, and the Mohr Coulomb yield criterion $f = 0$ define the plastic flow rate intensity $\dot{e}_{p}$. The yield and potential functions for shear yielding, in the principal axes formulation are defined by (Mohr, 1906) as:

$$f = \sigma_1 - \sigma_3 \left(\frac{1 + \sin \phi}{1 - \sin \phi} \right) + 2C \sqrt{\left(\frac{1 + \sin \phi}{1 - \sin \phi} \right)} \tag{23}$$

$$g = \sigma_1 - \sigma_3 \left(\frac{1 + \sin \psi}{1 - \sin \psi} \right) \tag{24}$$

For the tension yielding, the functions are

$$f = \sigma^{t} - \sigma_3 \tag{25}$$

$$g = -\sigma_3 \tag{26}$$

Where σ_1 and σ_3 are the minimum and maximum principal stresses (compression negative), C is the material cohesion, ϕ is the friction, ψ is the material dilation, σ^{t} is the tensile strength.

To implement this model, the viscoelastic response is calculated initially for the first timestep, defined to keep the system in quasi-static mechanical equilibrium. Followed by the calculation of the principal stresses and principal directions. Then a verification of the yield criterion takes place, if the criterion is not met $f \neq 0$, the plastic strain increments are added for the step and the

increment intensity $\lambda = \dot{e_p}\Delta t$ is computed to satisfy the yield criterion $f = 0$. This method follows the Mohr Coulomb model implementation, where the viscoelastic response replaces the "elastic guess" for the step.

2.6 Stress path

Changes in pore pressure generally result in changes of the total vertical and horizontal stresses acting on the reservoir. Geertsma (1973), proposed a theory based on the theory of linear poroelasticity (Biot, 1941), that relates the subsidence and stress changes with reservoir compaction, assuming equal elastic properties for the reservoir and the surrounding rock. Hettema et al. (2000) presents an equation to show the vertical stress changes induced by depletion above a compacting reservoir, that represents the Geertsma's theory

$$\Delta\sigma_v = \frac{h\Delta p}{r}\left(\frac{1-2v}{2-2v}\right) f\left(\frac{d}{r}\right) \tag{27}$$

Where (d) is the depth, (r) is the radius, (h) is the thickness and (v) is the Poisson's ratio, $(\Delta\sigma_v)$ is the vertical stress change, and (Δp) is the pore pressure change. For reservoir with a lateral extension greater than their depth $(r > d)$, the function $f(d/r) < 1$. Defining the parameter γ_v, to represent the vertical stress changes during depletion, Eq. (27), gives

$$\gamma_v = \frac{\Delta\sigma_v}{\Delta p} = \frac{h}{r}\left(\frac{1-2v}{2-2v}\right) f\left(\frac{d}{r}\right) \tag{28}$$

The stress changes induced by compaction are significantly small for laterally extensive reservoirs (Hettema et al., 2000).

The total stress path is defined as the ratio of total stress change to the pore pressure change (Geertsma, 1973) and it is represented mathematically as:

$$\gamma_j = \frac{\Delta\sigma_j}{\Delta p_f} \tag{29}$$

The subscript j represents the 3 principal stresses and p_f the reservoir pore pressure. While the mathematical expression to represent the effective stress path is:

$$\gamma'_j = \frac{\Delta\left(\sigma_j - \alpha p_f\right)}{\Delta p_f} \tag{30}$$

Where (α) is the Biot-Willis coefficient.

The total normal and shear stresses change because of a Poroelastic effect in the rock. Analyzing the same point on two or more Mohr circles, is a mechanism to understand how the stresses and pore pressure change in the reservoir. In general, the stress path behavior from an initial state (point A) to a final state (point A') is a function of reservoir properties and geometry. Figure 4 shows the possible total stress paths followed by a reservoir that undergoes depletion, while Figure 5 shows the possible effective stress paths.

Another way to express the stress path is as the ratio of the change in effective minimum horizontal stress $(\Delta\sigma'_h)$ to the change in effective vertical stress $(\Delta\sigma'_v)$:

$$K = \frac{\Delta\sigma'_h}{\Delta\sigma'_v} \tag{31}$$

The changes in effective horizontal and vertical stresses that accompany depletion are defined following the theory of poroelasticity (Rice & Cleary, 1976), as:

$$\Delta\sigma'_v = \Delta\sigma_v - \alpha\Delta p_f \tag{32}$$

$$\Delta\sigma'_H = \Delta\sigma_H - \alpha\Delta p_f \tag{33}$$

$$\Delta\sigma'_h = \Delta\sigma_h - \alpha\Delta p_f \tag{34}$$

The term $(\Delta\sigma_v)$ is the changes of total vertical stress, $(\Delta\sigma_H)$ is the changes of total maximum horizontal stress, $(\Delta\sigma_h)$ is the changes of total minimum horizontal stress, and (α) is the Biot-Willis coefficient that relates the effect of pore pressure and total stresses to the deformation of the rock (Zimmerman, 1991). Alpha takes values between 0 and 1; higher Biot's coefficients lead to higher reduction of the effective stresses due to pore pressure (Biot, 1941). Substituting Eq. (32) and (34) into Eq. (31), gives the following expression:

$$\mathrm{K} = \frac{\Delta\sigma_\mathrm{h} - \alpha\Delta\mathrm{p_f}}{\Delta\sigma_\mathrm{v} - \alpha\Delta\mathrm{p_f}} \tag{35}$$

Considering a laterally infinite reservoir, which elastic properties are the same as those of the surrounding rocks (homogeneous subsurface), If it is assumed that the reservoir compacts uniaxially (no lateral strain), and that fluid withdrawal does not change the total vertical stress $(\Delta\sigma_\mathrm{v} = 0)$ in the reservoir, which means that the vertical stress path is zero $(\gamma_\mathrm{v} = 0)$, the horizontal stress path is derived from Eq. (35):

$$-\alpha\mathrm{K}\Delta\mathrm{p_f} = \Delta\sigma_\mathrm{h} - \alpha\Delta\mathrm{p_f}$$

$$\Delta\sigma_\mathrm{h} = \alpha\Delta\mathrm{p_f}(1 - \mathrm{K})$$

$$\gamma_\mathrm{h} = \alpha(1 - \mathrm{K}) \tag{36}$$

Based on the previous assumption, the effective vertical and minimum horizontal stresses are defined as:

$$\Delta\sigma'_\mathrm{v} = -\alpha\Delta\mathrm{p_f} \tag{37}$$

$$\Delta\sigma'_\mathrm{h} = \mathrm{K}\Delta\sigma'_\mathrm{v} \tag{38}$$

Rearranging Eq. (36) and substitute the value of K into Eq. (38), the effective minimum horizontal stress is:

$$\Delta\sigma'_\mathrm{h} = \left(1 - \frac{\gamma_\mathrm{h}}{\alpha}\right)\Delta\sigma'_\mathrm{v} \tag{39}$$

To calculate the depletion coefficient, it is necessary to substitute Eq. (31) into Eq. (36):

$$\gamma_h = \alpha\left(1 - \frac{\Delta\sigma'_h}{\Delta\sigma'_v}\right) \tag{40}$$

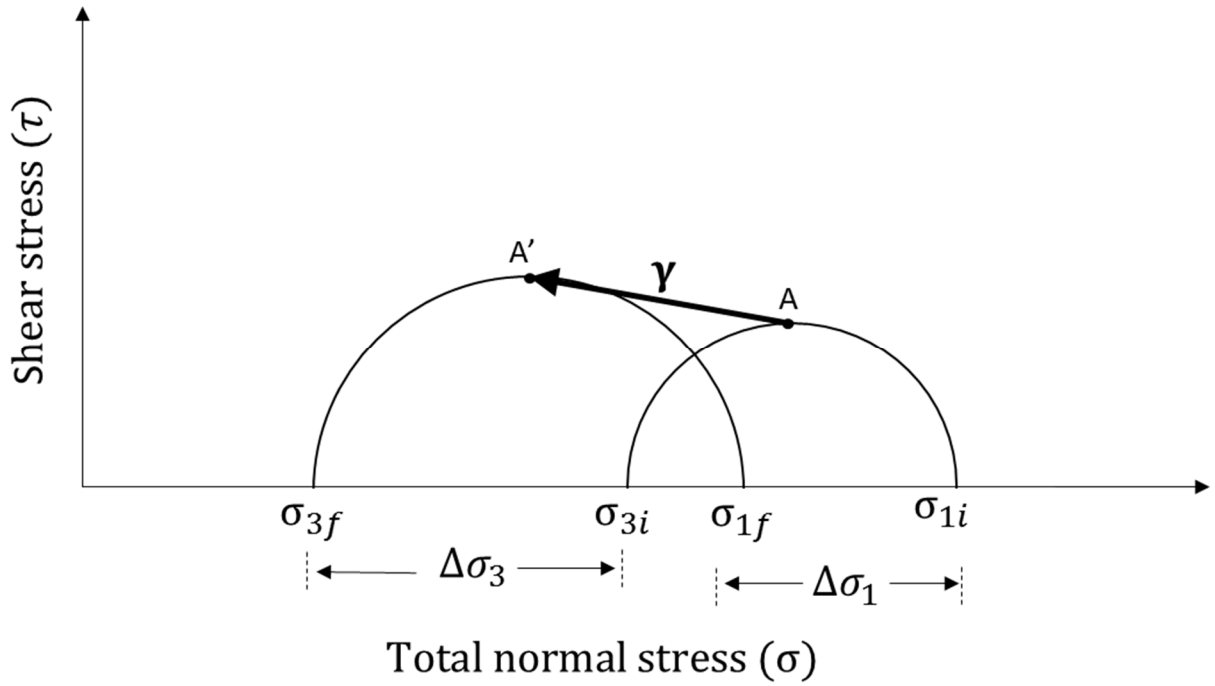


Figure 4. Simple illustration of the possible total stress path (γ) followed by a reservoir that undergoes depletion, analyzing the same point that moves from the position A to A'. The initial state is represented by the small Mohr circle and the final state by the big Mohr circle. Which means that depletion induces the total stresses to decrease, in this case, σ_3 decreases more than σ_1 which makes the Mohr circle diameter to increase.

Teufel et al. (1991) have argued the validity of the hypothesis based on the theory of linear poroelasticity, that assumes a laterally infinite reservoir with elastic properties that match the surroundings (no lateral strain). Additionally, Segall & Fitzgerald (1998) stated that assuming only vertical strain but no lateral, contradicts the field observations.

Eshelby (1957) proposed a relation to determine the stress and strain within an elliptical reservoir, which elastic and isotropic properties are different from the surrounding rocks. Posterior to this study, Rudnicki (1999) introduced an analytical model, based on Eshelby's formulation, to calculate the reservoir stress path coefficients for different geometries (reservoir aspect ratio: e = vertical/horizontal axis) and various Poisson's ratio.

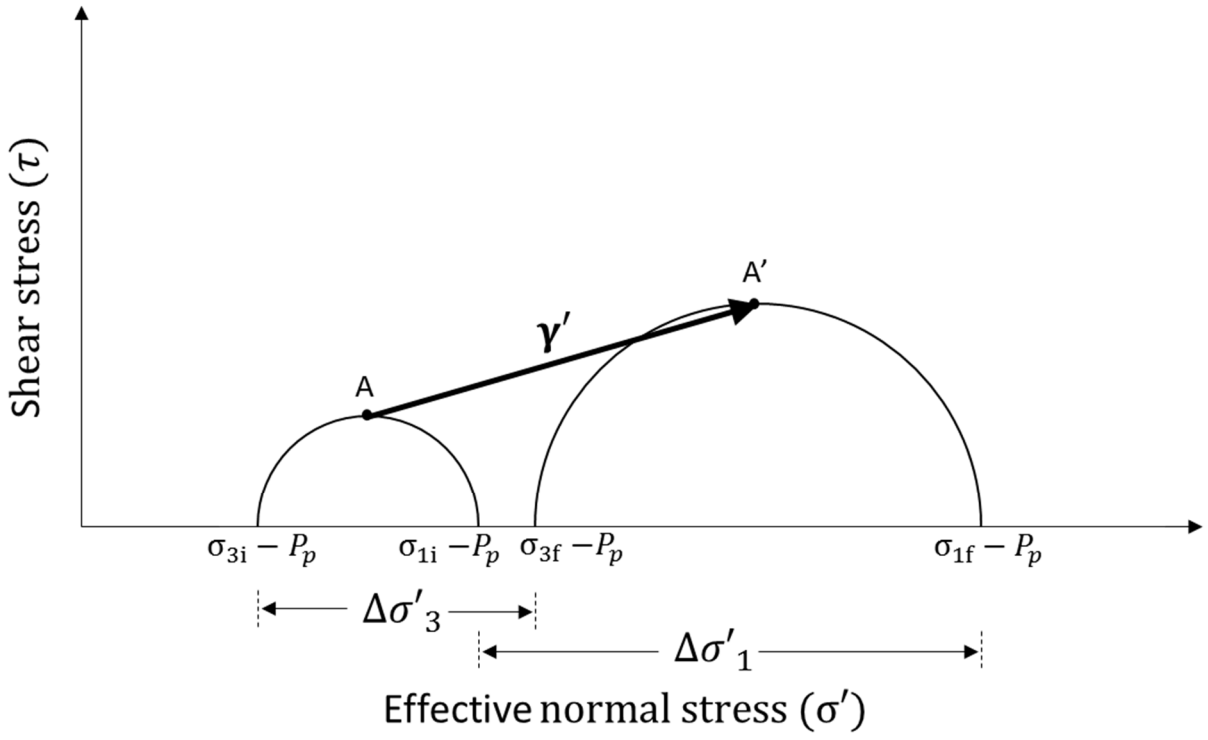


Figure 5. Simple illustration of the possible effective stress path (γ') followed by a reservoir that undergoes depletion, analyzing the same point that moves from the position A to A'. The initial state is represented by the small Mohr circle and the final state by the big Mohr circle. Which means that depletion induces the effective stresses to increase. The Mohr circle diameter changes because the total principal stresses σ_3 and σ_1 change in a different proportion.

Holt et al. (2004) adapted Rudnicki's model to demonstrate that the reservoir geometry and the contrast of elastic properties within and around the producing formation, control the stress path

and the effects linked to it. Other researchers studied and confirmed the same theory (Gheibi et al., 2016; Holt et al., 2016)).

In the field, the stress path can be determined by measuring the in-situ stresses in the formation while the pore pressure is altered. Warpinski et al. (1985) and Warpinski & Teufel (1989) measured the in situ stresses in sequences of sandstones and shales, finding out that the stresses in the sandstones are anisotropic. Anisotropic state of stress alters the matrix permeability and the rock compressibility (Bruno et al., 1991).

Hydraulic fracturing (mini-frac test), leak-off-test (LOT) or extended leak-off test (XLOT), are some of the techniques used to determine the minimum principal stress (S_3) (Economides & Nolte, 1989). The vertical stress is generally considered to be lithostatic, while the maximum horizontal stress (S_{Hmax}) can be obtained from indirect techniques that requires knowledge (S_3). For example, drilling-induced tensile fractures and wellbore breakouts (Barton et al., 1988).

2.7 Effects of stress path on compaction

The stress and pore pressure changes in the reservoir altered progressively the sediments porosity, permeability and rock compressibility, inducing compaction. Holt et al. (2004), provided a formulation based on the theory of linear poroelasticity, to calculate the compaction of a reservoir that experiences a reduction of pore pressure:

$$\frac{\Delta h}{h} = \alpha \frac{\left(1 - \frac{\gamma_v}{\alpha}\right) - 2v\left(1 - \frac{\gamma_h}{\alpha}\right)}{E}(-\Delta p_f) \tag{41}$$

Where h is the reservoir thickness, Δh is the compaction, E and v is the Young's modulus and Poisson's ratio of the drained rock framework, respectively; α is the Biot's coefficient, γ_v and γ_h is the vertical and horizontal stress path, respectively; Δp_f is the pore pressure change.

Analyzing compaction as a function of the reservoir geometry, Holt et al. (2004) observed that compaction decreases if the aspect ratio increases ($e = \text{vertical axis}/\text{horizontal axis}$). In addition, they evaluated the contrast of elastic properties between the reservoir (presented as an ellipsoidal inclusion) and the surroundings within the limits of linear poroelasticity, when the reservoir experiences depletion, and noticed that if a reservoir is soft compared to the rocks around it, the total vertical stress in the reservoir decreases more and the effective vertical stress increases less, which translates into a larger vertical stress path (γ_v) and less compaction in the reservoir because of the stiff rock above that sustains the overburden weight. In the opposite case (stiffer reservoir than the surroundings), the total minimum horizontal stress decreases less, while the effective minimum horizontal stress increases more; which induce small minimum horizontal stress path (γ_h) and lower compaction

Rhett & Teufel (1991) performed laboratory compression experiments on high porosity chalk ($\phi = 34\%$ to 39%) to simulate the stress path during production and subsequent waterflooding in the Ekosfik field. The results obtained from these tests indicated compaction of the formation after depletion followed by shear failure related to the high injection pressure of seawater while waterflooding. Which increases the fracture density maintaining the reservoir permeability (good productivity), despite compaction. Teufel et al. (1991b) conducted a study of the same formation in the Ekosfik field, analyzing the rate of effective stress changes ($K = \sigma'_{hmin}/\sigma'_v$) during production and concluded that the shear stresses in the chalk increased significantly after depletion causing compaction and over 4 meters of seafloor subsidence (see Figure 6). Additional studies on the influence of stress path on sandstone compressibility and matrix permeability (Rhett & Teufel, 1992), concluded that the reservoir compressibility is greater

under hydrostatic loading than under uniaxial strain, while the matrix permeability decreases under hydrostatic loading and increases for $K \leq 0.5$.

A research conducted in the Groningen field, The Netherlands, to demonstrate the influence of stress path in compaction during depletion, showed that the influence of stress path on compaction of the high porosity sandstone is controlled by the location of the stress path vector relative to the failure envelope. If the stress path reaches the failure envelope, the rock experiences inelastic compaction, which translates into more plastic deformation (Hettema et al. 2000).

A geomechanical model was developed by Schutjens et al. (2012) to predict the stress changes associated with the depletion in a reservoir pierced by two salt domes in the Pierce field, Aberdeen, UK. Schutjens et al. (2012) showed that the vertical and horizontal stress paths show a spatial distribution controlled by the dipping angle and the proximity to the salt, that resulted in compaction of the reservoir and expansion of the over and under-burden.

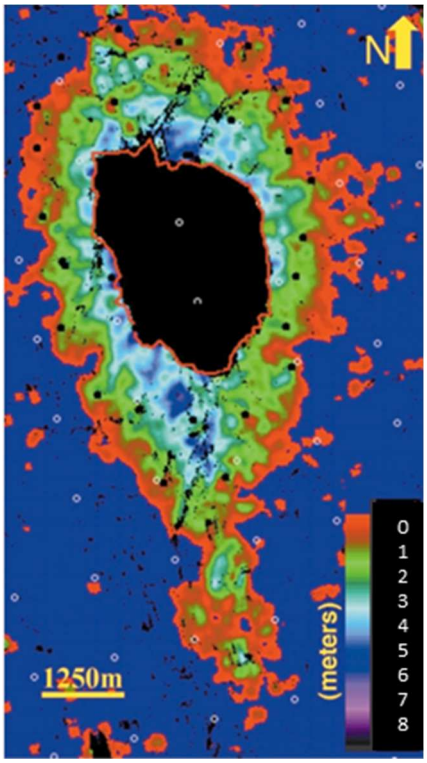


Figure 6. Ekofisk seismic-derived compaction map with water injection wells displayed as black dots from 1989 to 1999 (Guilbot & Smith, 2002).

Chapter 3: Geomechanical model

3.1 Model Geometry

A 3D finite difference geomechanical model was created using FLAC 3D, to determine the behavior of pore pressure, stress path and compaction in and around a reservoir pierced by a salt dome. We consider a salt dome surrounded by shale layers and a reservoir layer in the middle. The reservoir extends around just a portion of the salt (see Figure 7) 2590 m in x direction, 609 m in y-direction, and its thickness is 38 m. The reservoir dips at 45 degrees around the salt structure and becomes horizontal 204 m away from the dome.

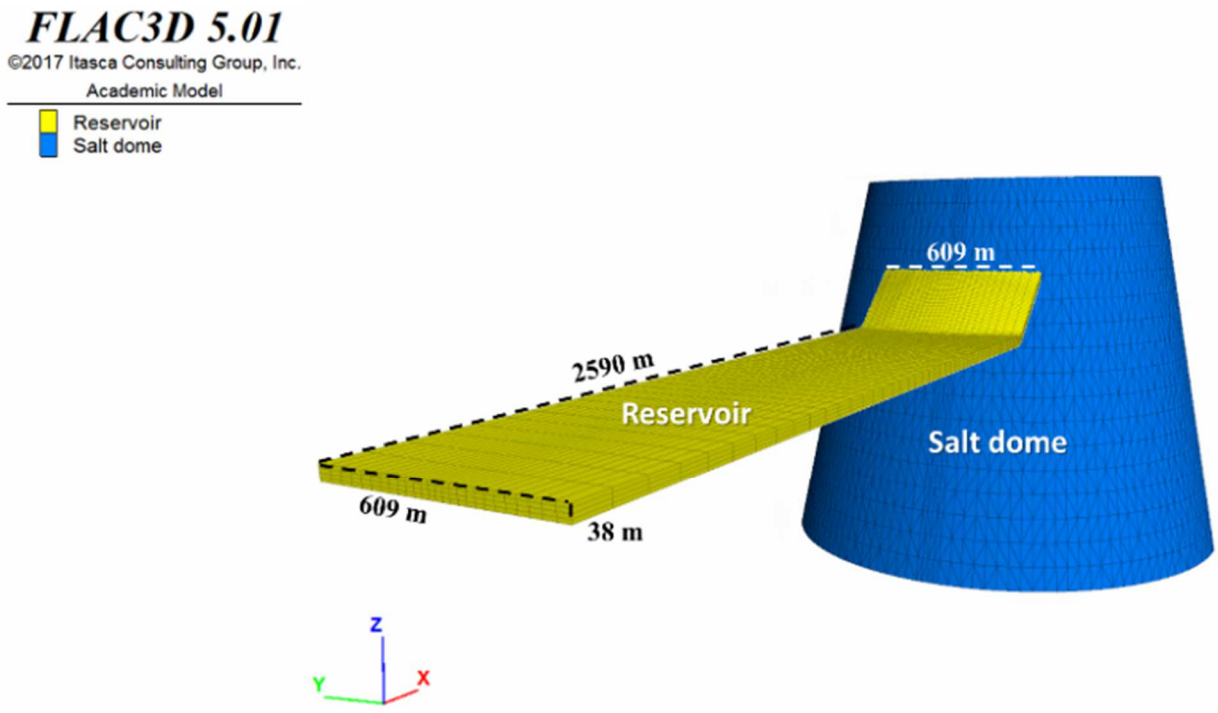


Figure 7. Reservoir dimensions. The size of the reservoir is 2590 m, 609 m and 38 m in x, y and z-direction.

The salt dome is half the shape of a cylindrical truncated cone, its height is 1524 m, the minimum radius is 595 m and its maximum radius is 930 m. The shale layers above and below

the reservoir have a thickness of 558 m and 927 m, respectively. There are 204 m of shale next to the reservoir and extends to the boundary of the model (See Figure 8).

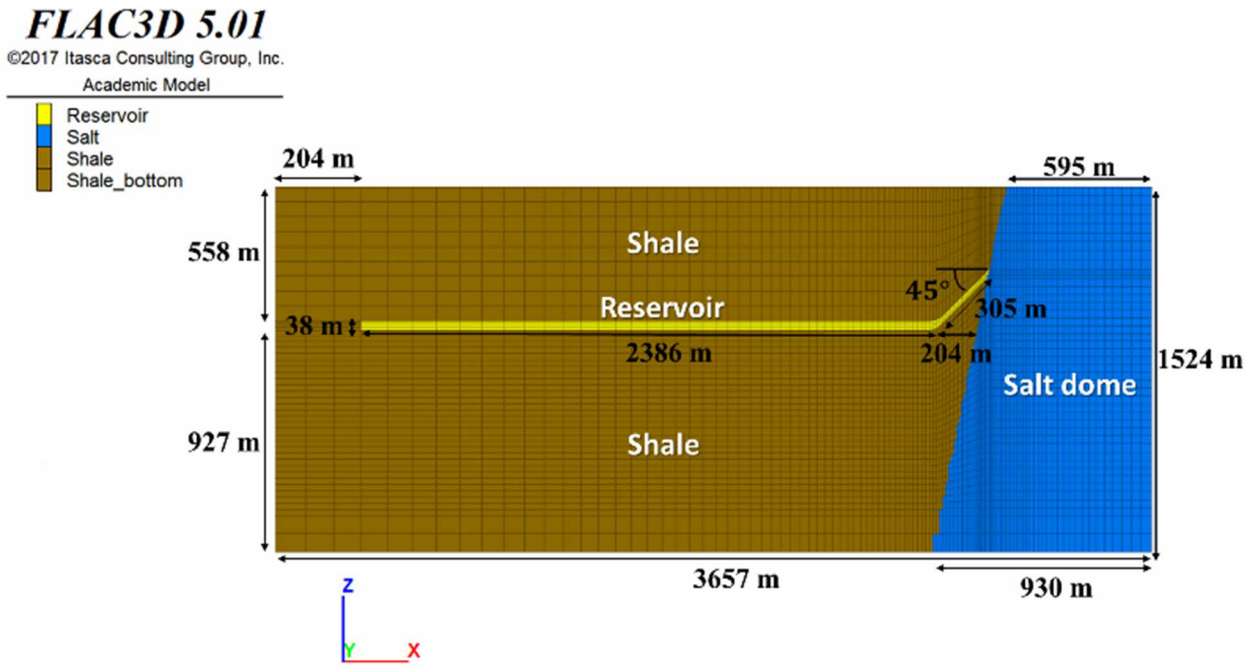


Figure 8. Cross-section of the model geometry in Y. This plot shows the extension and thickness of the reservoir, shale and salt dome.

The tilted reservoir and shale sediments have a smooth geometry, while the salt dome elements have a LEGO shape, to keep the same vertical size ratio for the elements (see Figure 9). The model has 287 thousand elements, which extend 3657 m in X-direction, 2133 m in Y-direction and 1524 m in Z-direction. The top of the model is 1524 m below ground level (see Figure 10). Elements are finer close to the salt/sediment interface, which is the area of interest, and become coarser toward the model boundaries.

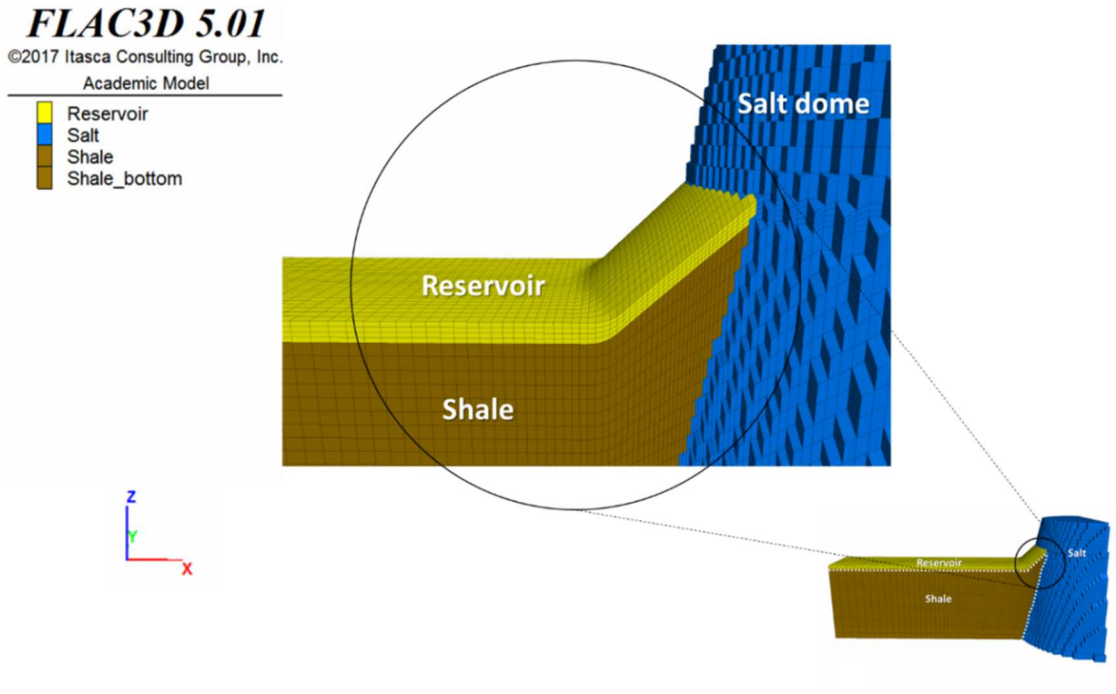


Figure 9. Model Geometry. The Reservoir layer (yellow) dips 45 degrees toward the salt dome (blue). The shale is constituted for 2 groups: lower shale (brown) and upper shale (brown).

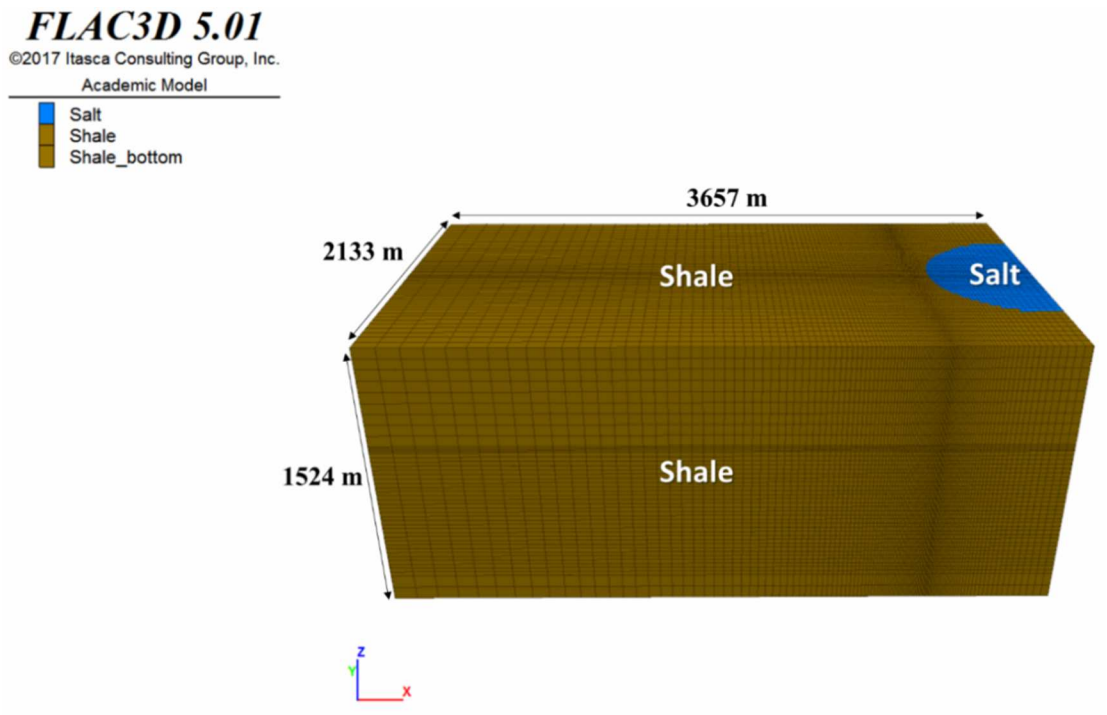


Figure 10. Model dimensions. The size of the model is 3657 m, 2133 m and 1524 m in x, y and z-direction.

3.2 Rock mechanical and fluid properties

The shale layers and the reservoir are treated as elastic materials and the Mohr Coulomb criterion is used to assess their failure response. A constitutive time-dependent model, Creep Power Law (Cpower), is used to simulate the salt creep deformation. The reservoir is assumed to be a Lower Miocene weak sandstone, which mechanical properties are described by Manzano Angeles (2014). We used the Pierre-1's shale mechanical properties defined by Islam and Skalle (2013) and Ojala (2011), and the Napoleonville salt dome properties from a test conducted by RE/SPEC (Ratigan, J.L., Nieland, J.D., and Osnes, 1993). Table 1 summarizes the mechanical properties implemented in our simulation and Table 2 the creep parameters of the salt. The salt cohesion value is set high to prevent shear failure.

Table 1. Rock mechanical input properties.

Rock Type	Reservoir	Shale	Salt
Density (Kg/m^3)	2252	2330	2162
Young Modulus (MPa)	10342	13858	31095
Poisson's Ratio	0.35	0.33	0.18
Bulk Modulus (MPa)	11514	13237	16202
Shear Modulus (MPa)	3833	5240	13168
Friction Angle	32.72	30	50
Cohesion (MPa)	4.7	10.5	68.9
Tensile strength (MPa)	6.9	7	1.6

Table 2. Creep power law input properties from Napoleonville salt dome

Parameter	Symbol	Value	Units
Power-law constant	A1	4.64E-32	1/yr
Power-law constant	A2	6.32E-24	1/yr
Power-law exponent	n1	5.5	-
Power-law exponent	n2	4	-
Reference stress	rs1	0	MPa
Reference stress	rs2	0.07	MPa

The rock porosity and permeability, for each formation is presented in Table 3. For simplicity, it is assumed that the reservoir is fully saturated with oil, and the overburden and shale are saturated with fresh water (see Table 4).

Table 3. Rock permeability and porosity data.

Rock Type	Reservoir	Shale	Salt
Porosity	0.18	0.24	0.01
Permeability (md)	2.47	$3.15x10^{-5}$	$1.00x10^{-21}$

Table 4. Rock saturation and fluid properties.

Rock Type	Reservoir	Shale	Salt
Saturation Fluid	Oil	Water	-
Saturation	1	1	0
Fluid Density (Kg/m^3)	815.5	1000	-

3.3 Boundary and initial conditions

The bottom of the model domain is fixed in the z-direction, but it can freely move in the x- and y-directions due to the lateral extent. This also prevents the sediments from failing in shear when the salt is allowed to creep. Rollers are applied to the sides, allowing the model to move freely in the z-direction (see Figure 11). The gravity is 9.8 $\mathrm{m/sec^2}$. Fluid flow is allowed between the reservoir and shale.

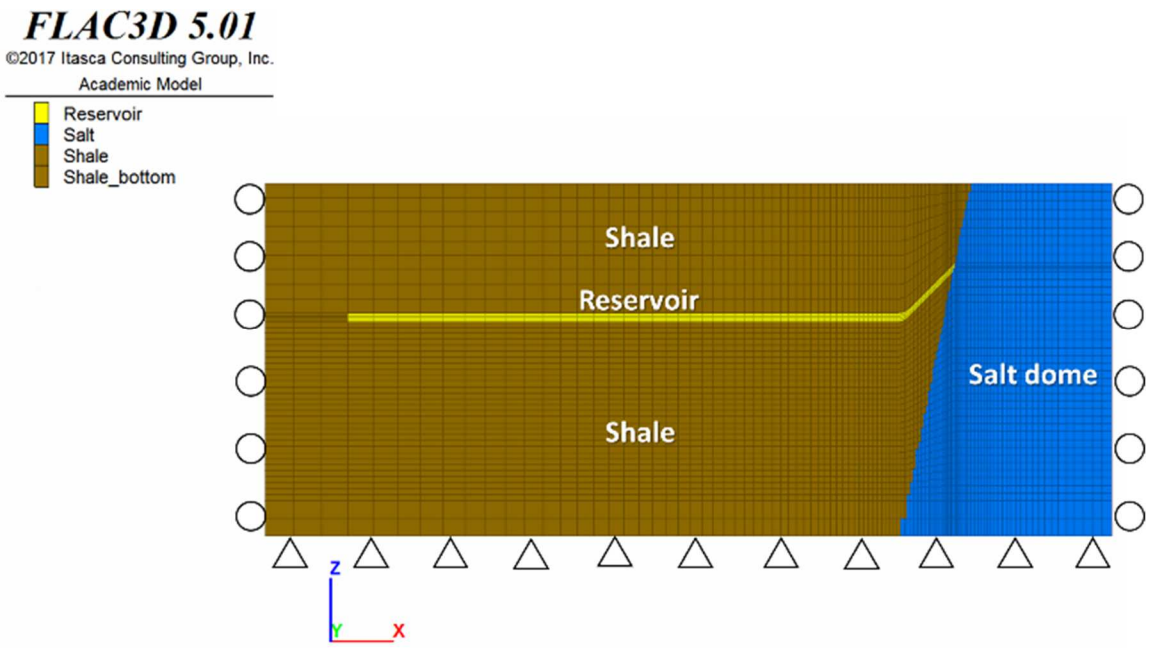


Figure 11. Model boundary conditions. Fix in the bottom, and rollers on the sides. The top can move freely on z-direction.

3.4 Initial conditions

The reservoir initial pore pressure gradient is $0.8x10^{-2}$ MPa/m, and the shale pore pressure is $0.98x10^{-2}$ MPa/m. The salt is nearly impermeable, and it is assumed to have a saturation equal to zero. The stresses are zero at the surface (depth=0). The overburden applied to the top of the model is different for the salt and shale. Layers above the salt are: 228 m of soft sediments, 76 m

of caprock and 1219 m of salt. Layers above the shale are 304 m of soft sediments, 990 m of shale and 228 m of sandstone.

The salt dome state of stress is assumed to be hydrostatic, so the total vertical, minimum and maximum horizontal stresses have the same magnitude, and increase at a gradient of $2.12x10^{-2}$ MPa/m in x-, y- and z- directions $(\sigma_{xx} = \sigma_{yy} = \sigma_{zz})$. It should be noticed that this equation represents a stress variation as a function of depth, that may not be valid for all the stress states present in the salt. The initial state of stress for the rest of the model is set as follows: The maximum total stress is vertical ($S_v = S_z = S_1$), the intermedium stress is horizontal in x-direction ($S_2 = S_x = S_{Hmax}$), and the minimum stress is horizontal in y-direction ($S_3 = S_y = S_{hmin}$), as it can be seen in Figure 12. The vertical stress gradient is calculated using the rock density, gravity and depth. Table 5, shows the vertical and horizontal stress gradients.

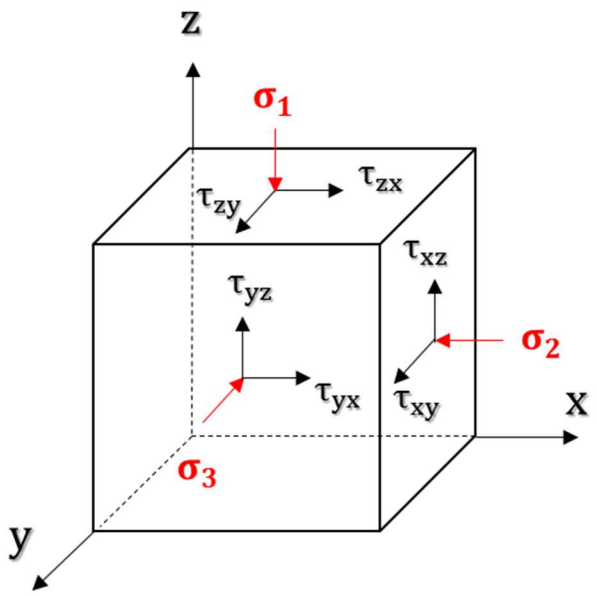


Figure 12. Stress tensor that represents the initial orientation of the principal stresses at a point in the model.

Table 5. Shale, Reservoir and Salt total stress gradients. The maximum principal stress is the vertical, the intermedium and the minimum are horizontal.

Rock Type	Reservoir	Shale	Salt
Maximum Stress Gradient (MPa/m)	$2.20x10^{-2}$	$2.28x10^{-2}$	$2.12x10^{-2}$
Intermedium Stress Gradient (MPa/m)	$1.85x10^{-2}$	$1.92x10^{-2}$	$2.12x10^{-2}$
Minimum Stress Gradient (MPa/m)	$1.74x10^{-2}$	$1.80x10^{-2}$	$2.12x10^{-2}$

Chapter 4: Simulation description

A model for fluid and creep calculations is configured. First, the mechanical model and material properties for each formation are assigned. The boundary conditions (rollers in the walls and pins at the bottom of the model and turned on gravity) are set and the overburden stress is applied to the top of the model. Then, the principal stresses for each zone are initialized, defining the stress gradients and thicknesses. A permeability isotropic fluid model is created, the fluid properties for the oil and water, and the porosity and permeability in each zone are assigned. Next, the initial pore pressure gradient is set according to the fluid density and thickness of the layers.

The simulation is run coupled for several time steps, with no creep until the model reached mechanical equilibrium. After reaching equilibrium, the maximum value of the Von Mises shear stress $\bar{\sigma}$ in the model is calculated and replaced into the power law equation, to find the maximum creep time step Δt_{max}^{cr}. Creep is run once the fluid flow results are obtained. To run creep, the automatic creep timestep (Dt) is initialized, updated during cycling, and controlled by the minimum (lfob) and maximum (ufob) unbalanced force ratio limits, latency, minimum (Mindt) and maximum (Maxdt) creep timestep, and a minimum (lmul) and maximum (umul) multipliers. In creep, the timestep increases (is multiplied by $\text{lmul} = 1.05$) if the unbalanced force ratio in the model falls below the limit defined ($\text{lfob} = 1\text{x}10^{-6}$) or decreases (is multiplied by $\text{umul} = 0.9$) if the unbalanced force ratio in the model exceeds the maximum limit defined ($\text{ufob} = 5\text{x}10^{-6}$). It is necessary to assign the minimum number of creep timesteps that must elapse before the timestep changes ($\text{latency} = 3$). Once the creep timestep (Dt) exceeds the minimum creep timestep ($\text{Mindt} = 1\text{x}10^{-8}$), it will not be allowed to fall below this value. Moreover, creep timestep size is not allowed to exceed the maximum creep timestep size.

The model was allowed to creep for 100,000 years to let the sediments and the salt reach equilibrium. The shear stress in the salt decreased (see Figure 13) and the principal stresses in the sediments around the dome reoriented: the maximum total principal stress S_1 is oriented parallel to the salt dome wall pointing downward. The intermediate total principal stress S_2 is oriented radially pointing outward from the salt dome. The minimum total principal stress S_3 is oriented circumferentially around the salt (see Figure 14).

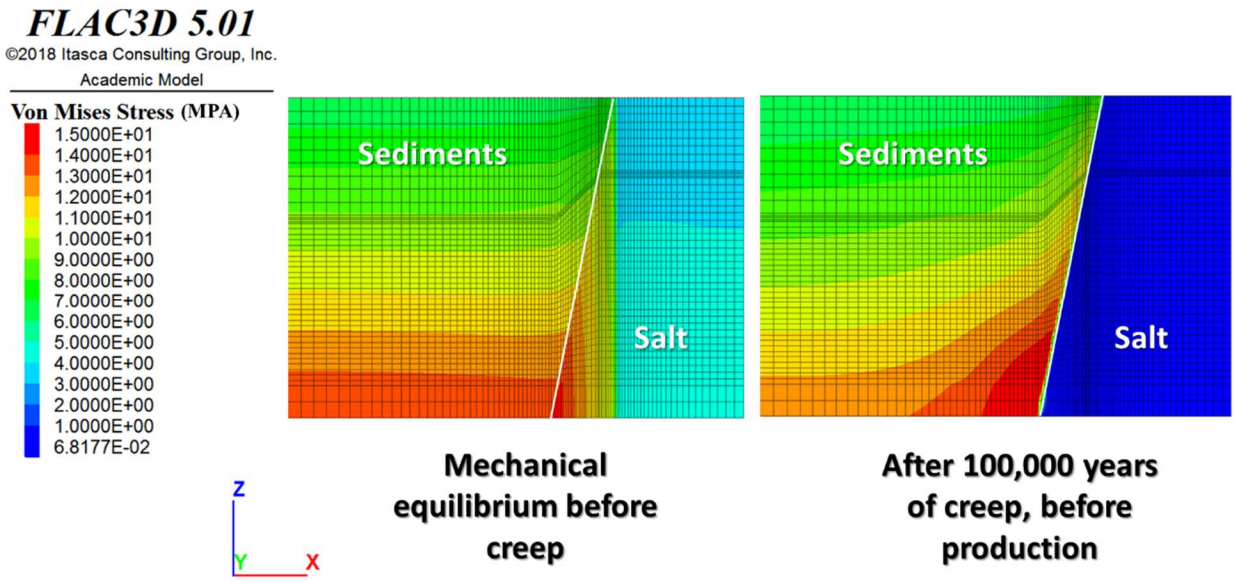


Figure 13. Von Mises shear stresses at mechanical equilibrium and after 100,000 years of creep. It is observed that the shear stresses in the salt decreased significantly because of plastic deformation of the salt, after 100,000 years of creep.

Once the initial stress of state is obtained, the parameter in the model are set to start production. To run fluid flow, the displacement and velocities in x-, y- and z-direction are set to zero. The production well is placed 122 m away from the salt dome and produced at a constant rate of 80 BOPD for 13 years. Once the fluid flow results are obtained for production, the velocities in x-, y- and z-direction are set to zero, and creep is run for 13 years, to see the effect of salt creep

during depletion. Additionally, the stress and pressure changes in the reservoir after shut-in are studied, letting the model reach a steady state. Once the fluid flow results for 3 years of pressure build up are obtained, creep is run for 3 years. Total simulation time: 16 years.

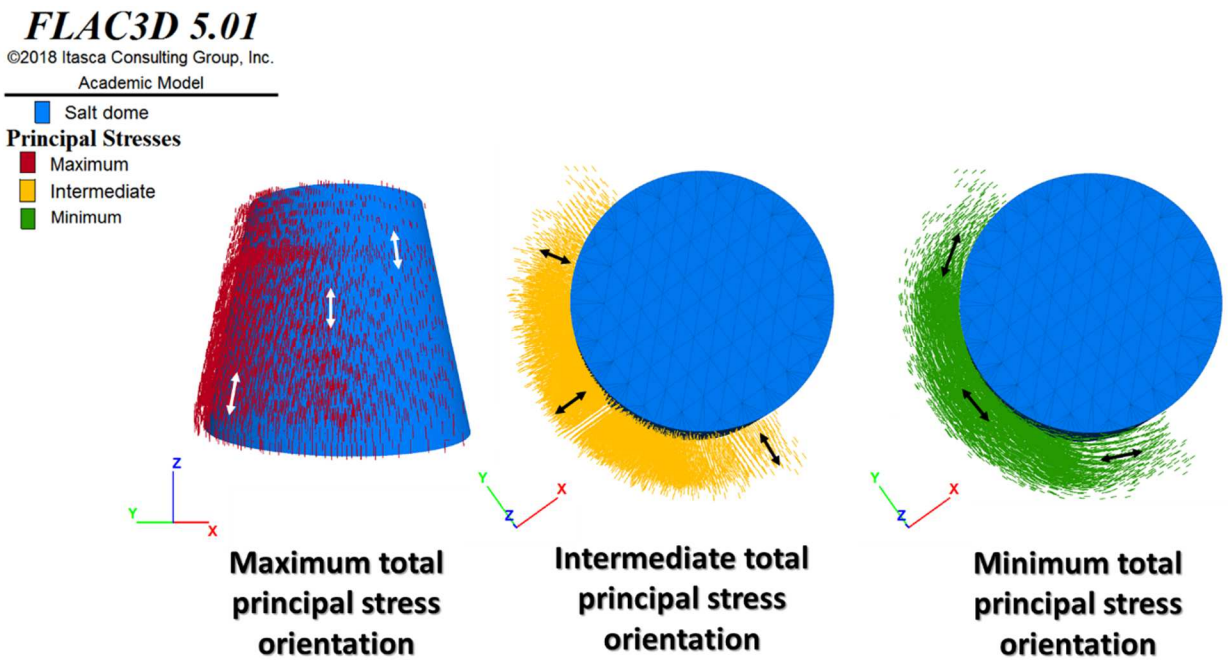


Figure 14. Orientation of the principal stresses around the salt dome before production. The arrows indicate the general trend of the stress vector orientation at that point.

Chapter 5: Results

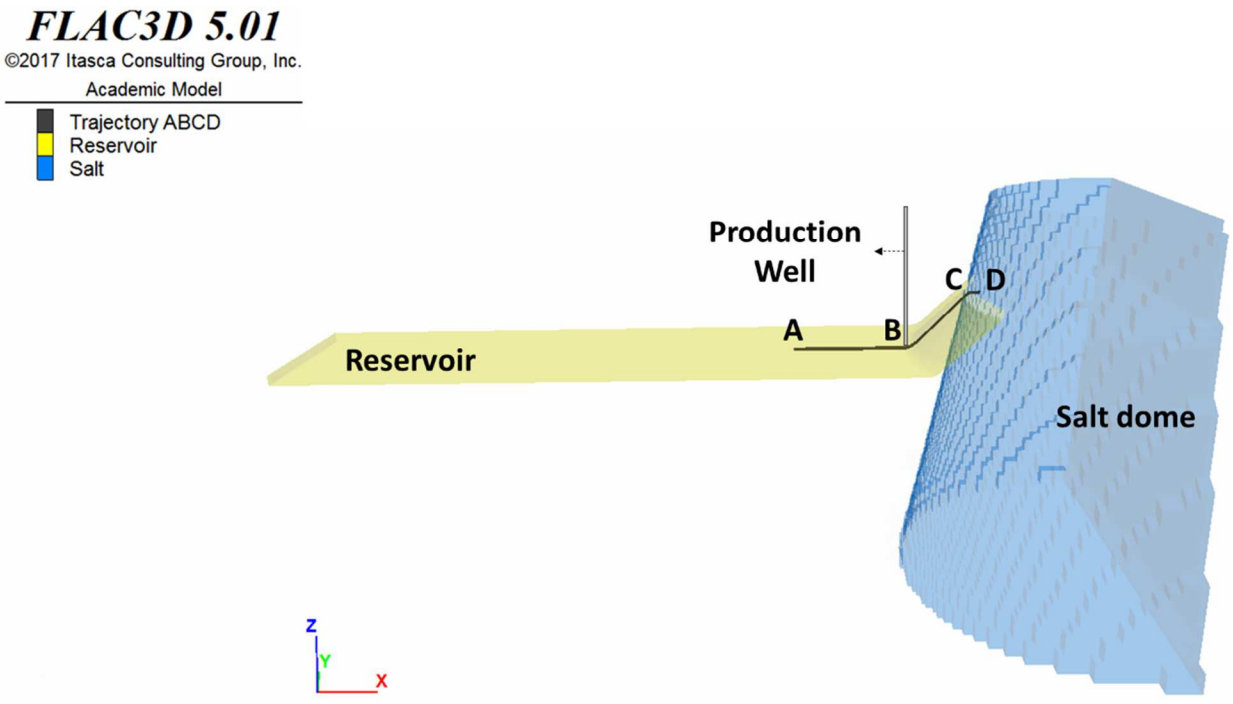
In this section we present the results for a tilted reservoir pierced by a salt dome that underwent production, followed by a pressure build up period. Table 6 shows the well schedule during the simulation time.

Table 6. Well schedule.

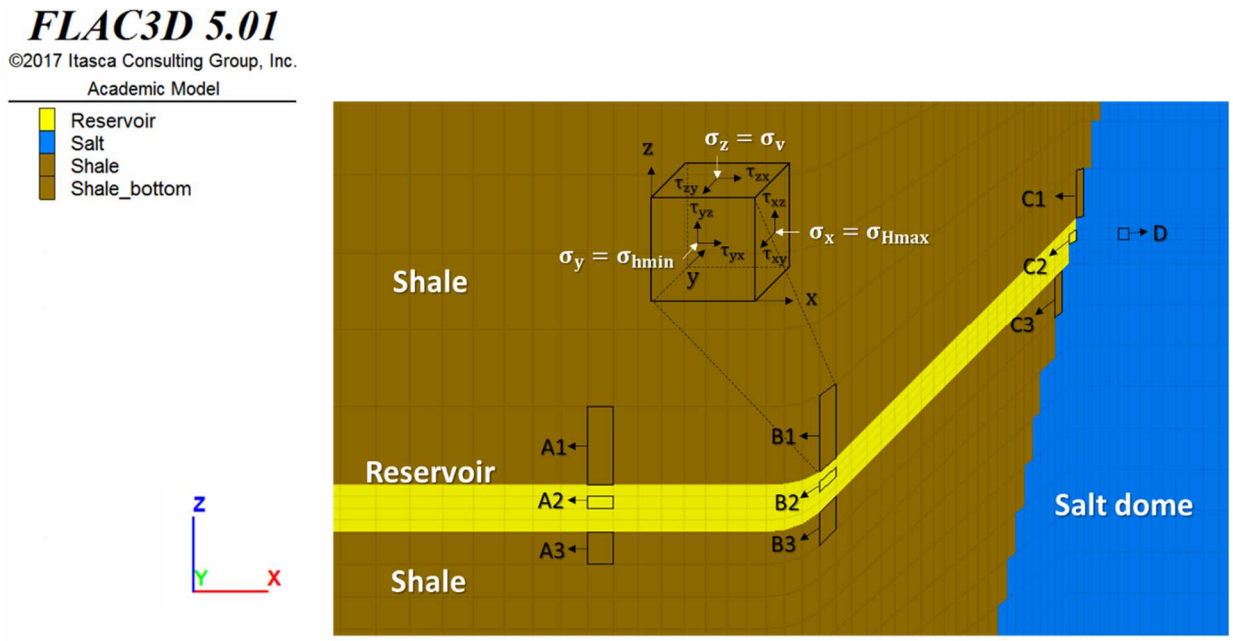
Well Status	Duration [year]
Production	13
Shut-in	3

To show the data as a function of distance from the salt/sediment interface, a trajectory ABCD of elements is defined, where the elements from points A to C belong to the reservoir, and from C to point D to the salt (see Figure 15(a)). The distance from point A to the well (point B) is 182.4 m, while the separation between the well and point C is 196.2 m.

Furthermore, a vertical subdivision of the segment ABC is defined to display the reservoir and shale information of elements located at representative places (flat region, around the well, salt/sediment interface), as can be seen in Figure 15(b). In addition, the elements with a black frame are used to analyze the changes in the pore pressure, total and effective stresses, stress path and compaction. Elements A1, B1 and C1 belong to the upper shale; A3, B3 and C3 pertain to the lower shale; while A2, B2 and C2 outline the reservoir elements.



(a)



(b)

Figure 15. (a) Trajectory ABCD along the reservoir and salt dome. Point A is in the flat region of the reservoir located 182.4 m apart from the well, point B represents the position of the well, point C is located at the salt/sediment interface, and D is 38 m inside the salt. (b) Vertical subdivision of the segment ABC along the shale and reservoir, including an element inside the salt (point D).

5.1 Pore pressure

Figure 16 shows the change of pore pressure values after 13 years of production. The maximum pore pressure drawdown in the reservoir occurred around the well (6.9 MPa) and is equivalent to 40% of the initial value. It is observed that the well location controls the depletion pattern. The pressure drop is higher at the salt/sediment interface (4.96 MPa ~ 31.9%), compared to point A2 (4.49 MPa ~ 25.9%), which is 8 m closer to the well. The previous behavior can be associated to the effect of gravity drainage.

The results obtained at points C1, C2 and C3 are not considered into the analysis of the dipping angle effect, because the elements at the salt/sediment interface are affected by the salt creep and may give a different perspective. Instead these elements will be studied separately to demonstrate the impact of salt deformation at the salt/sediment interface. The salt creep has a significant impact on the pore pressure drawdown at point C2 (5.21 MPa), which caused a change of the stress path followed by the other elements next to it (see Figure 16).

Figure 17(d) and Figure 18(d) show the pressure build up values after shut-in, where the fluid in the reservoir rises smoothly. The pore pressure in the reservoir increased 1.08 MPa in the flat region, 3.38 MPa around the well and 1.32 MPa at the salt/sediment interface (see Figure 19). The order of magnitude of these observations are consequent with the points that presented the highest depletion in the reservoir.

Although the initial pore pressure in the salt is set to zero, FLAC-3D contours are obtained from gridpoint-based values on the surfaces of zones in the range, which means that elements from the

salt (element with lower pore pressure) that share a gridpoint with the reservoir or shale, will not have a pore pressure of zero. Instead, the pore pressure of that element is calculated by volumetric averaging the lower and higher magnitude of the gridpoints that form the element, as it can be observed in the salt element next to the salt/sediment interface in Figure 16. The pressure in the salt at point D remain zero during production and after shut-in (see Figure 19).

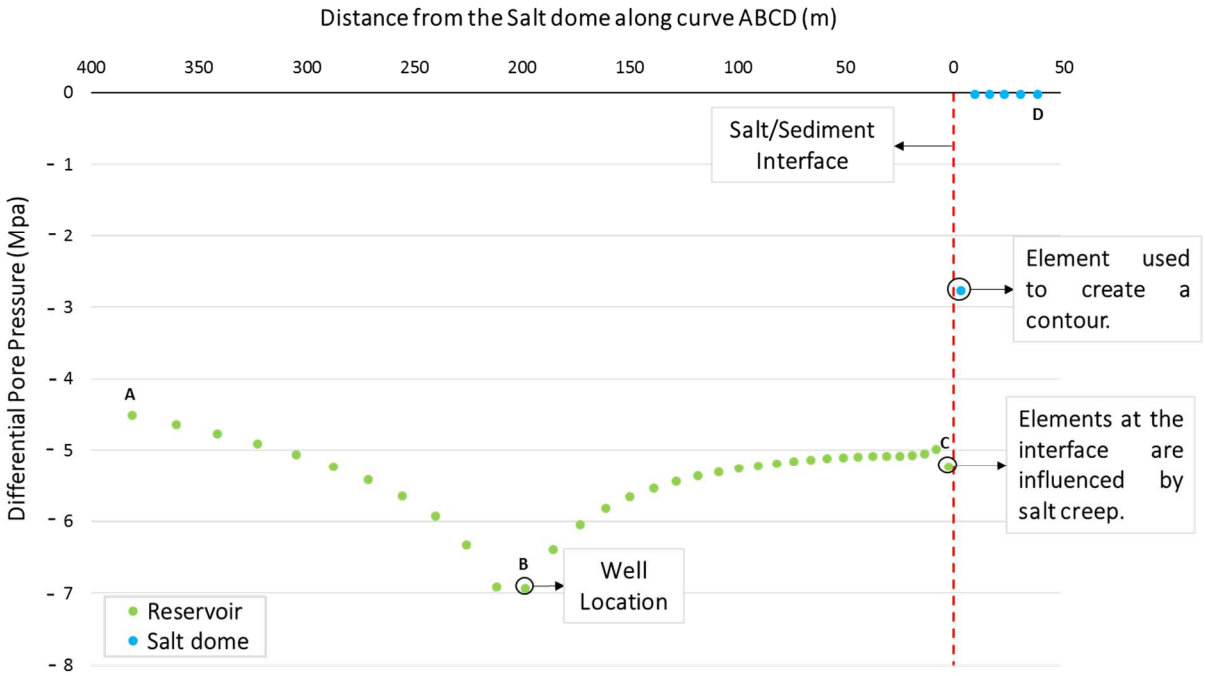


Figure 16. Differential pore pressure as a function of distance from the salt/sediment interface, along the curve ABCD defined in Figure 15. (a), after 13 years of production. Reservoir elements are represented in green, while salt elements are represented in blue. The pressure drawdown and pressure build up at a certain location is controlled by its location relative to the well. The salt pore pressure remains zero after production. The pore pressure of the reservoir elements at the salt/sediment interface is altered by the salt creep. The salt elements at the salt/sediment interface present a pore pressure different than zero, because the contour of this element interpolates the values of the sediment gridpoint (different than zero) and salt gridpoint (zero).

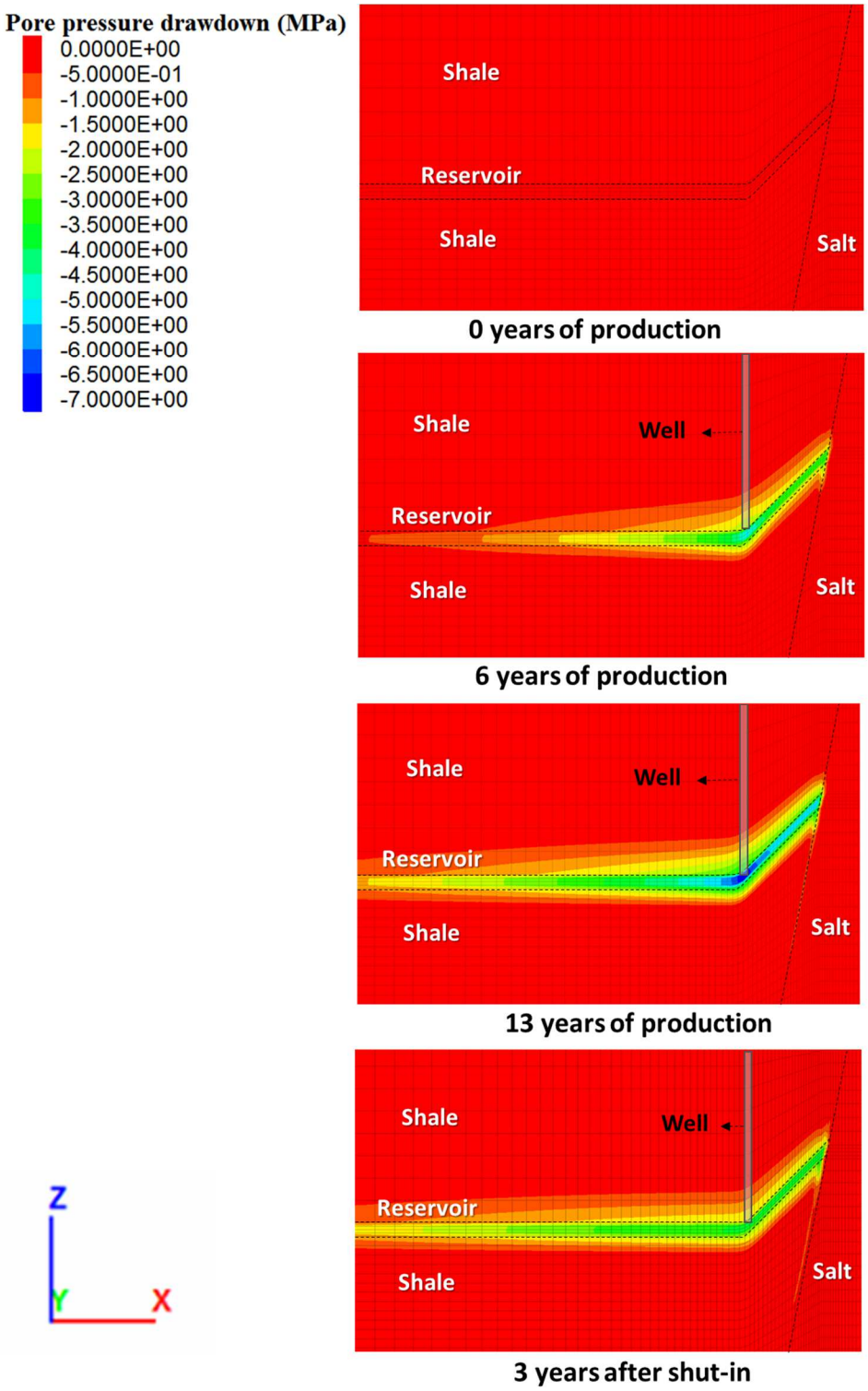


Figure 17. Pore pressure drawdown along a xz-plane in the middle of the reservoir. (a) Initial state, (b) 6 years of production, (c) 13 years of production and (d) 3 years of steady state. The highest depletion occurred along the reservoir and extends in the shale above and below the producing formation. Three years after shut-in, the pore pressure increased in the reservoir and shale.

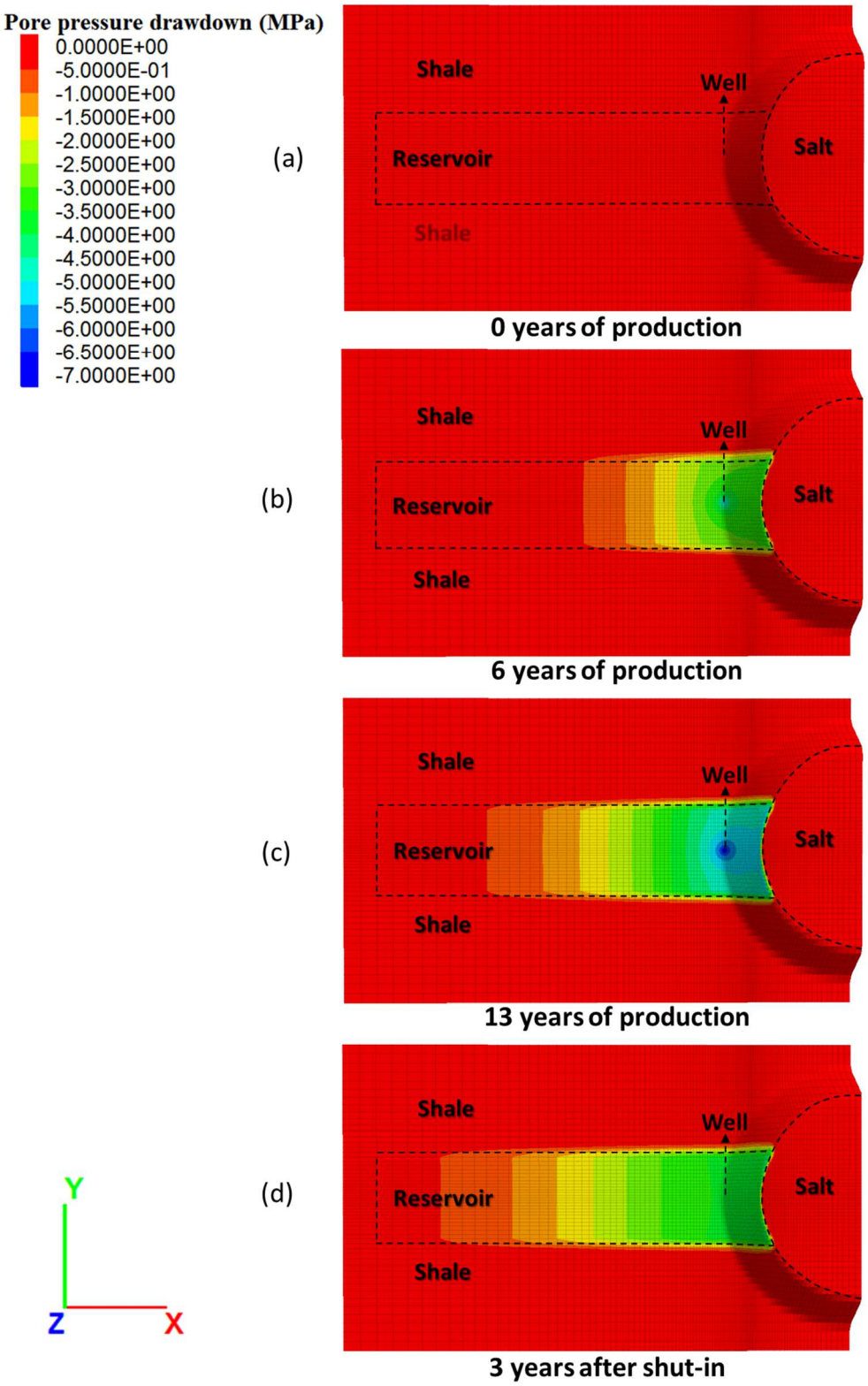


Figure 18. Pore pressure drawdown in the xy-plane through the middle of the reservoir. (a) Initial state, (b) 6 years of production, (c) 13 years of production and (d) 3 years of steady state. The depletion was higher at the salt/sediment interface than in the flat region. Three years after shut-in, the pore pressure in the reservoir stabilizes and distributes.

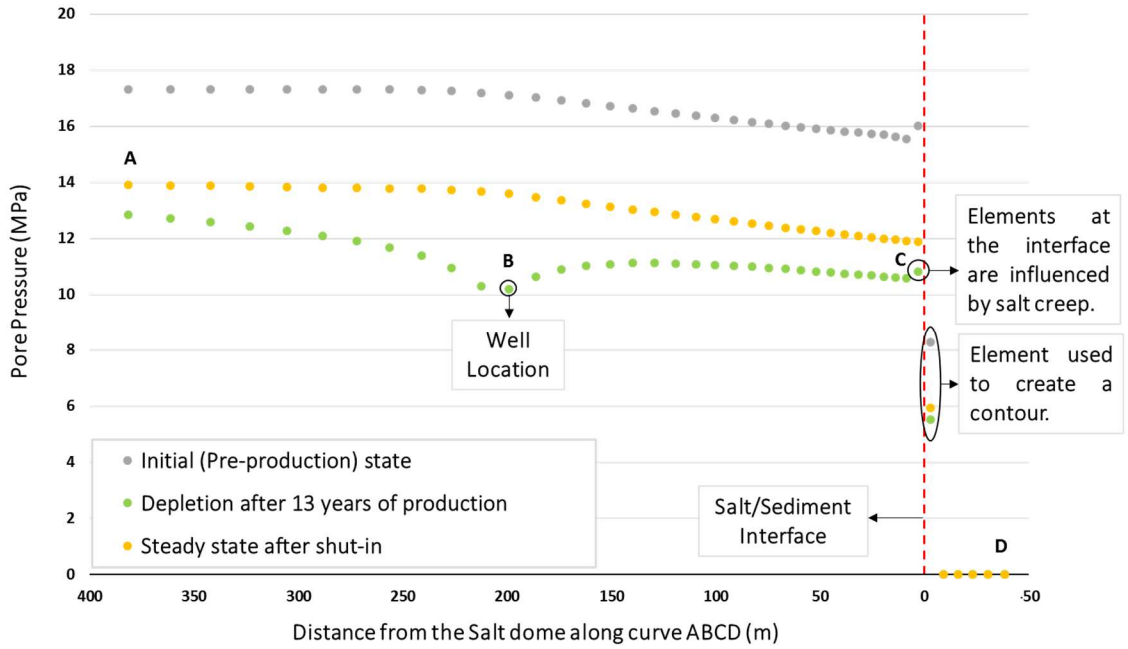


Figure 19. Pore pressure as a function of distance from the salt/sediment interface along the trajectory ABCD, defined in Figure 15. (a). The pressure drawdown and pressure build up at a certain location is controlled by its location relative to the well. The salt pore pressure remains zero after 16 years of simulation. The pore pressure of the reservoir elements at the salt/sediment interface is altered by the salt creep. The salt elements at the salt/sediment interface present a pore pressure different than zero, because the contour of this element interpolates the values of the sediment gridpoint (different than zero) and salt gridpoint (zero).

Figure 20 shows the pore pressure drawdown in the upper shale which is represented by the elements A1, B1 and C1 defined in Figure 15(b). It experienced up to 3.23 MPa of depletion above the well, followed by 2.3 MPa at the salt/sediment interface and 2.1 MPa at point A1. The pressure change at the salt/sediment interface is 0.2 MPa higher compared to the flat region. The pore pressure drawdown at point C1 is 0.37 MPa greater compared to the value of the element next to it, which is associated to the salt creep. Figure 17(d) shows the pressure build up values after shut-in: the pore pressure increased up to 1.4 MPa above the well, 0.61 MPa at the salt/sediment interface, and 0.5 MPa in the flat region (see Figure 19). The order of magnitude of

these observations are consequent with the points that presented the highest depletion in the reservoir.

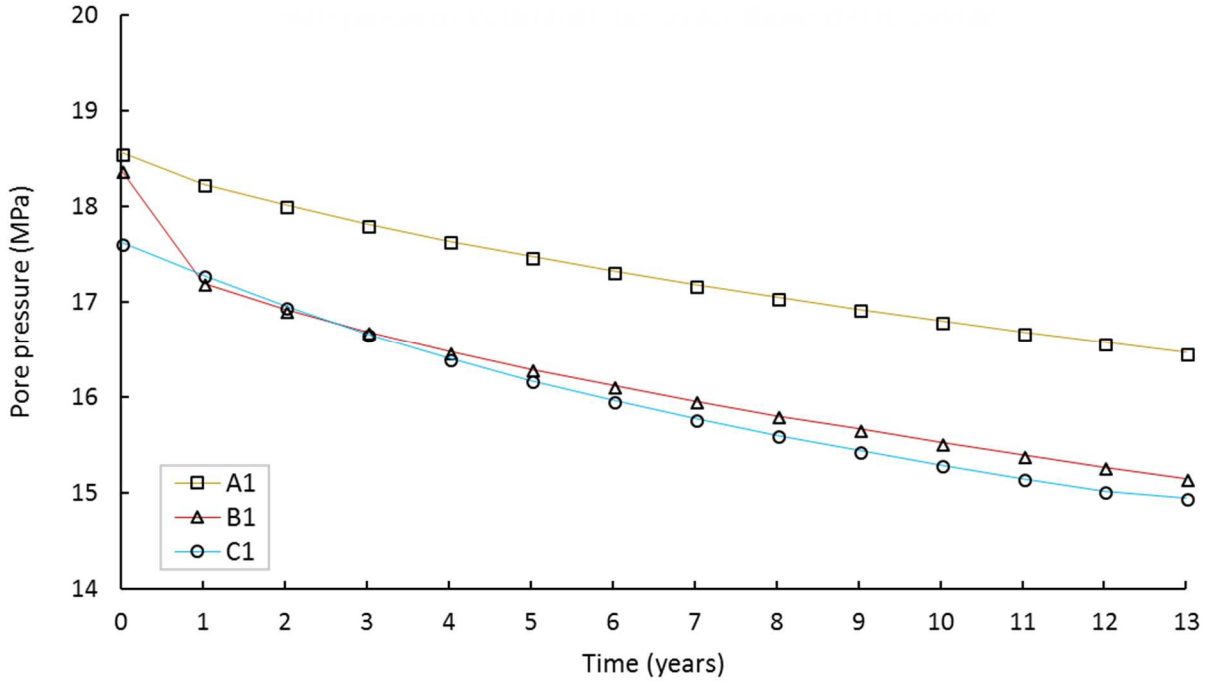


Figure 20. Pore pressure during production time of three upper shale elements (A1, B1 and C1), situated at different locations with respect to the dome, described in Figure 15(b). The element above the well, experienced the maximum pressure drawdown during the first year of production, followed by a change of the slope that decreases. The slope of the pressure at point C1 looks steeper than at point A1

Figure 21 shows the pore pressure drawdown in the lower shale which is represented by the elements A3, B3 and C3 shown in Figure 15(b). It experienced up to 3.96 MPa of depletion below the well, followed by 2.87 MPa at the salt/sediment interface and 2.42 MPa at point A3. From the previous results, it is observed that in general the lower shale depletion is higher compared to the upper shale (0.33 MPa more at point A, 0.73 MPa at point B and 0.57 MPa at point C). The pore pressure reduction at point C3 is 0.7 MPa greater compared to the magnitude of the element next to it, because of the salt. Figure 17(d) shows the pressure build up values

after shut-in: the pore pressure increased up to 1.5 MPa below the well, followed by 0.4 MPa at the salt/sediment interface, and 0.4 MPa in the flat region (see Figure 19). The order of magnitude of these observations are consequent with the points that presented the highest depletion in the reservoir.

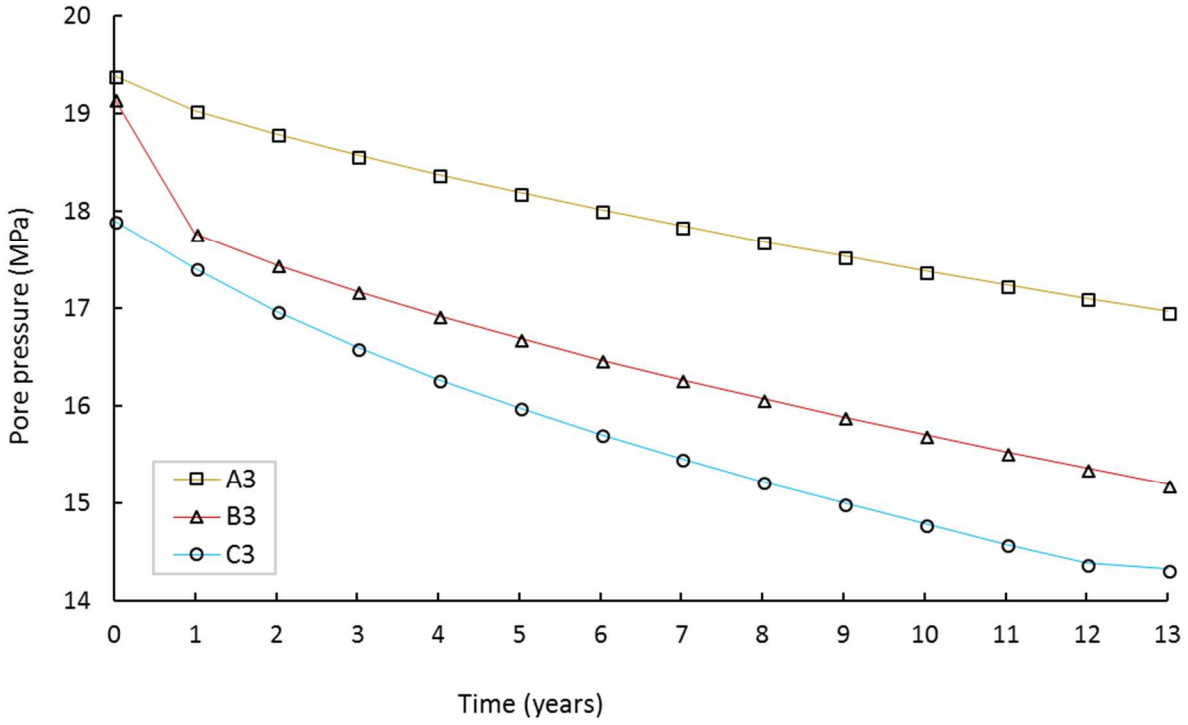


Figure 21. Pore pressure during production time of three lower shale elements (A3, B3 and C3) situated at different locations with respect to the dome, described in Figure 15(b). The element below the well experienced more depletion.

5.2 Total and effective vertical stresses

Figure 22 shows the change of total vertical stress ($\Delta\sigma_{zz}$) values after 13 years of production. The reservoir experienced the maximum total vertical stress (σ_{zz}) reduction at the salt/sediment interface (1.7 MPa ~ 4%), followed by 1.41 MPa (3%) around the well, and 0.24 MPa (0.5%) at

point A. It can be observed that the proximity to the salt and the dipping angle controls the $\Delta\sigma_{zz}$, for this reason there are major changes around the dome, compared to the flat region.

As stated before, the results obtained at points C1, C2 and C3 are not considered into the analysis of the dipping angle effect, to avoid misleading conclusions. Instead these elements will be studied separately to demonstrate the impact of salt deformation at the salt/sediment interface. Analyzing the effect of salt creep on the vertical stress at the salt/sediment interface, it is observed that the reservoir element at point C2 is 0.23 MPa greater, compared to the green element next to it (see Figure 22).

Figure 23(d) and Figure 24(d), show how the vertical stress recovered after shut-in: the total vertical stresses in the reservoir increased up to 0.89 MPa around the well, 0.4 MPa at the salt/sediment interface and 0.07 MPa in the flat region (see Figure 25). The stresses recovery was higher around the well than at the salt/sediment interface, it may be associated to a major pressure build up at the well location, compared to the salt/sediment interface (see Figure 19). In contrast, the total vertical stresses in the salt increased 0.42 MPa at point D, after 13 years of production and decreased 0.12 MPa after 3 years of shut-in (see Figure 25).

Figure 26 shows the change of effective vertical stress ($\Delta\sigma'_{zz}$) in the reservoir after 13 years of production. The effective vertical stress is calculated using the Eq. (32), described in chapter 2. The reservoir experienced the maximum σ'_{zz} increment around the well (5.49 MPa ~ 18%), followed by 4.25 MPa (13.7%) at point A2, and 3.26 MPa (12%) at the salt/sediment interface. It is observed that the $\Delta\sigma'_{zz}$ at a point is controlled by its location relative to the well, and that the

effective vertical stress in the flat region is 1 MPa higher, compared to the salt/sediment interface. The previous observation occurs because gravity drainage enhances the pore pressure drawdown near the salt/reservoir interface.

Figure 27(d) and Figure 28(d), show the $\Delta\sigma'_{zz}$ values after shut-in along the reservoir. The stresses decreased up to 2.5 MPa around the well, followed by 1 MPa at point A2, and 0.9 MPa at the interface (see Figure 29). The order of magnitude of these observations are consequent with the points that presented the highest effective stress increment in the reservoir. The effective vertical stresses in the salt are the same as the total vertical stresses because the pore pressure did not change after production or shut-in (see Figure 19).

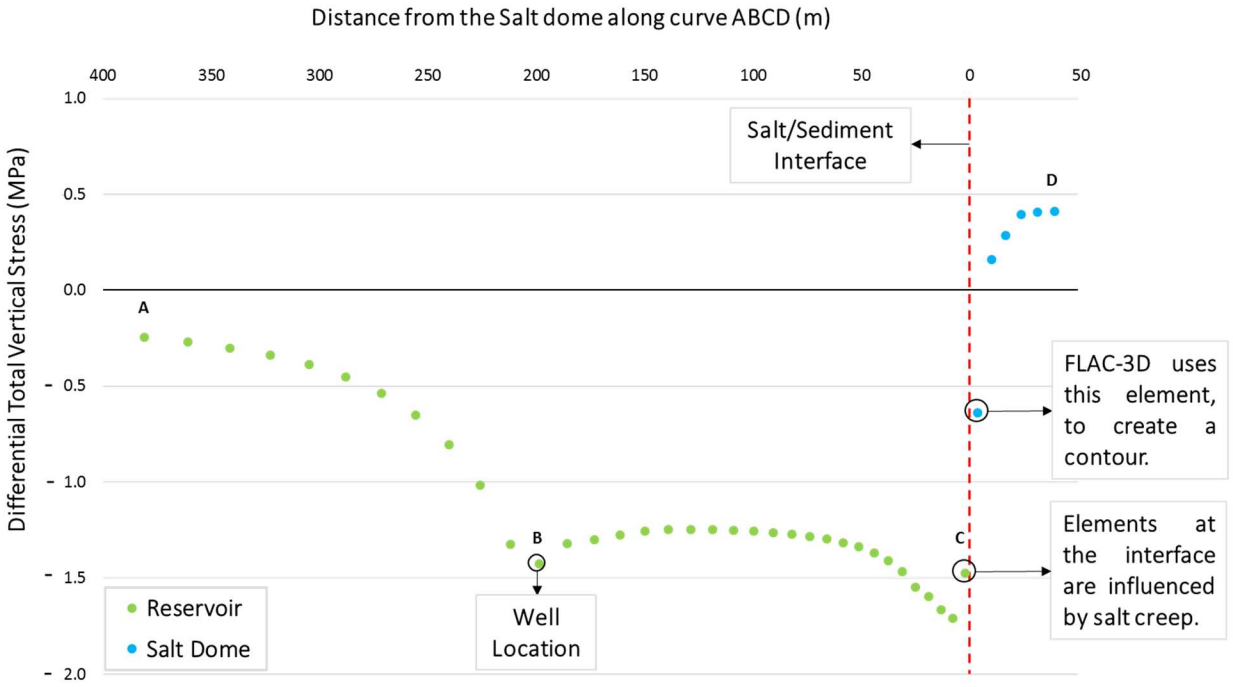


Figure 22. Change of total vertical stress as a function of distance from the salt/sediment interface, along the curve ABCD, after 13 years of production. Reservoir elements are represented in green, while salt elements are represented in blue. The total vertical stress decreased toward the dome and increases in the salt. The effect of a production well on the total stress resulted in higher reduction around higher depleted zone. The total vertical stress of the reservoir elements at the salt/sediment interface is altered by the salt creep. The salt elements at the salt/sediment interface present a total vertical stress different than the salt elements next to it, because the contour of this element interpolates the values of the sediment and salt gridpoints.

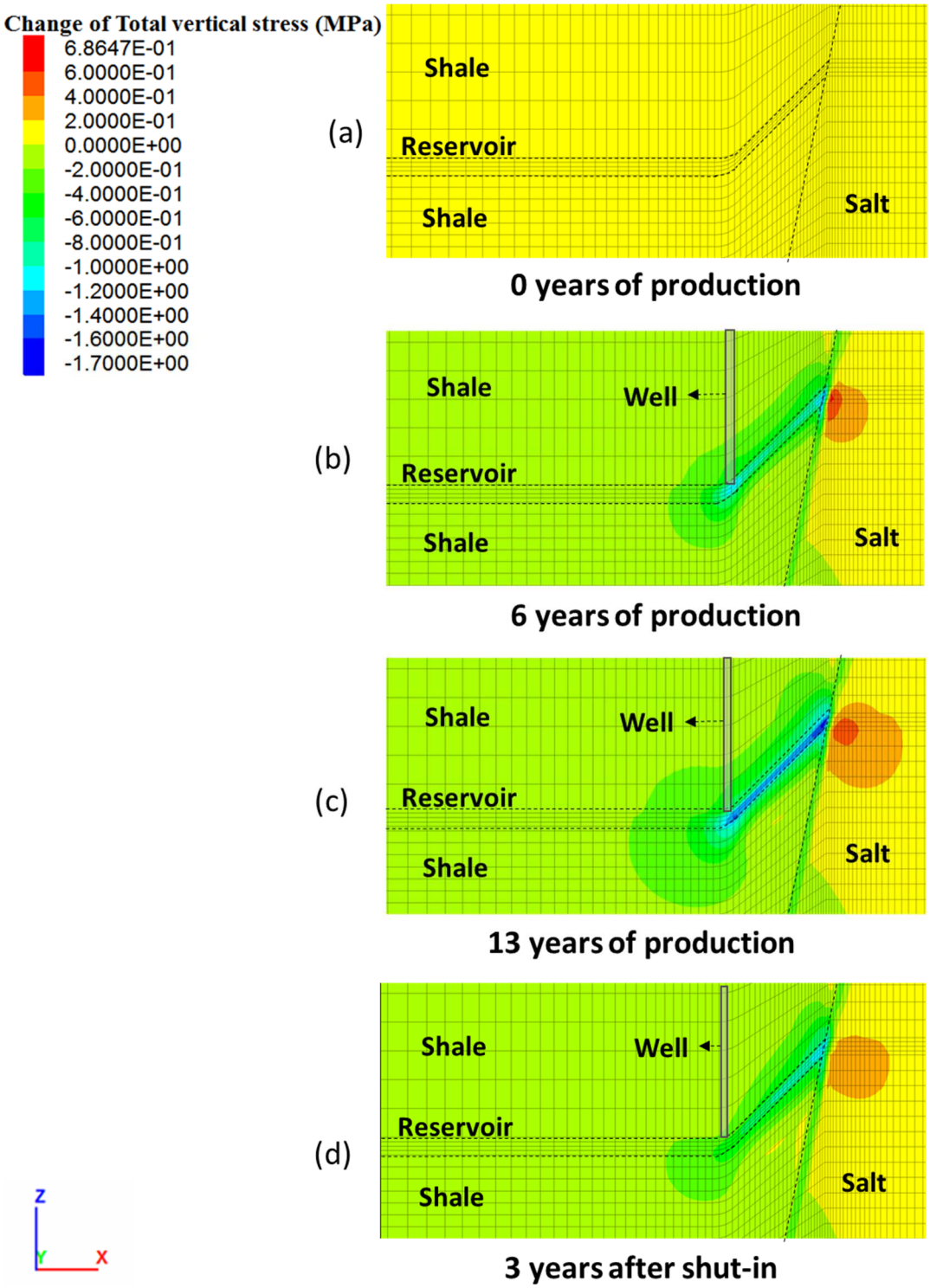


Figure 23. Total vertical stress changes along a xz-plane in the middle of the reservoir. (a) Initial state, (b) 6 years of production, (c) 13 years of production and (d) 3 years of steady state. The total vertical stress decreased in the reservoir, reaching the maximum reduction along the dipping layer. While it increased in the salt right next to the reservoir interface. Three years after shut-in, σ_{zz} increases in the reservoir and decreases in the salt, looking for a steady state.

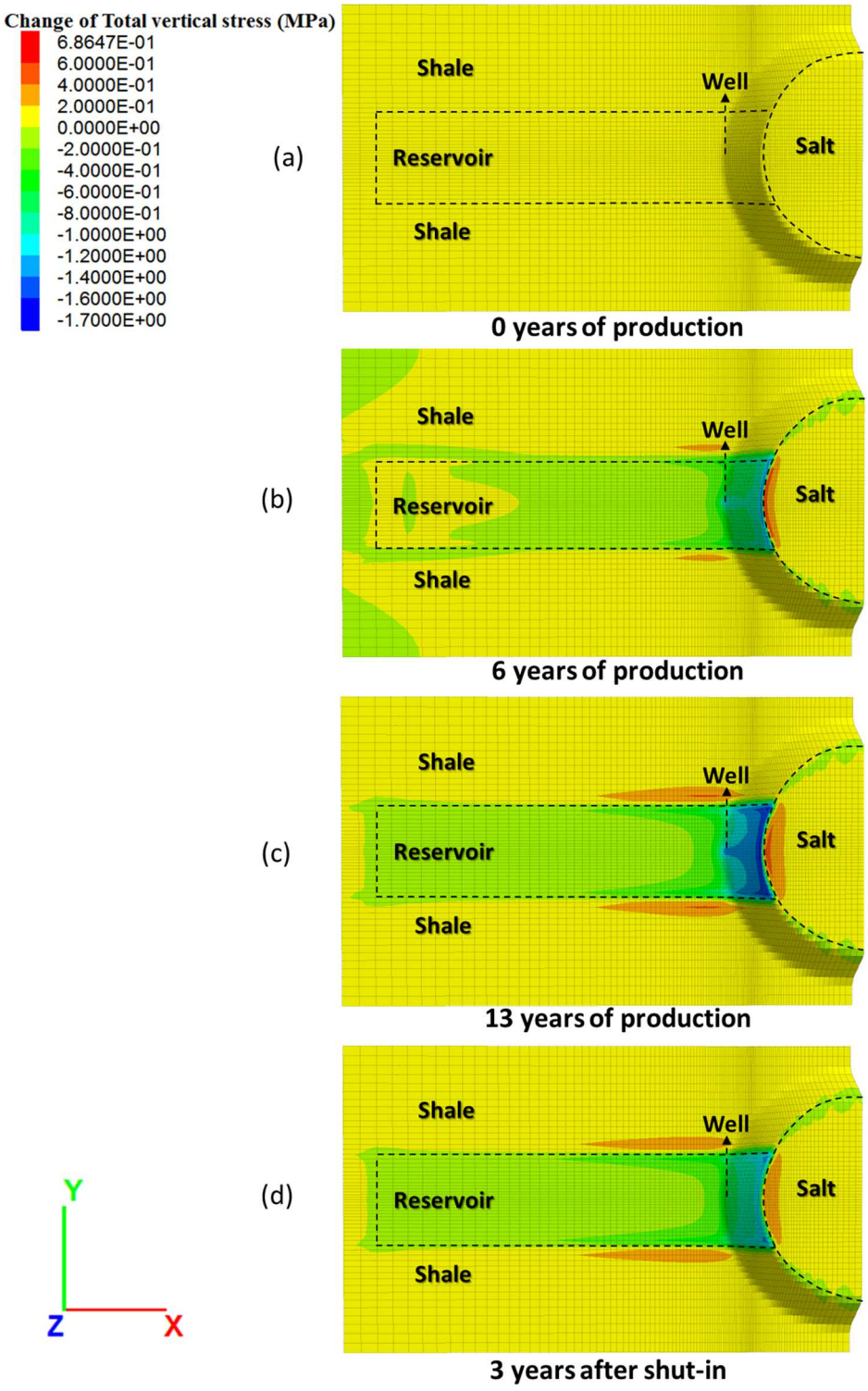


Figure 24. Total vertical stress changes in the xy-plane through the middle of the reservoir. (a) Initial state, (b) 6 years of production, (c) 13 years of production and (d) 3 years of steady state. The total vertical stress decreased toward the dome and the well location impact the stress pattern along the dipping layer. While it increased in the salt right next to the reservoir interface. Three years after shut-in, σ_{zz} increases in the reservoir as the pore pressure in the reservoir stabilizes.

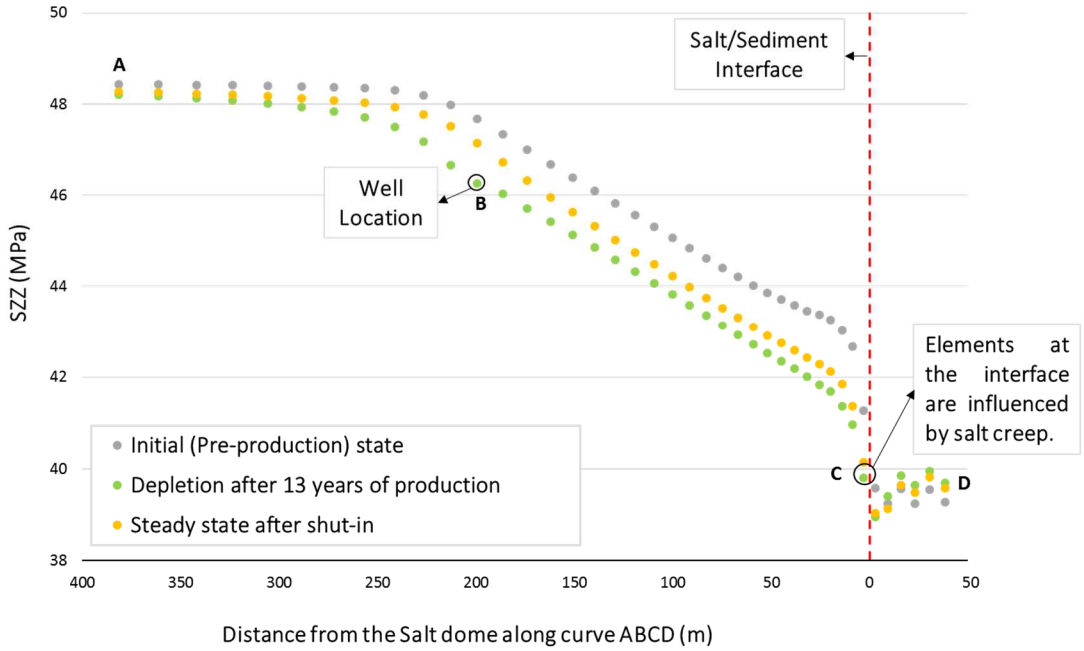


Figure 25. Total vertical stress as a function of distance from the salt/sediment interface, along the trajectory ABCD. The total vertical stress during and after production is controlled by the dipping angle and the proximity to the salt dome. The vertical stresses in the salt increased after production and decreased after shut-in. The total vertical stress of the reservoir elements at the salt/sediment interface is altered by the salt creep. The salt elements at the salt/sediment interface present a total vertical stress different than the salt elements next to it, because the contour of this element interpolates the values of the sediment and salt gridpoints.

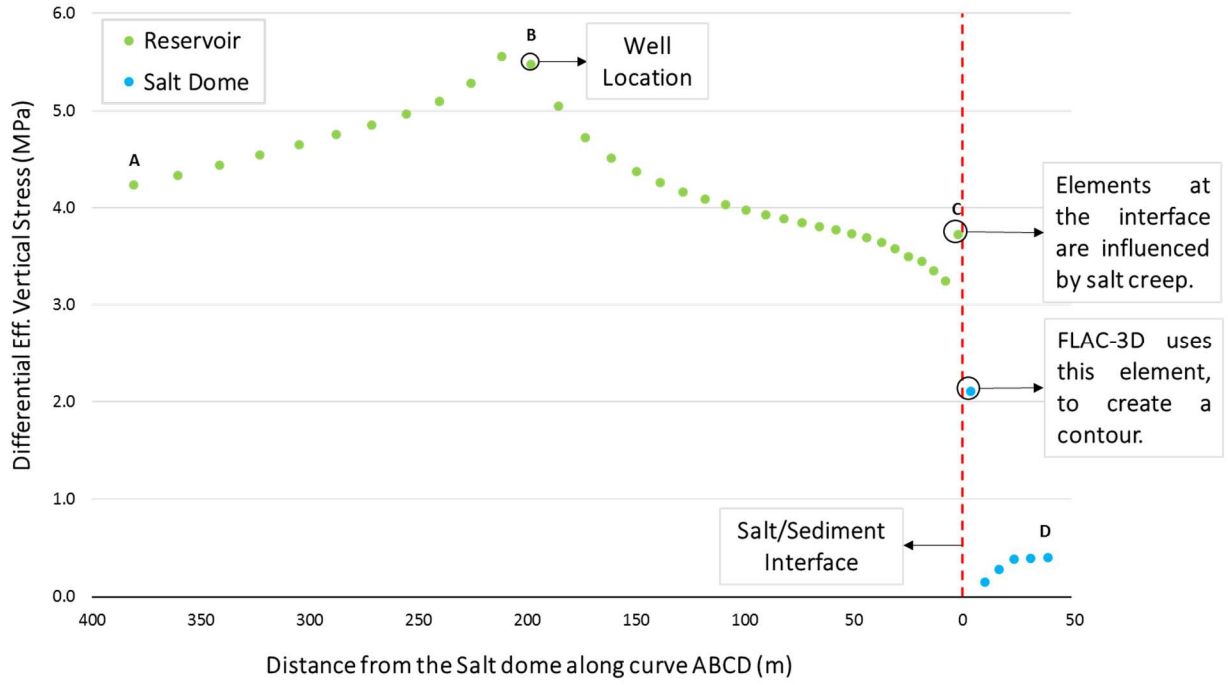


Figure 26. Change of effective vertical stress as a function of distance from the salt/sediment interface, along the curve ABCD, after 13 years of production. Reservoir elements are represented in green, while salt elements are represented in blue. The highest increment occurred at point B. The effective vertical stress increased more at point A that at the salt/sediment interface. The effective vertical stress of the reservoir elements at the salt/sediment interface is altered by the salt creep. The salt elements at the salt/sediment interface present an effective vertical stress different than the salt elements next to it, because the contour of this element interpolates the values of the sediment and salt gridpoints.

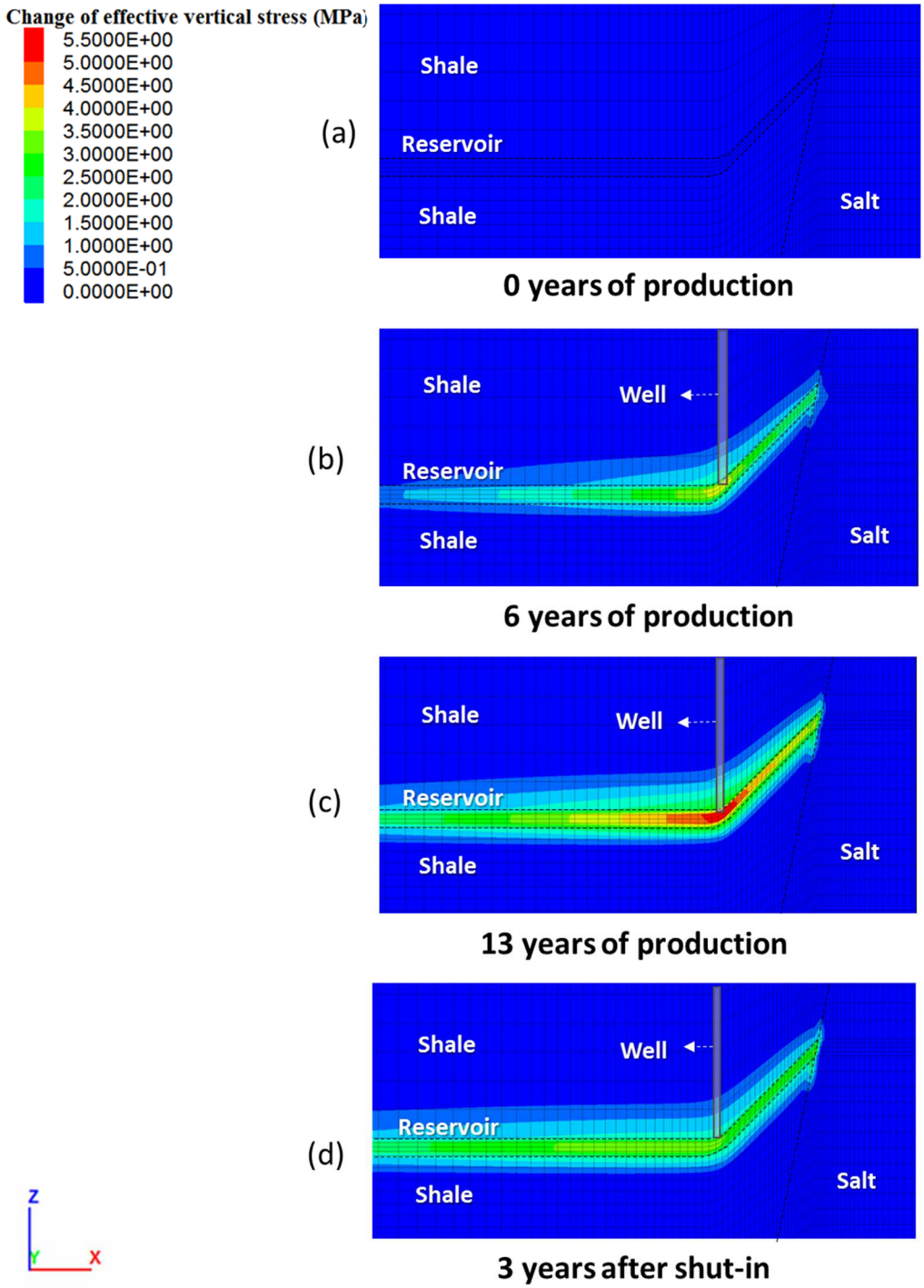


Figure 27. Effective vertical stress changes in the xz-plane through the middle of the reservoir. (a) Initial state, (b) 6 years of production, (c) 13 years of production and (d) 3 years of steady state. The effective vertical stress is controlled by the well location and increased in the reservoir and shale. The value of the effective stress in the salt corresponds to the change of the total vertical stresses, according to Eq. (32), because the pore pressure in the salt remains zero during and after production. Three years after shut-in, the σ'_{zz} decreases in the model.

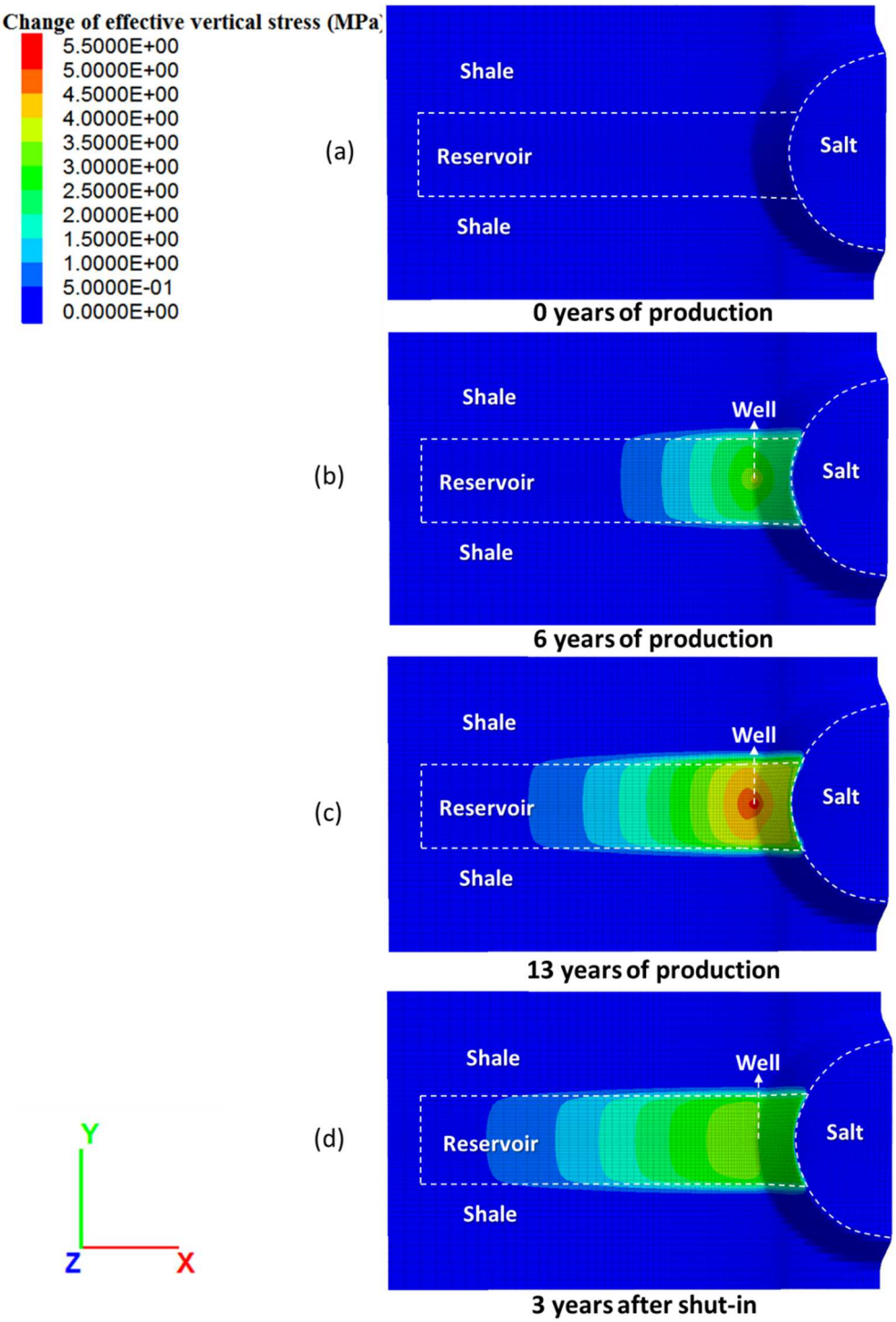


Figure 28. Effective vertical stress changes in the xy-plane through the middle of the reservoir. (a) Initial state, (b) 6 years of production, (c) 13 years of production and (d) 3 years of steady state. The effective vertical stress is controlled by the well location and increased with depletion. The value of the effective stress in the salt corresponds to the change of the total vertical stresses, according to Eq. (32), because the pore pressure in the salt remains zero during and after production. Three years after shut-in, the σ'_{zz} decreased in the model.

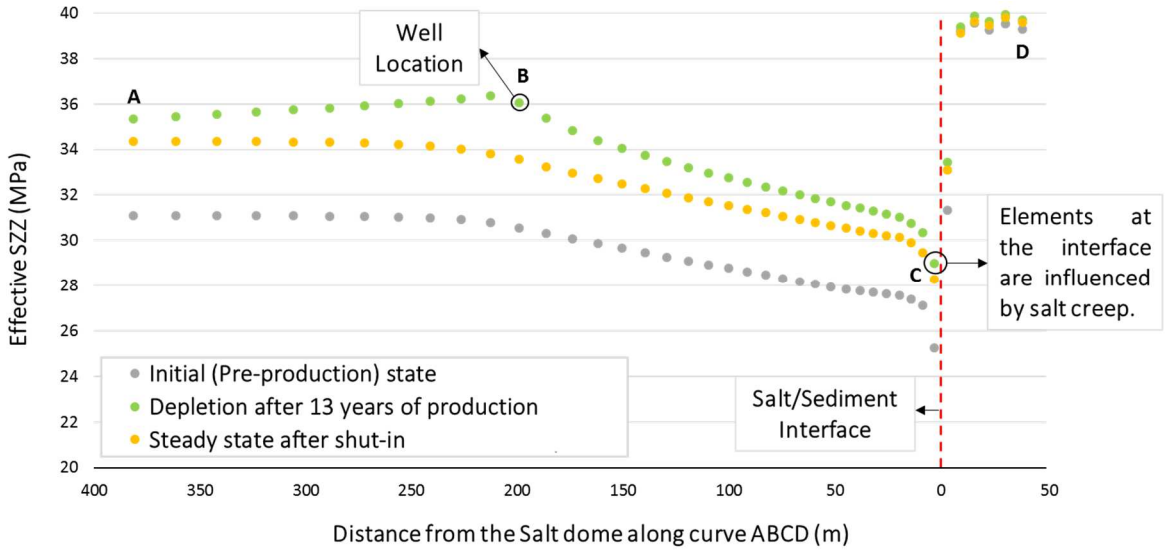


Figure 29. Effective vertical stress as a function of distance from the salt/sediment interface, along the trajectory ABCD defined in Figure 15(a). The major increment of σ'_{zz} was 5.57 MPa around the well. After shut-in, the σ'_{zz} decreased 0.97 MPa at point B. The effective vertical stress of the reservoir elements at the salt/sediment interface is altered by the salt creep. The salt elements at the salt/sediment interface present an effective vertical stress different than the salt elements next to it, because the contour of this element interpolates the values of the sediment and salt gridpoints.

Figure 30, shows the total vertical stress changes in the upper shale which is represented by the elements A1, B1 and C1 as shown in Figure 15(b). The stress reduction experienced by these elements in order of magnitude was 0.99 MPa (2.3%) at the salt/sediment interface, 0.68 MPa (1.4%) at point B1 and 0.21 MPa (0.5%) at point A1. The total vertical stress at the salt/sediment interface is 0.77 MPa lower compared to the flat region, because the $\Delta\sigma_{zz}$ is controlled by the proximity to the salt and the dipping angle. Figure 23(d) shows the $\Delta\sigma_{zz}$ values after shut in the well in the upper shale. The stresses increased up to 0.42 MPa above the well, 0.24 MPa at the salt/sediment interface and 0.06 MPa in the flat region. The stresses recovery was higher above the well than at the salt/sediment interface because the pressure built up more at point B1, compared to the salt/sediment interface (see Figure 19).

The effective vertical stress changes in the upper shale which is represented by the elements A'1, B'1 and C'1 as shown in Figure 15(b), are plotted in Figure 30. The stress increment experienced by these elements in order of magnitude was 2.55 MPa (9%) above the well, 1.88 MPa (6.6%) at point A'1 and 1.32 MPa (5.2%) at the salt/sediment interface. The σ'_{zz} in the flat region is 0.57 MPa higher compared to the value at the salt/sediment interface. Figure 27(d) shows the $\Delta\sigma'_{zz}$ values after shut-in in the upper shale. The stresses decreased up to 0.97 MPa above the well, 0.41 MPa in the flat region, and 0.37 MPa at the salt/sediment interface.

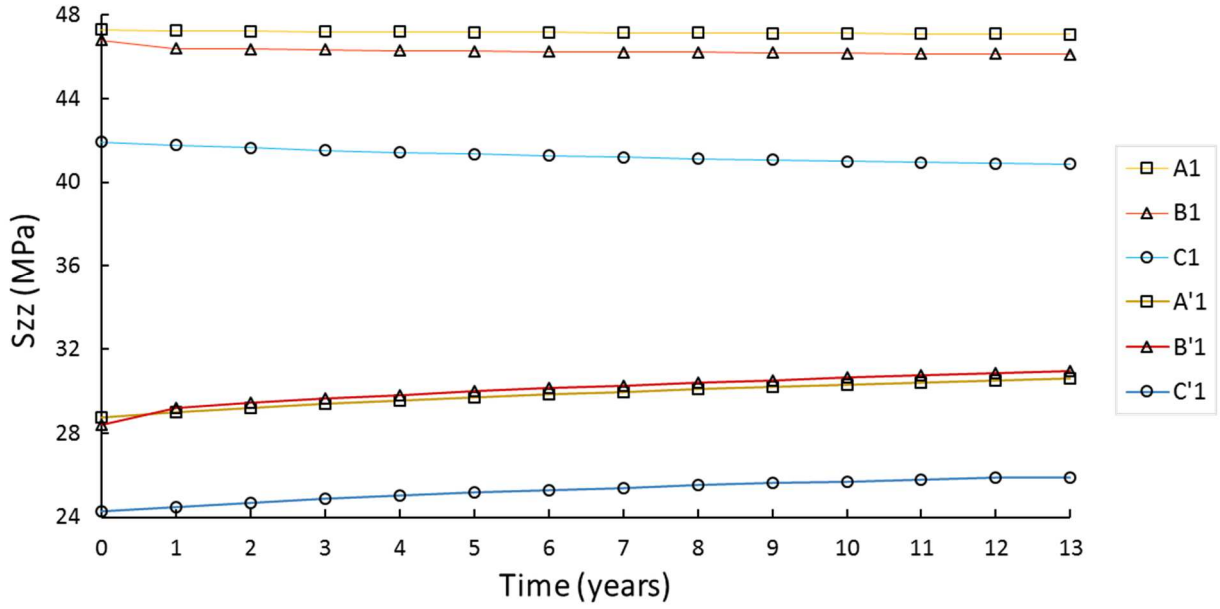


Figure 30. Total vertical stress (A1, B1 and C1) and effective vertical stress (A'1, B'1 and C'1) during production time for three upper shale elements, situated at different locations with respect to the dome, described in Figure 15(b). The element at the salt/sediment interface experienced the maximum σ_{zz} reduction, while the element above the well experienced the highest σ'_{zz} increment, with production.

Figure 31, shows the total vertical stress changes in the lower shale which is represented by the elements A3, B3 and C3 shown in Figure 15(b). The stress reduction experienced by these elements in order of magnitude was 0.97 MPa (2%) below the well, 0.84 MPa (1.9%) at the salt/sediment interface and 0.25 MPa (0.5%) at point A3. The total vertical stress at the salt/sediment interface is 0.59 MPa lower compared to the flat region, because the $\Delta\sigma_{zz}$ is controlled by the well location and the dipping angle. Analyzing the results of both the upper and lower shale, it can be seen that the σ_{zz} decreased 0.29 MPa more below the well than above, however the σ_{zz} decreased 0.15 MPa more in the upper shale/salt interface than in the lower shale/salt interface. The total vertical stress change at point C3 is 0.22 MPa higher compared to the magnitude of the element next to it, because of the salt creep. Figure 23(d) shows the $\Delta\sigma_{zz}$ values after shut in the well in the lower shale. The vertical stresses increased up to 0.5 MPa above the well, 0.19 MPa at the salt/sediment interface and 0.07 MPa in the flat region. The stresses recovery was higher above the well than at the salt/sediment interface because the pressure built up more at point B3, compared to the salt/sediment interface (see Figure 19).

Figure 31, shows the effective vertical stress changes in the lower shale which is represented by the elements A'3, B'3 and C'3 shown in Figure 15 (b). The stress increment experienced by these elements in order of magnitude was 3 MPa (10%) below the well, 2.18 MPa (7.3%) in the flat region, and 2.03 MPa (7.6%) at the salt/sediment interface. Analyzing the results of both the upper and lower shale, it can be seen that the σ'_{zz} increased (0.72 MPa at the salt/sediment interface, 0.44 MPa below the well, 0.29 MPa in the flat region) more in the lower than upper shale. The effective vertical stress change at point C3 is 0.49 MPa higher compared to the magnitude of the element next to it, because of the salt creep. Figure 27(d) shows the $\Delta\sigma'_{zz}$

values after shut-in in the lower shale. The stresses decreased up to 0.97 MPa below the well, 0.33 MPa in the flat region, and 0.28 MPa at the salt/sediment interface.

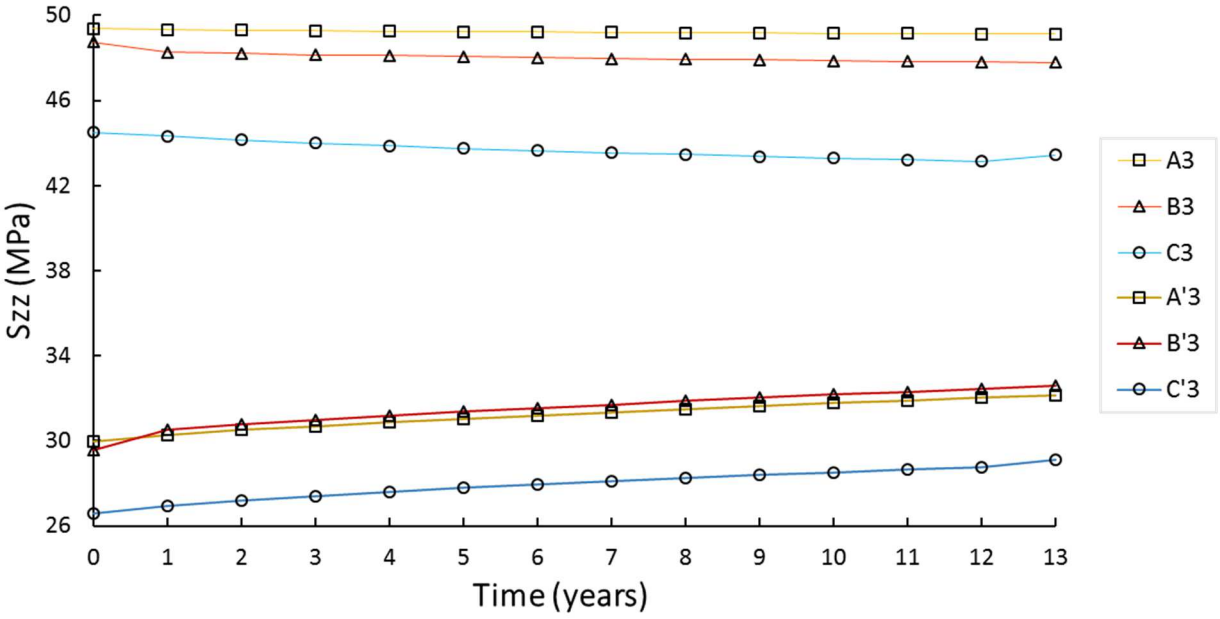


Figure 31. Total vertical stress (A3, B3 and C3) and effective vertical stress (A'3, B'3 and C'3) during production time of three lower shale elements situated at different locations with respect to the dome, described in Figure 15(b). The element at the salt/sediment interface experienced the maximum σ_{zz} reduction, while the element below the well experienced the highest σ'_{zz} increment, with production.

5.3 Total and effective maximum horizontal stresses

Figure 32 shows the change of total maximum horizontal stress (σ_{xx}) values after 13 years of production. It is observed that the reduction of the maximum horizontal stress in the reservoir is controlled by the well location. Where the major σ_{xx} reduction occurred 24 m away from the well in the flat side of the reservoir (2.39 MPa ~ 5.7%), followed by 2.08 MPa (5%) at point A2, and 1.04 MPa (2.6%) at the salt/sediment interface. Studying the effect of salt creep on the total maximum horizontal stress at the salt/sediment interface, it is observed that the reservoir element at point C2 is 1.04 MPa lower, compared to the green element next to it, because it is altered by

the salt creep. The total maximum horizontal stress in the salt decreased 0.38 MPa at point D after 13 years of production

Figure 33(d) and Figure 34(d), show how the total maximum horizontal stress recovered after shut-in: the total maximum horizontal stress increased up to 1.13 MPa around the well, 0.51 MPa in the flat region, 0.29 at the salt/sediment interface and 0.07 MPa in the salt (see Figure 35). The stresses recovery was higher around the well where the major pressure built up (see Figure 19).

Figure 36 shows the effective maximum horizontal stresses change ($\Delta\sigma'_{xx}$) in the reservoir increased after production. The effective maximum horizontal stresses is calculated using the Eq. (33), described in chapter 2. It is observed that the increment of σ'_{xx} is controlled by the well location and extends toward the dipping layer. The maximum increment occurred at point B2 (4.52 MPa ~ 18.2%), followed by 3.92 MPa (16.2%) at the interface, and 2.41 MPa (9.8%) at point A2. Evaluating the previous outcomes, the effective maximum horizontal stress at the interface is 1.52 MPa higher, compared to the flat region. Figure 33(d) and Figure 34(d) show the $\Delta\sigma'_{xx}$ values after shut-in along the reservoir. The σ'_{xx} in the reservoir decreased up to 2.25 MPa around the well, followed by 1 MPa at the salt/sediment interface, and 0.6 MPa at point A2. The effective maximum horizontal stresses in the salt are the same as the total maximum horizontal stresses after production and pressure build up (see Figure 19).

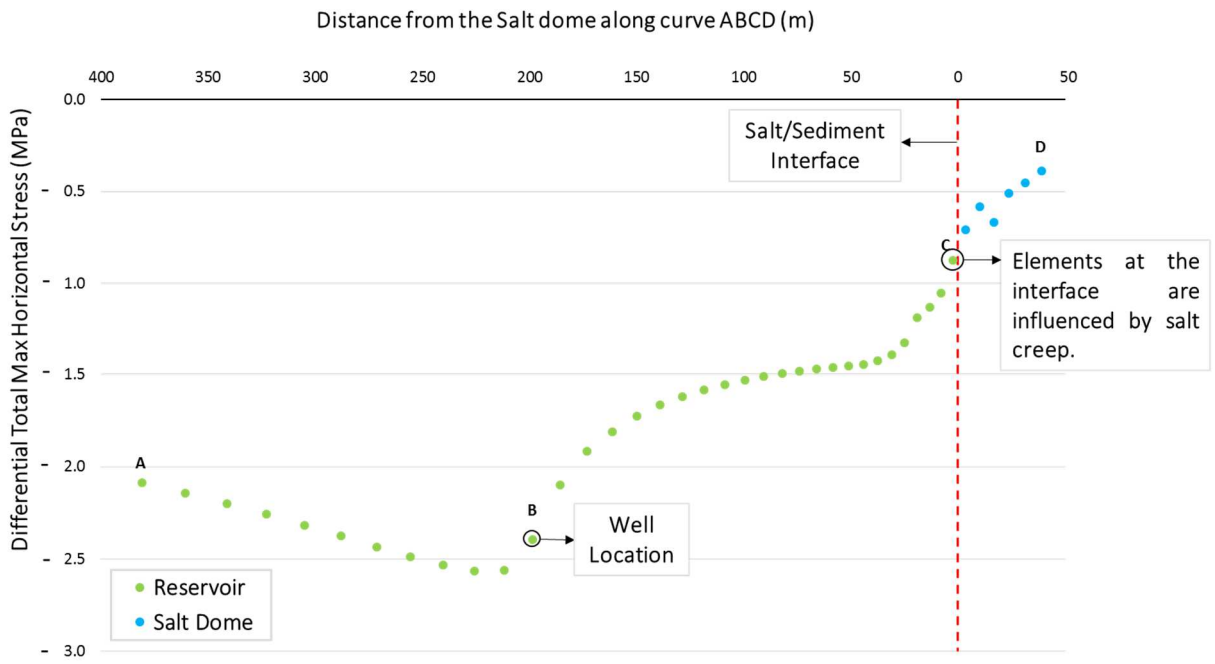


Figure 32. Change of total maximum horizontal stress as a function of distance from the salt/sediment interface, along the curve ABCD, after 13 years of production. Reservoir elements are represented in green, while salt elements are represented in blue. The highest reduction of the total maximum horizontal stress occurs 24 m away from the well, in the flat region. Lower reduction of the total maximum horizontal stress around the dome, compared to the flat zone. It decreased up to 0.68 MPa in the salt. The total maximum horizontal stress of the reservoir elements at the salt/sediment interface is altered by the salt creep. The salt elements at the salt/sediment interface present a total maximum horizontal stress different than the salt elements next to it, because the contour of this element interpolates the values of the sediment and salt gridpoints.

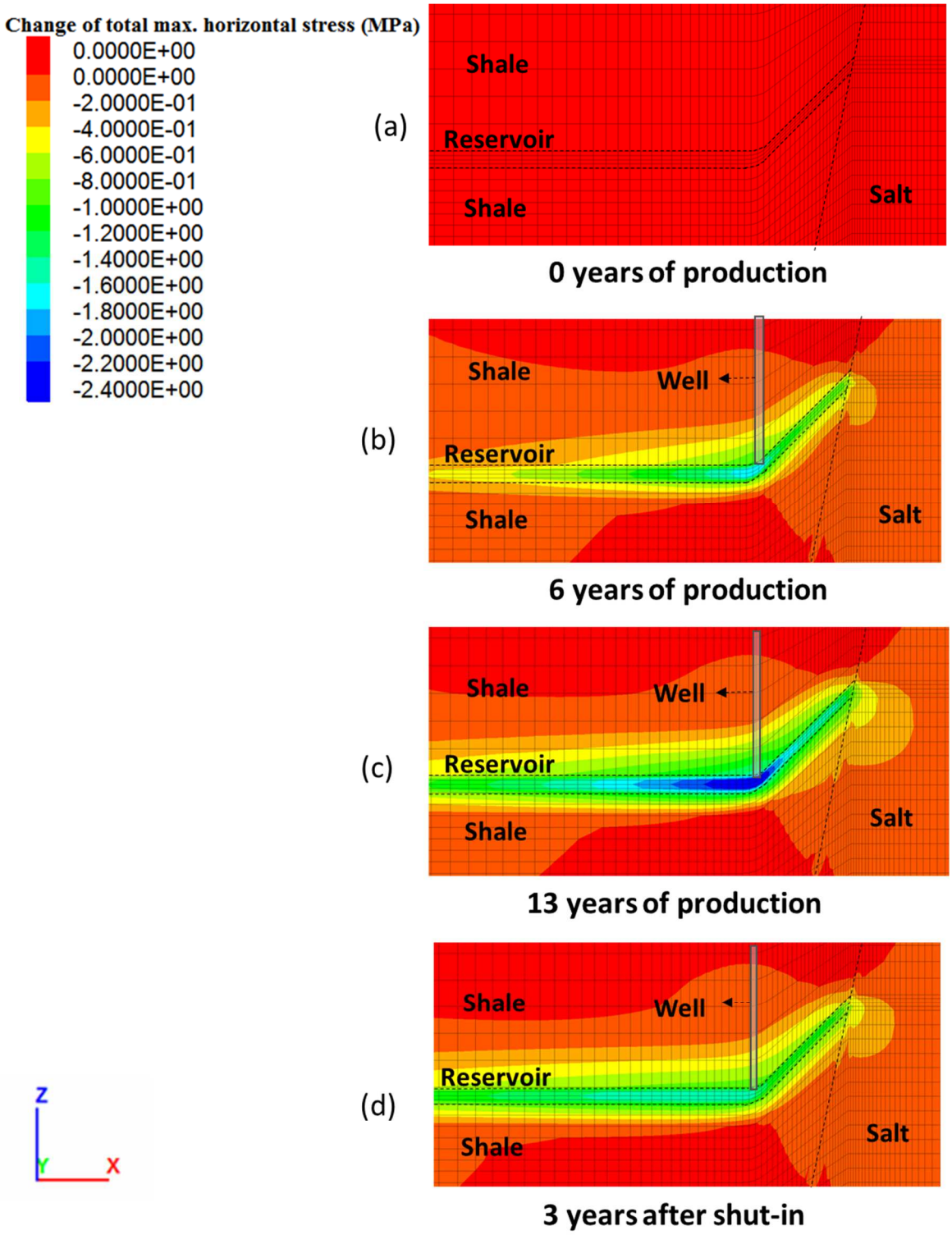


Figure 33. Total maximum horizontal stress changes in the xz-plane through in the middle of the reservoir. (a) Initial state, (b) 6 years of production, (c) 13 years of production and (d) 3 years of steady state. The reduction of σ_{xx} in the reservoir is function of the well location and, extends toward the flatten area. Three years after shut-in, σ_{xx} increases in the reservoir and the salt.

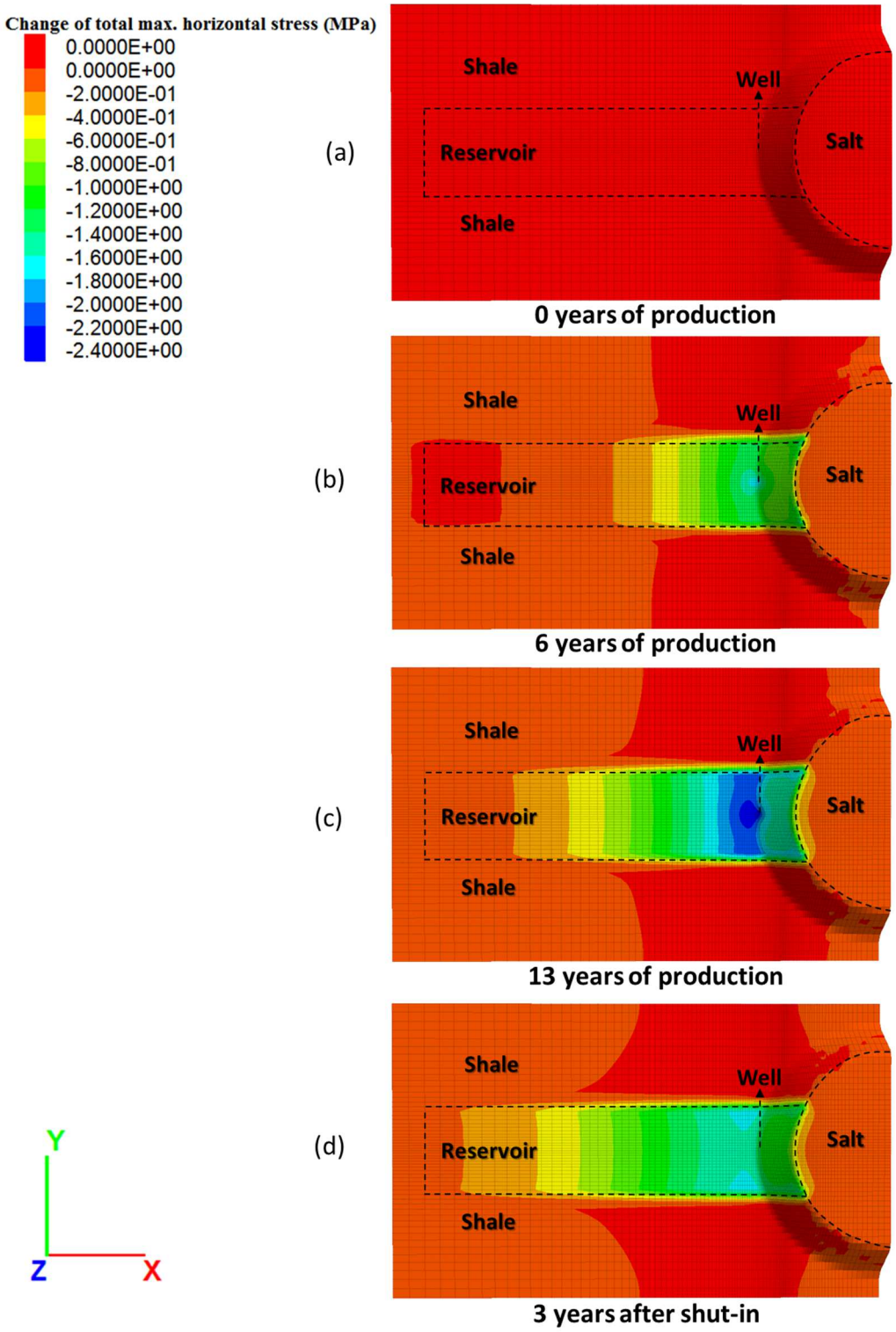


Figure 34. Total maximum horizontal stress changes in the xy-plane through the middle of the reservoir. (a) Initial state, (b) 6 years of production, (c) 13 years of production and (d) 3 years of steady state. The reduction of σ_{xx} in the reservoir is function of the well location and, extends toward the flatten area. Three years after shut-in, σ_{xx} increases in the reservoir and the salt.

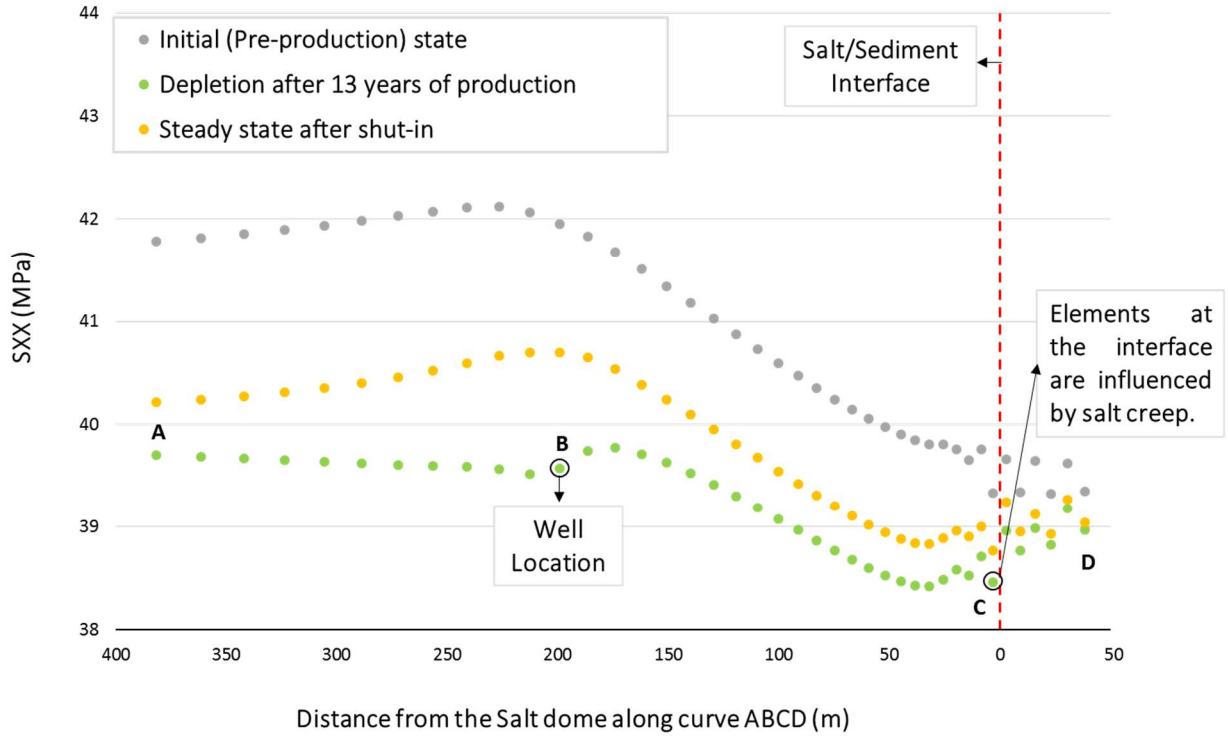


Figure 35. Total maximum horizontal stress as a function of distance from the salt/sediment **interface, along the trajectory ABCD. The σ_{xx} decreased after production and increased after shut-in, with the major change around the well (point B). The total maximum horizontal stress of the reservoir elements at the salt/sediment interface is altered by the salt creep. The salt elements at the salt/sediment interface present a total maximum horizontal stress different than the salt elements next to it, because the contour of this element interpolates the values of the sediment and salt gridpoints.**

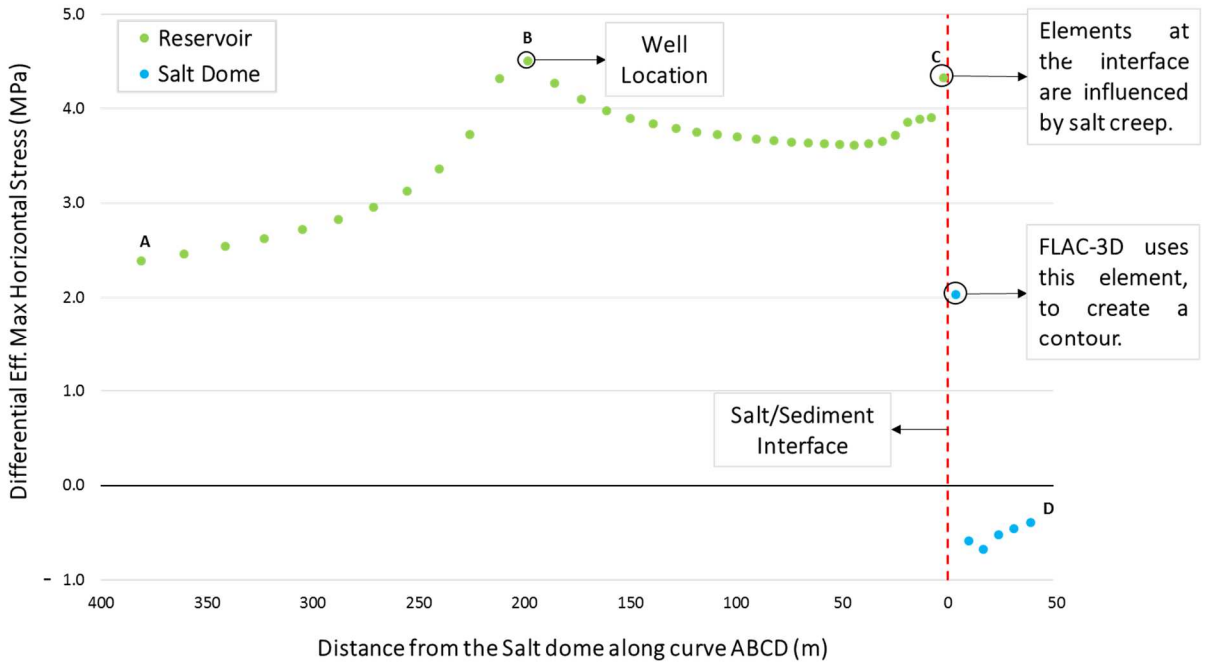


Figure 36. Change of effective maximum horizontal stress as a function of distance from the salt/sediment interface, along the curve ABCD, after 13 years of production. Reservoir elements are represented in green, while salt elements are represented in blue. The σ'_{xx} increased along the reservoir and decreased in the salt, with a major increment at the salt/sediment interface, compared to the flat region. The effective maximum horizontal stress of the reservoir elements at the salt/sediment interface is altered by the salt creep. The salt elements at the salt/sediment interface present an effective maximum horizontal stress different than the salt elements next to it, because the contour of this element interpolates the values of the sediment and salt gridpoints.

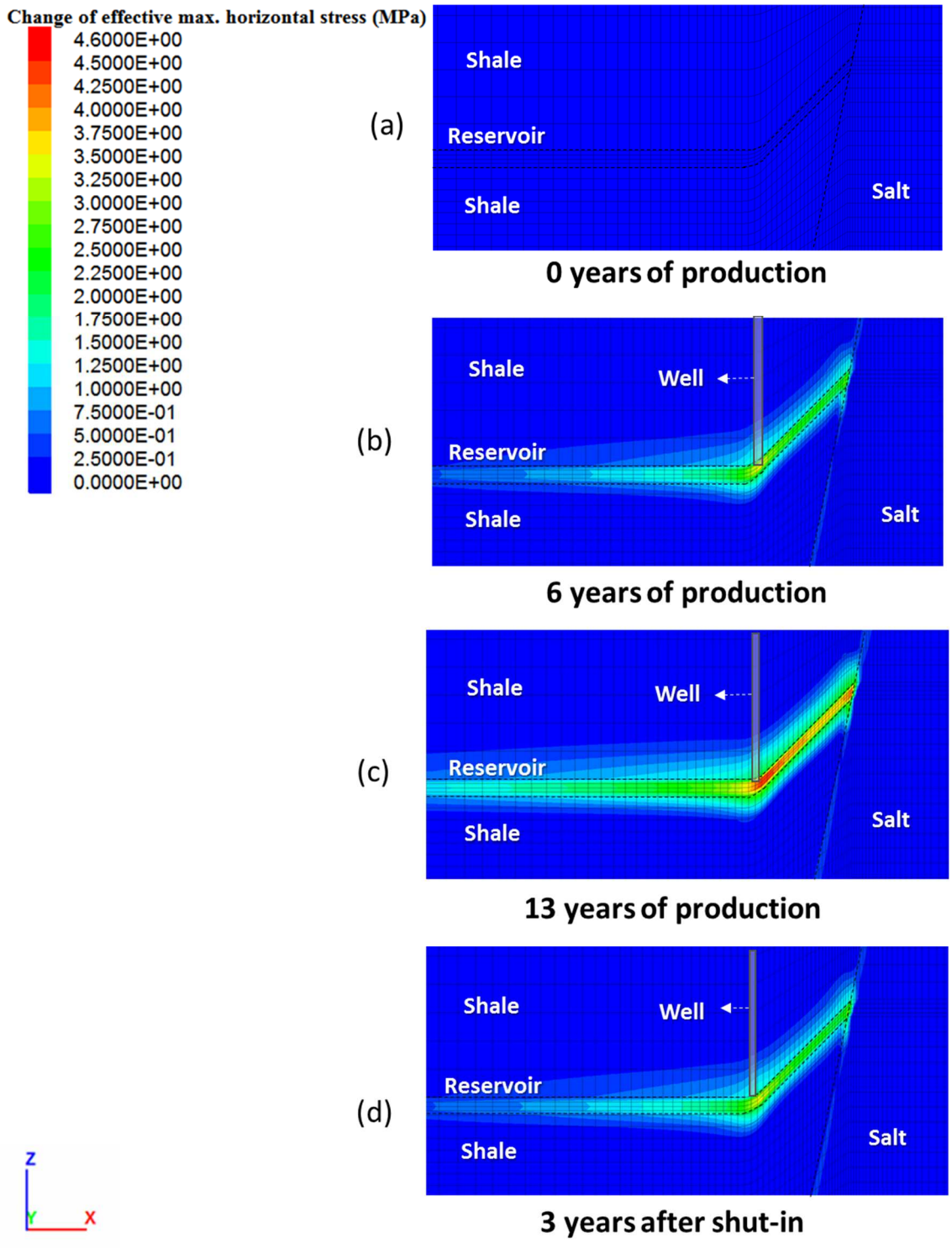


Figure 37. Effective maximum horizontal stress changes in the xz-plane through the middle of the reservoir. (a) Initial state, (b) 6 years of production, (c) 13 years of production and (d) 3 years of steady state. The σ'_{xx} is controlled by the well location and increases after production in the reservoir and shale. Three years after shut-in, the σ'_{xx} decreases in the model.

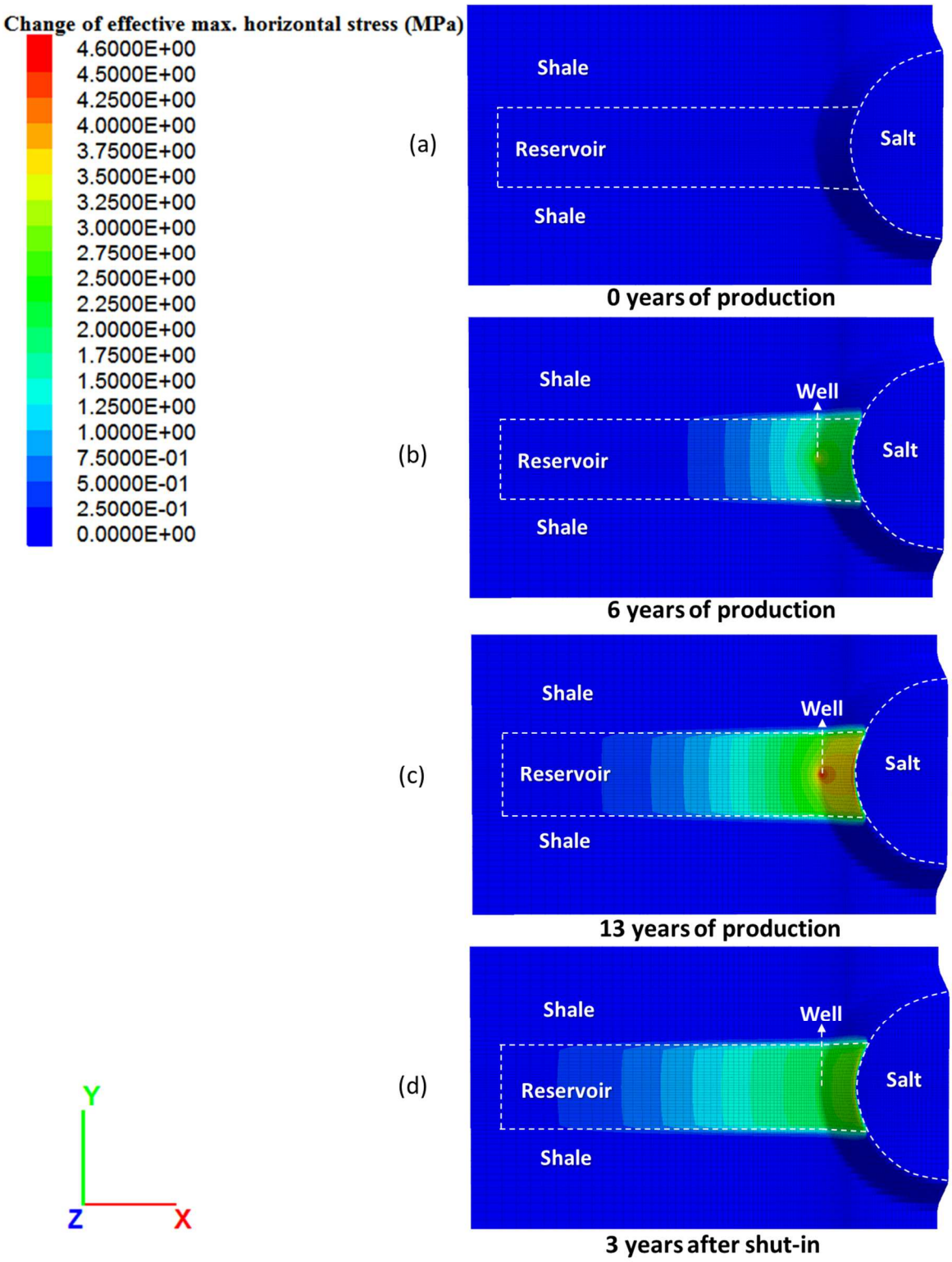


Figure 38. Effective maximum horizontal stress changes in the xy-plane through the middle of the reservoir. (a) Initial state, (b) 6 years of production, (c) 13 years of production and (d) 3 years of steady state. The σ'_{xx} is controlled by the well location and the dipping angle and increases with depletion. Three years after shut-in, the σ'_{xx} decreased in the model.

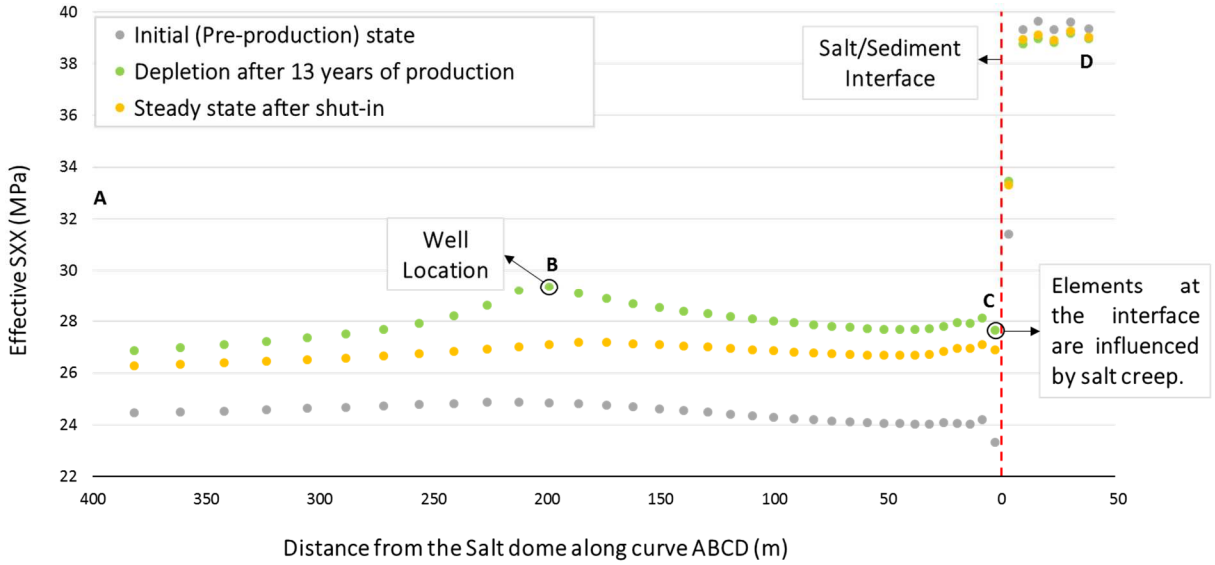


Figure 39. Effective maximum horizontal stress as a function of distance from the salt/sediment interface, along the trajectory ABCD. The increment of the effective maximum horizontal stresses caused by production goes up to 4.5 MPa at the well location. Once the well shuts in, the pressure in the reservoir builds up and stabilizes. During this period, the stress decreased up to 2.5 MPa in the reservoir. The effective maximum horizontal stress of the reservoir elements at the salt/sediment interface is altered by the salt creep. The salt elements at the salt/sediment interface present an effective maximum horizontal stress different than the salt elements next to it, because the contour of this element interpolates the values of the sediment and salt gridpoints.

Studying the behavior of σ_{xx} during the production time, the upper shale which is represented by the elements A1, B1 and C1 as shown in Figure 15(b), experienced the major reduction of σ_{xx} at point B1 (1.30 MPa ~ 3.1%), followed by the element at point A1 (1.02 MPa ~ 2.5%) and finally at the salt/sediment interface (0.3 MPa ~ 0.8%). The σ_{xx} reduction at the salt/sediment interface is 0.72 MPa less compared to the flat region (see Figure 40). Three years after shut-in, the σ_{xx} in the upper shale barely increased: 0.24 MPa in the flat region, 0.49 MPa above the well and it did not change at the salt/sediment interface (see Figure 33).

Studying the behavior of σ'_{xx} during production inthe upper shale, which is represented by the elements A1, B1 and C1 as shown in Figure 15(b), the σ'_{xx} increased in the reservoir: up to 2 MPa (9%) at the salt/sediment interface, followed by 1.93 MPa (8.4%) above the well and 1 MPa (4.8%) where the dipping angle is 0°. The σ'_{xx} in the flat region is 0.92 MPa smaller compared to the value at the salt/sediment interface (see Figure 40). Three years after shut-in, the σ'_{xx} in the upper shale slightly decreased: 0.24 MPa in the flat region, 0.91 MPa above the well and 0.61 MPa at the salt/sediment interface (see Figure 37).

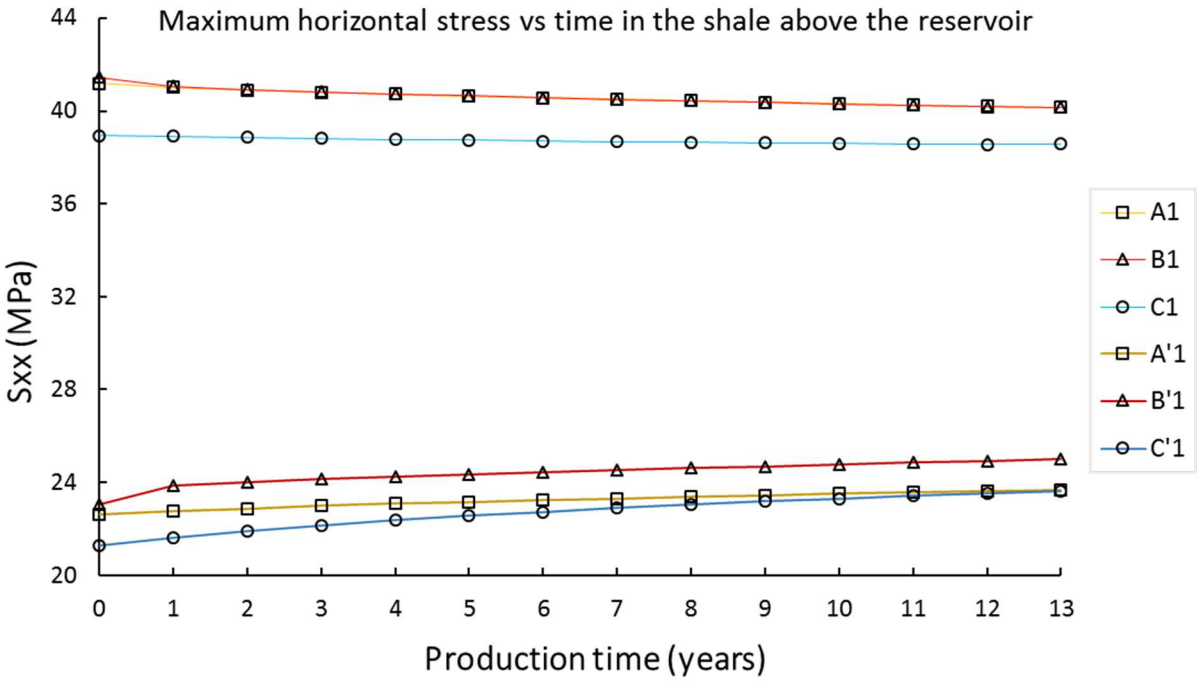


Figure 40. Total maximum horizontal stress (A1, B1 and C1) and effective maximum horizontal stress (A'1, B'1 and C'1) during production time of three upper shale elements, situated at different locations with respect to the dome, described in Figure 15(b). The total maximum horizontal stress decreased in the upper shale and the effective maximum horizontal stress increased. The σ_{xx} decreased more above the well, while the σ'_{xx} increased more at the salt/sediment interface.

Doing the same analysis for the lower shale which is represented by the elements A3, B3 and C3 shown in Figure 15(b), it is observed that the total maximum horizontal stress decreases more at point B3 (1.33 MPa ~ 3.1%), followed by the element at point A3 (1.16 MPa ~ 2.7%) and finally at the salt/sediment interface (0.96 MPa ~ 2.3%). From the previous results, the σ_{xx} component decreased more for lower shale than for the upper shale (0.14 MPa at point A, 0.03 MPa at point B and 0.65 MPa at the salt/sediment interface), as it is shown in Figure 41. Three years after shut-in, the σ_{xx} in the lower shale increased 0.19 MPa in the flat region, 0.45 MPa above the well and 0.24 MPa at the salt/sediment interface (see Figure 33).

Performing the same study for the lower shale which is characterized by the elements A3, B3 and C3 shown in Figure 15(b), it is observed that the effective maximum horizontal stress increases more at point B3 (2.63 MPa ~ 11%), followed by the element at the salt/sediment interface (1.92 MPa ~ 8.2%) and finally point A3 (1.26 MPa ~ 5.4%). From the previous results, the σ'_{xx} varies slightly between the upper and lower shale (0.19 MPa at point A, 0.71 MPa at point B and 0.08 MPa at the salt/sediment interface), as it is shown in Figure 41). Three years after shut-in, the σ'_{xx} in the lower shale decreased 0.21 MPa in the flat region, 1.02 MPa above the well and 0.23 MPa at the salt/sediment interface (see Figure 37).

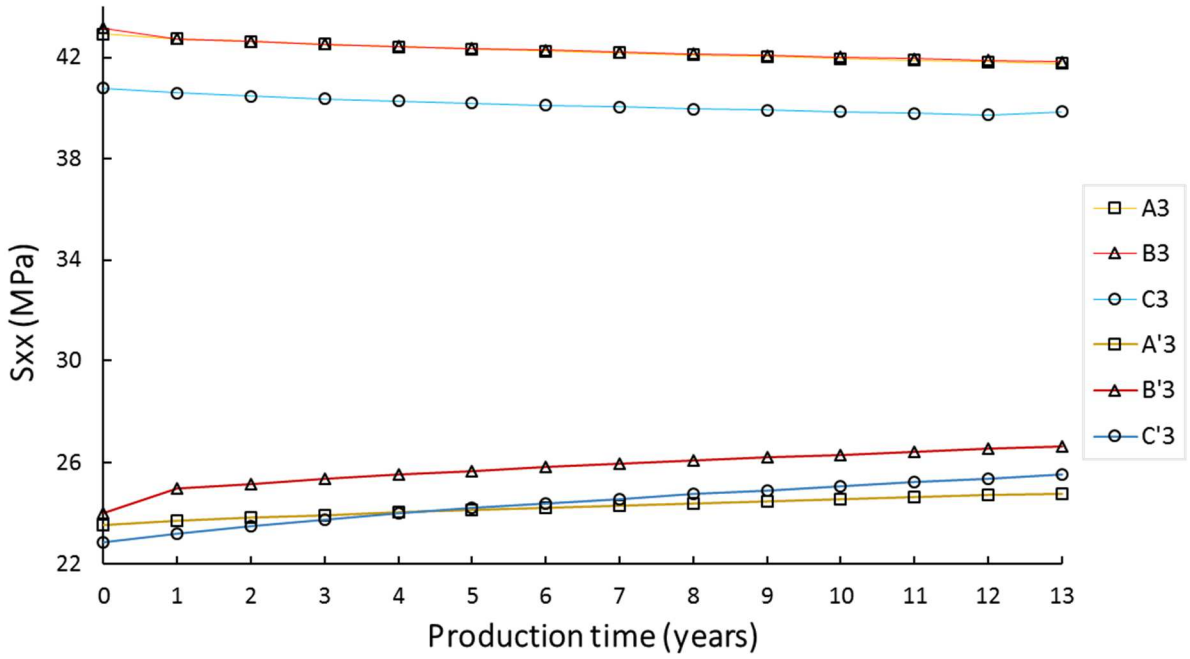


Figure 41. Total maximum horizontal stress (A1, B1 and C1) and effective maximum horizontal stress (A'1, B'1 and C'1) during production time of three lower shale elements situated at different locations with respect to the dome, described in Figure 15(b). The element below the well, experienced the maximum σ_{xx} reduction and the highest σ'_{xx} increment during production.

5.4 Total and effective minimum horizontal stresses

Figure 42 shows the total minimum horizontal stress changes ($\Delta\sigma_{yy}$) in the reservoir after production. It is observed that the reduction of the minimum horizontal stresses is governed by the well location and has more impact on the dipping layer compared to the flatten area. The maximum σ_{yy} reduction occurred around the well (3 MPa ~ 8.1%), followed by the changes at the salt/sediment interface (2.45 MPa ~ 7.7%), and at point A2 (2 MPa ~ 5.3%).

Analyzing the impact of the salt flow on the total minimum horizontal stress at the salt/sediment interface, it is noticed that the stress change of the reservoir element at point C2 is 0.24 MPa less, compared to the green element next to it. The total minimum horizontal stresses in the salt

decreased close to the salt/sediment interface but did not change at point D (38 m inside the dome).

Figure 43(d) and Figure 44(d), show how the total minimum horizontal stress recovered after shut-in: the σ_{yy} increased up to 1.4 MPa at point B2, 0.61 MPa at the salt/sediment interface and 0.47 MPa in the flat region. The total minimum horizontal stresses in the salt increased less than 5 MPa (see Figure 45).

Figure 46 shows the effective minimum horizontal stresses change $(\Delta\sigma'_{yy})$ in the reservoir increased after production. The effective minimum horizontal stresses is calculated using Eq. (34), defined in chapter 2. It may be said that the increment of σ'_{yy} is a function of the well location. Where the major increase happened (3.92 MPa ~ 20%), followed by the changes at the salt/sediment interface (2.52 MPa ~ 15.6%) and at point A2 (2.49 MPa ~ 12%). Examining the aforementioned results, the effective minimum horizontal stress at the salt/sediment interface does not change significantly with respect to the flatten area.

Figure 47(d) and Figure 48(d) show the $\Delta\sigma'_{yy}$ values after shut-in along the reservoir. The σ'_{yy} in the reservoir decreased up to 1.98 MPa around the well, accompanied by 0.71 MPa at the salt/sediment interface, and 0.61 at point A2. The effective minimum horizontal stresses in the salt are the same as the total minimum horizontal stresses after production and pressure build up (see Figure 49).

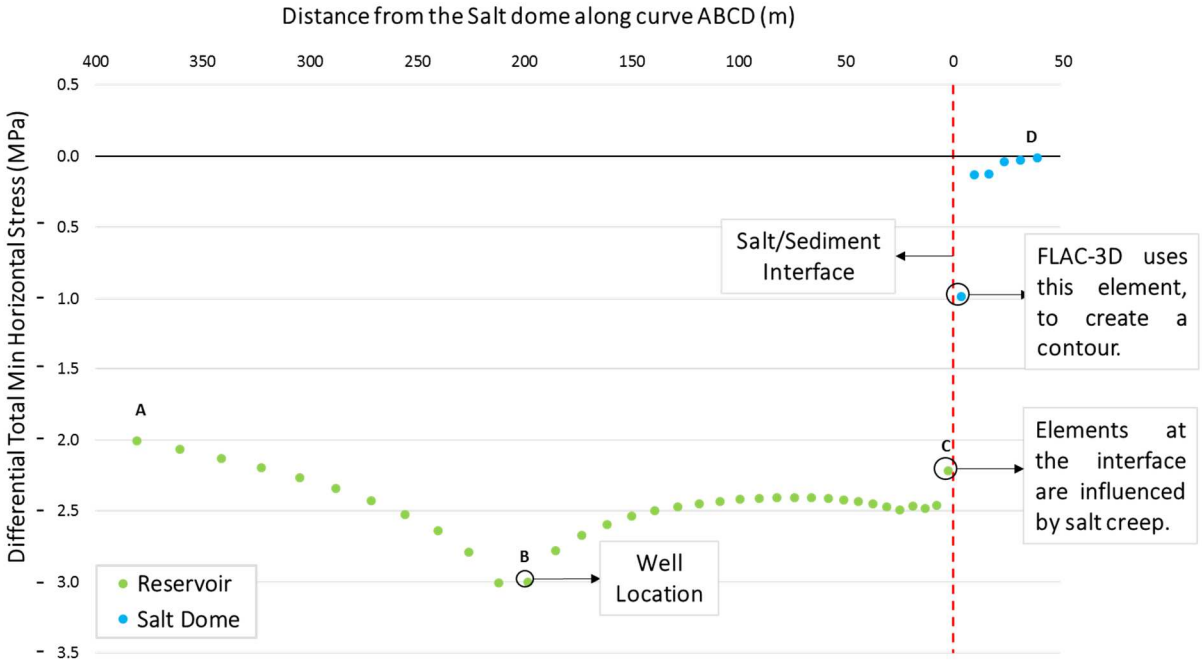


Figure 42. Change of total minimum horizontal stress as a function of distance from the salt/sediment interface, along the curve ABCD, after 13 years of production. Reservoir elements are represented in green, while salt elements are represented in blue. The σ_{yy} is controlled by the well location, where it presented the maximum decrease. The total minimum horizontal stress of the reservoir elements at the salt/sediment interface is altered by the salt creep. The salt elements at the salt/sediment interface present a total minimum horizontal stress different than the salt elements next to it, because the contour of this element interpolates the values of the sediment and salt gridpoints.

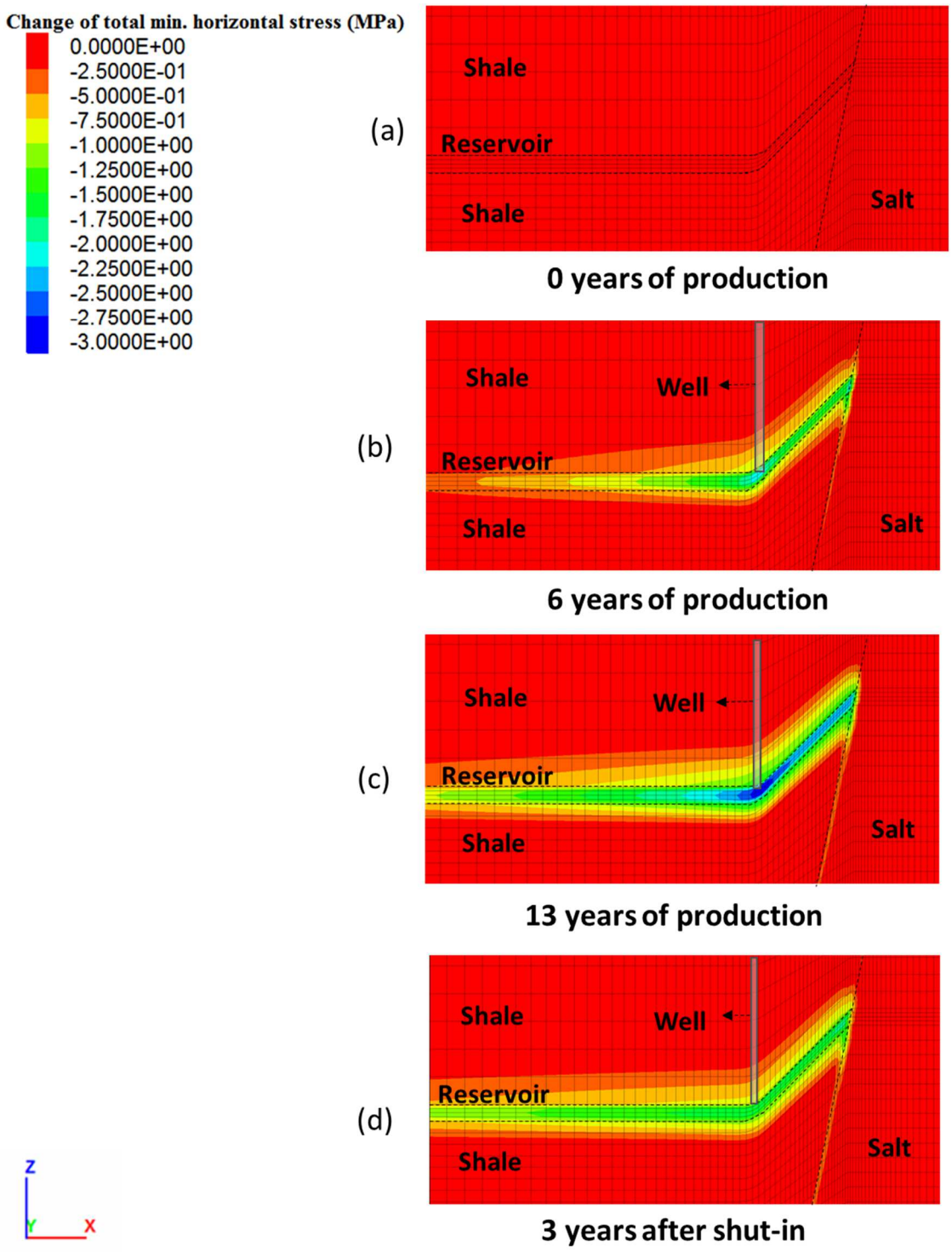


Figure 43. Total minimum horizontal stress changes along a xz-plane in the middle of the reservoir. (a) Initial state, (b) 6 years of production, (c) 13 years of production and (d) 3 years of steady state. The reduction of σ_{yy} in the reservoir is function of the well location and, extends toward the dipping layer. Three years after shut-in, σ_{yy} increases in the reservoir and the salt, reaching a steady state.

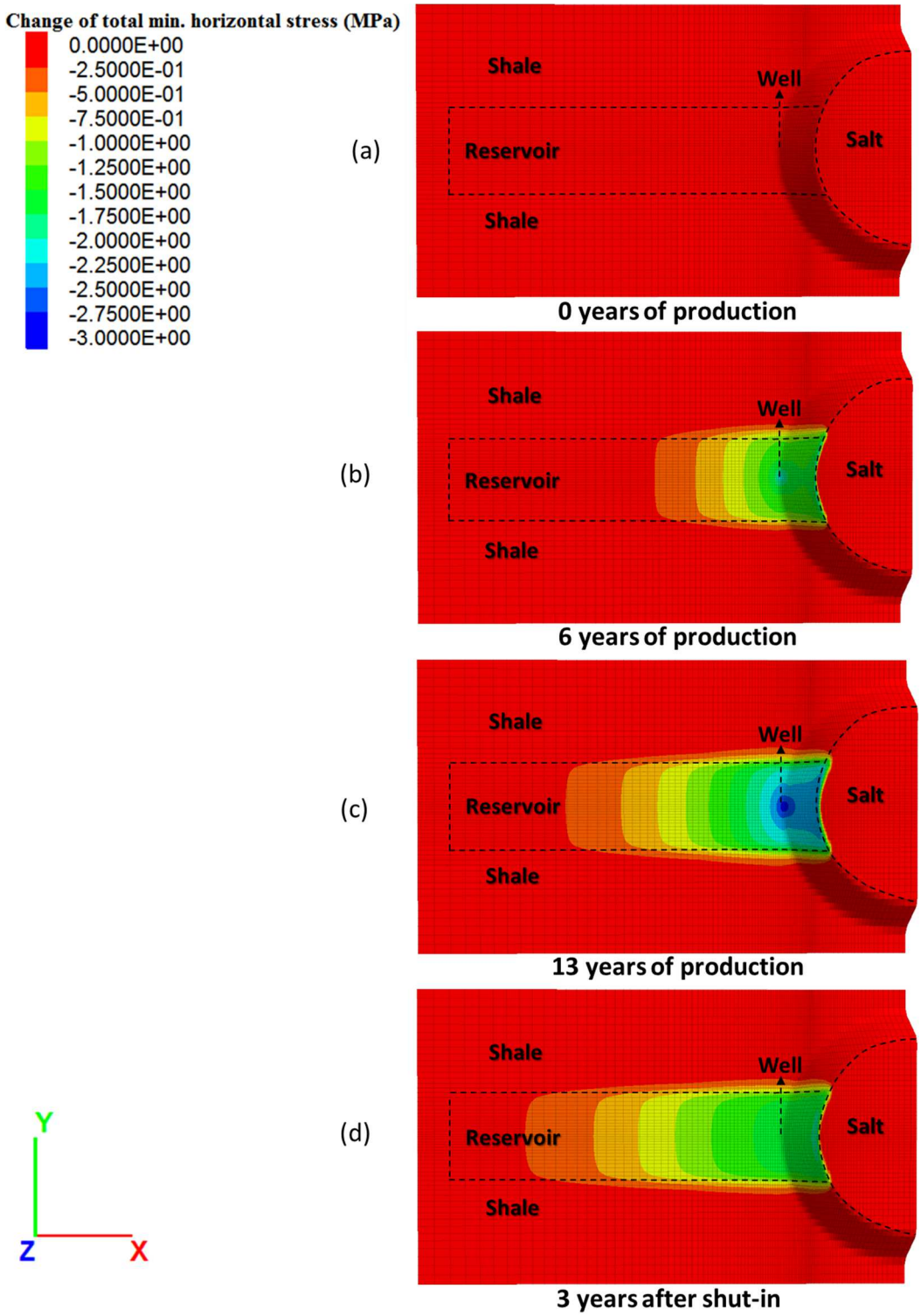


Figure 44. Total minimum horizontal stress changes in the xy-plane through the middle of the reservoir. (a) Initial state, (b) 6 years of production, (c) 13 years of production and (d) 3 years of steady state. The reduction of σ_{yy} in the reservoir is function of the well location and, extends toward the dipping layer. Three years after shut-in, σ_{yy} increases in the reservoir and the salt, reaching a steady state.

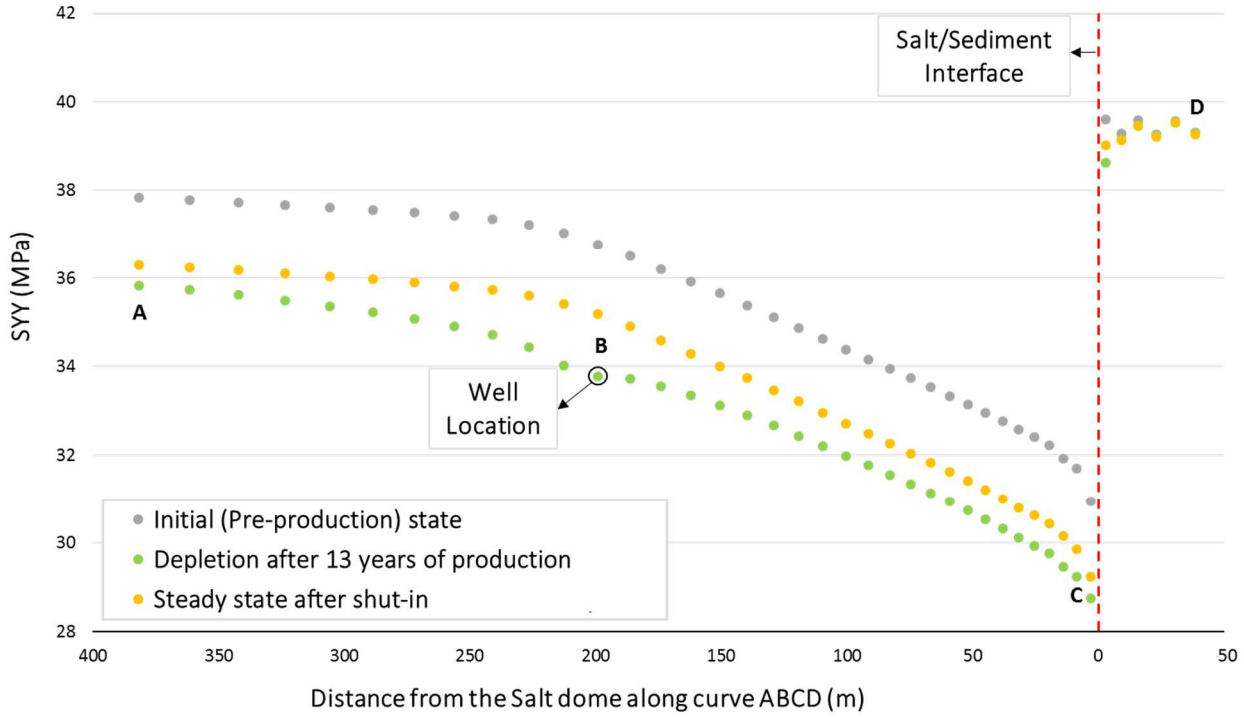


Figure 45. Total minimum horizontal stress along the trajectory ABCD. The σ_{yy} decreased after production and increased three years after shut-in. The minimum horizontal stress in the salt hardly change during the simulation. The total minimum horizontal stress of the reservoir elements at the salt/sediment interface is altered by the salt creep. The salt elements at the salt/sediment interface present a total minimum horizontal stress different than the salt elements next to it, because the contour of this element interpolates the values of the sediment and salt gridpoints.

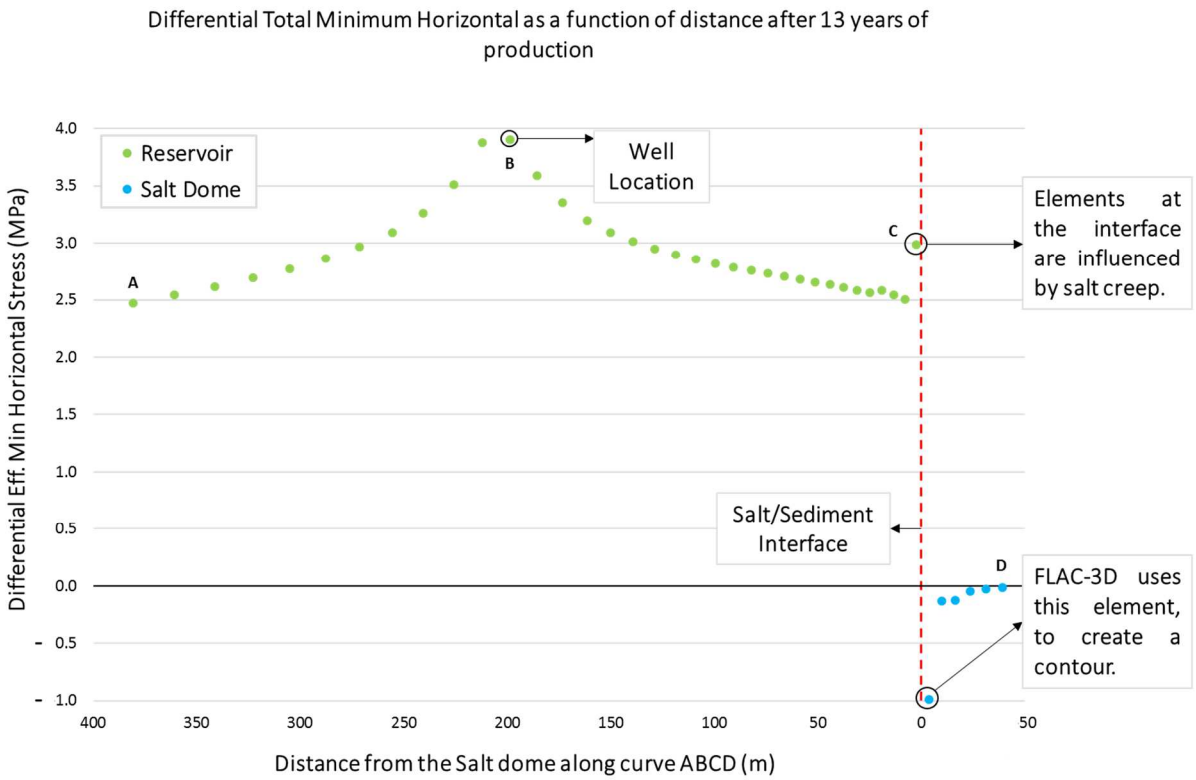


Figure 46. Change of effective minimum horizontal stress as a function of distance from the salt/sediment interface, along the curve ABCD, after 13 years of production. Reservoir elements are represented in green, while salt elements are represented in blue. The effective minimum horizontal stress increased along the reservoir and the salt. Where the major increment happened at point B2. The σ'_{yy} change is greater at the salt/sediment interface, compared to the flat region. The effective minimum horizontal stress of the reservoir elements at the salt/sediment interface is altered by the salt creep. The salt elements at the salt/sediment interface present an effective minimum horizontal stress different than the salt elements next to it, because the contour of this element interpolates the values of the sediment and salt gridpoints.

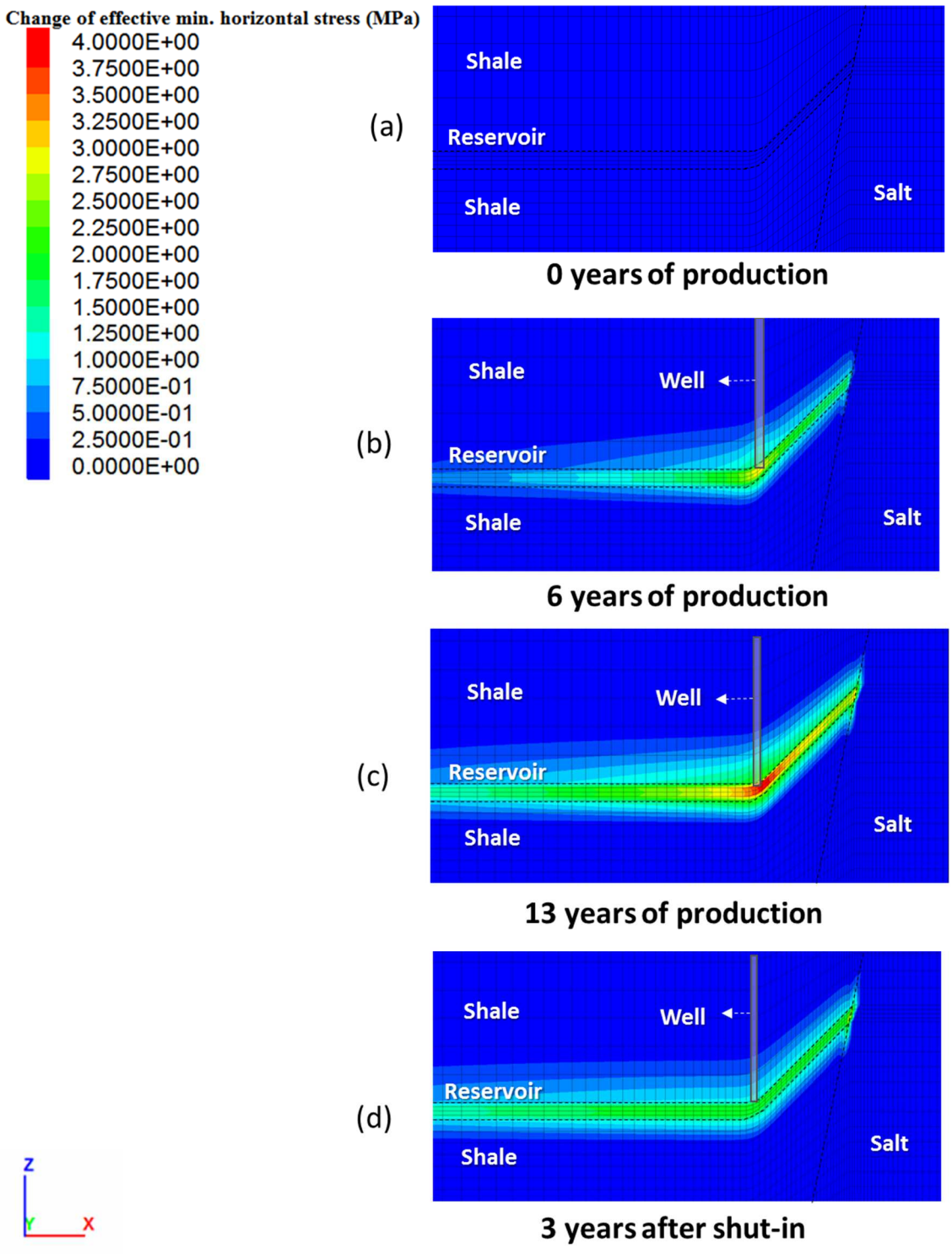


Figure 47. Effective minimum horizontal stress changes along a xz-plane in the middle of the reservoir. (a) Initial state, (b) 6 years of production, (c) 13 years of production and (d) 3 years of steady state. The σ'_{yy} is controlled by the well location and increases after production in the reservoir and shale. Three years after shut-in, the σ'_{yy} decreases in the model.

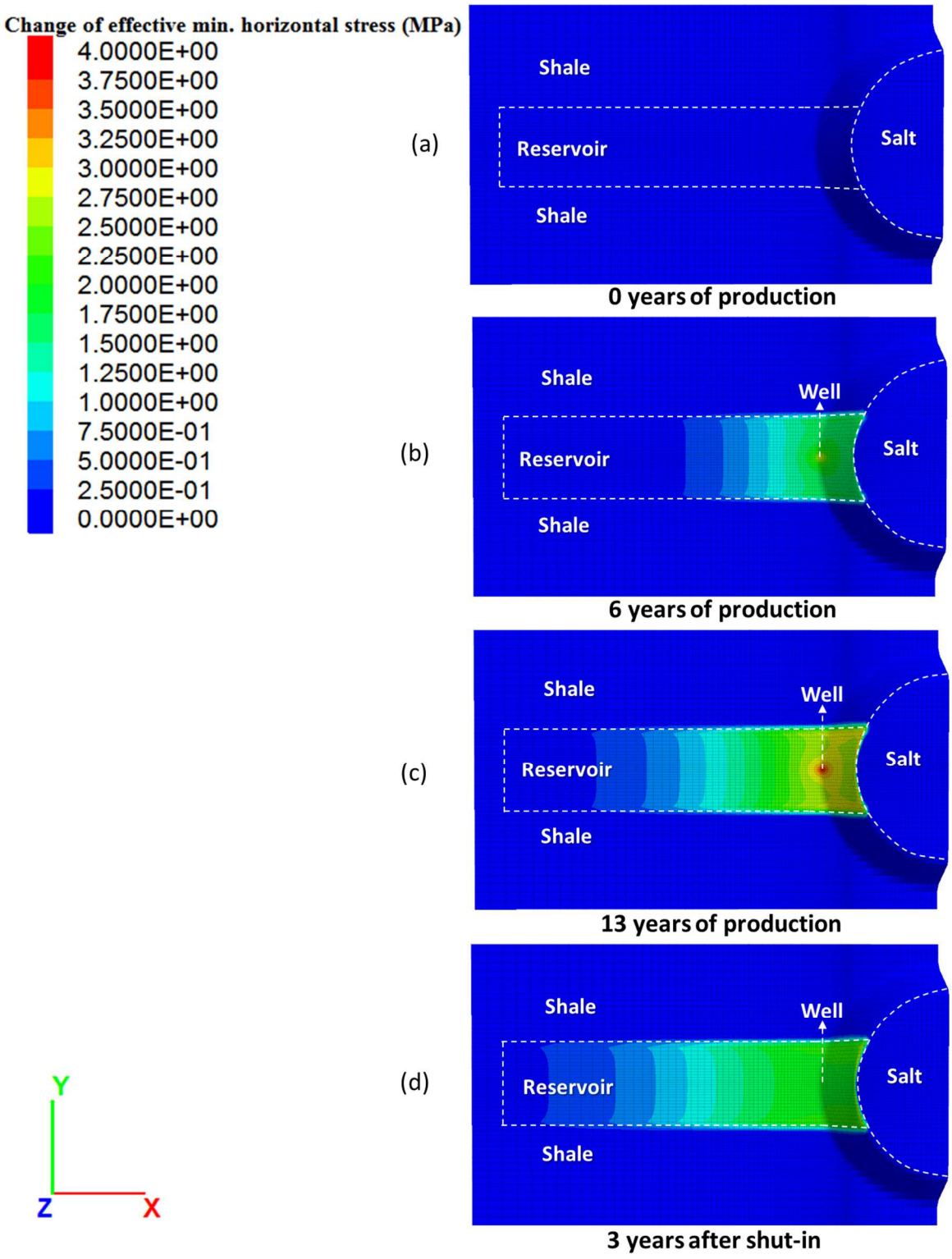


Figure 48. Effective minimum horizontal stress changes along a xy-plane in the middle of the reservoir. (a) Initial state, (b) 6 years of production, (c) 13 years of production and (d) 3 years of steady state. The σ'_{yy} is controlled by the well location and increases with depletion. Three years after shut-in, the σ'_{yy} decreased in the model.

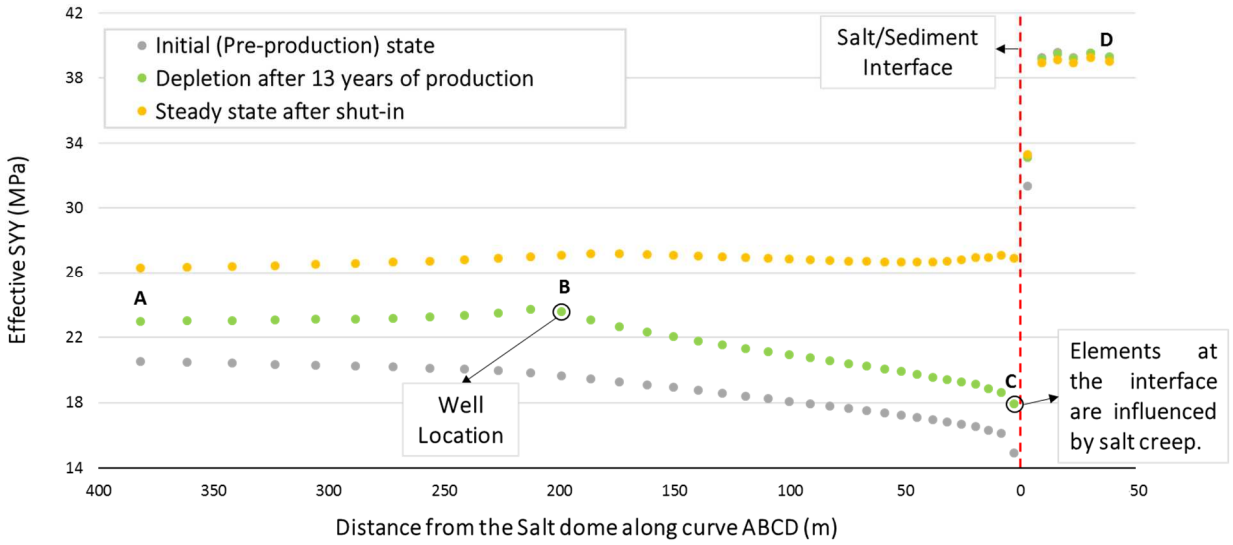


Figure 49. Effective minimum horizontal stress along the trajectory ABCD. The increment of the σ'_{yy} caused by production goes up to 3.91 MPa at the well location. Three years after shut-in, the σ'_{yy} increased up to 1.4 MPa around the well. The effective and total stresses in the salt are the same. The effective minimum horizontal stress of the reservoir elements at the salt/sediment interface is altered by the salt creep. The salt elements at the salt/sediment interface present an effective minimum horizontal stress different than the salt elements next to it, because the contour of this element interpolates the values of the sediment and salt gridpoints.

Studying the behavior of σ_{yy} during the production time, the upper shale which is represented by the elements A1, B1 and C1 as shown in Figure 15(b), experienced the major reduction of σ_{yy} at point B1 (1.32 MPa ~ 3.7%), followed by the element at the salt/sediment interface (1.13 MPa ~ 3.7%) and finally at point A1 (0.89 MPa ~ 2.4%). The σ_{yy} reduction at the salt/sediment interface is 0.24 MPa greater compared to the flat region (see Figure 50). Three years after shut-in, the σ_{yy} in the upper shale increased 0.19 MPa in the flat region, 0.51 MPa above the well and 0.25 MPa at the salt/sediment interface (see Figure 43).

Reviewing the behavior of σ'_{yy} during the production time, the upper shale which is represented by the elements A1, B1 and C1 as shown in Figure 15(b), experienced the major increment of

σ'_{yy} around the well (1.92 MPa ~ 11%), followed by the element at point A1 (1.21 MPa ~ 6.6%) and finally at the salt/sediment interface (1.17 MPa ~ 8.5%). The difference of σ'_{yy} between the flat region and the salt/sediment interface is less than 0.1 MPa (see Figure 50). Three years after shut-in, the σ'_{yy} in the upper shale decreased: 0.28 MPa in the flat region, 0.89 MPa above the well and 0.36 MPa at the salt/sediment interface (see Figure 47).

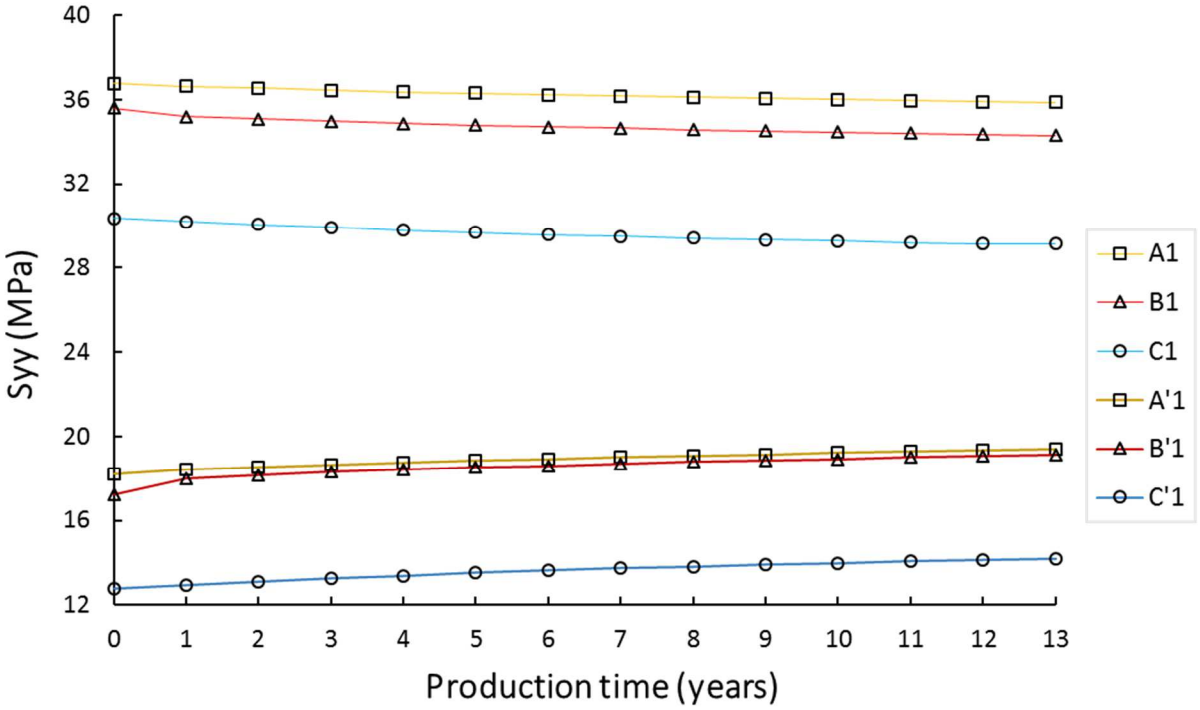


Figure 50. Total minimum horizontal stress (A1, B1 and C1) and effective maximum horizontal stress (A'1, B'1 and C'1) during production time of three upper shale elements, situated at different locations with respect to the dome, described in Figure 15(b). The element above the well experienced the maximum σ_{yy} reduction and the highest σ'_{yy} increment.

Doing the same analysis for the lower shale which is represented by the elements A3, B3 and C3 shown in Figure 15(b), it is observed that the total maximum horizontal stress decreases more at point B3 (1.72 MPa ~ 4.9%), followed by the element at the salt/sediment interface (1.57 MPa ~

4.9%) and finally at point A3 (1.09 MPa ~ 2.8%). From the previous information, it can be notice that the σ_{yy} varies slightly between the upper and lower shale, where the major change occurs close to the dome (0.19 MPa at point A, 0.4 MPa at point B and 0.44 MPa at the salt/sediment interface), as it is shown in Figure 51. Three years after shut-in, the σ_{yy} in the lower shale increased 0.16 MPa in the flat region, 0.55 MPa above the well and 0.27 MPa at the salt/sediment interface (see Figure 43).

Performing the same analysis for the lower shale which is characterized by the elements A3, B3 and C3 shown in Figure 15(b), it is observed that the effective minimum horizontal stress increases more at point B3 (2.24 MPa ~ 12.5%), followed by the element at point A3 (1.34 MPa ~ 7.1%) and finally at the salt/sediment interface (1.31 MPa ~ 5.4%). From the previous outcomes, it can be observed that the σ'_{yy} does not vary significantly between the upper and lower shale (0.13 MPa at point A, 0.33 MPa at point B and 0.13 MPa at the salt/sediment interface). The effective minimum horizontal stress change at point C3 is 0.49 MPa higher compared to the magnitude of the element next to it, because of the salt creep (see Figure 51). Three years after shut-in, the σ'_{yy} in the lower shale decreased 0.24 MPa in the flat region, 0.92 MPa above the well and 0.19 MPa at the salt/sediment interface (see Figure 47).

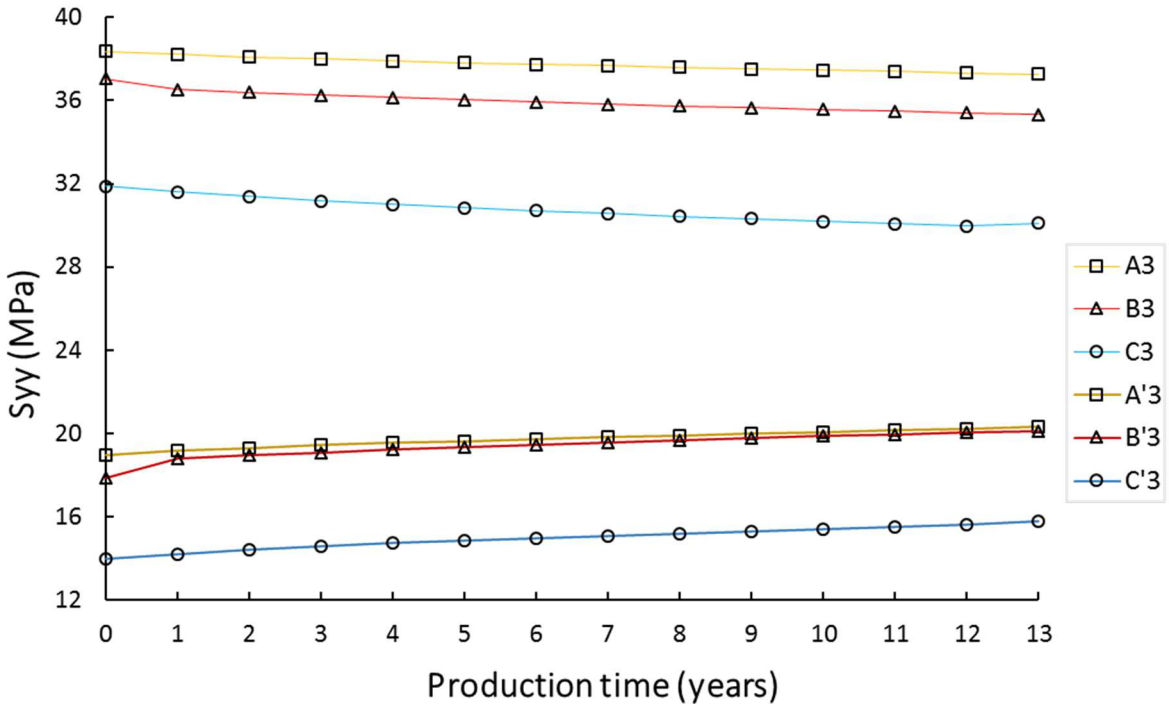


Figure 51. Total minimum horizontal stress (A1, B1 and C1) and effective maximum horizontal stress (A'1, B'1 and C'1) during production time of three lower shale elements situated at different locations with respect to the dome, described in Figure 15(b). The element above the well, experienced the maximum σ_{yy} reduction and the highest σ'_{yy} increment.

5.5 The xy-component of total stress tensor

The xy-component of total stress tensor (S_{xy}) in the reservoir slightly changed. But evaluating the behavior of S_{xy} is important to determine what controls the increment or reduction in our model. From this study, it is observed that S_{xy} is controlled by the well location and dip angle of the reservoir. Depletion increases the shear stresses and concentrates them up to $2.5x10^{-2}$ MPa around the well and up to $4.37x10^{-2}$ MPa close to the salt/sediment interface, after 13 years of production. The magnitude of the stress perturbation of the element at point C2 is $2.5x10^{-2}$ MPa lower, compared to the green element next to it (see Figure 52), this is a consequence of the salt creep effect. Three years after shut-in, the stress perturbation decreases as a result of the pressure

build up (see Figure 53(d)). The shear stresses in the salt diminish in the opposite direction to the salt/sediment interface. After shut-in, the results were the same (see Figure 54).

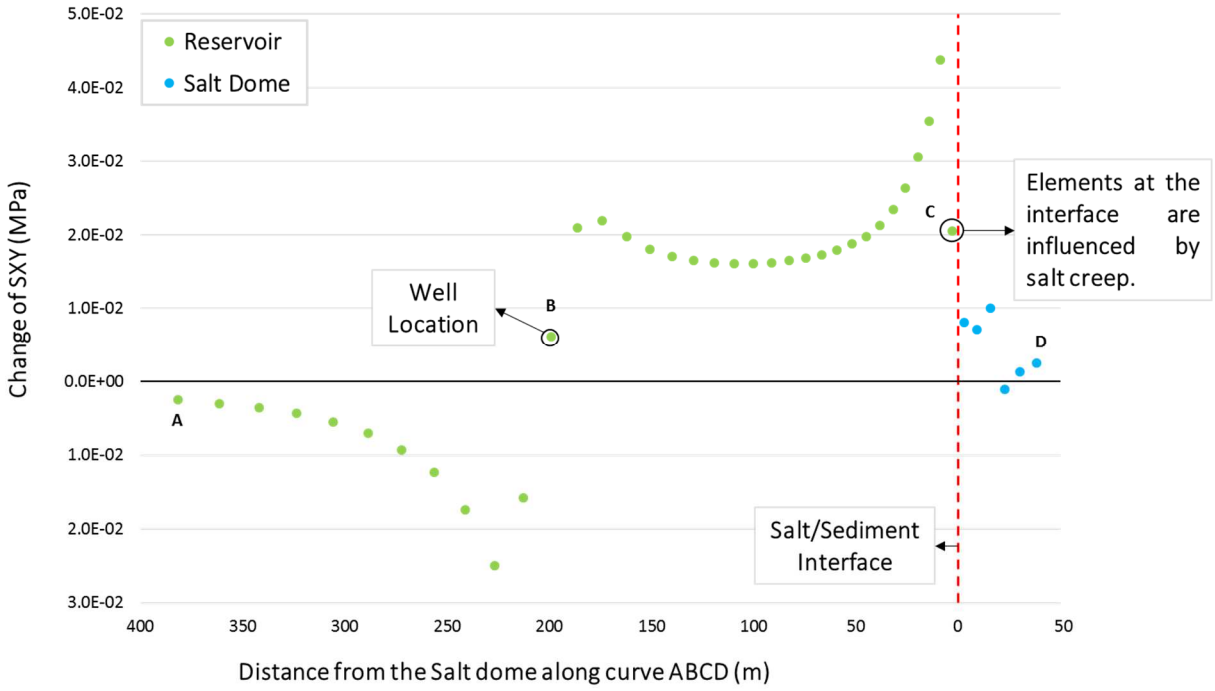


Figure 52. Change of S_{xy} total stress as a function of distance from the salt/sediment interface, along the curve ABCD, after 13 years of production. Reservoir elements are represented in green, while salt elements are represented in blue. The stress perturbation magnitude increases slightly and concentrates toward the well location and toward the salt/sediment interface. However, the stress perturbation in the salt tend to dissipate as a result of the salt creep, because the salt cannot sustain shear stresses.

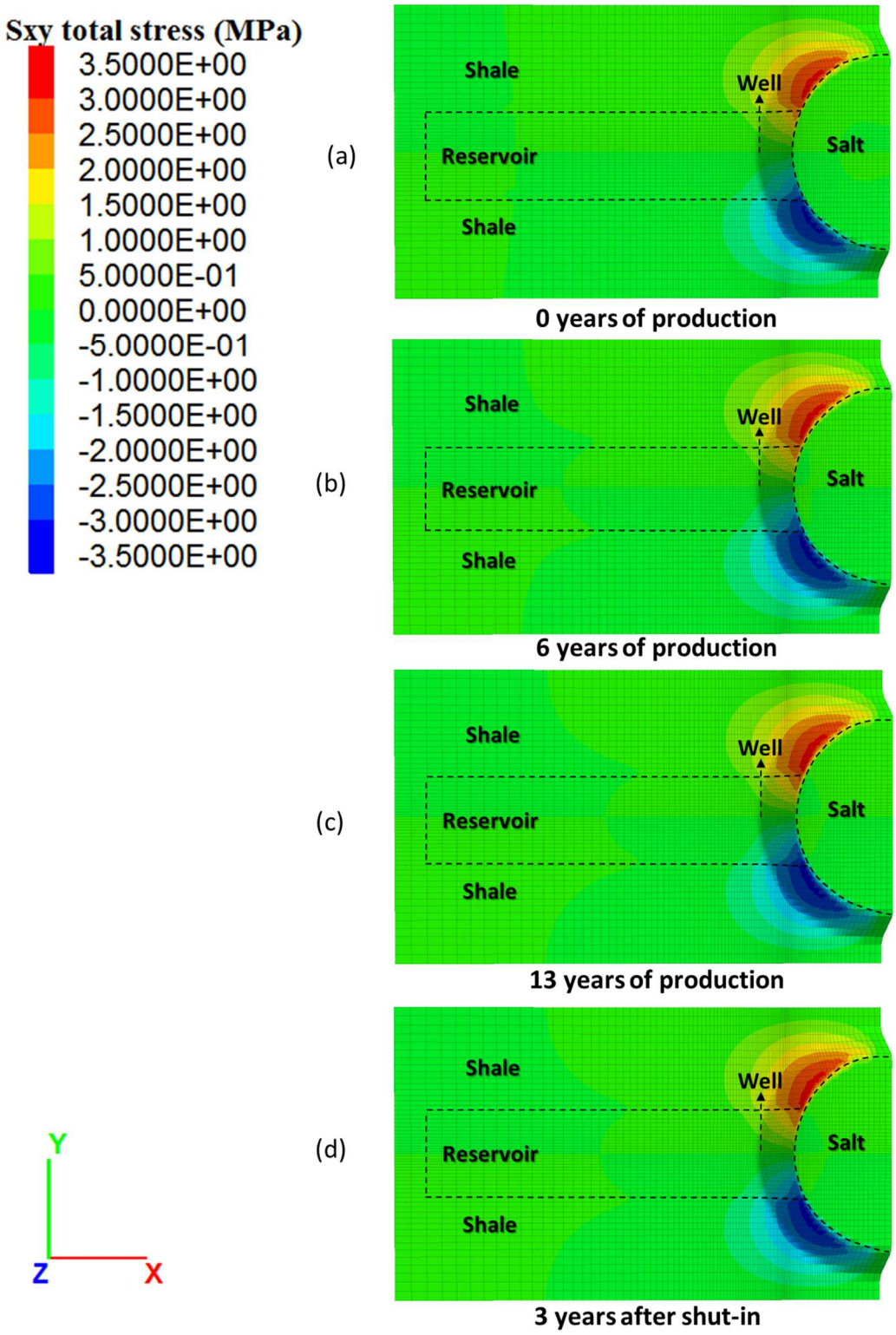


Figure 53. S_{xy} total stress in the xy-plane through the middle of the reservoir. (a) Initial state, (b) 6 years of production, (c) 13 years of production and (d) 3 years of steady state. The shear stresses increase with production, which is a result of the vertical and horizontal stress changes.

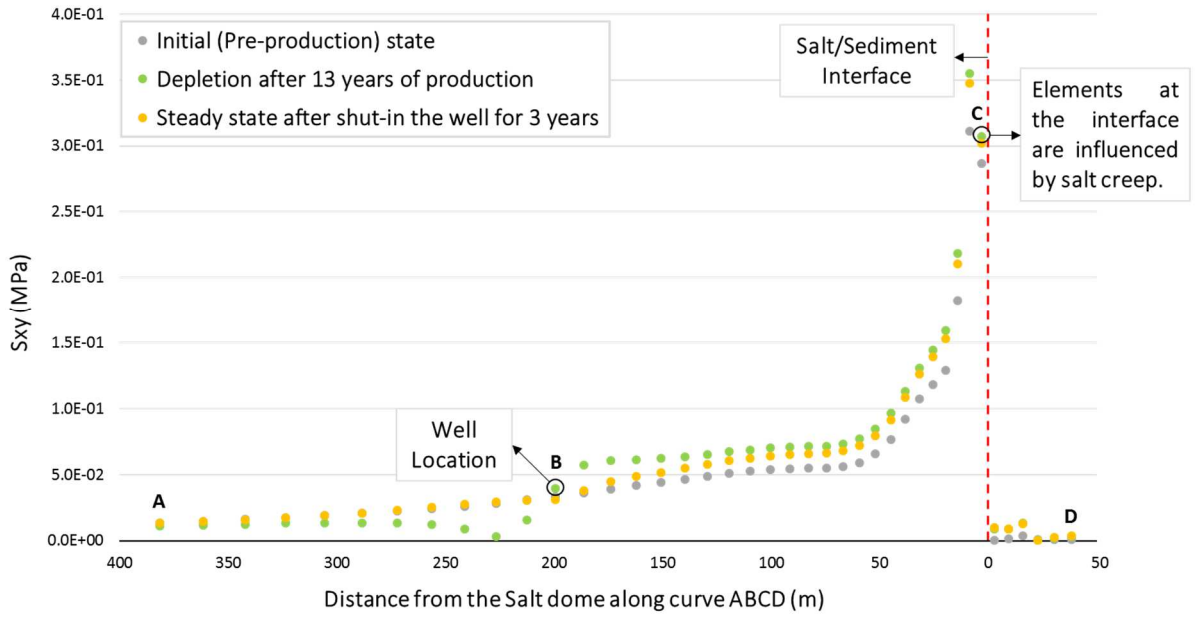


Figure 54. S_{xy} total stress along the trajectory ABCD. The stress perturbation magnitude increases with depletion around the well and toward the salt/sediment interface.

Studying the behavior of S_{xy} during the production time in the upper shale, which is represented by the elements A1, B1 and C1 as shown in Figure 15(b), we observed that the stress perturbation increased up to $0.8x10^{-2}$ MPa at the salt/sediment interface, while it decreased above the well and flat area (see Figure 55).

Doing the same analysis for the lower shale which is represented by the elements A3, B3 and C3 shown in Figure 15(b), we observed that the stress perturbation increased up to $2.5x10^{-2}$ MPa at the salt/sediment interface, followed by $2.3x10^{-2}$ MPa below the well, while it decreased up to $0.2x10^{-2}$ MPa in the flat area. From the previous information, it can be notice that the S_{xy}changes more in the lower shale than in the upper shale ($2.0x10^{-2}$ MPa at point B and $2.0x10^{-2}$ MPa at the salt/sediment interface), as it is shown in Figure 56.

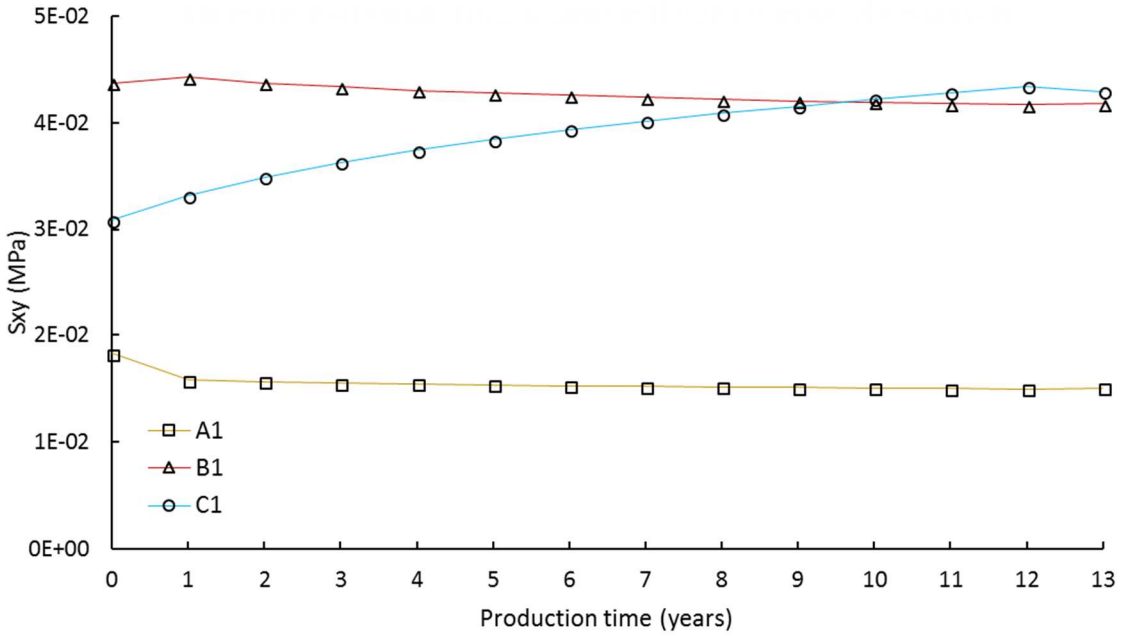


Figure 55. S_{xy} total stress during production time of three upper shale elements (A1, B1 and C1), situated at different locations with respect to the dome, described in Figure 15(b). The stress perturbation magnitude in the upper shale increases at the salt/sediment interface, while it decreases above the well and in the flat area.

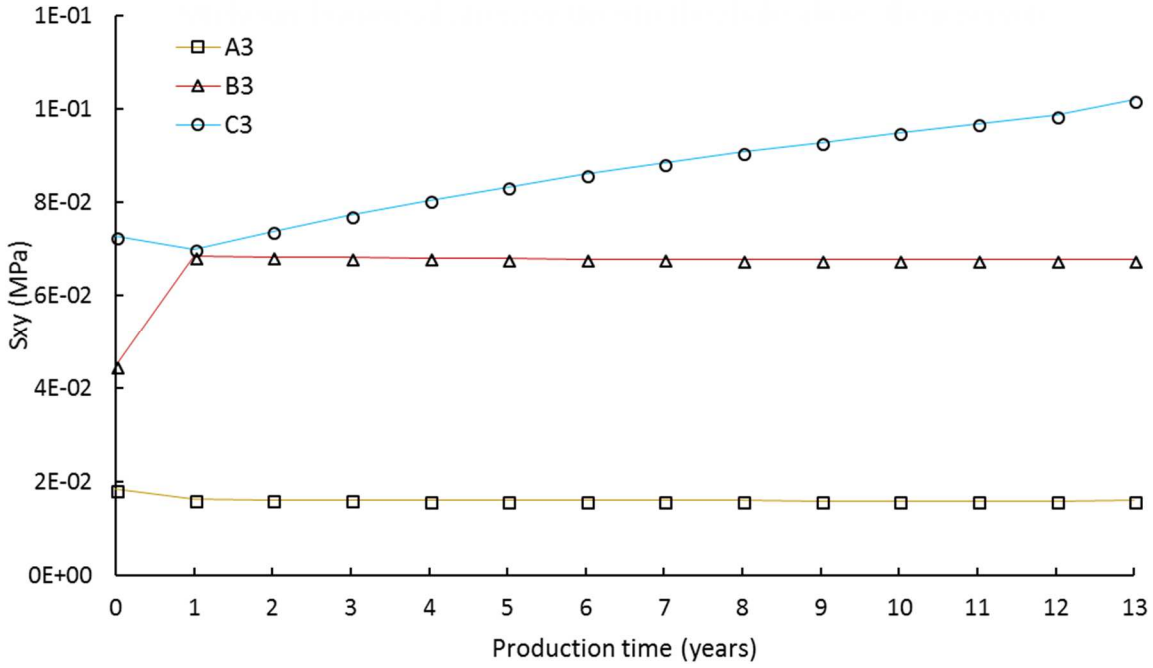


Figure 56. S_{xy} total stress during production time of three lower shale elements (A3, B3 and C3) situated at different locations with respect to the dome, described in Figure 15(b). The stress perturbation magnitude in the lower shale increases at the salt/sediment interface and below the well, while it decreases in the flat area.

5.6 The yz-component of total stress tensor

The yz-component of total stress tensor (S_{yz}) in the reservoir did not vary considerably, but it is important to consider its behavior during production. From Figure 57, it is observed that S_{yz} is controlled by the well location and dipping angle. Which increases the induced shear stresses and concentrates them up to $0.88x10^{-2}$ MPa around the well and up to $5.23x10^{-2}$ MPa at the salt/sediment interface. However, the induced shear stresses decreased up to $1.23x10^{-2}$ MPa in the zone where the reservoir dipping angle is 45°, after 13 years of production. The stress perturbation magnitude of the element at point C2 is $2.0x10^{-2}$ MPa greater, compared to the green element next to it, this is a consequence of the salt creep effect. Three years after shut-in, the stress perturbation diminishes as a result of the pressure build up (see Figure 58(d)). The shear stresses in the salt decrease in the opposite direction to the salt/sediment interface. After shut-in, there were not significant changes in the salt (see Figure 59).

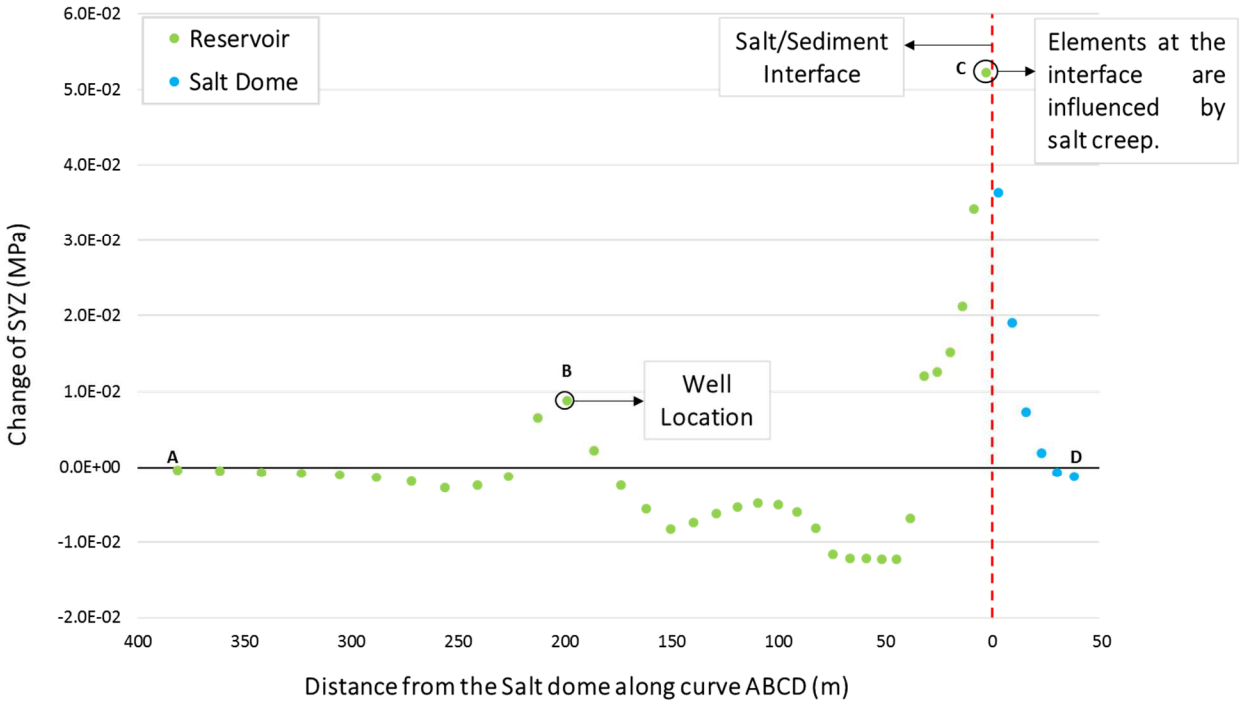


Figure 57. Change of S_{yz} total stress as a function of distance from the salt/sediment interface, along the curve ABCD, after 13 years of production. Reservoir elements are represented in green, while salt elements are represented in blue. The stress perturbation magnitude increases slightly and concentrates toward the well location and toward the salt/sediment interface. However, the stress perturbation decreased in the area with a steeper dipping angle (up to 0.012 MPa). The stress perturbation in the salt tend to dissipate as a result of the salt creep, because the salt cannot sustain shear stresses.

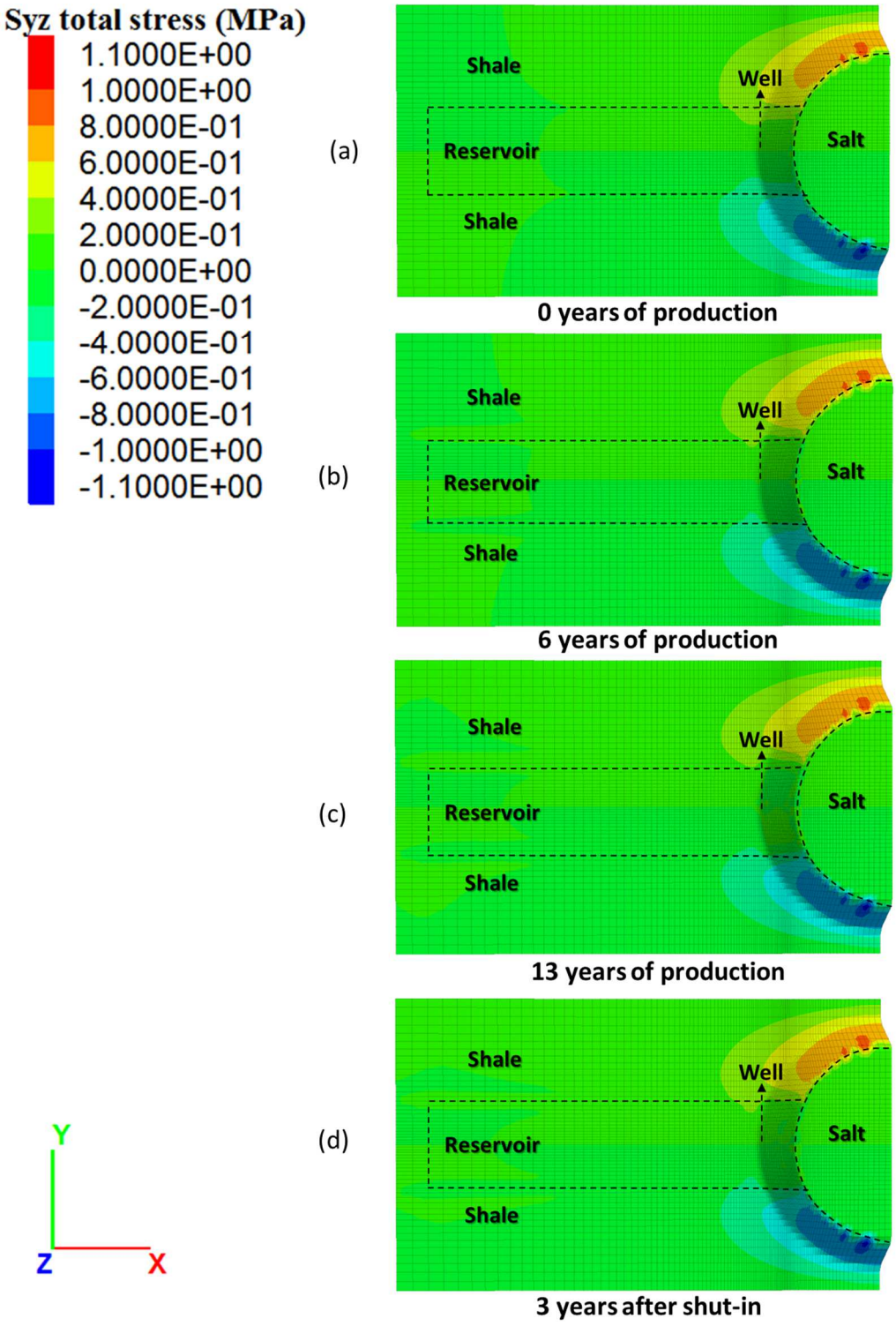


Figure 58. S_{yz} total stress in the yz-plane through the middle of the reservoir. (a) Initial state, (b) 6 years of production, (c) 13 years of production and (d) 3 years of steady state. The shear stresses decreased in the sides of the reservoir toward the well location during production, which is a result of the vertical and horizontal stress changes.

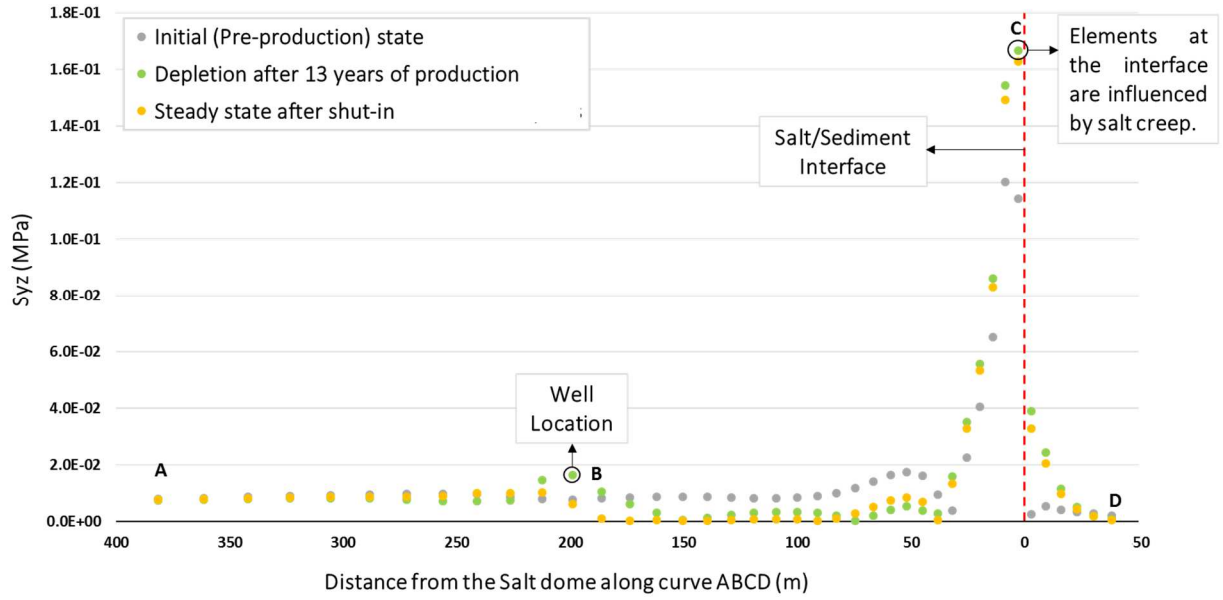


Figure 59. S_{yz} total stress along the trajectory ABCD. The shear stresses tend to increase toward the salt dome, where the dipping angle is steeper. The stress perturbation magnitude increases with depletion around the well and toward the salt/sediment interface and decreases in the area with a steeper dipping angle.

Studying the behavior of S_{yz} during the production time in the upper shale, which is represented by the elements A1, B1 and C1 as shown in Figure 15(b), we observed that the stress perturbation increased up to $1.3x10^{-2}$ MPa above the well, while it decreased up to $0.7x10^{-2}$ MPa at the salt/sediment interface (see Figure 60).

Performing the same analysis for the lower shale which is represented by the elements A3, B3 and C3 shown in Figure 15(b), we observed that the stress perturbation increased up to $0.4x10^{-2}$ MPa below the well, while it decreased up to $0.5x10^{-2}$ MPa at the salt/sediment interface, followed by $0.3x10^{-2}$ MPa in the flat area (see Figure 61). From the previous information, it can be notice that the S_{yz} changes more in the upper shale than in the lower shale at points A and B, but the opposite behavior is observed at the salt/sediment interface.

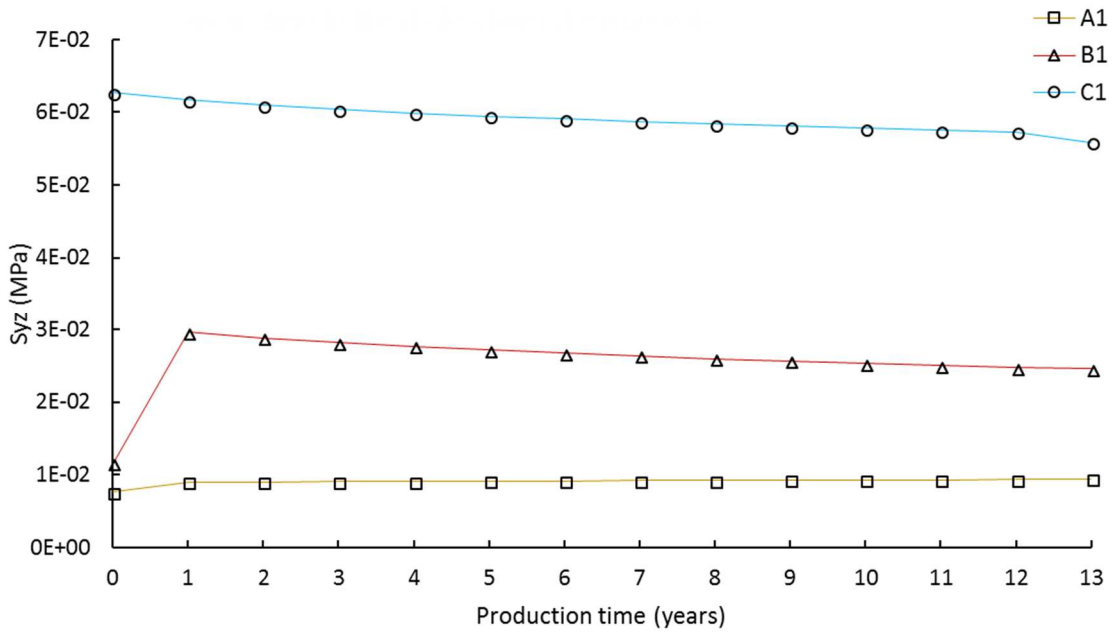


Figure 60. S_{yz} total stress during production time of three upper shale elements (A1, B1 and C1), situated at different locations with respect to the dome, described in Figure 15(b). The stress perturbation magnitude in the upper shale increases above the well and in the flat area, while it decreases at the salt/sediment interface.

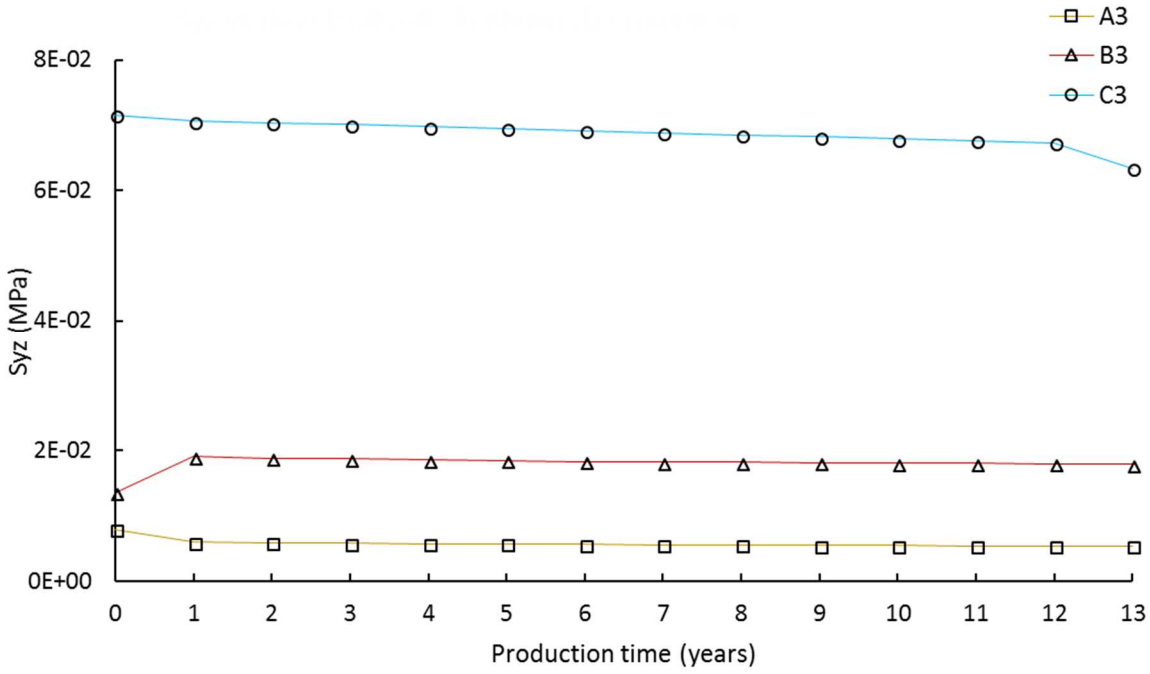


Figure 61. S_{yz} total stress during production time of three lower shale elements (A3, B3 and C3) situated at different locations with respect to the dome, described in Figure 15(b). The stress perturbation magnitude in the lower shale increases below the well, while it decreases at the salt/sediment interface and in the flat area.

5.7 The xz-component of the total stress tensor

The xz-component of the total stress tensor (S_{xz}) in the reservoir is controlled by the dipping angle and the well location. Which increases the induced shear stresses and concentrates them up to $8.42x10^{-1}$ MPa at the salt/sediment interface and $5.34x10^{-1}$ MPa around the well, after 13 years of production. The stress perturbation magnitude of the element at point C2 is $1.9x10^{-1}$ MPa lower, compared to the green element next to it (see Figure 62), this is a consequence of the salt creep effect. After shut-in, the stress perturbation decreases as a result of the pressure build up (see Figure 63(d)). The shear stresses in the salt increase after production and diminish as it moves into the dome. However, after shut-in, the S_{xz} in the salt decreases (see Figure 64).

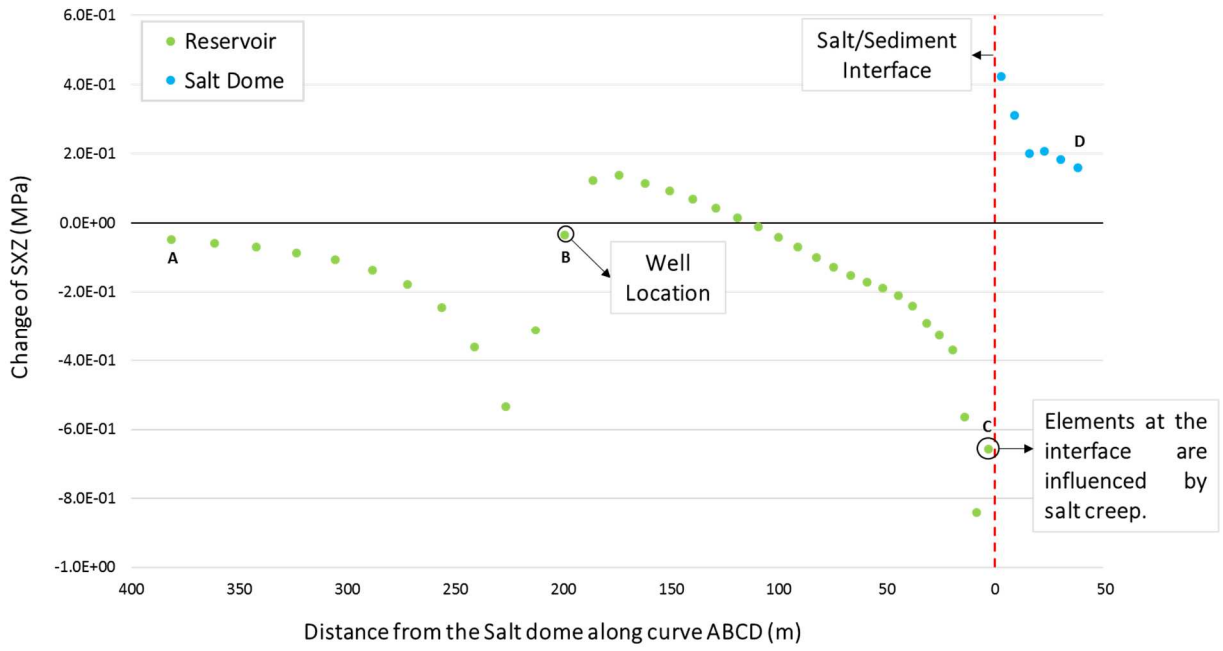


Figure 62. Change of S_{xz} total stress as a function of distance from the salt/sediment interface, along the curve ABCD, after 13 years of production. Reservoir elements are represented in green, while salt elements are represented in blue. The stress perturbation magnitude increases slightly and concentrates toward the well location and toward the salt/sediment interface. However, the stress perturbation in the salt tend to dissipate as a result of the salt creep, because the salt cannot sustain shear stresses.

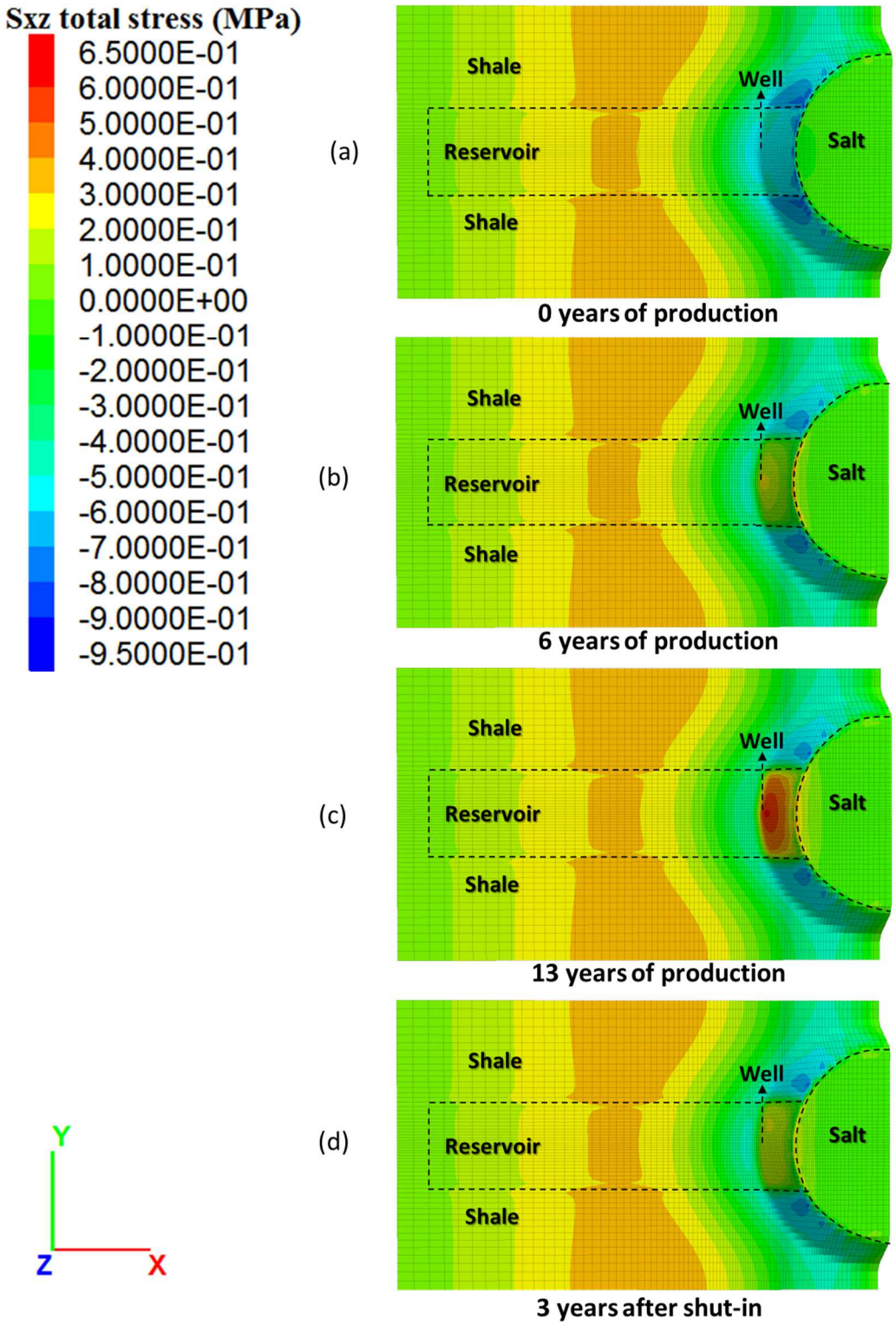


Figure 63. S_{xz} total stress along a xz-plane in the middle of the reservoir. (a) Initial state, (b) 6 years of production, (c) 13 years of production and (d) 3 years of shut in. The shear stresses increased with production around the well and extended toward the salt/sediment interface.

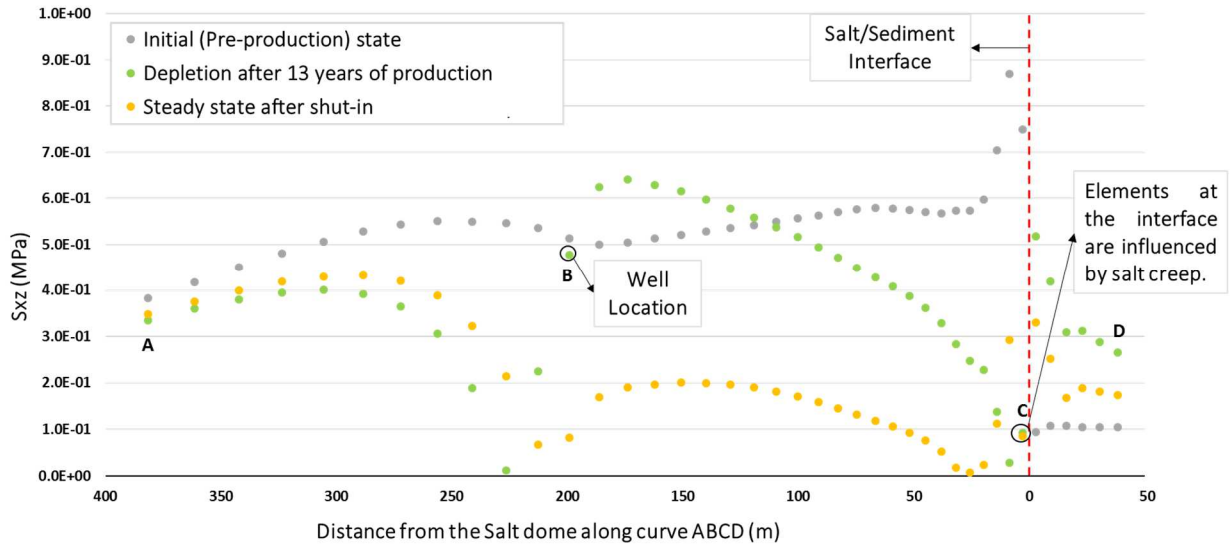


Figure 64. S_{xz} total stress along the trajectory ABCD. The stress perturbation magnitude increases with depletion around the well and decreases toward the salt/sediment interface.

Reviewing the behavior of S_{xz} during production time in the upper shale, which is represented by the elements A1, B1 and C1 as shown in Figure 15(b), we observed that the stress perturbation decreased up to $6.36x10^{-1}$ MPa, followed by $5.12x10^{-1}$ MPa above the well, while it slightly increased in the flat area (see Figure 65).

Performing the same analysis for the lower shale, which is represented by the elements A3, B3 and C3 shown in Figure 15(b), we observed that the stress perturbation decreased $1.11x10^{-1}$ MPa in the flat region, $1.28x10^{-1}$ MPa below the well and $3.16x10^{-1}$ MPa the salt/sediment interface (see Figure 66). From the previous results, it is observed that S_{xz} changes more in the upper shale than in the lower shale for points A, B and C.

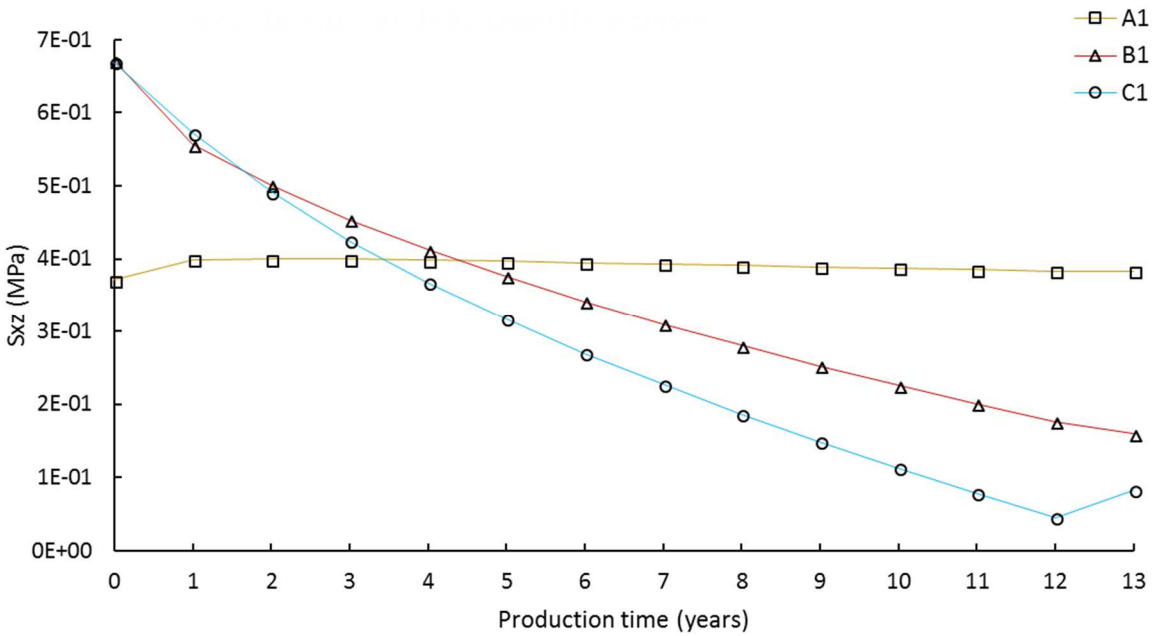


Figure 65. S_{xz} total stress during production time of three upper shale elements (A1, B1 and C1), situated at different locations with respect to the dome, described in Figure 15(b). The stress perturbation magnitude in the upper shale decreases at the salt/sediment interface and above the well, while it slightly increases in the flat area.

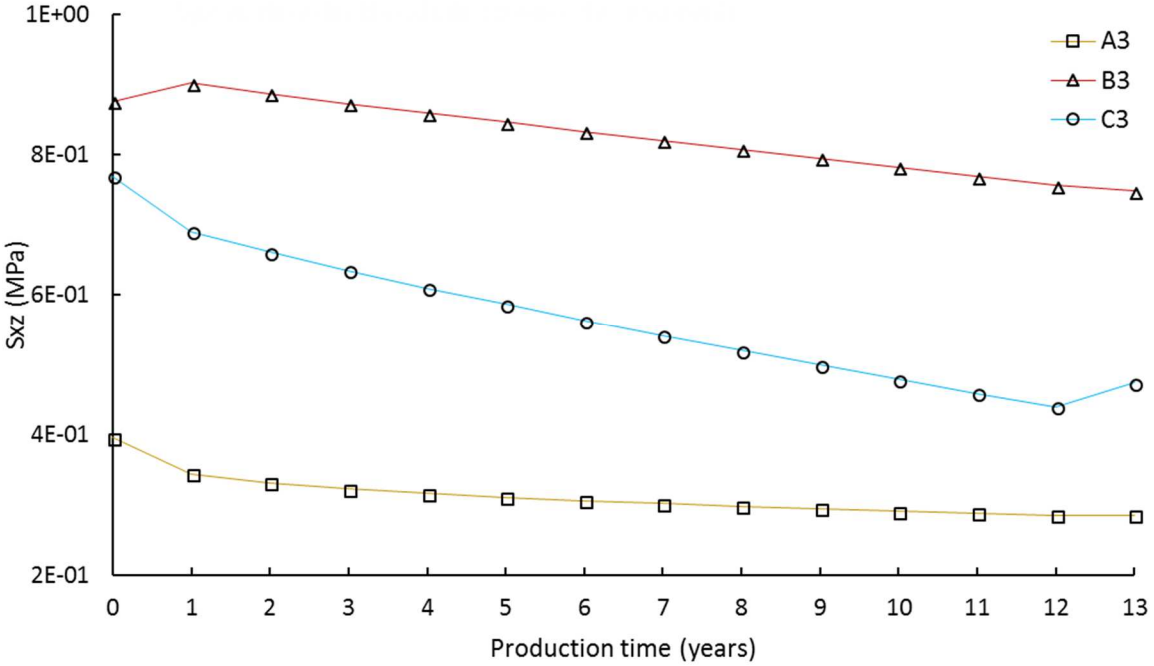


Figure 66. S_{xz} total stress during production time of three lower shale elements (A3, B3 and C3) situated at different locations with respect to the dome, described in Figure 15(b). The stress perturbation magnitude in the lower shale decreases below the well, at the salt/sediment interface and flat area.

5.8 Total and effective stress path

To analyze the effect of the stress and pore pressure changes in the reservoir and upper/lower shale during production, Mohr circles are plotted at 9 different locations defined in Figure 15(b), using the effective and total principal stresses. In order to avoid misleading results from the elements at point C (affected by the deformation of the salt), we did our analysis taking the element next to it and called it for this particular case point C.

The total stress path during production followed by the reservoir in the flat region (point A2), where the well is located (point B2) and at the salt/sediment interface (point C2), is shown by Figure 67(a), Figure 67(b) and Figure 67(c), respectively. Where a point with the same orientation is followed in every Mohr circle and indicated with an apostrophe (’) that it was the same point after 6 years and (’’) after 13 years of production. Then these points are joined to see how the minimum and maximum principal stresses changed with depletion.

Evaluating the Mohr circles in Figure 67, it is important to say that the radius of the circles increased because depletion induces changes of the total stresses in the reservoir, as a result of a poroelastic effect in the rock. The total stress path is controlled by the distance from the salt dome, where it exhibited the minimum value (0.075), followed by point B1 (0.194) and A1 (0.355).

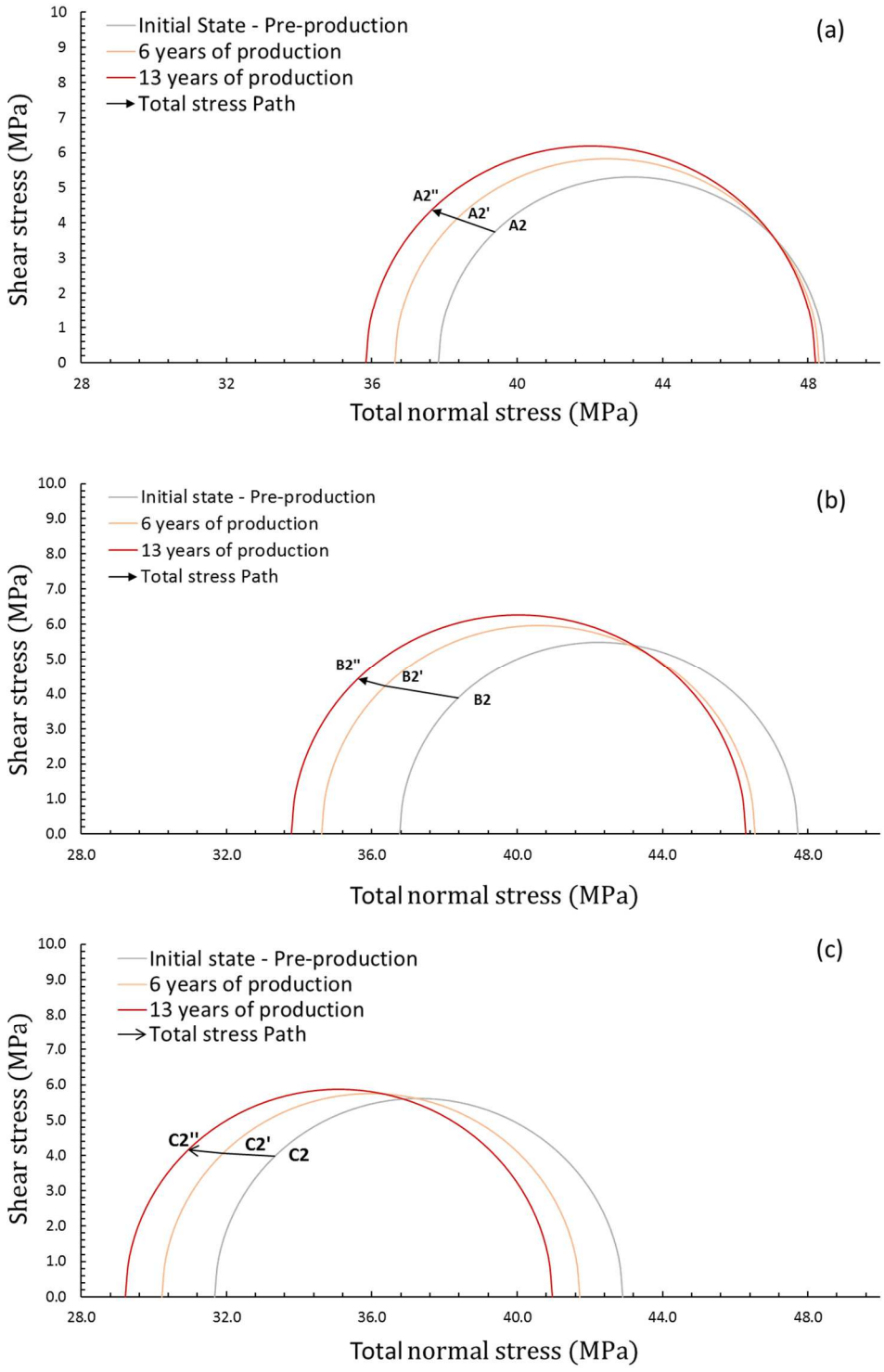


Figure 67. Mohr circles and total stress path during production at different locations in the reservoir: (a) flat area, (b) well location and (c) salt/reservoir interface. It is observed that depletion induces the total stresses to decrease, however, σ_3 decreases more than σ_1 which makes the Mohr circle diameter to increase.

The total stress path during production followed by the upper shale in the flat region (point A1), above the well (point B1) and at the salt/sediment interface (point C1), is shown by Figure 68(a), Figure 68(b) and Figure 68(c), respectively. Evaluating the Mohr circles, it is important to say that the total stress path is controlled by the distance from the salt dome, where it exhibited the minimum value (0.019), followed by point B1 (0.154) and A1 (0.301).

The total stress path during production followed by the lower shale in the flat region (point A3), below the well (point B3) and at the salt/sediment interface (point C3), is shown by Figure 69(a), Figure 69(b) and Figure 69(c), respectively. Analyzing the Mohr circles, it is significant to notice that the total stress path in the lower shale has a different trend than the reservoir and upper shale. Which presented the highest value in the flat area (0.302), followed by point B3 (0.152) and C3 (0.149).

The effective stress path during production followed by the reservoir in the flat region (point A2), where the well is located (point B2) and at the salt/sediment interface (point C2), is shown by Figure 70(a), Figure 70(b) and Figure 70(c), respectively. Evaluating the Mohr circles, it is important to say that the effective stress path is controlled by the distance from the salt dome: at point A2 is 0.225, which is higher compared to the results obtained at point B2 (0.13) and C2 (0.068).

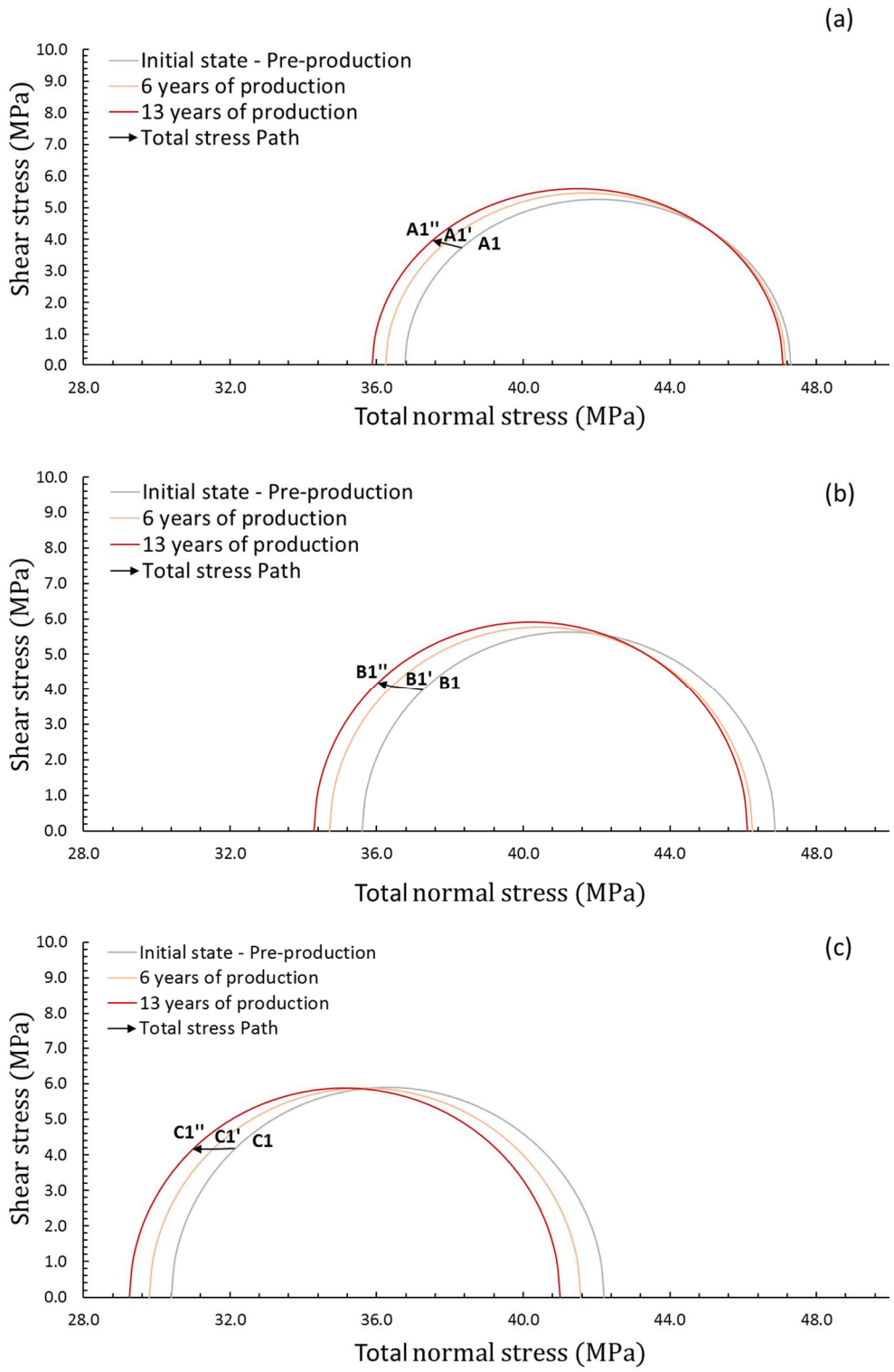


Figure 68. Mohr circles and total stress path during production at different locations in the upper shale: (a) flat area, (b) above the well and (c) salt/upper shale interface. It is observed that depletion induces the total stresses to decrease, however, σ_3 decreases more than σ_1 which makes the Mohr circle diameter to increase.

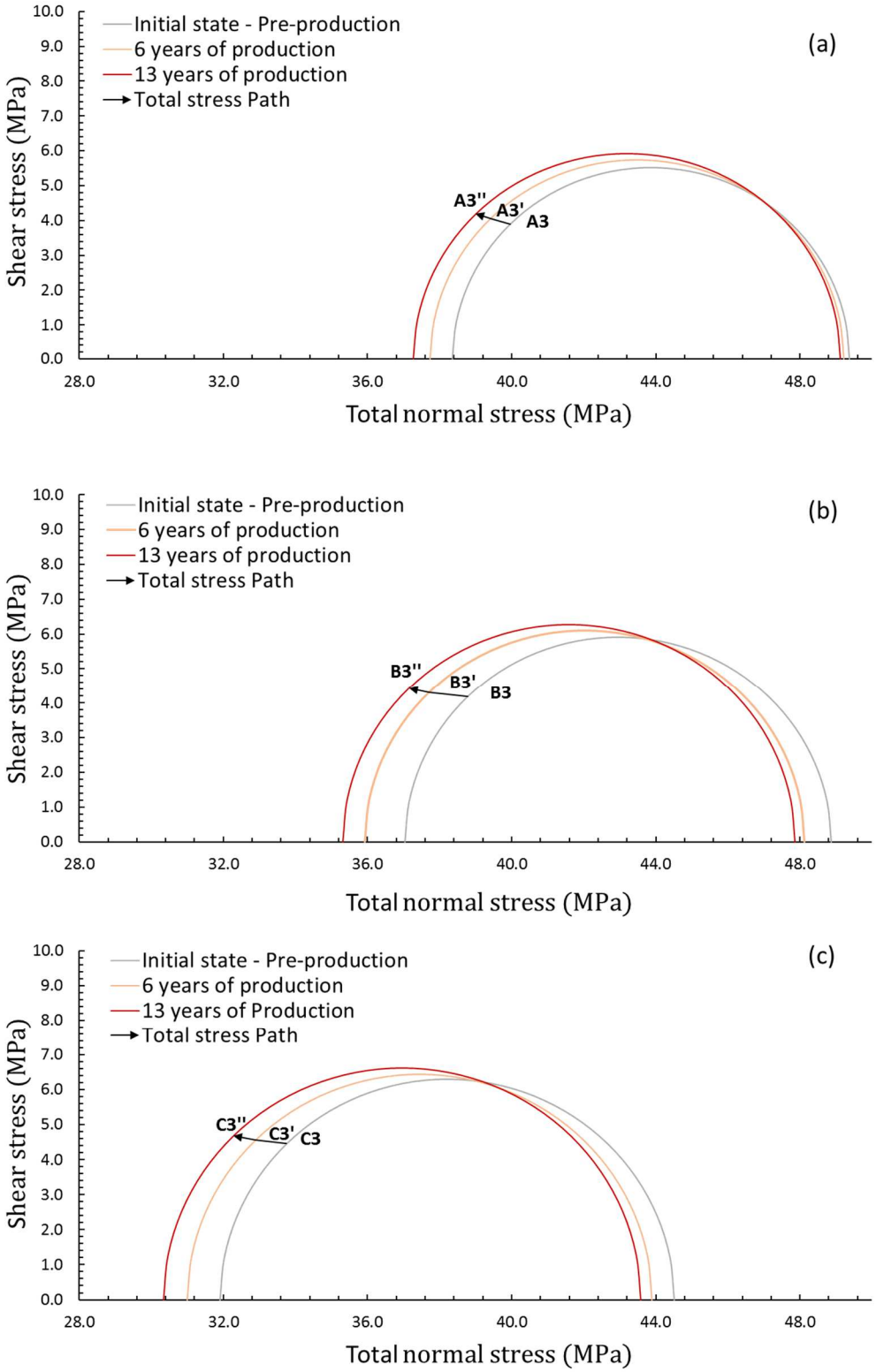


Figure 69. Mohr circles and total stress path during production at different locations in the lower shale: (a) flat area, (b) below the well and (c) salt/lower shale interface. It is observed that depletion induces the total stresses to decrease, however, σ_3 decreases more than σ_1 which makes the Mohr circle diameter to increase.

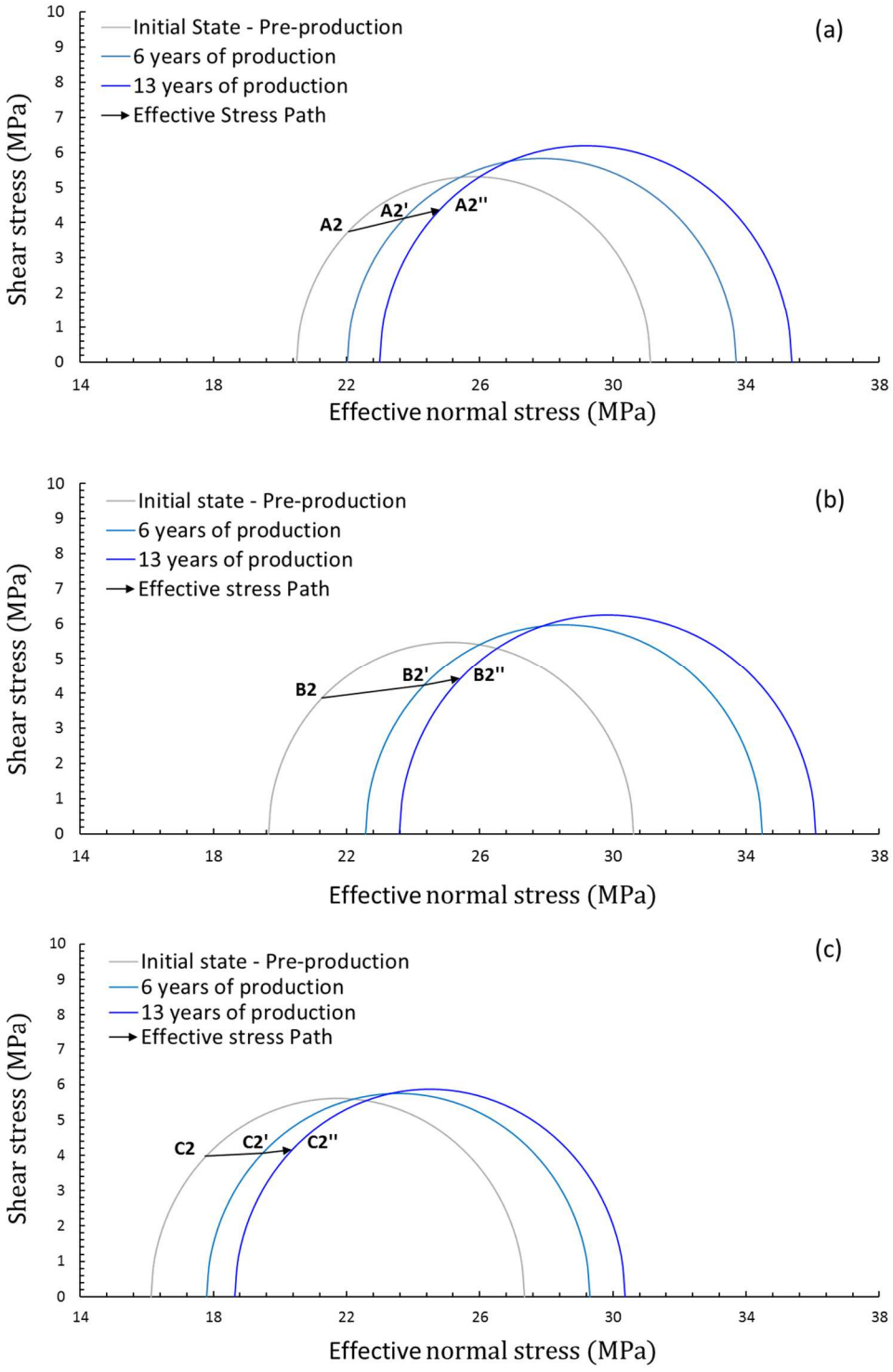


Figure 70. Mohr circles and effective stress path during production at different locations in the reservoir: (a) flat area, (b) well location and (c) salt/reservoir interface. It is observed that depletion induces the effective stresses to increase. The Mohr circle diameter changes because the total principal stresses σ_3 and σ_1 change in a different proportion.

The effective stress path during production followed by the upper shale in the flat region (point A1), above the well (point B1) and at the salt/sediment interface (point C1), is shown by Figure 71(a), Figure 71(b) and Figure 71(c), respectively. Evaluating the Mohr circles, it is important to say that the effective stress path is controlled by the distance from the salt dome, where it exhibited the minimum value (0.018), followed by point B1 (0.094) and A1 (0.183).

The effective stress path during production followed by the lower shale in the flat region (point A3), below the well (point B3) and at the salt/sediment interface (point C3), is shown by Figure 72(a), Figure 72(b) and Figure 72(c), respectively. Analyzing the Mohr circles, it is significant to notice that the effective stress path in the lower has a different trend than the reservoir and upper shale. Which presented the highest value in the flat area (0.2), followed by point C3 (0.159) and B3 (0.103).

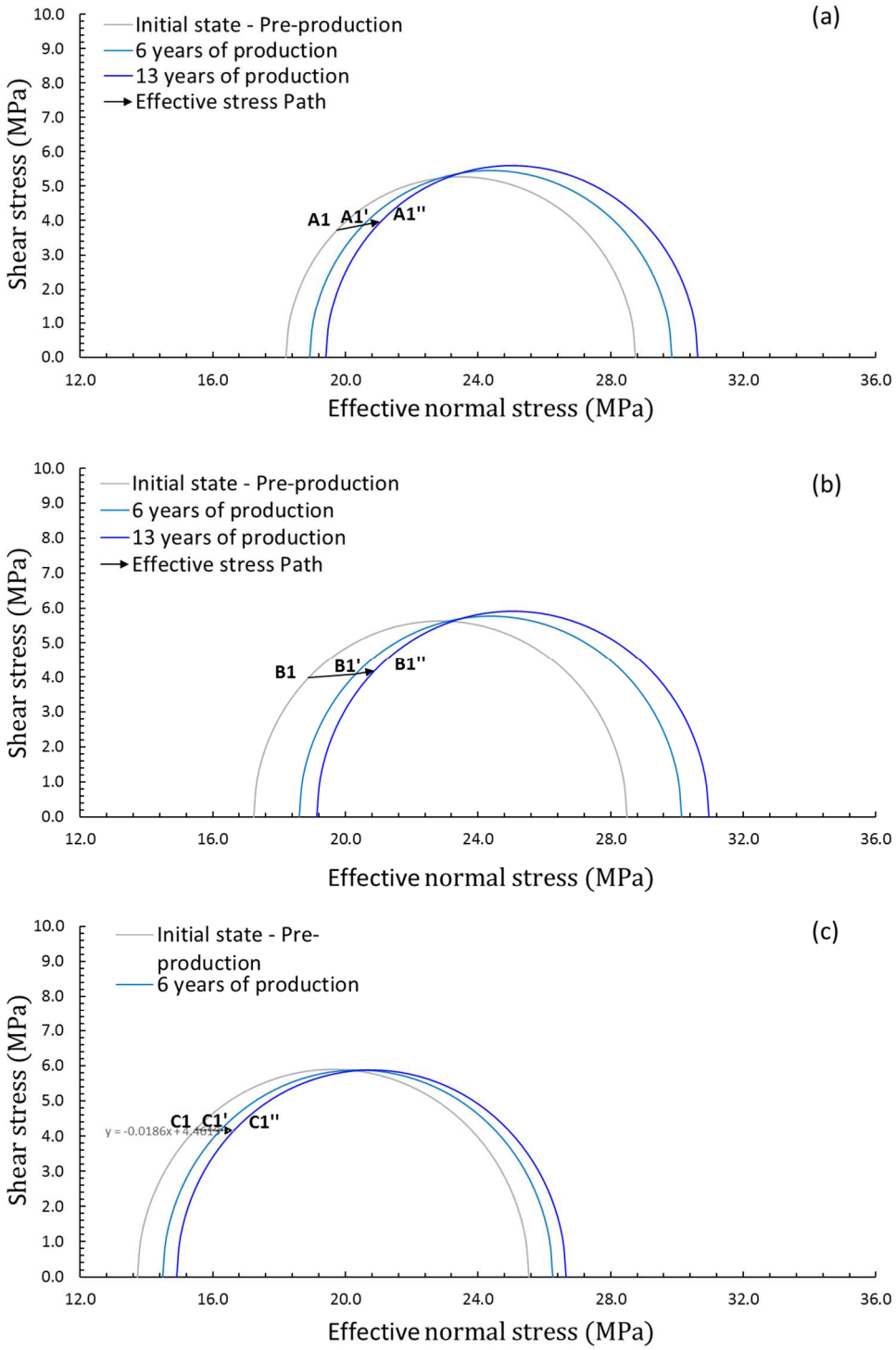


Figure 71. Mohr circles and effective stress path during production at different locations in the upper shale: (a) flat area, (b) above the well and (c) salt/upper shale interface. It is observed that depletion induces the effective stresses to increase. The Mohr circle diameter changes because the total principal stresses σ_3 and σ_1 change in a different proportion.

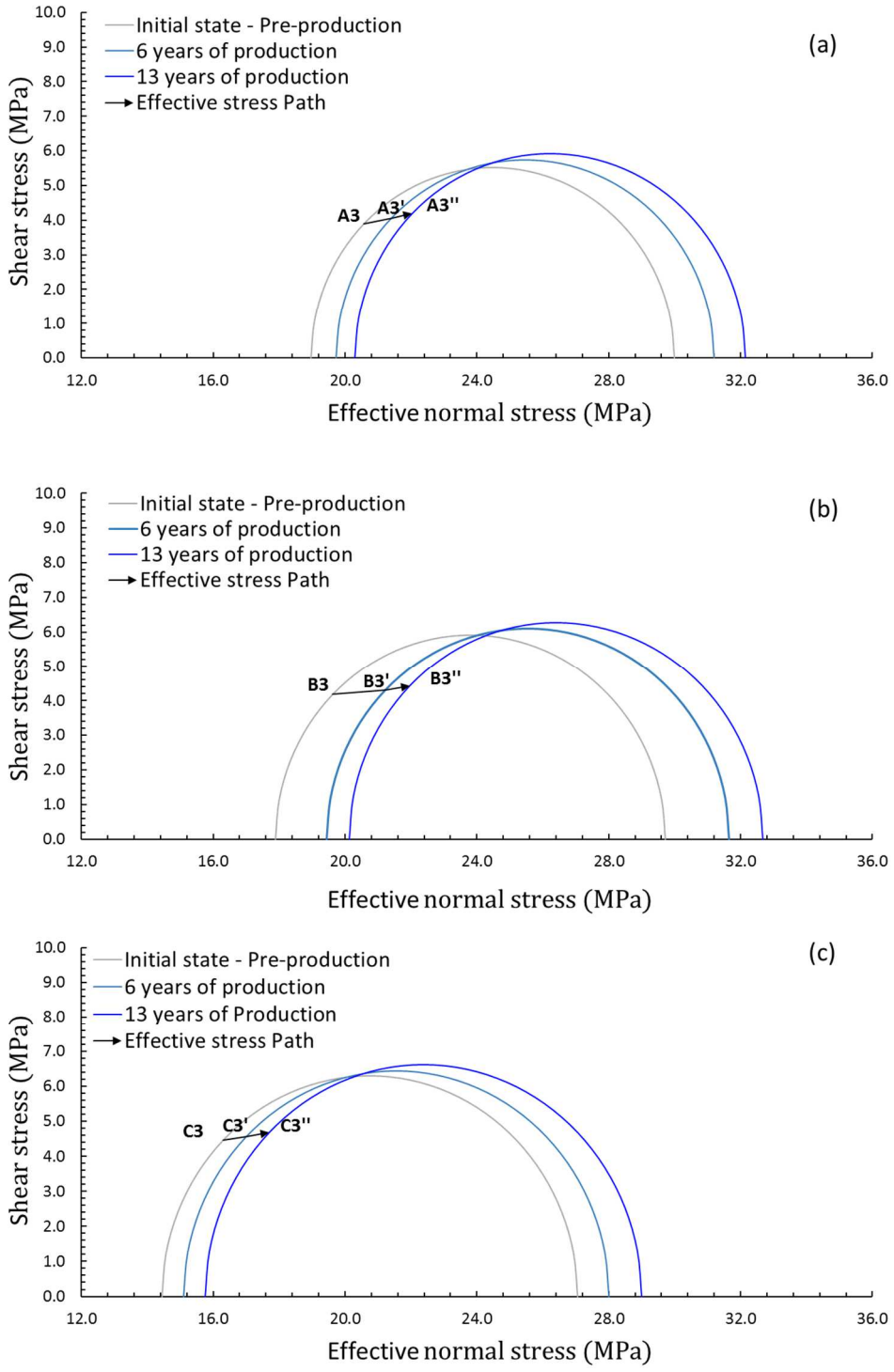


Figure 72. Mohr circles and effective stress path during production at different locations in the lower shale: (a) flat area, (b) below the well and (c) salt/lower shale interface. It is observed that depletion induces the effective stresses to increase. The Mohr circle diameter changes because the total principal stresses σ_3 and σ_1 change in a different proportion.

5.9 Total and effective vertical stress path

The total vertical stress path ($\gamma_v = \gamma_z$) is calculated using the Eq.(29), described in chapter 2. In the reservoir, the γ_v increased toward the dome, reaching the maximum value at the salt/sediment interface (0.34), followed by 0.2 at point B, and 0.05 in the flat region. Which indicated that γ_v is 6 times greater at the salt/sediment interface, compared to point A. The element at point C is affected by the salt creep, where the value of γ_v is 0.061 lower compared to the green element next to it (see Figure 73, Figure 74 and Figure 75).

The effective vertical stress path ($\gamma'_v = \gamma'_z$) is calculated using the Eq.(30), described in chapter 2. This equation considers the reservoir Biot's coefficient, which is 1 for this scenario. In this case, Eq.(30) becomes: $\gamma'_v = \left(\frac{\Delta\sigma_v}{\Delta p_f}\right) - 1$. Figure 73, shows a spatial distribution of γ'_v in the model, controlled by the proximity to the salt and the dipping angle. It decreased less at the salt/sediment interface (0.66), followed by 0.8 at point B, and 0.95 at point A. Which indicated that γ'_v decreased 6 times more in the flat region, compared to the salt/sediment interface. The γ_v decreased 0.061 more in the element at point C compared to the green element next to it, because of the salt creep.

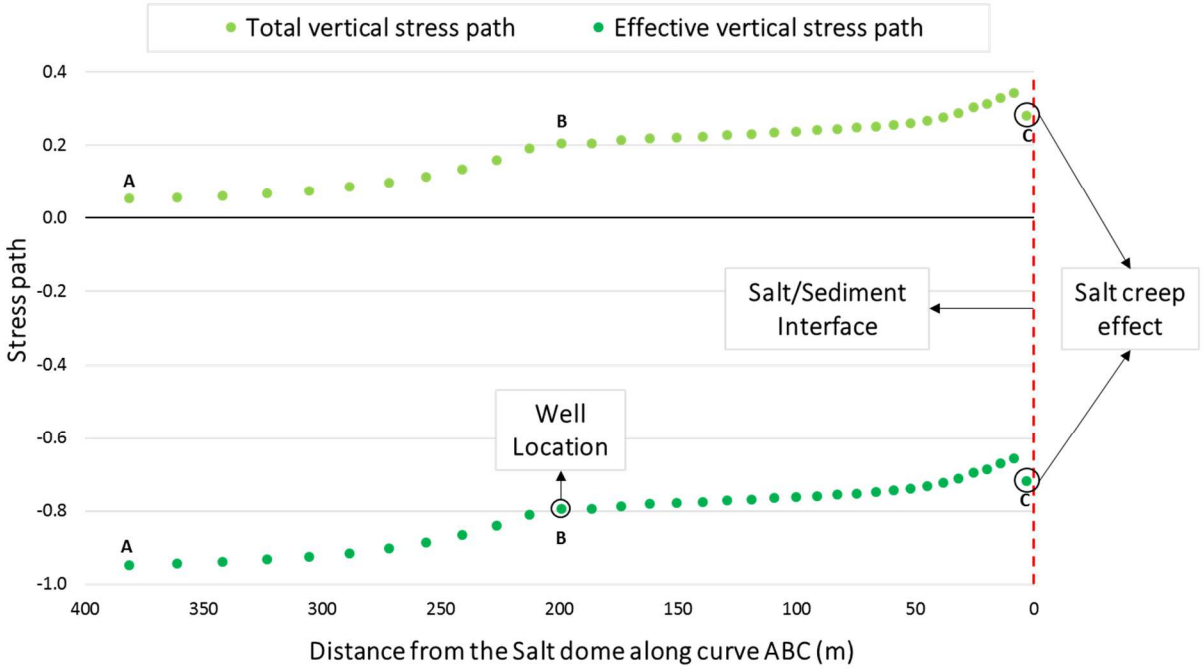


Figure 73. Total and effective vertical stress path as a function of distance from the salt/sediment interface, along the curve ABCD, after 13 years of production. The vertical stress path may be controlled by the dipping angle and the distance from the salt dome. Where the maximum value of γ_v occurred at the salt/sediment interface (0.34) and the minor in the flatten area. The salt creep affects the element at the salt/sediment interface (point C2), which presents a lower magnitude of γ_v, compared to the green element next to it. The spatial distribution of γ'_v is controlled by the dipping angle and the proximity to the salt. It decreased less at the salt/sediment interface, compared to point A. The resultant value of γ'_v in element at point C is altered by the salt creep.

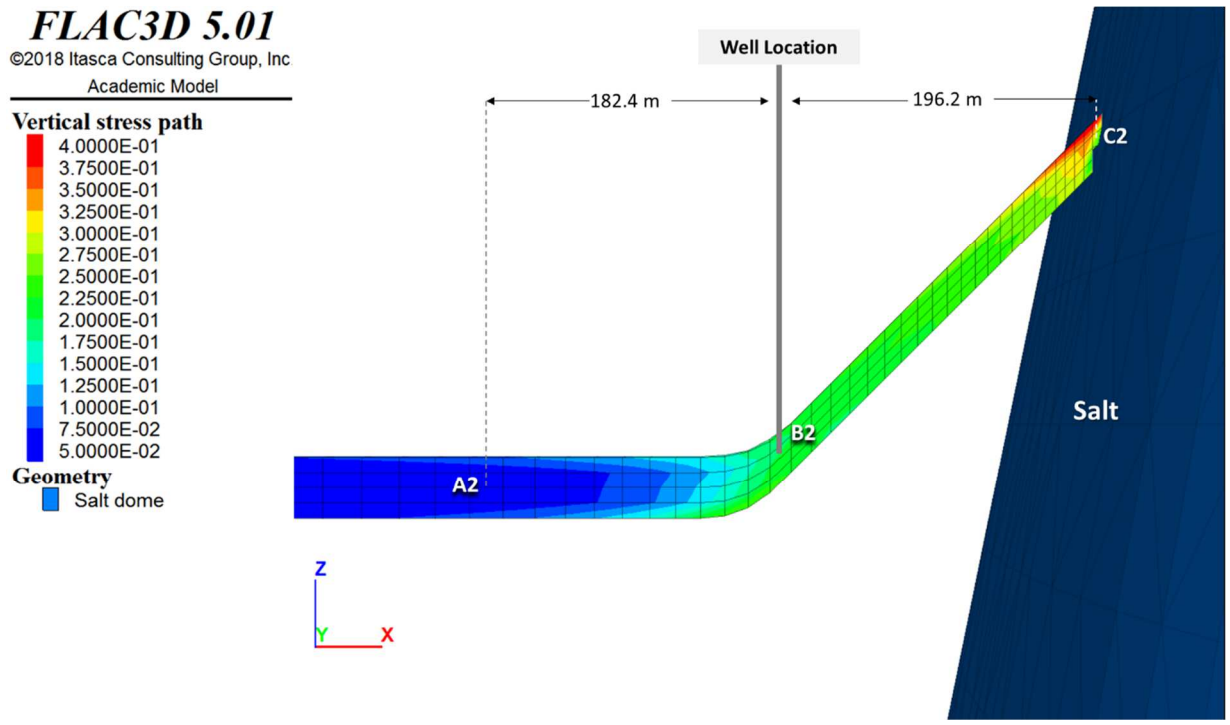


Figure 74. Total vertical stress path contour along curve ABC in the reservoir. The vertical stress path seems to be controlled by the dipping angle, which increases toward the salt/sediment interface.

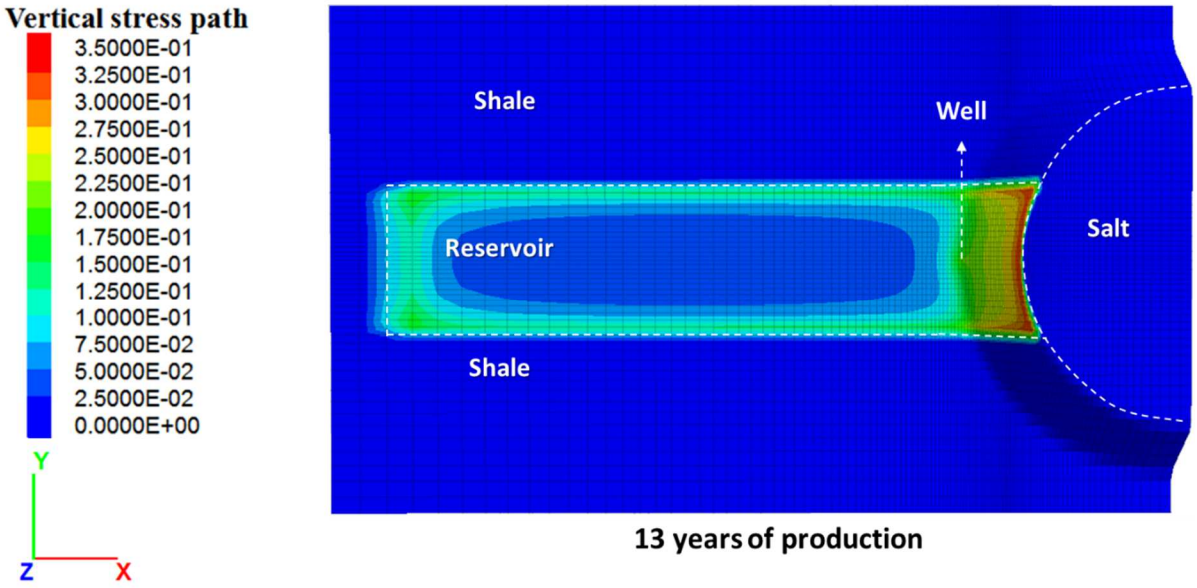


Figure 75. Total vertical stress path contour along a xy-plane in the middle of the reservoir after 13 years of production. The γ'_{zz} is controlled by the dipping angle, which increases toward the salt/sediment interface. However, the γ'_{zz} seems to be affected by the boundaries of the reservoir.

5.10 Total and effective maximum horizontal stress path

The total maximum horizontal stress path ($\gamma_H = \gamma_x$) is calculated using the Eq.(29), described in chapter 2. Tn the reservoir, the γ_H decreased toward the dome, reaching the lowest value at the salt/sediment interface (0.21), followed by 0.346 around the well and 0.464 at point A. Which showed that γ_H is 2.2 times higher at point A, compared to the value at the salt/sediment interface. It is noticed that γ_H of the element at point C is 0.043 lower compared to the green element next to it, because of the salt creep effect (see Figure 76, Figure 77 and Figure 78).

The effective maximum horizontal stress path ($\gamma'_H = \gamma'_x$) is calculated using the Eq.(30), described in chapter 2. This equation considers the reservoir Biot's coefficient, which is 1 for this scenario. In this case, Eq.(30) becomes: $\gamma'_H = \left(\frac{\Delta\sigma_H}{\Delta p_f}\right) - 1$. Figure 76, shows a spatial distribution of γ'_H in the model, controlled by the proximity to the salt and the dipping angle. It decreased more at the salt/sediment interface (0.79), followed by 0.654 at point B, and 0.536 at point A. Which indicated that γ'_H decreased 2.2 times more at the salt/sediment interface, compared to point A. The γ_H decreased 0.043 more in the element at point C compared to the green element next to it, because of the salt creep.

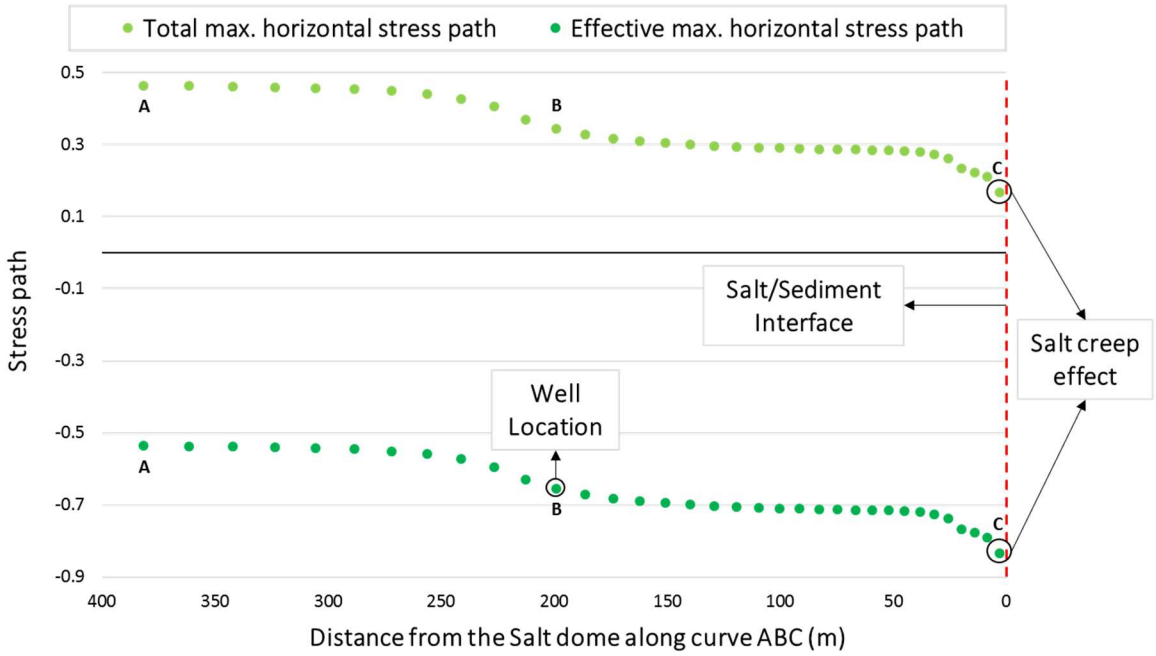


Figure 76. Total and effective maximum horizontal stress path as a function of distance from the salt/sediment interface, along the curve ABCD, after 13 years of production. The maximum horizontal stress path is controlled by the dipping angle and proximity to the salt dome, where the minimum value of γ_H occurred at the salt/sediment interface (0.21) and the major in the flat area. The spatial distribution of γ'_H is controlled by the dipping angle and the proximity to the salt. It decreased more at the salt/sediment interface, compared to point A. The resultant value of γ'_H in element at point C is altered by the salt creep.

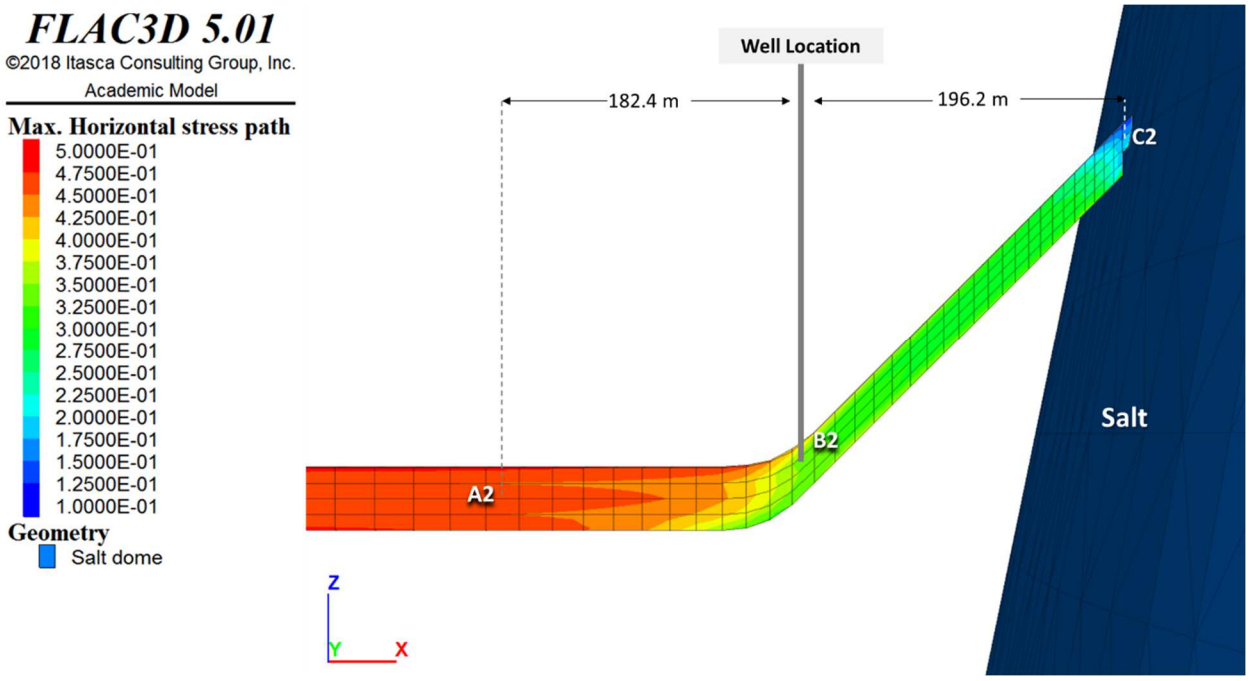


Figure 77. Total maximum horizontal stress path contour along curve ABC. The γ_{Hmax} is function of the dipping angle and the proximity to the salt. Which indicates major changes at point A2, compared to the salt/sediment interface.

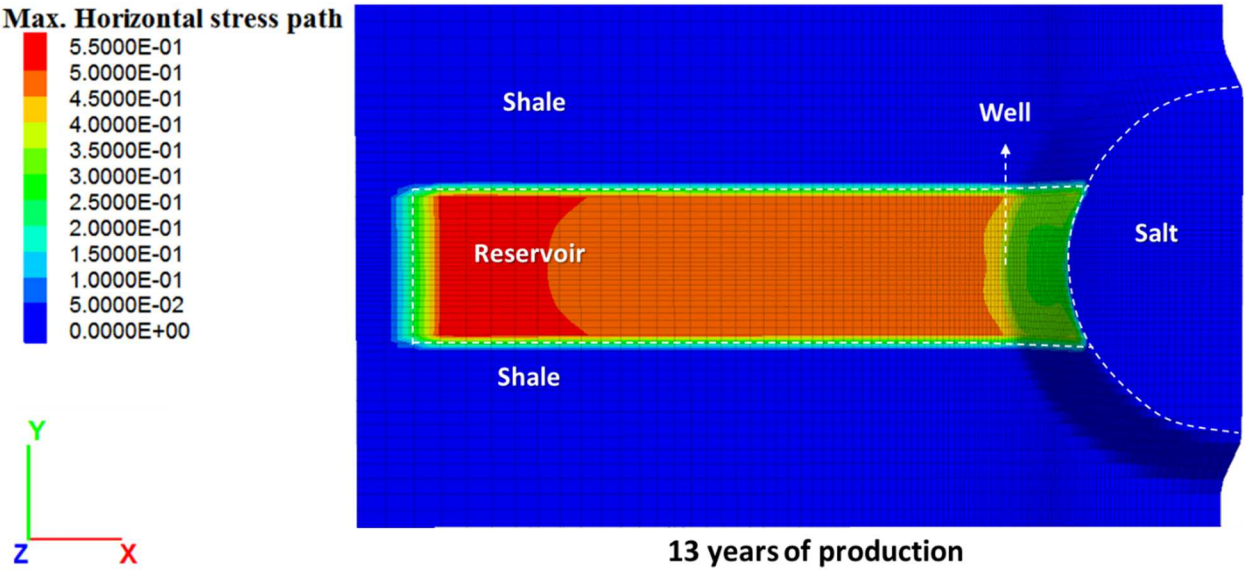


Figure 78. Total maximum horizontal stress path contour along a xy-plane in the middle of the reservoir after 13 years of production. The γ'_{xx} is controlled by the dipping angle, which decreases toward the salt/sediment interface.

5.11 Total and effective minimum horizontal stress path

The total minimum horizontal stress path $(\gamma_h = \gamma_y)$ is calculated using the Eq.(29), described in chapter 2. In the reservoir, the γ_h tends to increase toward the dome, reaching the maximum value at the salt/sediment interface (0.491), followed by 0.445 in the flat region and 0.433 around the well. The γ_h is 10% higher at the salt/sediment interface, compared to point A. The element at point C is affected by the deformation of the salt, where the value of γ_h is 0.069 lower compared to the green element next to it (see Figure 79, Figure 80 and Figure 81).

The effective minimum horizontal stress path $(\gamma'_h = \gamma'_y)$ is calculated using the Eq.(30), described in chapter 2. This equation considers the reservoir Biot's coefficient, which is 1 for this scenario. In this case, Eq.(30) becomes: $\gamma'_h = \left(\frac{\Delta\sigma_h}{\Delta p_f}\right) - 1$. Figure 79, shows a spatial distribution of γ'_h in the model, controlled by the proximity to the salt and the dipping angle. It decreased less at the salt/sediment interface (0.514), followed by 0.555 at point A, and 0.567 at point B. Which indicated that γ'_h decreased 2.2 times more at the salt/sediment interface, compared to point A. The γ_h decreased 0.069 more in the element at point C compared to the green element next to it, because of the salt creep.

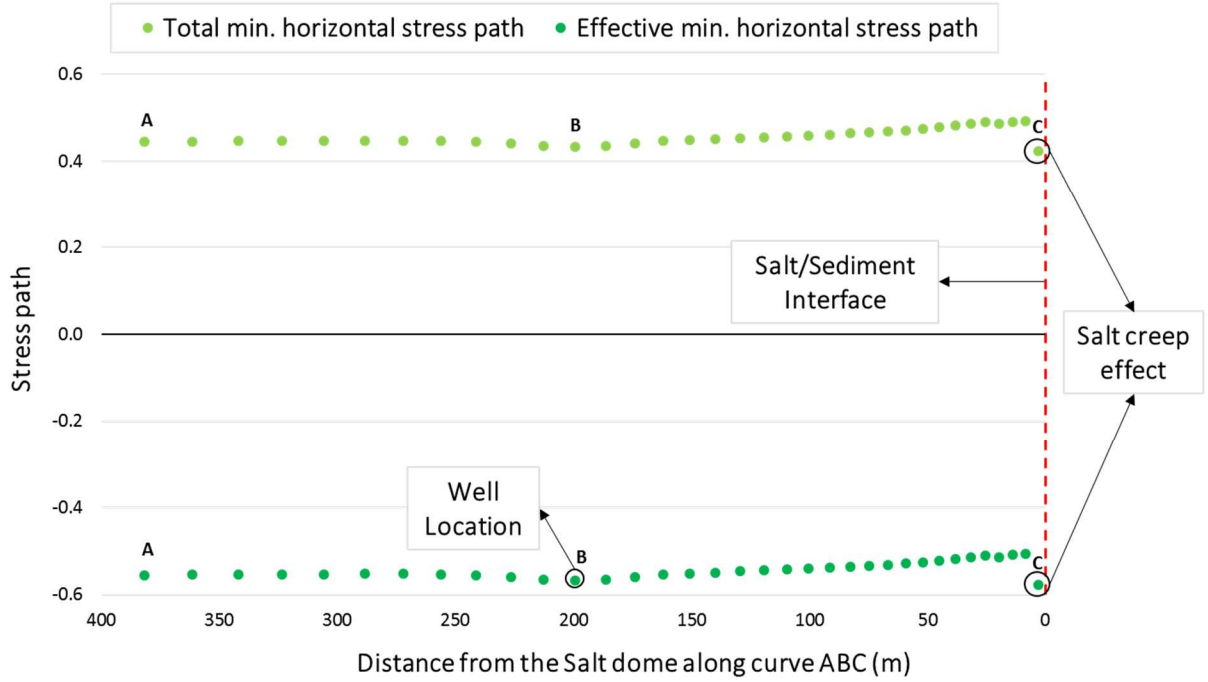


Figure 79. Total and effective minimum horizontal stress path as a function of distance from the salt/sediment interface, along the curve ABCD, after 13 years of production. The minimum horizontal stress path is controlled by the well location, the proximity to the salt and the dipping angle. Where the maximum value of γ_h happened at the salt/sediment interface (0.493) and the lowest where the well is located. The value of γ_h at point C2 is not considered into the analysis, because it is altered by the salt creep. Which gives a wrong idea about the impact of the dipping angle. The spatial distribution of γ'_h is controlled by the well location, the dipping angle and the proximity to the salt. It decreased less at the salt/sediment interface, compared to point B. The resultant value of γ'_h in element at point C is altered by the salt creep.

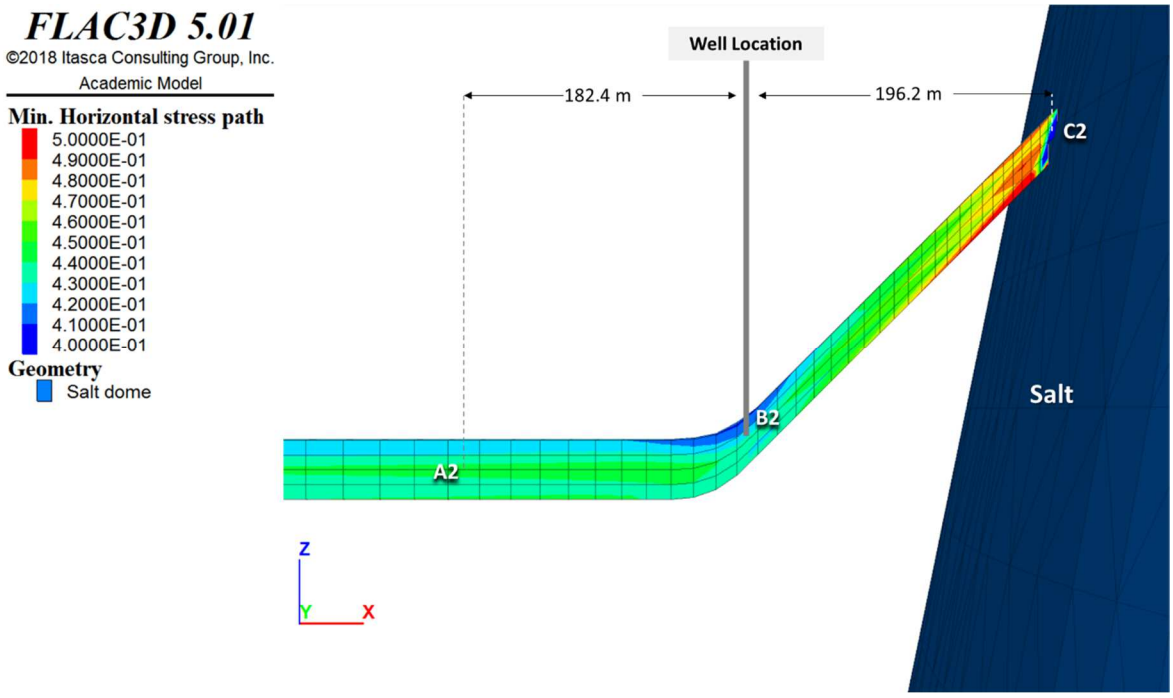


Figure 80 Total minimum horizontal stress path contour along curve ABC. The minimum horizontal stress path increases toward the dome. Where the salt creep has a strong impact on the elements at the salt/sediment interface, decreasing the magnitude of γ_{hmin}.

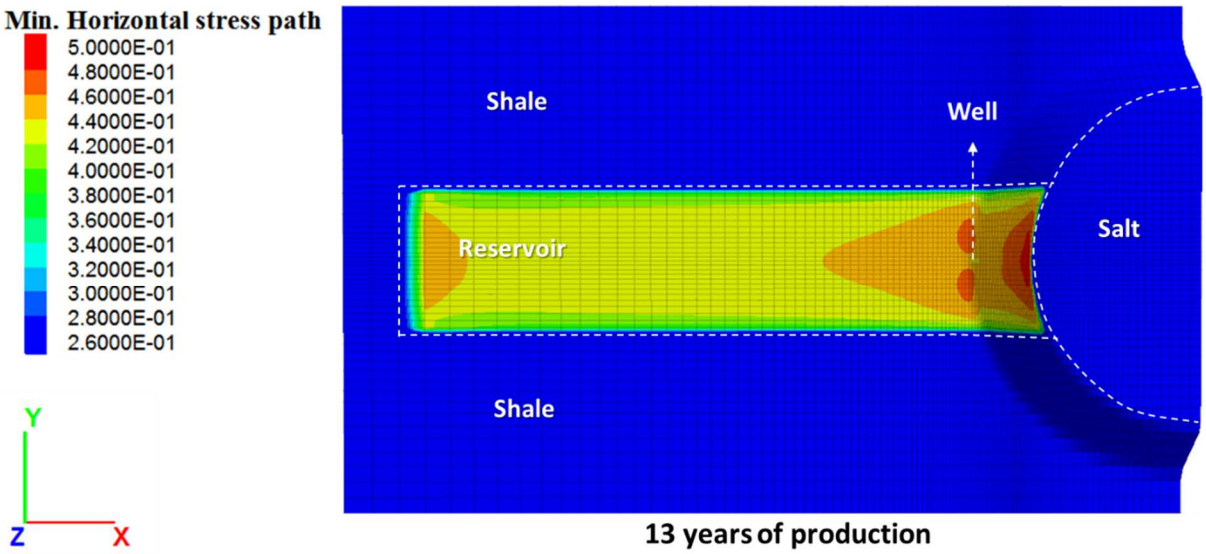


Figure 81. Total minimum horizontal stress path contour along a xy-plane in the middle of the reservoir after 13 years of production. The γ'_{yy} is controlled by the dipping angle, which increases toward the salt/sediment interface. However, the well location affects the γ'_{yy}, which decreases around the borehole.

5.12 Volumetric strain

The volumetric strain is defined as the ratio of the change in volume of a body to the original volume ($e_v = \Delta V/V$). Figure 82 shows the volumetric strain of the reservoir and salt along the trajectory ABCD, defined in Figure 15.(a), after 13 years of production. It is important to mention that negative volumetric strain means that the volume of the element is decreasing or shrinking, while positive e_v represents expansion.

Pore pressure depletion induced the elements in the reservoir to shrink and salt elements at the salt/sediment interface to expand (See Figure 83(c) and Figure 84(c)). In the reservoir the e_v is controlled by the well location, where it exhibited the largest volumetric strain ($-3.9\text{x}10^{-4}$), followed by $-2.77\text{x}10^{-4}$ at the salt/sediment interface, and $-2.62\text{x}10^{-4}$ in the flat region. The element at point C2 compacted $1.02\text{x}10^{-5}$ less compared to the green element next to it, because of the effect of salt creep. The volume of the salt elements at the salt/sediment interface increased ($3.27x10^{-6}$). Three years after shut-in, the pressure built up in the reservoir inducing expansion of the elements that had previously shrunk (see Figure 83(d) and Figure 84(d)).

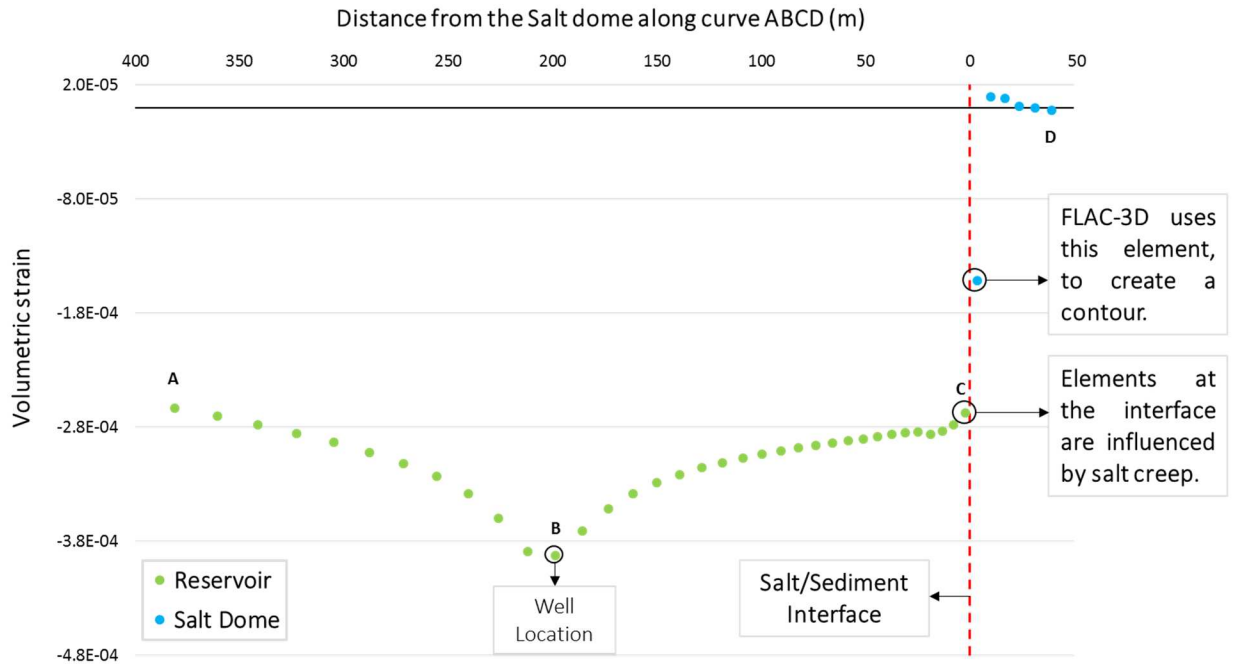


Figure 82. Volumetric strain as a function of distance from the salt/sediment interface, after 13 years of production. Reservoir elements are represented in green, while salt elements are represented in blue. The volumetric strain is controlled by the well location, where the reservoir experienced the major compaction (-3.9×10^{-4}). In addition, the element at the salt/sediment interface is analyzed and noticed that it shrunk more than the element at point A. The salt exhibited expansion at the salt/sediment interface.

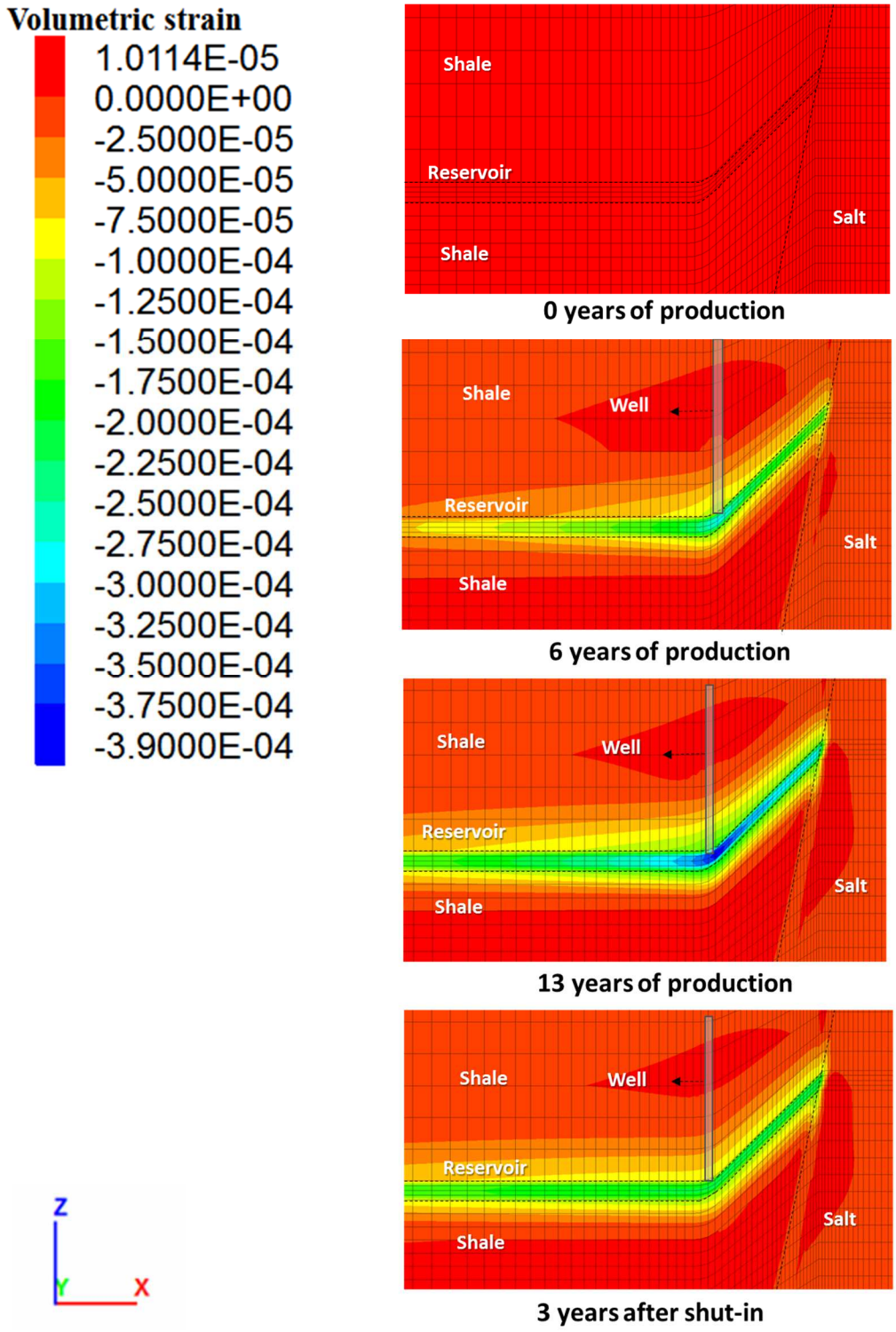


Figure 83. Volumetric strain behavior after 6 and 13 years of production, and 3 years after shut-in on a xz-plane in the middle of the reservoir. The reservoir and shale exhibit compaction after 13 years of production, with a stronger impact around the well (-3.9$x10^{-4}$). Three years after shut in the well, the pressure built up, increasing the volume of the reservoir and shale elements.

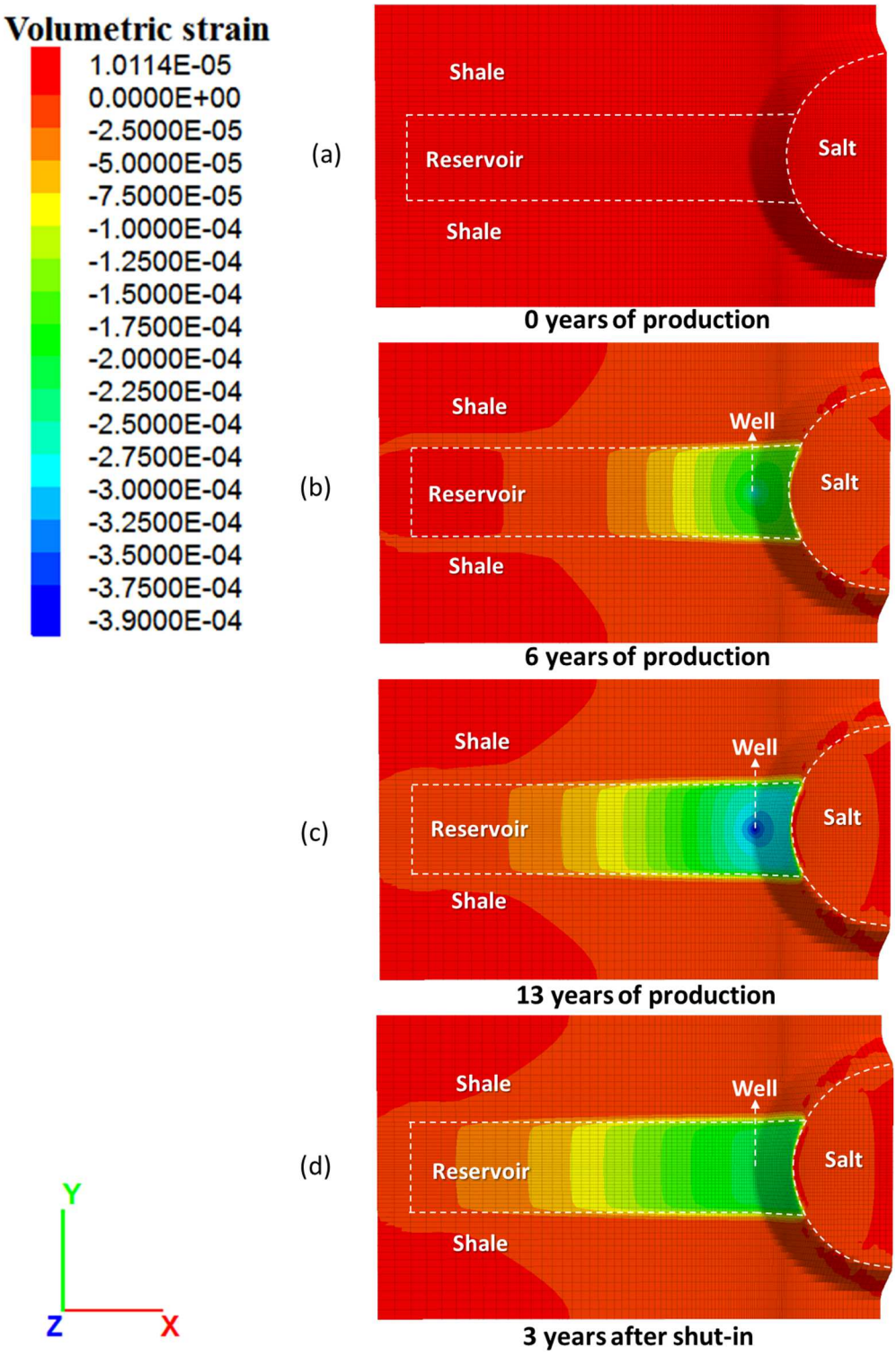


Figure 84. Volumetric strain behavior along a xy-plane in the middle of the reservoir. (a) Initial state, (b) 6 years of production, (c) 13 years of production and (d) 3 years of steady state. The reservoir exhibited compaction that increases with depletion, which is controlled by the well location. Three years after shut in the well, the pressure built up, increasing the volume of the reservoir elements.

Chapter 6: Sensitivity analysis

A sensitivity analysis is performed based on 6 additional study cases, to determine the impact of different rock properties and dipping angle on the stress path and pore pressure in the reservoir. The parameters assigned to Case 1, also called the base case (BC), that were changed in the analyzed study cases, and the magnitude of each of them are given in Table 7. Figure 85 shows the geometry of Case 4, where the reservoir dips at an angle of 70°.

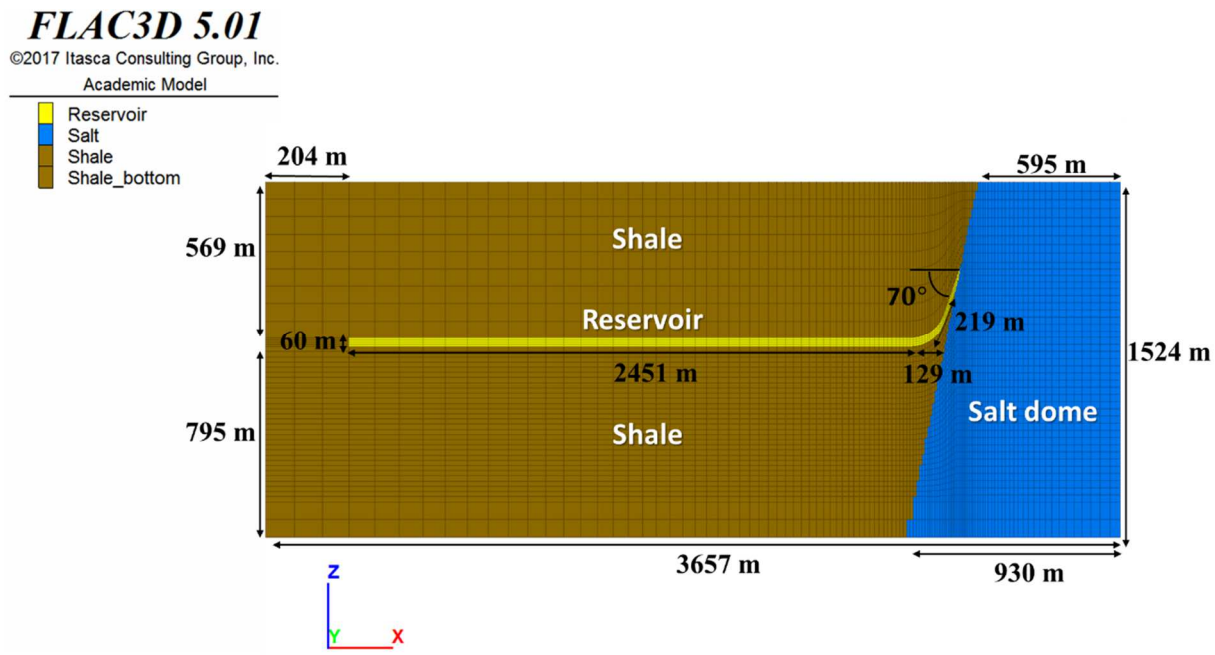


Figure 85. Cross-section of the model geometry in Y of Case 4. This plot shows the extension and thickness of the reservoir, shale and salt dome.

Table 7. Parameters studied during the sensitivity analysis.

Case	Salt Permeability md	Reservoir Young Modulus MPa	Reservoir Dipping Angle [°]	Reservoir Porosity [%]	Reservoir Pore Compressibility MPa^{-1}	Reservoir Biot Coefficient	Shale Biot Coefficient
1 - BC	1.00E-21	10342	45	18	3.32E-04	1	1
2	1.00E-19	*	*	*	*	*	*
3	*	5171	*	*	*	*	*
4	*	*	70	*	*	*	*
5	*	*	*	30	*	*	*
6	*	*	*	*	1.67E-04	*	*
7	*	*	*	*	*	0.9	0.6
* Same value as BC							

6.1 Pore pressure

Increasing the salt permeability from $1x10^{-21}$ md to $1x10^{-19}$ md did not change the pore pressure drawdown in the reservoir. While reducing the reservoir Young's modulus to half of its initial value resulted in less depletion along the producing formation: 0.2 MPa ~ 4.4% lower in the flat region, 0.3 MPa ~ 4.2% around the well and 0.14 MPa ~ 2.8% at the salt/sediment interface. The same behavior is observed after increasing the dipping angle, but the pore pressure decreased less: 0.8 MPa ~ 12.3% at point B, 0.4 MPa ~ 9.9% at point A and 0.2 MPa ~ 3.6% at Point C). Another parameter tested was the sandstone's porosity, after increasing it from 18% to 30%, the reservoir depletion was 0.5 MPa lower at points A, B and C, as it can be seen in Figure 86.

When the reservoir pore compressibility is reduced to one-half of its original value, the pressure drawdown increased by 0.1 MPa at points A (1.4%), point B (1.3%), and point C (1.7%). The same happened when the reservoir and shale Biot's coefficient is reduced, which resulted in major depletion: 0.5 MPa more at points A, B and C (see Figure 86).

Case 7 caused the greatest pressure drawdown in the reservoir, followed by Case 6. While Case 4, Case 3 and Case 5, reduced depletion in the reservoir. Case 4 shows an increment of the pore pressure drawdown in the steeper dipping area toward the dome. The pore pressure in the salt remains zero after the sensitivity analysis (see Figure 87).

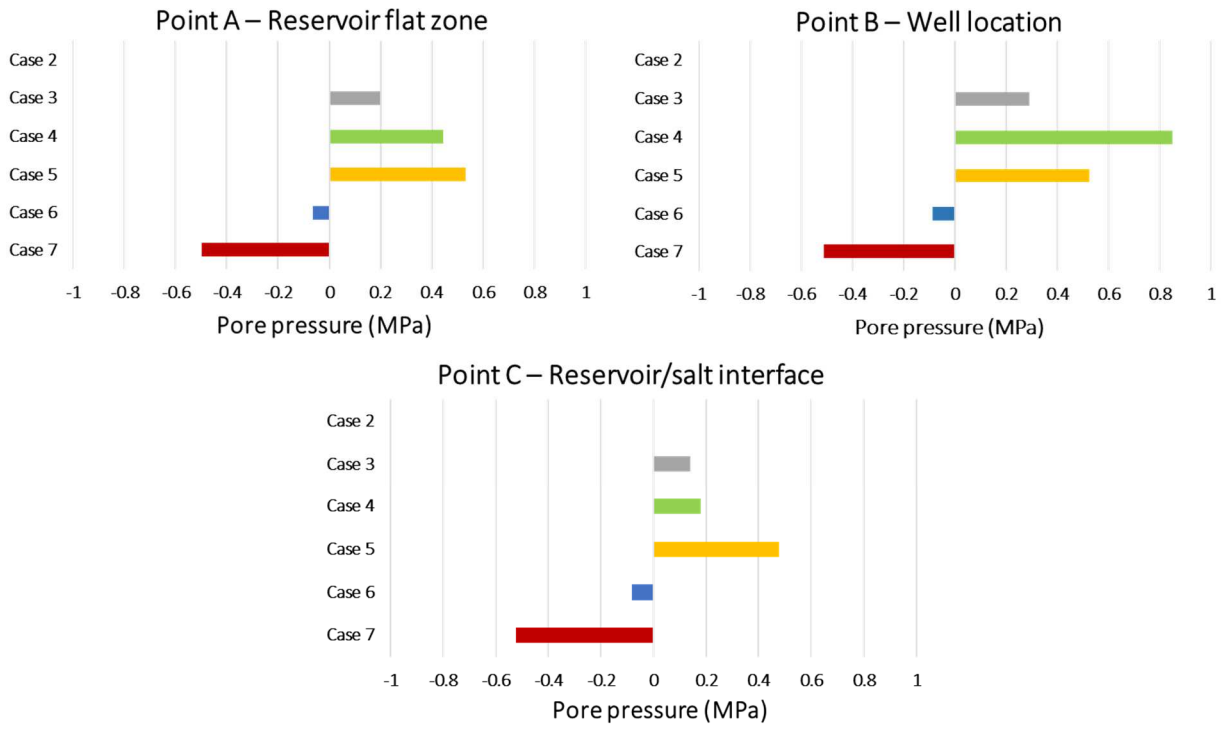


Figure 86. Pore pressure drawdown behavior with respect to BC at different locations, after 13 years of production. The parameters that impacted more the depletion in the reservoir was the Biot's coefficient and the dipping angle. The former induced additional pressure drawdown (up to 0.5 MPa), while the dipping angle decreased the pressure drop up to 0.8 MPa.

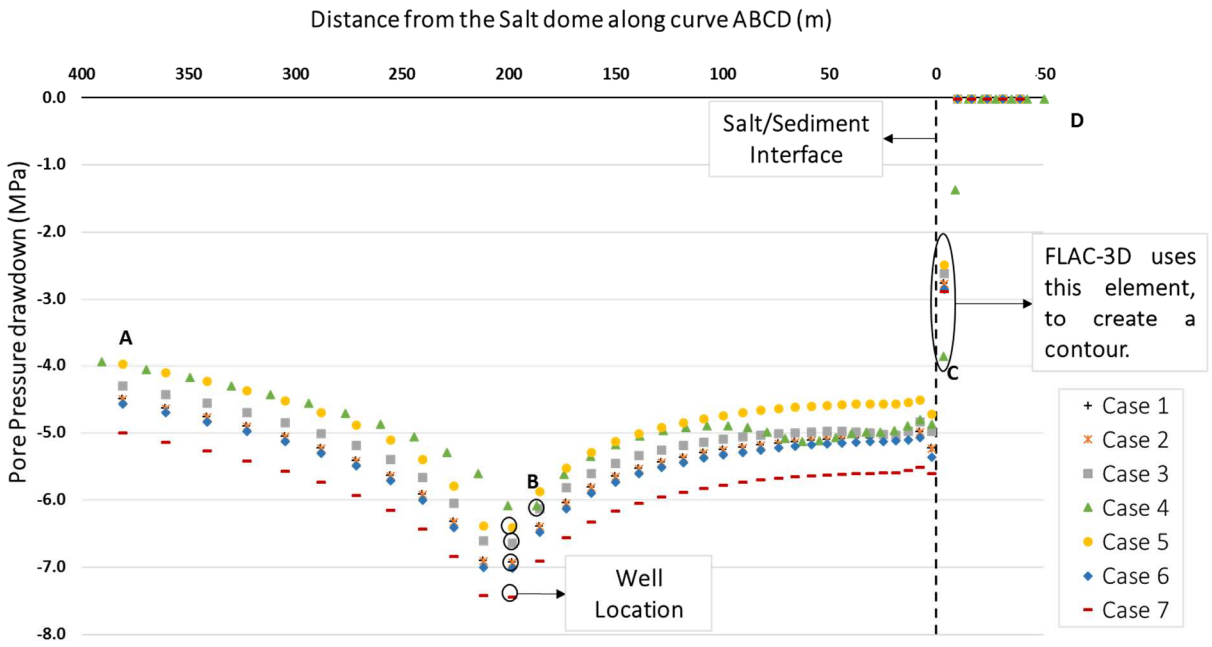


Figure 87. Pore pressure drawdown in the reservoir along trajectory ABCD, as a function of distance from the salt/sediment interface, after 13 years of production. Case 6 and 7 increased depletion in the reservoir, while Case 3, 4 and 5 decreased the pressure drop. Besides this behavior, the depletion observed in Case 4 tends to increase around the steeper dipping area.

6.2 Total and effective vertical stresses

The total vertical stress (σ_{zz}) in the reservoir are compared to Case 1, which is the base case. The σ_{zz} did not vary after increasing the salt permeability from $1x10^{-21}$ md to $1x10^{-19}$. Reducing the reservoir Young's modulus from 10,342 MPa to 5,171 MPa resulted in larger stress changes in the flat region and around the well, 0.1 MPa in each case. While the differential stresses decreased 0.1 MPa at the salt/sediment interface and at point D. Additionally, increasing the dipping angle from 45° to 70°, the σ_{zz} changes increased by 0.2 MPa at points C and D, and 0.1 at point A, while it decreased by 0.2 MPa around the well. The highest vertical stress reduction was 2.2 MPa and occurred in the area with steeper dipping angle (Case 4). Increasing the reservoir porosity from 18% to 30%, did not altered the vertical stresses in the flat region and

point D, but lowered the reduction of σ_{zz} by 0.1 MPa around the well and 1 at the salt/sediment interface. Decreasing the reservoir pore compressibility to half of its original value did not cause significant changes at points A and D, while the σ_{zz} was 0.2 MPa less at points B and C. Analyzing the results obtained from Case 7, not significant changes are seen at points A, C and D, but the stress reduction was 0.1 MPa less around the well (see Figure 88). The parameters that influenced more the total vertical stress changes along curve ABCD were the dipping angle and the reservoir Young's modulus and the pore compressibility (see Figure 89).

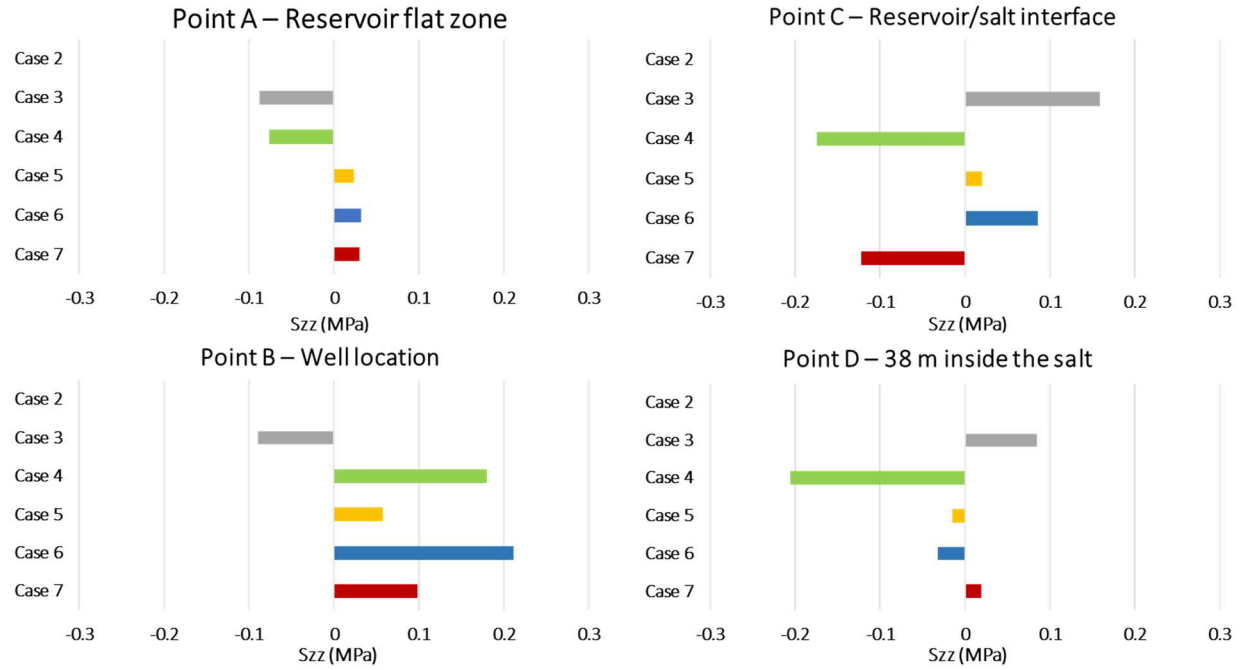


Figure 88. Total vertical stress behavior with respect to BC at different locations, after 13 years of production. The total vertical stresses did not vary significantly in the reservoir or the salt. The parameters that attenuated the σ_{zz} changes in the reservoir were the pore compressibility and the dipping angle. The former caused less reduction of σ_{zz}, while the dipping angle decreased more

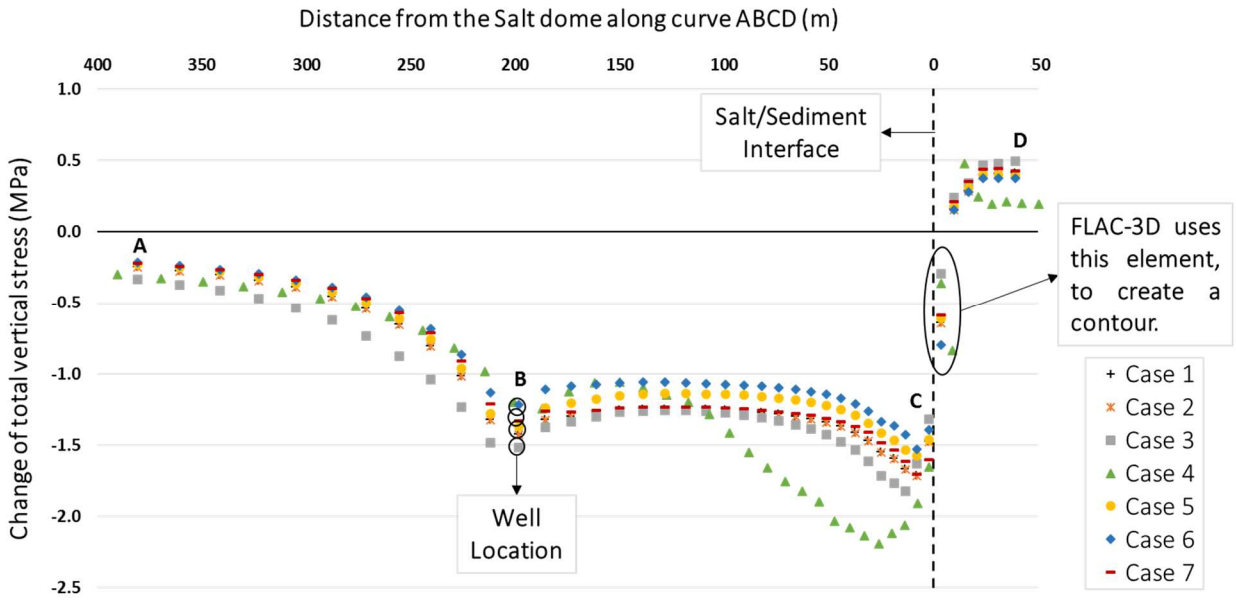


Figure 89. Change of total vertical stress in the reservoir along trajectory ABCD, as a function of distance from the salt/sediment interface after 13 years of production. Case 3 and 4 reduced more the total vertical stress in the reservoir, with a major impact along the steeper dipping area, while Case 5, 6 and 7 presented less reduction of the σ_{zz}.

The highest effective vertical stress (σ'_{zz}) increment occurs around the well (up to 6.2 MPa), and it is induced by reducing the reservoir Biot coefficient. The minimum effective stress change at the salt/sediment interface is associated to a higher dipping angle (2.8 MPa). The parameters that increased the σ'_{zz} in the reservoir are the pore compressibility and Biot coefficient, while the dipping angle, the Young's modulus and the porosity presented a lower increment of the effective stresses (see Figure 90).

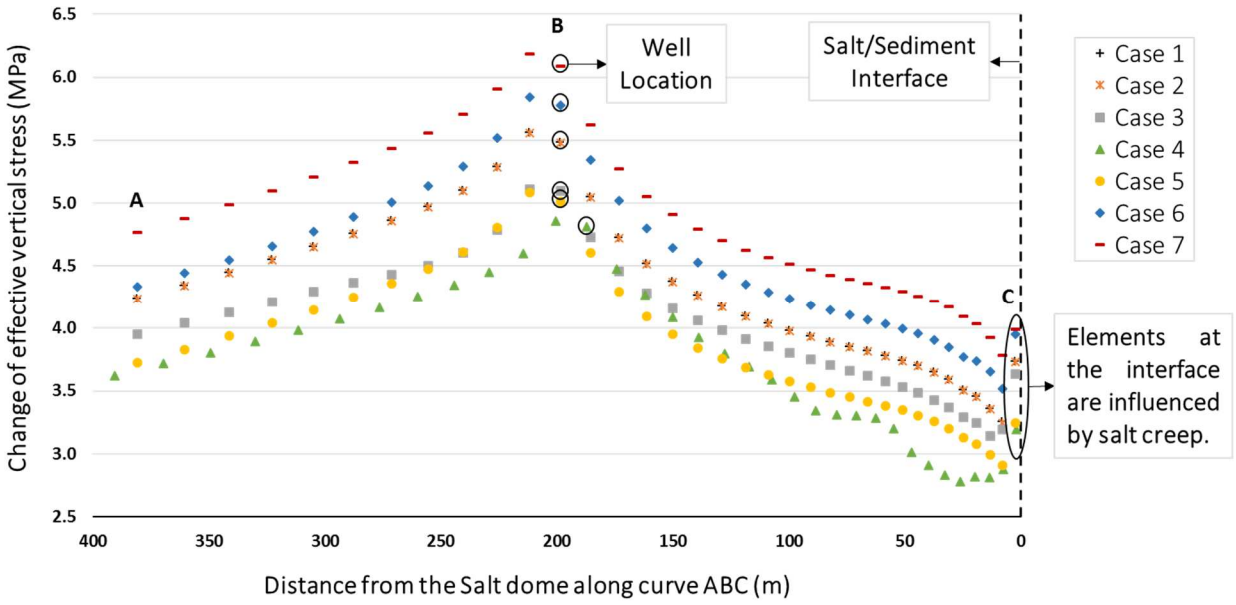


Figure 90. Change of effective vertical stress in the reservoir along trajectory ABC, as a function of distance from the salt/sediment interface, after 13 years of production. Case 3, 4 and 5 presented the lowest effective stress magnitude along the reservoir, while case 6 and 7 increased the σ'_{zz}.

6.3 Total and effective maximum horizontal stress

The total maximum horizontal stress (σ_{xx}) in the reservoir and salt changed the same amount for cases 1 and 2, along the trajectory ABCD. The total maximum horizontal stress did not change at points A and C, after decreasing the reservoir Young's modulus to half of its original value, but around the well it decreased by 0.08 MPa, compared to Case 1. After increasing the dipping angle to 70°, the stress reduction was 0.4 MPa more around the well, while it was 0.12 MPa less at point A, 0.57 MPa lower at the salt/sediment interface and 0.28 MPa smaller at point D, compared to BC. The previous case exhibited the maximum stress drop around the well (0.59 MPa) and the lowest stress drop in the steeper dipping zone (0.87 MPa). In the scenario where the reservoir porosity increased from 18% to 30%, σ_{xx} decreased by 0.24 MPa at point A, 0.16 at point B and 0.08 MPa at point C, but did not changed in the salt at point D. The same behavior is observed after decreasing the reservoir pore compressibility, σ_{xx} decreased by 0.32 MPa at point

A, 0.36 MPa at point B, 0.1 MPa at point C, but did not changed in the salt. Reducing the reservoir and shale Biot's coefficient, did not show σ_{xx} changes in the flat region, but it increased 0.11 MPa at point B, 0.06 MPa at the salt/sediment interface and decreased the same amount at D (see Figure 91). The parameters that influenced more the total maximum horizontal stress changes along curve ABCD were the dipping angle, the reservoir porosity and pore compressibility (see Figure 92).

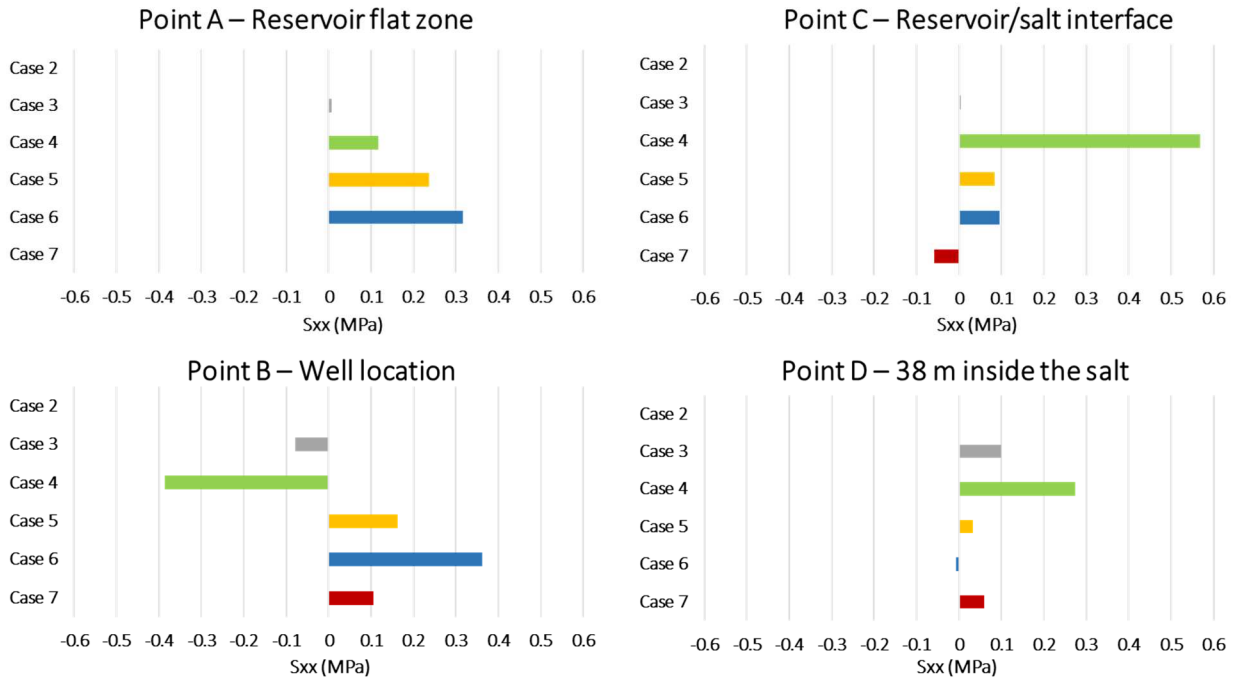


Figure 91. Total maximum horizontal stress behavior with respect to BC at different locations, after 13 years of production. The dipping angle and the pore compressibility were the parameters that altered more the total maximum stress changes in the reservoir and the salt. Where Case 4 experienced the major reduction of σ_{xx} around the well, and the lowest at the salt/sediment interface.

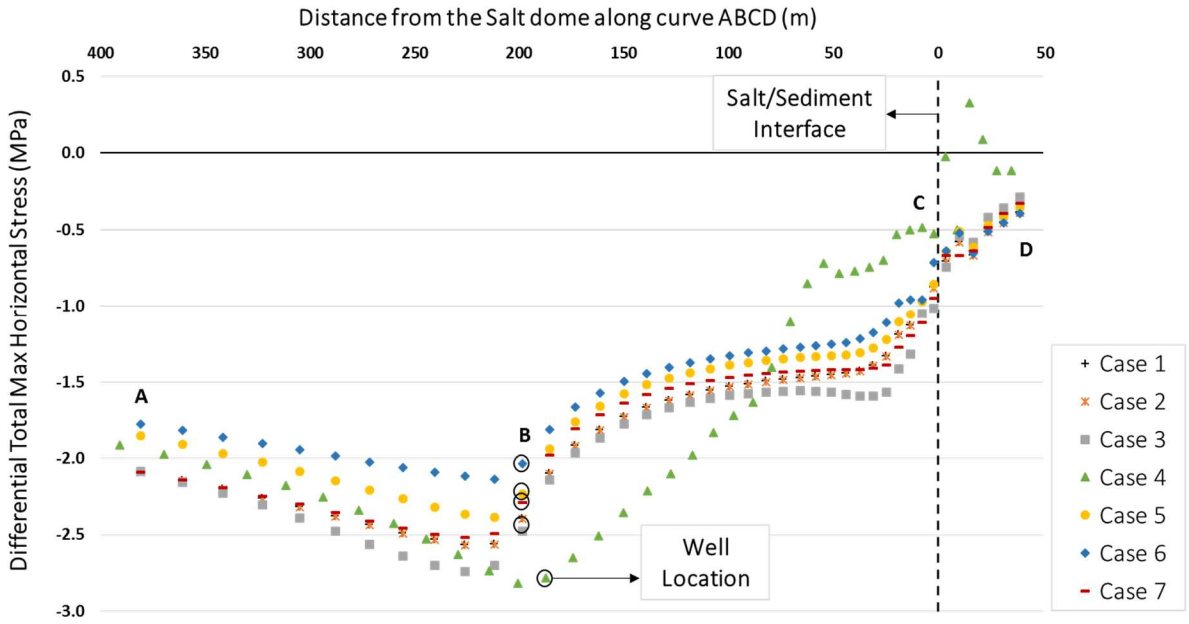


Figure 92. Change of total maximum horizontal stress in the reservoir along trajectory ABCD, as a function of distance from the salt/sediment interface after production. Case 3 and 4 reduced more the σ_{xx}, with a major impact around the well, extending 107 m toward the dome; beyond this point σ_{xx} decreased less than the other cases. Case 5, 6 and 7 presented less reduction of the σ_{xx}.

The highest effective maximum horizontal stress (σ'_{xx}) increment occurs around the well (up to 5.1 MPa), and it is induced by reducing the reservoir Biot's coefficient. The minimum effective stress increment at the salt/sediment interface was 3.5 MPa and is associated to a higher reservoir porosity, while the lowest σ'_{xx} in the flat region was 2.08 MPa and 3.3 MPa at point B related to a higher dipping angle. The parameters that increased the σ'_{xx} in the reservoir are the pore compressibility and the Biot's coefficient, while the dipping angle, the reservoir porosity and Young's modulus reduced the increment of the effective maximum horizontal stresses (see Figure 93).

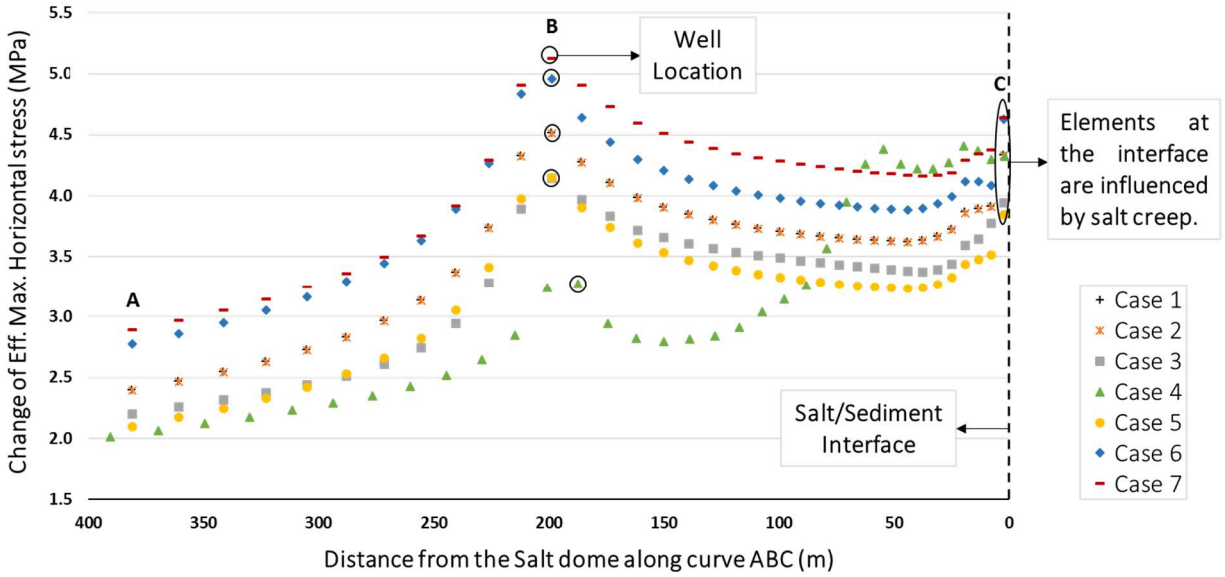


Figure 93. Change of effective maximum stress in the reservoir along trajectory ABC, as a function of distance from the salt/sediment interface, after 13 years of production. Cases 3 and 5 presented lower effective stress magnitude along the reservoir, while Cases 6 and 7 reported highest σ'_{xx}. Case 4 presented the lowest σ'_{xx} value from point A to 107 m from the well toward the salt dome, where the σ'_{xx} increased above the BC.

6.4 Total and effective minimum horizontal stress

The total minimum horizontal stress (σ_{yy}) did not change significantly, after increasing the salt permeability compared to BC. Reducing the reservoir Young's modulus to one-half of its original value, the horizontal stress did not change in the flat zone or around the well, compared to BC, but it was 0.1 MPa smaller at the salt/sediment interface and at point D. The results obtained after increasing the dipping angle to 70°, show that the stress reduction is 0.1 MPa lower at points A, 0.12 MPa smaller at point B and 0.32 MPa less at the salt/sediment interface, while the stresses did not change at point D. The previous behavior occurred after increasing the reservoir porosity, the results show that the stress reduction is 0.23 MPa lower at points A, 0.21 MPa smaller at point B and 0.21 MPa less at the salt/sediment interface, while the stresses did not change at point D. The same happens in the reservoir after decreasing the reservoir pore

compressibility, where the stress reduction is 0.32 MPa lower at points A, 0.48 MPa smaller at point B and 0.28 MPa less at the salt/sediment interface, with no stress changes at point D. Reducing the reservoir and shale Biot coefficient, the horizontal stress did not change at points A, C and D, and it was 0.1 MPa smaller around the well. (see Figure 94).

The maximum stress drop occurred around the well when the reservoir Young's modulus was lower and the lower stress changes in the producing formation were related to Case 6. The parameters that influenced more the total minimum horizontal stress changes along curve ABCD were the reservoir pore compressibility, the porosity and the dipping angle (see Figure 95).

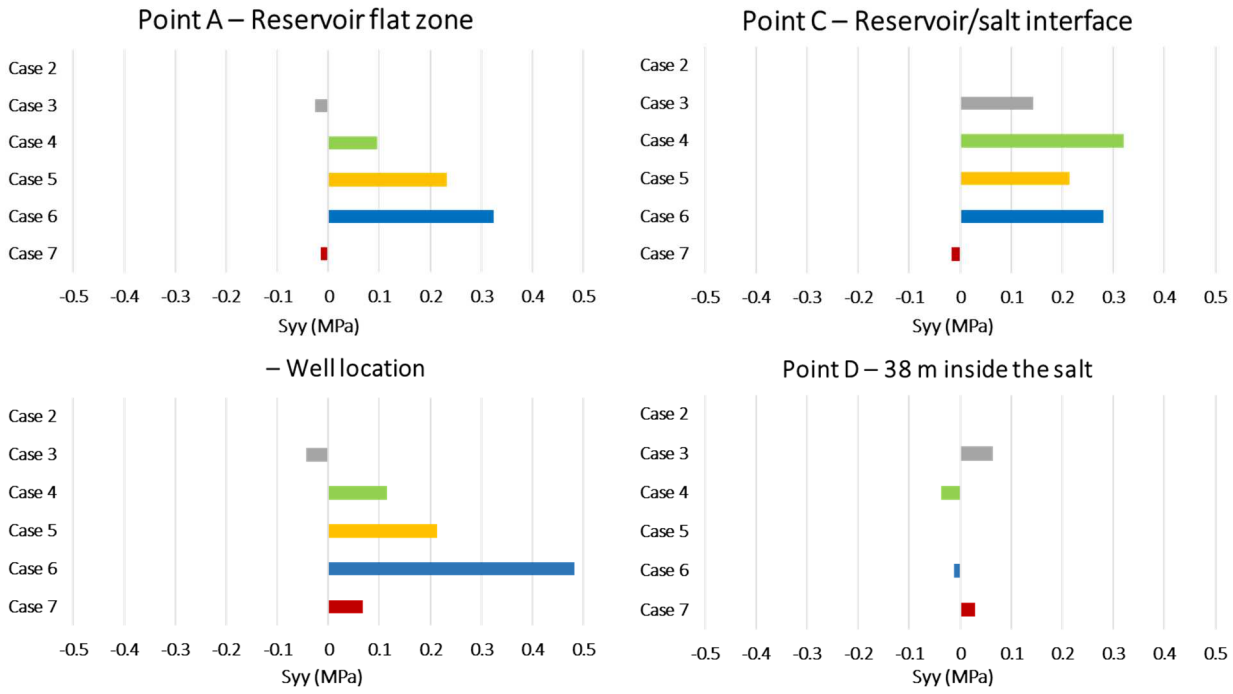


Figure 94. Total minimum horizontal stress behavior with respect to BC at different locations, after 13 years of production. The dipping angle, the reservoir pore compressibility and porosity were the parameters that altered more the total maximum stress changes in the reservoir. However, Case 3 presented the maximum reduction of σ_{yy} where the well is located.

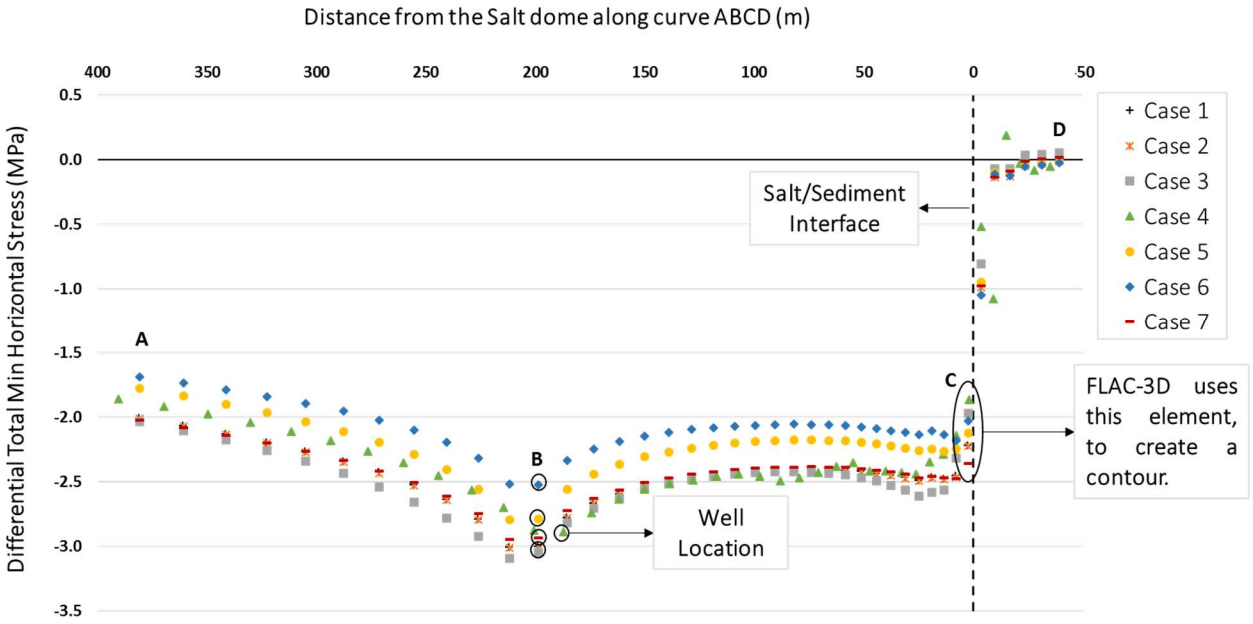


Figure 95. Change of total minimum horizontal stress in the reservoir along trajectory ABCD, as a function of distance from the salt/sediment interface, after 13 years of production. Case 3 reduced more the σ_{yy} in the reservoir, with a major impact around the well, while the σ_{yy} decreased less in Cases 4, 5 and 6. The σ_{yy} is more affected at the salt/sediment interface, compared to flat area.

The highest effective minimum horizontal stress (σ'_{yy}) increment occurs around the well (up to 4.5 MPa), and it is induced by reducing the reservoir Biot's coefficient 10% and the pore compressibility by half the initial value. The minimum σ'_{yy} change along the curve ABC occurred at point A (2.1 MPa) and is associated to a steeper dipping angle. The parameters that increased the σ'_{yy} in the reservoir were the pore compressibility and the Biot coefficient, while the Young's modulus, the porosity and the dipping angle experienced less σ'_{yy} increment (see Figure 96).

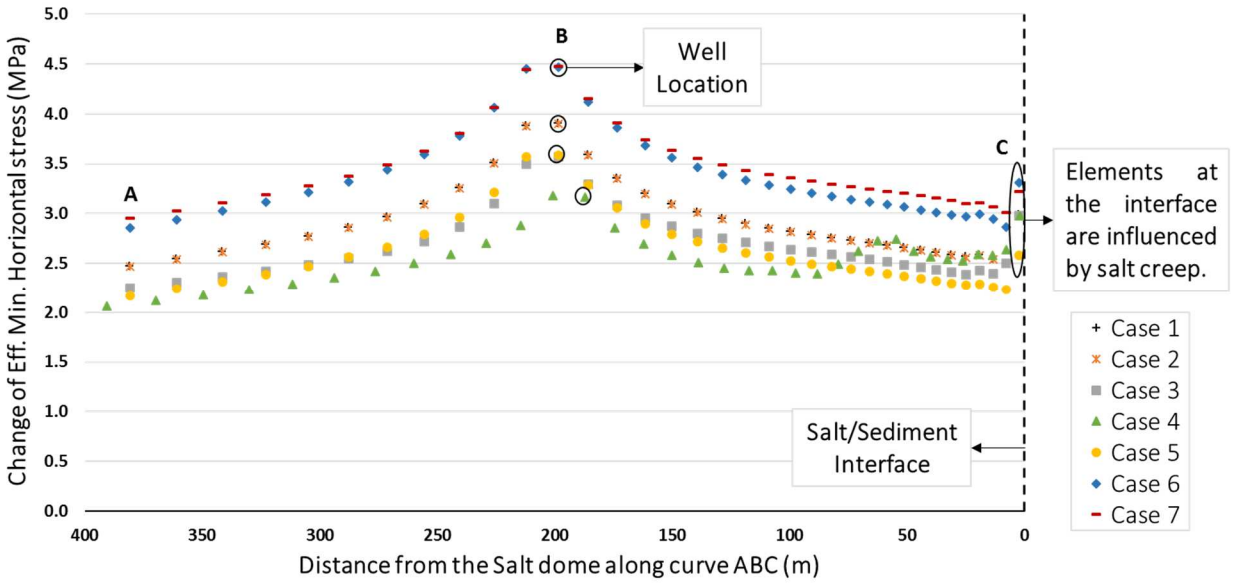


Figure 96. Change of effective minimum stress in the reservoir along trajectory ABC, as a function of distance from the salt/sediment interface, after 13 years of production. Case 3 and 5 presented the lowest effective stress value along the reservoir, while case 6 and 7 experienced the maximum effective stresses. The resultant σ'_{yy} for Case 4 is altered around the steeper dipping area, where it increased.

6.5 The xy-component of total stress tensor

The xy-component of total stress tensor (S_{xy}) along the trajectory ABCD defined in Figure 15(a) are very low, but the impact of the different parameters on the trend followed by Case 1 in the reservoir is analyzed (see Figure 97). There are not significant S_{xy} changes observed in the flat region for any of the studied cases. The S_{xy} did not change after increasing the salt permeability from $1x10^{-21}$ md to $1x10^{-19}$. However, reducing the reservoir Young's modulus to one-half of its original value, decreased the induced shear stresses $6.0x10^{-3}$ MPa less around the well and increased them $2.4x10^{-3}$ MPa more at the salt/sediment interface, compared to BC. In addition, increasing the dipping angle to 70° increased the S_{xy} $6.4x10^{-3}$ MPa more at point B and $2.2x10^{-2}$ MPa at point D, and decreased $1.6x10^{-2}$ MPa less at the salt/sediment interface, compared to Case 1. In the scenario where the reservoir porosity increased, the S_{xy} decreased

$1.7x10^{-3}$ MPa less at the salt/sediment interface, compared to BC. The results after decreasing the reservoir pore compressibility show no significant changes of S_{xy} at points A and D; however, it increased $2.9x10^{-3}$ MPa more around the well and decreased $1.4x10^{-2}$ MPa less at the salt/sediment interface, compared to Case 1. Reducing the reservoir Biot's coefficient to 0.9, the S_{xy} decreased $3.4x10^{-3}$ MPa less around the well and $1x10^{-3}$ MPa at point D, compared to BC. The maximum stress drop occurred at the left side of the well for Case 5, while Case 3 represented the major stresses increment at the salt/sediment interface. Case 4 caused the highest S_{xy} increment 20.5 m inside the salt. The parameters that influenced more the induced shear stresses along curve ABCD were the dipping angle, the reservoir Young's modulus and the pore compressibility (see Figure 98).

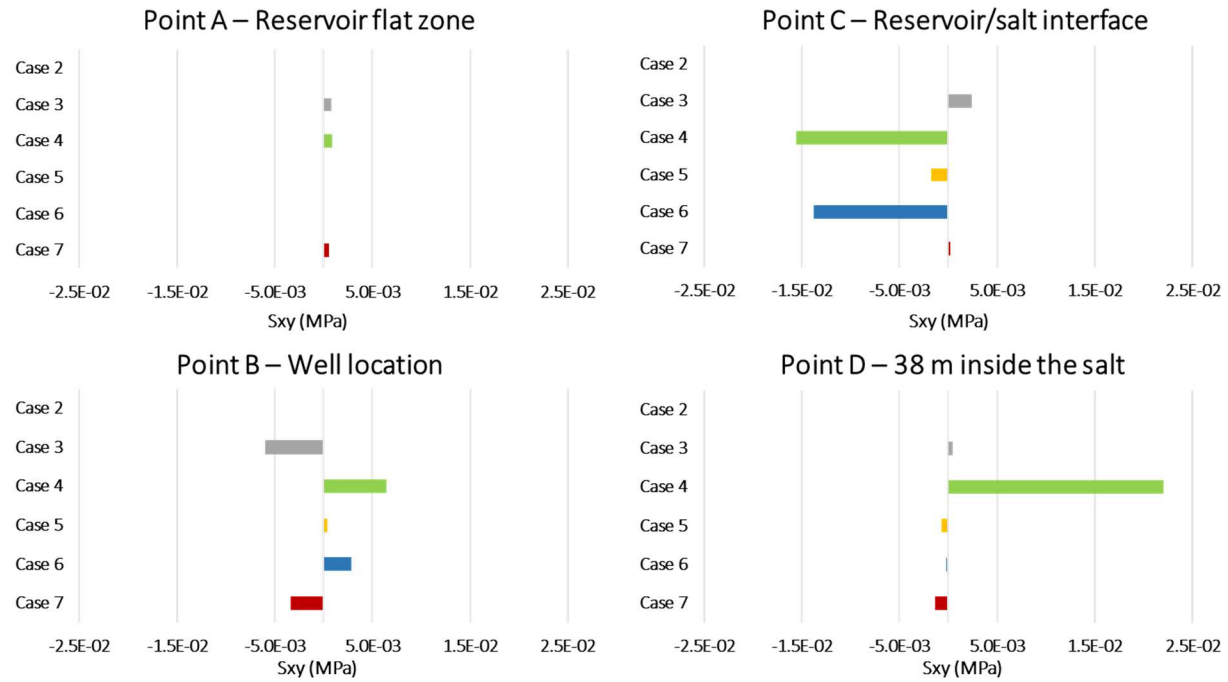


Figure 97. The S_{xy} total stress behavior with respect to BC at different locations, after 13 years of production. The dipping angle, the reservoir Young's modulus and the pore compressibility were the parameters that affected more the shear stresses in the reservoir. However, Case 4 presented the highest value of S_{xy} inside the salt.

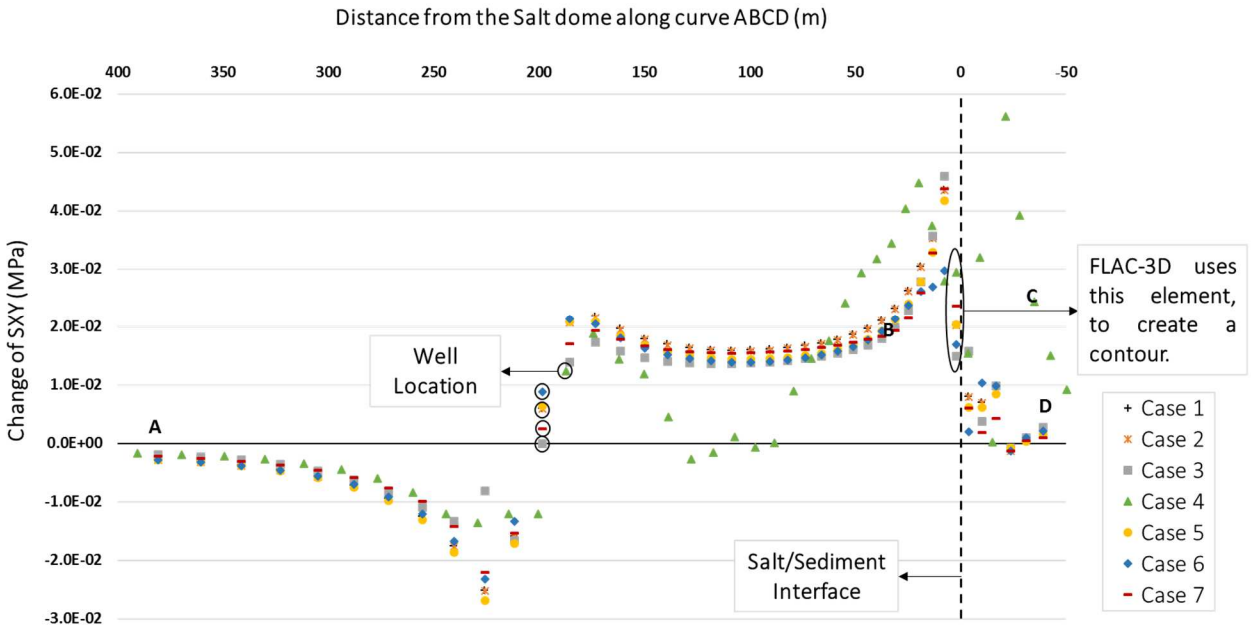


Figure 98. Change of S_{xy} in the reservoir along trajectory ABCD, as a function of distance from the salt/sediment interface, after 13 years of production. The effect of higher reservoir porosity is to increase the induced shear stresses and concentrate them close to the well, while the other cases have the opposite impact. However, the stress perturbation magnitude at the salt/sediment interface increases for reservoirs less stiff.

6.6 The yz-component of total stress tensor

The yz-component of total stress tensor (S_{yz})along the trajectory ABCD defined in Figure 15(a) are very low, but the impact of the different parameters on the trend followed by Case 1 in the reservoir is analyzed (see Figure 99). There are not significant Syz changes observed in the flat region for any of the studied cases. The S_{yz} did not change after increasing the salt permeability from $1x10^{-21}$ md to $1x10^{-19}$. However, lowering the reservoir Young's modulus to one-half of its original value, increased the induced shear stresses $3.6x10^{-3}$ MPa more around the well and at the salt/sediment interface, compared to BC. Additionally, increasing the dipping angle to 70° increased the S_{yz} $9.3x10^{-3}$ MPa more at point B and $4.2x10^{-3}$ MPa at point D, and decreased $3.7x10^{-2}$ MPa at the salt/sediment interface, compared to Case 1. In the scenario where the

reservoir porosity increased, the S_{yz} did not vary at points A and D, but it increased $1.4x10^{-3}$ MPa more at point B and $1.3x10^{-3}$ MPa less at the salt/sediment interface, compared to BC. The results after decreasing the reservoir pore compressibility show no changes of S_{yz} at points A and D, but it increased $3.3x10^{-3}$ MPa less around the well and $8.3x10^{-3}$ MPa less at the salt/sediment interface, compared to Case 1. Finally, lowering the reservoir Biot's coefficient to 0.9, the S_{yz} did not vary significantly at points A, B and D, but it increased $2.5x10^{-3}$ MPa less at the salt/sediment interface, compared to BC. The maximum stress drop occurred in the steeper dipping area for Case 7, which presented the maximum stress increment at the salt/sediment interface. The shear stresses toward the salt dome decreased for Case 4, while they increased for the other cases. The parameters that influenced more the induced shear stresses along curve ABCD were the dipping angle, the reservoir Young's modulus and the pore compressibility (see Figure 100).

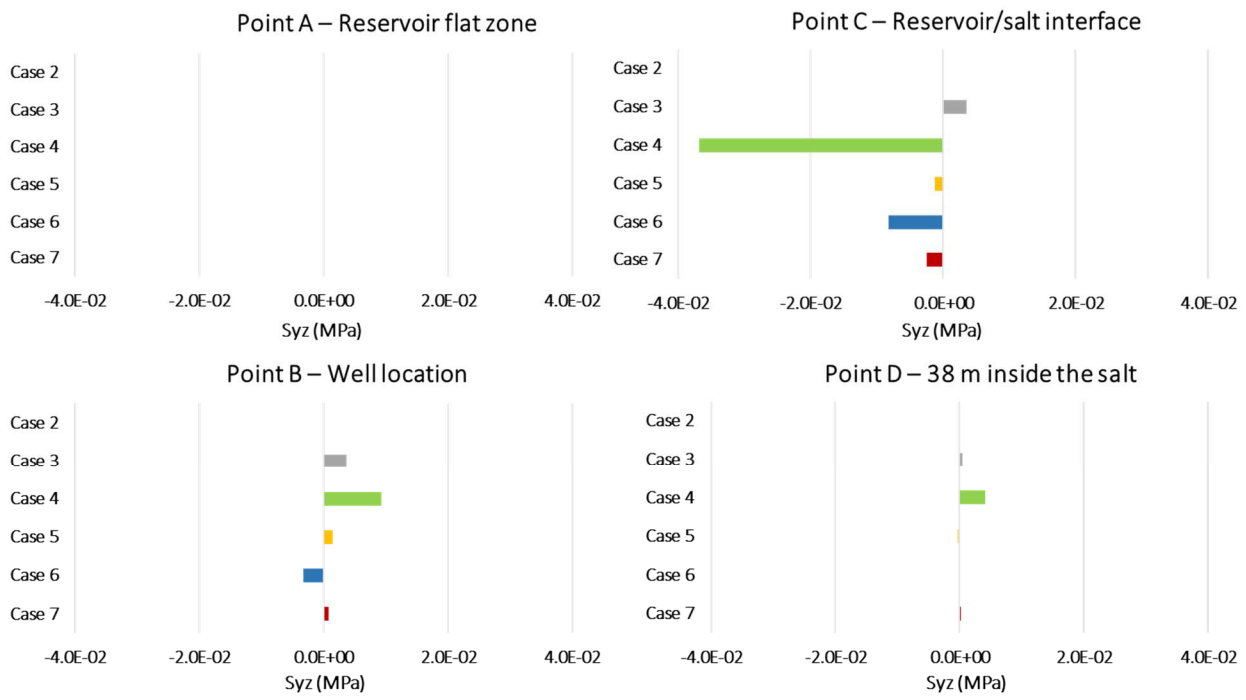


Figure 99. The Syz total stress behavior with respect to BC at different locations, after 13 years of production. The dipping angle, the reservoir Young's modulus and the pore compressibility were the parameters that affected more the shear stresses at points B, C and D. However, Case 4 presented the major reduction of S_{yz} at the salt/sediment interface.

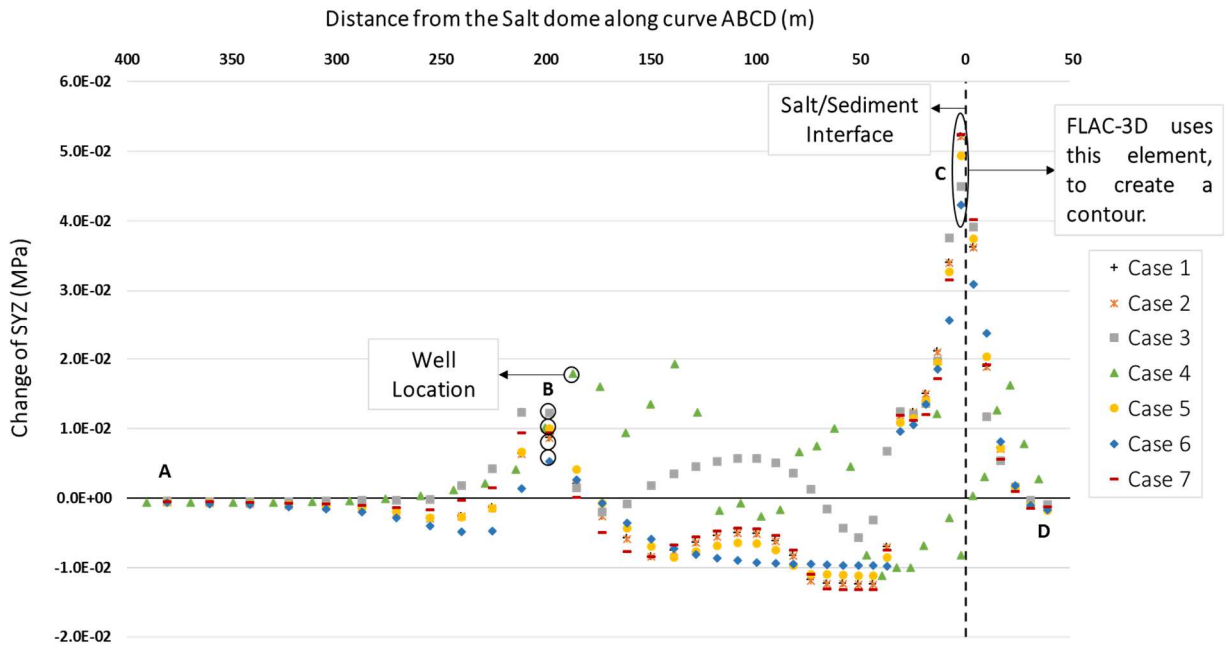


Figure 100. Change of S_{yz} in the reservoir along trajectory ABCD, as a function of distance from the salt/sediment interface, after 13 years of production. The lower reservoir Biot's coefficient caused the maximum S_{yz} increment at the salt/sediment interface, and the highest S_{yz} reduction in the steeper dipping area of the producing layer. The S_{yz} tend to decrease inside the salt.

6.7 The xz-component of total stress tensor

The xz-component of total stress tensor (S_{xz}) along the trajectory ABCD defined in Figure 15(a) are very low, but the impact of the different parameters on the trend followed by Case 1 in the reservoir is analyzed (see Figure 101). There are not significant S_{xz} changes observed in the flat region for any of the studied cases. The S_{xz} did not change after increasing the salt permeability from $1x10^{-21}$ md to $1x10^{-19}$. However, lowering the reservoir Young's modulus to one-half of its original value, decreased the induced shear stresses $3.4x10^{-1}$ MPa less at the salt/sediment interface, while it increased $6.7x10^{-1}$ MPa more around the well and $9.4x10^{-2}$ MPa more at point D, compared to BC. In addition, increasing the dipping angle to 70° decreased the S_{xz} $2.8x10^{-1}$ MPa more at point B, $1.5x10^{-1}$ MPa less at the salt/sediment interface and increased

$3.5x10^{-1}$ MPa more at point D, compared to Case 1. In the scenario where the reservoir porosity increased, the S_{xz} decreased $5.4x10^{-2}$ MPa more at point B, $6.9x10^{-2}$ MPa less at the salt/sediment interface, and increased $2.7x10^{-2}$ MPa less at point D, compared to BC. The results after decreasing the reservoir pore compressibility show that S_{xz} decreased $5.9x10^{-1}$ MPa more around the well, $1.2x10^{-1}$ MPa less at the salt/sediment interface, while it increased $5.0x10^{-2}$ MPa less, compared to Case 1. Reducing the reservoir Biot's coefficient to 0.9, the S_{xz} decreased $2.4x10^{-2}$ MPa more at point B, $2.1x10^{-2}$ MPa less at the salt/sediment interface, while it increased $2.8x10^{-2}$ MPa less at point D, compared to BC.

The maximum stress increment in the reservoir (0.8 MPa) occurred in the dipping area and was induced by lowering the reservoir Young's modulus. It also represented the highest stress increment in the salt (0.4 MPa). Increasing the dipping angle to 70° caused the maximum S_{xz} reduction in the reservoir close to the dome (0.9 MPa). It is observed that the shear stresses are controlled by the well location and the dipping angle. The parameters that influenced more the induced shear stresses along curve ABCD were the dipping angle, the reservoir Young's modulus and the pore compressibility (see Figure 102).

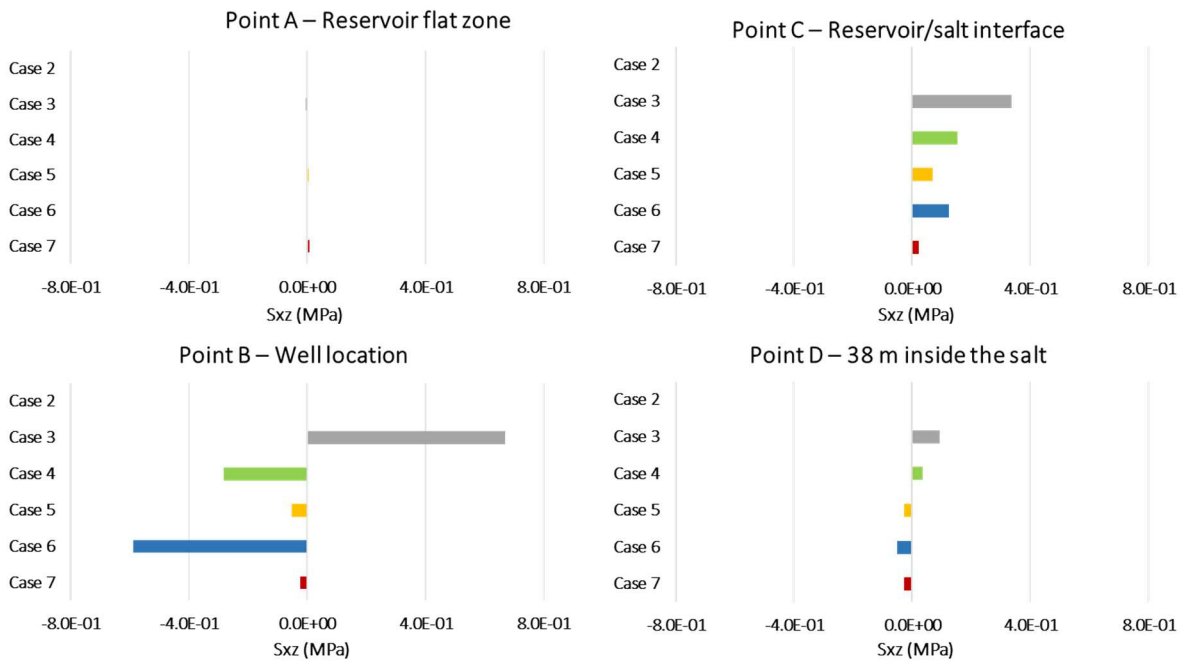


Figure 101. The S_{xz} total stress behavior with respect to BC at different locations, after 13 years of production. The highest induced shear stress values occurred at point B. The dipping angle, the reservoir Young's modulus and the pore compressibility were the parameters that affected more the S_{xz} at points B, C and D. However, Case 3 presented the largest increment of S_{xz} at point B and Case 6 caused the largest reduction in the same location.

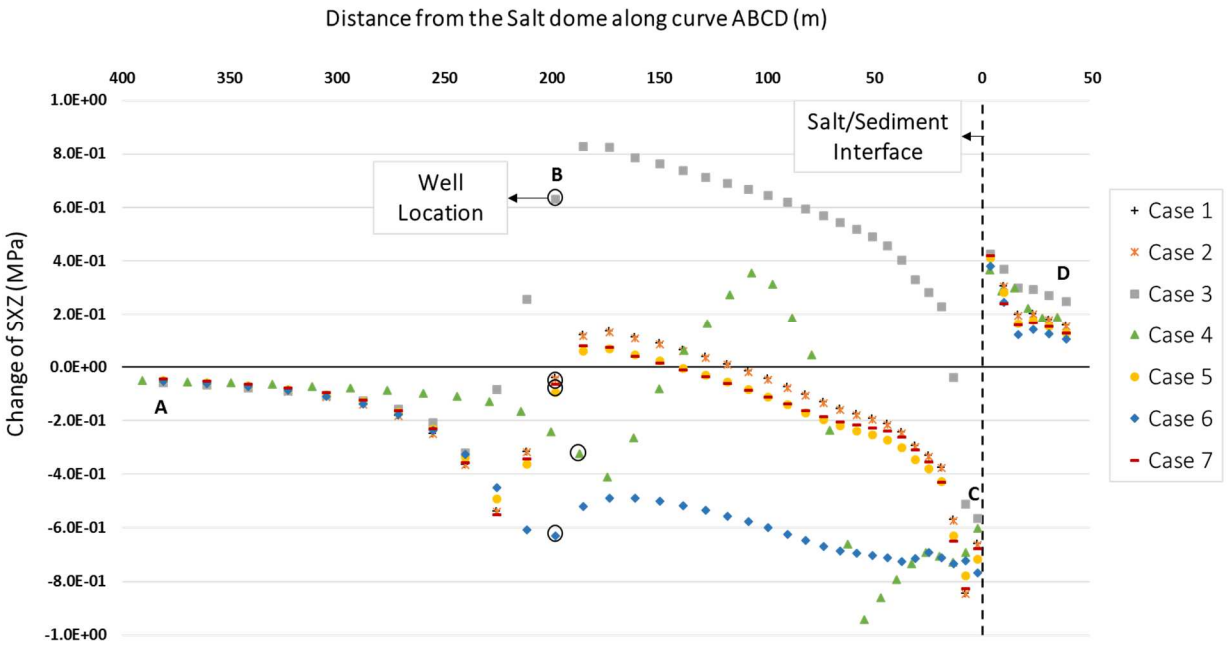


Figure 102. Change of S_{xz} in the reservoir along trajectory ABC, as a function of distance from the salt/sediment interface, after 13 years of production. The lower reservoir Young's modulus induced the highest increment of shear stresses around the well which extended toward the steeper dipping area, while reducing the pore compressibility induced the maximum S_{xz} in the same zone. However, Case 4 originated the mayor reduction of S_{xz} at the salt/sediment interface.

6.8 Total and effective vertical stress path

The total vertical stress path ($\gamma_v = \gamma_z$) in the reservoir is the same for cases 1 and 2. Reducing the reservoir Young's modulus increased the vertical stress path by 0.02 at points A and B and decreased it by 0.01 at point C, compared to BC. For the scenario where the dipping angle is 70°, the stress path did not change at point B, but it is 0.02 greater at point A and 0.05 at point C. Case 4 caused the highest γ_z in the reservoir and occurred in the area with steeper dipping angle. The vertical stress path results obtained from the case with lower reservoir porosity did not changed at point A, but it increased by 0.01 at points B and C. Lower reservoir pore compressibility decreased the γ_z by 0.01 at point A, 0.03 at point B, and 0.04 at point C,

compared to Case 1. Decreasing the reservoir Biot's coefficient, the γ_z decreased by 0.01 at point A, by 0.03 at point B and by 0.03 at the salt/sediment interface (see Figure 103).

The effective vertical stress path ($\gamma'_v = \gamma'_z$) is calculated using the Eq.(30), described in chapter 2. This equation considers the reservoir Biot's coefficient, which is 1 for cases 2 to 6 and 0.9 for case 7. Under these conditions, Eq.(30) becomes: $\gamma'_v = \left(\frac{\Delta\sigma_v}{\Delta p_f}\right) - 1$ for cases 2 to 6 and $\gamma'_v = \left(\frac{\Delta\sigma_v}{\Delta p_f}\right) - 0.9$ for case 7. Figure 104, shows that γ'_v in the reservoir is the same for cases 1 and 2. For a lower reservoir Young's modulus, the γ'_v decreased 0.02 less at points A and B and 0.01 more at point C, compared to BC. For the scenario where the dipping angle is 70°, the γ'_v decreased 0.02 less at point A and 0.05 at point C, but it decreased the same than Case 1 at point B. Case 4 experienced the lowest reduction of γ'_z in the area with steeper dipping angle. For a lower reservoir porosity, the γ'_v did not changed at point A, but it decreased 0.01 less at points B and C. For a lower reservoir pore compressibility, the γ_z' decreased 0.01 more at point A, 0.03 more at point B, and 0.04 more at point C, compared to Case 1. When the reservoir Biot's coefficient was reduced from 1 to 0.9, the γ'_z decreased 0.09 less at point A, 0.07 less at point B and 0.07 less at the salt/sediment interface.

The effective vertical stress path decreased less, for the case with higher dipping angle in the steeper dipping area, for the case with lower sandstone Biot's coefficient which reduces the impact of the pore pressure changes.

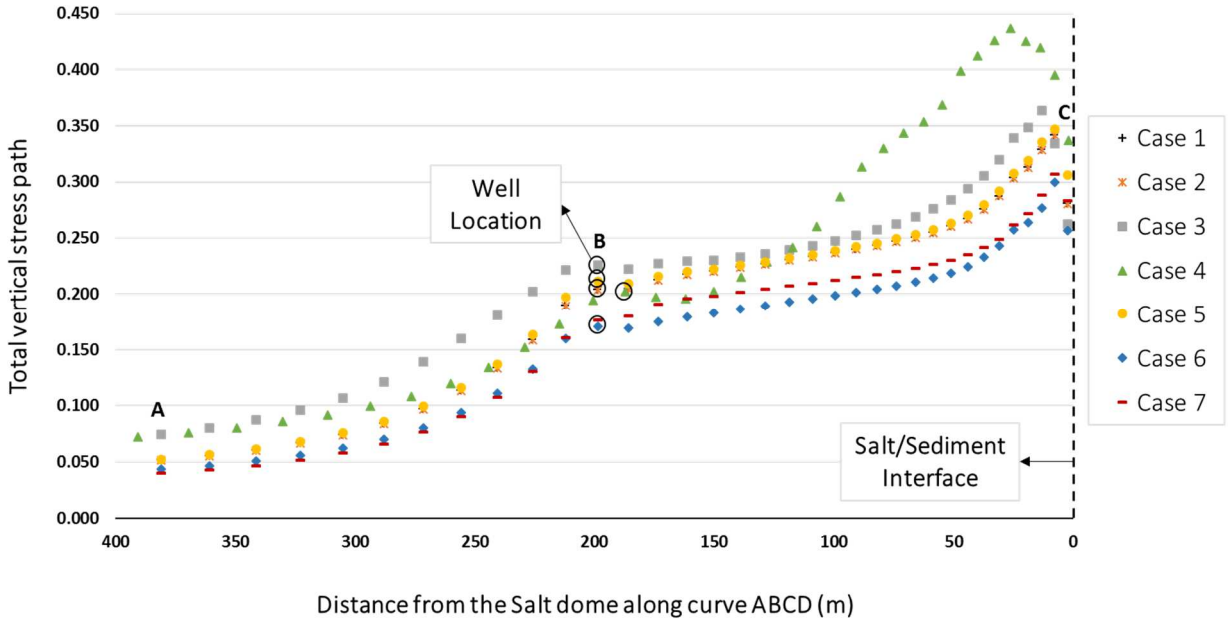


Figure 103. Total vertical stress path in the reservoir along trajectory ABC, as a function of distance from the salt/sediment interface, after 13 years of production. Cases 3, 4 and 5 increased the resultant stress path along the reservoir, where Case 4 exhibited the maximum increment in the steeper dipping area toward the dome. In the contrary, cases 6 and 7 decreased the γ_z in the producing formation.

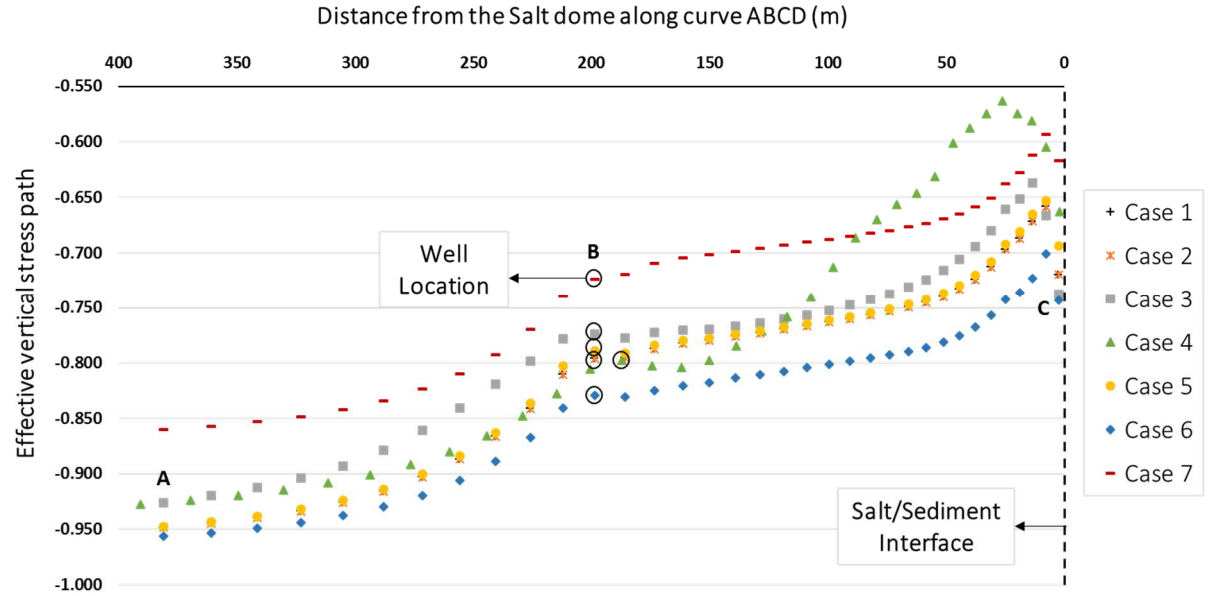


Figure 104. Effective vertical stress path in the reservoir along trajectory ABC, as a function of distance from the salt/sediment interface, after 13 years of production. The γ'_v decreased less for cases 3, 4 and 7, where Case 4 exhibited the minor reduction in the steeper dipping area toward the dome. In the contrary, case 6 decreased more the γ'_z along the reservoir.

6.9 Total and effective maximum horizontal stress path

The total maximum horizontal stress path ($\gamma_H = \gamma_{xx}$) in the reservoir is the same for cases 1 and 2. Reducing the reservoir Young's modulus increased γ_H by 0.02 at point A, 0.03 at point B and 0.01 at point C, compared to BC. For the scenario where the dipping angle is 70°, the stress path increased by 0.02 at point A and 0.11 at point B but decreased by 0.11 at the salt/sediment interface. Case 4 caused the minimum γ_H in the reservoir and occurred in the area with steeper dipping angle. The maximum horizontal stress path results obtained from the case with lower reservoir porosity did not changed at any point along curve ABC. Lower reservoir pore compressibility decreased the γ_H by 0.08 at point A, 0.06 at point B, and 0.02 at point C, compared to Case 1. Reducing the reservoir Biot's coefficient, the γ_H decreased by 0.05 at point A, 0.04 at point B and 0.01 at the salt/sediment interface (see Figure 105).

The effective maximum horizontal stress path ($\gamma'_H = \gamma'_x$) is calculated using the Eq.(30), described in chapter 2. This equation considers the reservoir Biot's coefficient, which is 1 for cases 2 to 6 and 0.9 for case 7. Under these conditions, Eq.(30) becomes: $\gamma'_H = \left(\frac{\Delta\sigma_H}{\Delta p_f}\right) - 1$ for cases 2 to 6 and $\gamma'_H = \left(\frac{\Delta\sigma_H}{\Delta p_f}\right) - 0.9$ for case 7. Figure 106, shows that γ'_H in the reservoir is the same for cases 1, 2 and 5. For a lower reservoir Young's modulus, the γ'_H decreased 0.02 less at point A, 0.03 at point B and 0.01 at point C, compared to BC. For the scenario where the dipping angle is 70°, the γ'_H decreased 0.02 less at point A and 0.11 at point B, but it decreased 0.11 more at the salt/sediment interface. Case 4 experienced the major reduction of γ'_H in the area with steeper dipping angle. For a lower reservoir pore compressibility, the γ'_H decreased 0.08 more at point A, 0.06 more at point B, and 0.02 more at point C, compared to Case 1. When the

reservoir Biot's coefficient was reduced from 1 to 0.9, the γ'_H decreased 0.05 less at point A, 0.04 less at point B and 0.01 less at the salt/sediment interface.

The effective maximum horizontal stress path decreased more for the case with higher dipping angle in the steeper dipping area and when the reservoir pore compressibility is decreased by 0.5. While γ'_H decreased less when the sandstone Biot's coefficient is lower, which reduces the impact of the pore pressure changes.

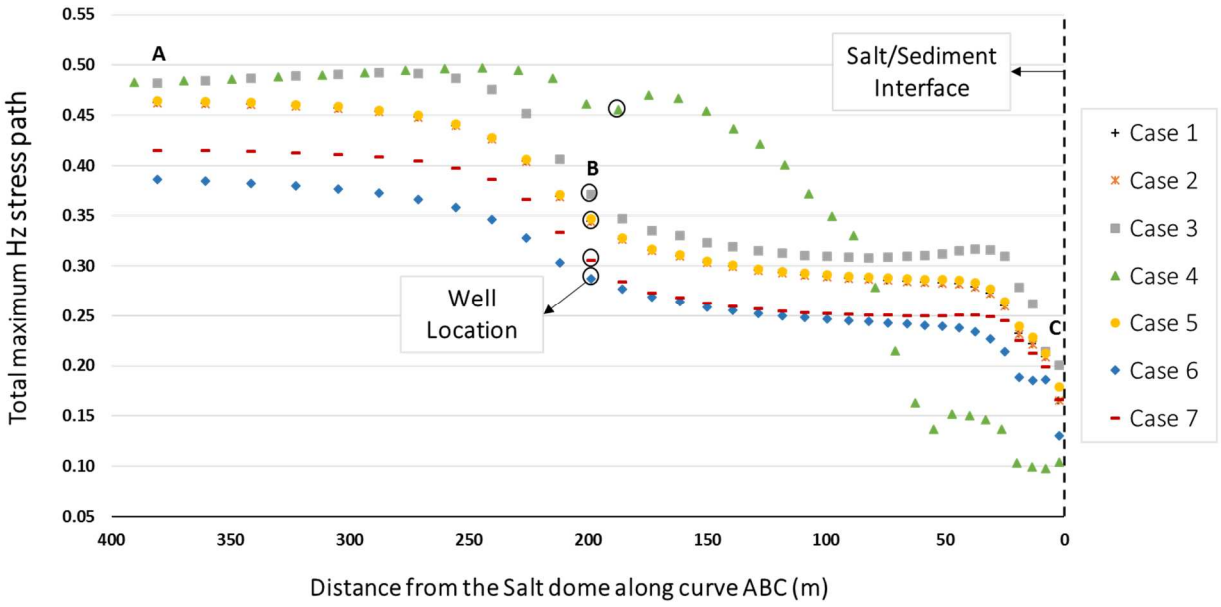


Figure 105. Total maximum horizontal stress path in the reservoir along trajectory ABC, as a function of distance from the salt/sediment interface, after 13 years of production. Cases 3 and 4 increased the resultant stress path along the reservoir, but in the steeper dipping area Case 4 exhibited the minimum stress path value in the producing formation. In addition, cases 6 and 7 decreased the γ_H in the reservoir.

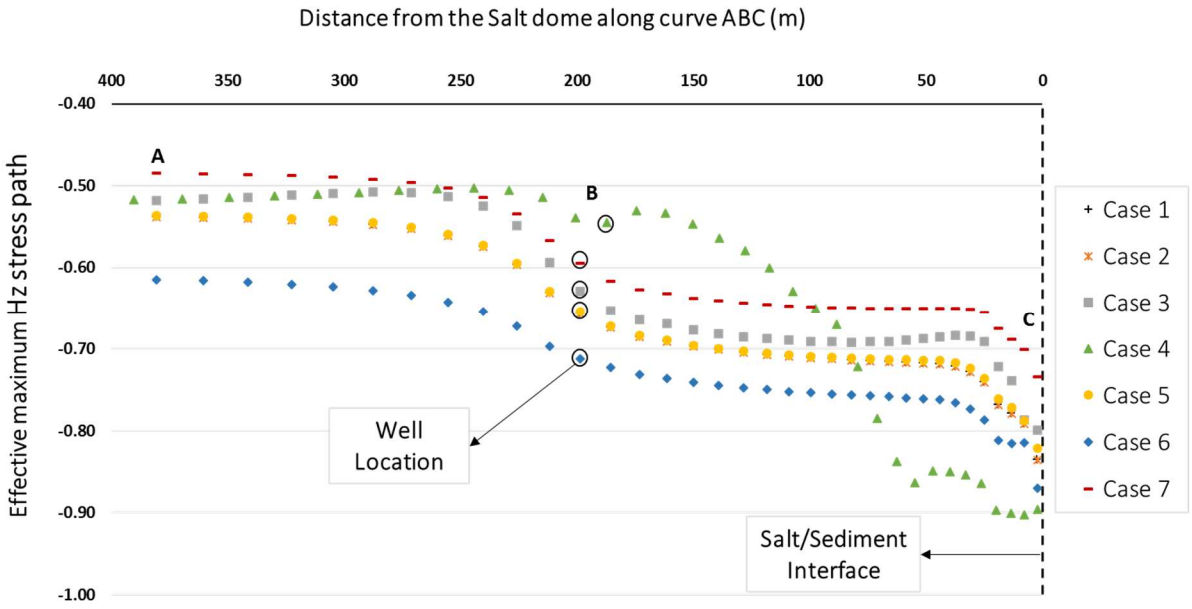


Figure 106. Effective maximum horizontal stress path in the reservoir along trajectory ABC, as a function of distance from the salt/sediment interface, after 13 years of production. The γ'_H decreased less for cases 3, 4 and 7, where Case 4 exhibited the major reduction in the steeper dipping area toward the dome. In the contrary, case 6 decreased more the γ'_H along the reservoir.

6.10 Total and effective minimum horizontal stress path

The total minimum horizontal stress path $(\gamma_h = \gamma_y)$ in the reservoir is the same for cases 1 and 2. Reducing the reservoir Young's modulus increased γ_h by 0.03 at points A and B and decreased it by 0.02 at the salt/sediment interface, compared to BC. Case 3 caused the maximum γ_h in the reservoir and occurred in the area with steeper dipping angle. For the scenario where the dipping angle is 70°, the stress path increased by 0.03 at point A and 0.04 at point B but decreased by 0.05 at point C. The minimum horizontal stress path results obtained from the case with lower reservoir porosity did not changed at any point along the curve ABC. Lower reservoir pore compressibility decreased the γ_h by 0.08 at point A, 0.07 at point B, and 0.06 at point C, compared to Case 1. Case 6 caused the minimum γ_h in the reservoir and occurred around the

well. Lowering the reservoir Biot's coefficient, the γ_h decreased by 0.04 at points A, B and C (see Figure 107).

The effective minimum horizontal stress path $(\gamma'_h = \gamma'_y)$ is calculated using the Eq.(30), described in chapter 2. This equation considers the reservoir Biot's coefficient, which is 1 for cases 2 to 6 and 0.9 for case 7. Under these conditions, Eq.(30) becomes: $\gamma'_h = \left(\frac{\Delta\sigma_h}{\Delta p_f}\right) - 1$ for cases 2 to 6 and $\gamma'_h = \left(\frac{\Delta\sigma_h}{\Delta p_f}\right) - 0.9$ for case 7. Figure 108, shows that γ'_h in the reservoir is the same for cases 1, 2 and 5. For a lower reservoir Young's modulus, the γ'_h decreased 0.03 less at points A and B and 0.02 more at the salt/sediment interface, compared to BC. For the scenario where the dipping angle is 70°, the γ'_h decreased 0.03 less at point A and 0.04 at point B, but it decreased 0.05 more at the salt/sediment interface. For a lower reservoir pore compressibility, the γ'_h decreased 0.08 more at point A, 0.07 at point B, and 0.06 at point C, compared to Case 1. When the reservoir Biot's coefficient was reduced from 1 to 0.9, the γ'_h decreased 0.04 less at points A, B and at the salt/sediment interface.

The effective minimum horizontal stress path decreased more for the case with higher dipping angle in the steeper dipping area and when the reservoir pore compressibility is decreased by 0.5. While γ'_h decreased less when the sandstone Biot's coefficient is lower, which reduces the impact of the pore pressure changes.

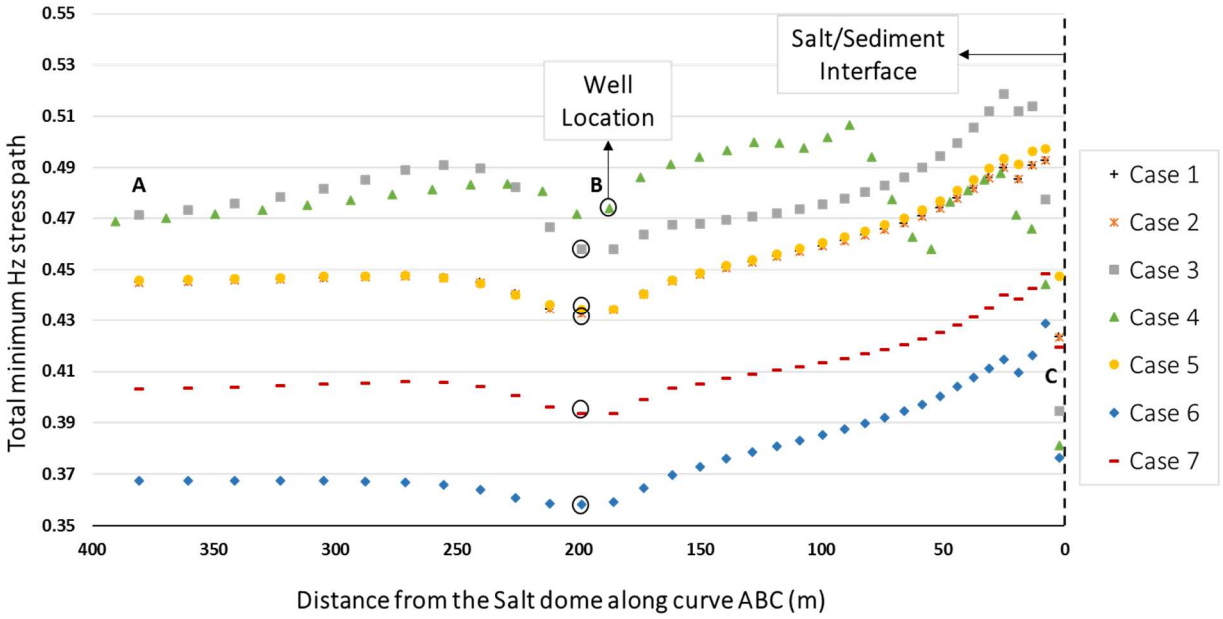


Figure 107. Total minimum horizontal stress path in the reservoir along trajectory ABC, as a function of distance from the salt/sediment interface, after 13 years of production. Cases 3 and 4 increased the resultant stress path along the reservoir, but in the steeper dipping area Case 4 decreased toward the salt dome. In addition, cases 6 and 7 decreased the γ_h in the reservoir, where case 6 induced the lowest minimum horizontal stress path along the curve ABC.

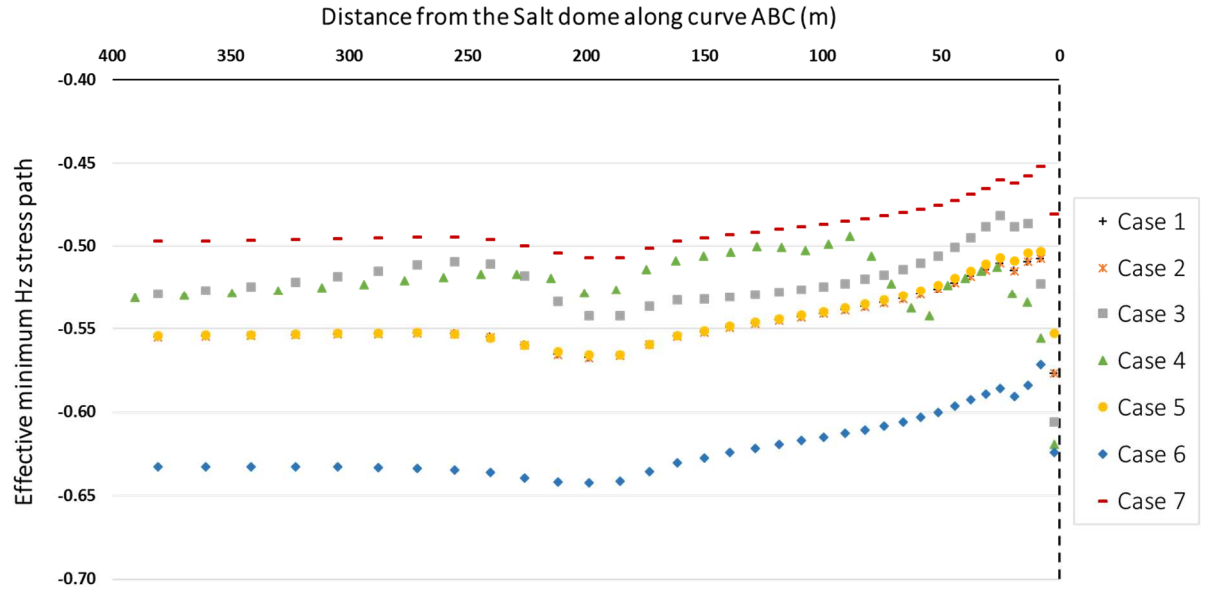


Figure 108. Effective minimum horizontal stress path in the reservoir along trajectory ABC, as a function of distance from the salt/sediment interface, after 13 years of production. The γ'_h decreased less for cases 3, 4 and 7. In the contrary, case 6 decreased more the γ'_h along the reservoir and case 4 decreased more in the steeper dipping area.

6.11 Volumetric strain

The volumetric strain ($e_v = \Delta V/V$) of the reservoir and salt along the trajectory ABCD, defined in Figure 15(a), after 13 years of production. Increasing the salt permeability from $1x10^{-21}$ md to $1x10^{-19}$ md, did not change the volumetric strain in the formations. After the reservoir Young's modulus is reduced to half of its original value, the reservoir compaction increased by $2.06x10^{-4}$ at point A, $2.97x10^{-4}$ around the well and $2.16x10^{-4}$ at the salt/sediment interface, compared to BC. Increasing the dipping angle originated more compaction in the reservoir, it increased $1.78x10^{-4}$ at point A, $2.13x10^{-4}$ at point B and $2.22x10^{-4}$ at the salt/sediment interface. The reservoir elements in the steeper dipping area shrunk more in Case 4. Higher porosity caused less compaction in the producing formation, it was $0.73x10^{-4}$ less at points A, $1.07x10^{-4}$ at point B and $0.76x10^{-4}$ at point C. Lowering the reservoir pore compressibility, the compaction decreased by $0.30x10^{-4}$ MPa at point A, $0.28x10^{-4}$ MPa at point B and $0.26x10^{-4}$ at the salt/sediment interface, compared to Case 1. Reducing the reservoir Biot coefficient did not change significantly the volumetric strain in the reservoir, compared to the base case (see Figure 109).

There reservoir experienced more compaction at the salt/sediment interface, compared to the magnitude at point A. Additionally, the case where the dipping angle is 70°, presented more compaction along the steeper dipping area (see Figure 110).

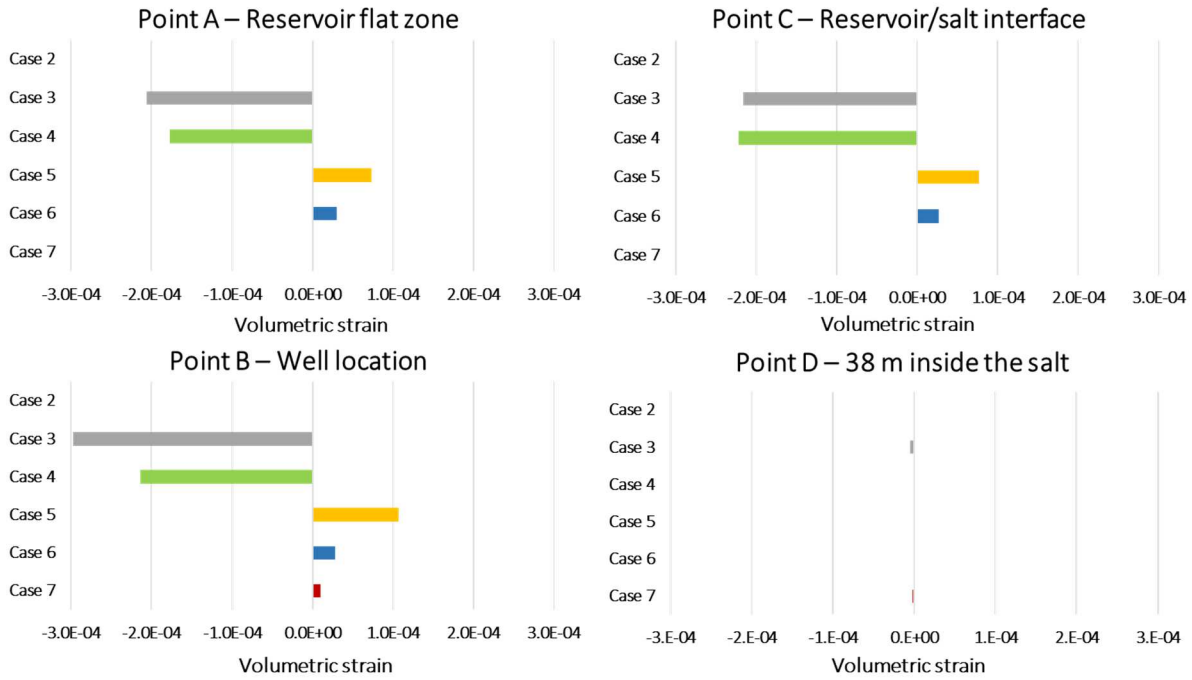


Figure 109. Vertical strain behavior with respect to BC at different locations, after 13 years of production. The major volumetric strain changes in order of magnitude occurred at point B, point C and point A. The dipping angle and the reservoir Young's modulus increased compaction during production, while cases 5, 6 and 7 experienced less compaction at points A, B and C.

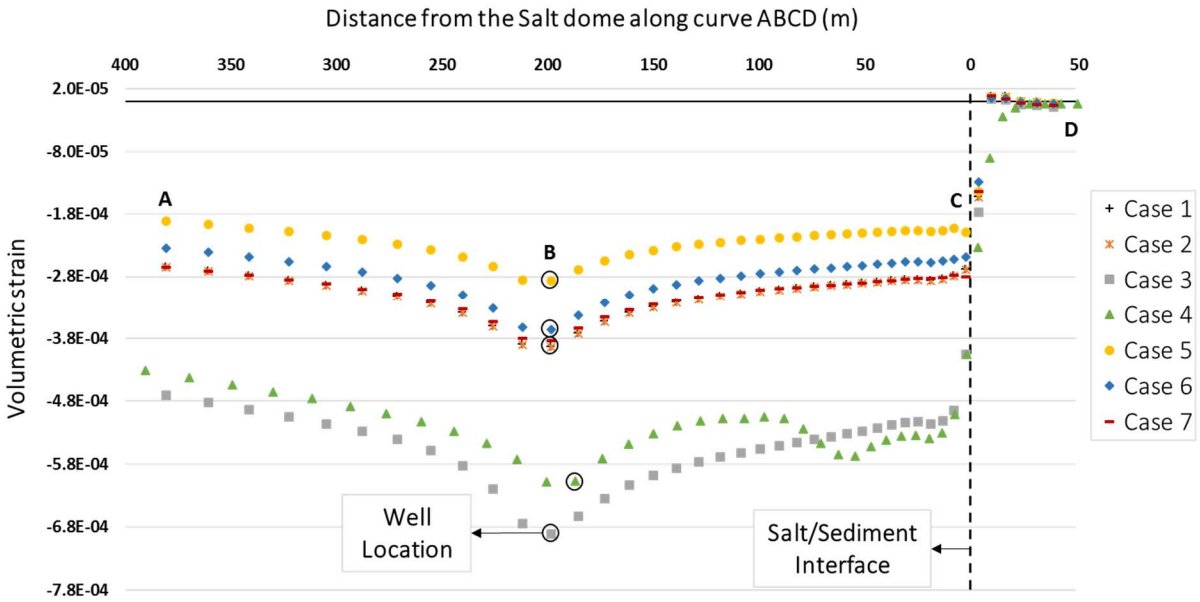


Figure 110. Volumetric strain in the reservoir along trajectory ABCD, as a function of distance from the salt/sediment interface, after 13 years of production. Lower Young's modulus and higher dipping angle, increased compaction in the reservoir, reaching the major value around the well. Moreover, compaction at the salt/sediment interface is greater compared to point A.

Conclusions

Stress changes associated with depletion of a reservoir near a salt dome has been numerically studied using FLAC3D. A sensitivity analysis was performed to evaluate the influence of rock properties and dipping angle on the resultant trends. The following conclusions can be drawn from this work:

1. The reduction of total horizontal stresses due to production are more significant (the total maximum horizontal stress decreased up to 2.55 MPa and the total minimum horizontal stress up to 3 MPa) than of the vertical stress (up to 1.7 MPa), with the highest variation of the vertical and the minimum horizontal stresses close to the salt dome where gravity drainage plays an important role on pore pressure drawdown near the salt/reservoir interface (compared to the changes in the flat zone). However, the increment of the effective horizontal stresses are less significant (the effective maximum horizontal stress increased up to 4.52 MPa and the effective minimum horizontal stress up to 3.92 MPa) than of the vertical components (up to 5.57 MPa), with the highest variation close to the well.

2. The total and effective vertical and horizontal stress paths results vary locally in the reservoir, controlled by the proximity to the salt and the dipping angle. Furthermore, the stress path in the reservoir is influenced by the well location that determines the depletion pattern along the reservoir.

3. The stress paths for a reservoir that extends laterally to infinity are different than for a tilted reservoir.

4. The volumetric strain that is experience in the reservoir and surrounding formations during depletion has been calculated. The compaction observed in the reservoir, and upper and lower shale, is strongly dependent on the depletion pattern, with major changes at the salt/sediment interface compared to the flat zone. Simulations show that reservoir with lower Young's modulus and higher dipping angles increased the total vertical and horizontals stress paths resulting in more compaction. The maximum volumetric strain of the base case in the reservoir was $-3.9\text{x}10^{-4}$, while the volumetric strain for the cases of lower Young's modulus and higher dipping angle was $-6.88\text{x}10^{-4}$ and $-6.05\text{x}10^{-4}$, respectively.

5. It was found that the stress state, pore pressure and the volumetric strains of the elements at the reservoir-salt interface are affected by the salt creep and the dipping angle (higher pore pressure drawdown, lower total vertical and horizontal stress reduction, higher effective vertical and horizontal stress increment and less compaction, than the reservoir element next to it) Therefore, it is necessary to include the impact of creep and dipping angle to accurately predict the sediment deformation and tendency to failure of tilted reservoirs.

References

Baar, C. A. (1977). *APPLIED SALT-ROCK MECHANICS 1*. Amsterdam: Elsevier Scientific Publishing Company.

Barton, C. A., Zoback, M. D., & Burns, K. L. (1988). In-situ stress orientation and magnitude at the Fenton Geothermal Site, New Mexico, determined from wellbore breakouts. *Geophysical Research Letters*, *15*(5), 467–470. https://doi.org/10.1029/GL015i005p00467

Biot, M. A. (1941). General theory of three-dimensional consolidation. *Journal of Applied Physics*, *12*(2), 155–164. https://doi.org/10.1063/1.1712886

Bruno, M. S., Bovberg, C. A., & Nakagawa, F. M. (1991). Anisotropie Influence on the Permeability of Weakly Cemented Sandstones. *American Rock Mechanics Association, The 32nd U*.

Carter, N. L., & Hansen, F. D. (1983). Creep of rocksalt. *Tectonophysics*. https://doi.org/10.1016/0040-1951(83)90200-7

Coble, R. L. (1963). A Model for Boundary Diffusion Controlled Creep in Polycrystalline Materials. *Journal of Applied Physics*. https://doi.org/10.1063/1.1702656

Coulomb, C. A. (1776). Essai sur une application des règles de Maximis & Minimis à quelques Problèmes de Statique, relatifs à l'Architecture. *Mémoires de Mathématique et de Physique, Présentés à l'Académie Royale Des Sciences, Par Divers Savans, & Lûs Dans Ses Assemblées*, *7*, 343–382.

Cristescu, N., & Hunsche, U. (1991). Determination of Nonassociated Constitutive Equation for Rock Salt from Experiments. In *Finite Inelastic Deformations - Theory and Applications*. Germany.

Durup, G., & Xu, J. (1993). Comparative study of certain constitutive laws used to describe the rheological deformation of salts. *SERIES ON ROCK AND SOIL MECHANICS*, *20*, 75–84.

Dusseault, M. B., Maury, V., & Sanfilippo, F. (2004). Drilling Around Salt : Stresses , Risks , Uncertainties. *Stress The International Journal on the Biology of Stress*. Retrieved from http://www.onepetro.org/mslib/app/Preview.do?paperNumber=ARMA-04-647&societyCode=ARMA

Economides, M. J., & Nolte, K. G. (1989). *Reservoir Simulation*. (M. J. Economides & K. G. Nolte, Eds.) (Third Edit). John Wiley & Sons LTD.

Ehgartner, B. L., & Sobolik, S. R. (2002). 3-D cavern enlargement analyses. *Sandia National Laboratories, Albuquerque*.

Eshelby, J. D. (1957). The determination of the elastic field of an ellipso{ï}dal inclusion, and related problems. In *Proceedings of the Royal Society of London, series {A}, Mathematical and Physical Sciences* (pp. 376–396).

Fredrich, J. T., Coblentz, D., Fossum, A. F., & Thorne, B. J. (2003). Stress Perturbations Adjacent to Salt Bodies in the Deepwater Gulf of Mexico. *SPE Annual Technical Conference and Exhibition*, (October), 5–8. https://doi.org/10.2118/84554-MS

Geertsma, J. (1973). A basic theory of subsidence due to reservoir compaction: the homogeneous case. *Verh. K. Geol. Mijnbouwk. Gen.*, *28*, 43–62.

Gheibi, S., Holt, R. M., & Vilarrasa, V. (2016). Stress path Evolution during Fluid injection into Geological Formations. *American Rock Mechanics Association*.

Goodman, R. E. (1989). *Introduction to Rock Mechanics* (Second). John Wiley & Sons.

Guilbot, J., & Smith, B. (2002). 4-D constrained depth conversion for reservoir compaction estimation: Application to Ekofisk Field. *The Leading Edge*. https://doi.org/10.1190/1.1463782

Halbouty, M. T. (1979). *Salt domes Gulf Region, United States and Mexico*. Gulf Publishing Company.

Halbouty, M. T., & Hardin, G. C. (1956). Genesis of salt domes of gulf coastal plain. *AAPG*, *40*, 737–746.

Harper, J. G., & Dorn, J. E. (1957). Acta Metallurgical, *5*, 654.

Heard, H. C. (1972). Steady-state flow in polycrystalline halite at pressure of 2 kilobars. *Flow and Fracture of Rocks. American Geophysical Union, Geophysical Monograph*, 191–210.

Heidari, M., Nikolinakou, M. A., Flemings, P. B., & Hudec, M. R. (2017). A simplified stress analysis of rising salt domes. *Basin Research*, *29*(3), 363–376. https://doi.org/10.1111/bre.12181

Heidari, M., Nikolinakou, M. A., Hudec, M. R., & Flemings, P. B. (2016). Geomechanical analysis of a welding salt layer and its effects on adjacent sediments. *Tectonophysics*, *683*, 172–181. https://doi.org/10.1016/j.tecto.2016.06.027

Herrmann, W., Wawersik, W. R., & Lauson, H. S. (1980). Analysis of Steady State Creep of Southeastern New Mexico Bedded Salt.

Hettema, M. H. H., Schutjens, P. M. T. M., Verboom, B. J. M., & Gussinklo, H. J. (2000). Production-Induced Compaction of a Sandstone Reservoir: The Strong Influence of Stress Path. *Spe Reservoir Evaluation & Engineering*, *3*(4), 342–347. https://doi.org/10.2118/65410-pa

Holt, R. M., Gheibi, S., & Lavrov, A. (2016). Where does the stress path lead? Irreversibility and hysteresis in reservoir geomechanics. In *50th US Rock Mechanics / Geomechanics Symposium 2016* (Vol. 2).

Holt, R. M., Li, L., & Fjaer, E. (2004). Consequences of Depletion-Induced Stress Changes on

Reservoir Compection and Recovery. *Th North America Rock Mechanics Symposium (NARMS*.

Hou, Z., & Lux, K.-H. (1998). A new elastic/viscoplastic model for salt rock included damage and accelerated creep based on the Continuum-Damage-Mechanics. *Geotechnik*, *21*(3).

Hunsche, U., & Hampel, A. (1999). Rock salt—the mechanical properties of the host rock material for a radioactive waste repository. *Engineering Geology*, *52*(3), 271–291. https://doi.org/10.1016/S0013-7952(99)00011-3

Islam, M. A., & Skalle, P. (2013). An experimental investigation of shale mechanical properties through drained and undrained test mechanisms. *Rock Mechanics and Rock Engineering*, *46*(6), 1391–1413. https://doi.org/10.1007/s00603-013-0377-8

Itasca, I. (2012). *FLAC-3D User's Manual* (5.0). Minneapolis.

Jackson, M. P. A., & Galloway, W. E. (1984). Petroleum Traps And Associated Facies Of Salt Domes: Unit 20: Principles. In *Structural and depositional styles of Gulf Coast Tertiary continental margins: application to hydrocarbon exploration* (p. 226). Tulsa, Okla. : American Association of Petroleum Geologists.

Jin, J., & Cristescu, N. D. (1998). An elastic/viscoplastic model for transient creep of rock salt. *International Journal of Plasticity*, *14*(1–3), 85–107. https://doi.org/10.1016/S0749-6419(97)00042-9

Manzano Angeles, D. (2014). *Integration of Geomechanical Parameters and Numerical Simulation for an Offshore Reservoir in the Gulf of Mexico*. UNIVERSITY OF CALGARY.

Mohr, O. (1906). *Abhandlungen aus dem Gebiet der Technischen Mechanik*. Berlin: Verlag Von Wilhelm Ernst & Sohn.

Munson, D. E. (1998). Analysis of multistage and other creep data for domal salts. *Sandia National Laboratories, Albuquerque*.

Norton, F. H. (1929). *Creep of Steel at High TemperaturesNo Title*. New York: McGraw-Hill Book Company.

Ojala, I. O. (2011). The effect of CO2 on the mechanical properties of reservoir and cap rock. In *Energy Procedia* (Vol. 4, pp. 5392–5397). https://doi.org/10.1016/j.egypro.2011.02.523

Park, B.-Y., Ehgartner, B. L., Lee, M. Y., & Sobolik, S. R. (2005). Three dimensional simulation for Big Hill Strategic Petroleum Reserve (SPR). *Sandia National Laboratories, Albuquerque*.

Ratigan, J.L., Nieland, J.D., and Osnes, J. D. (1993). Rock Mechanics Aspects of Natural Gas Storage in Domal Salt. In *Solution Mining Research Institute*. Lafayette, Louisiana.

Rhett, D. W., & Teufel, L. W. (1991). Water injection-induced shear fracture in the Ekosfik

field. *American Rock Mechanics Association*.

Rhett, D. W., & Teufel, L. W. (1992). Effect of Reservoir Stress Path on Compressibility and Permeability of Sandstones. *Proceedings of SPE Annual Technical Conference and Exhibition*, 965–972. https://doi.org/10.2523/24756-MS

Rice, J. R., & Cleary, M. P. (1976). Some basic stress diffusion solutions for fluid-saturated elastic porous media with compressible constituents. *Reviews of Geophysics*. https://doi.org/10.1029/RG014i002p00227

Rudnicki, J. W. (1999). Alteration of Regional Stress By Reservoirs And Other Inhomogeneities: Stabilizing Or Destabilizing? In *9th ISRM Congress, 25-28 August,* (p. 9).

Rutter, E. H. (1983). Pressure solution in nature, theory and experiment. *Journal of the Geological Society*. https://doi.org/10.1144/gsjgs.140.5.0725

Schutjens, P. M. T. M., Snippe, J. R., Mahani, H., Turner, J., Ita, J., & Mossop, A. P. (2012). Production-Induced Stress Change in and Above a Reservoir Pierced by Two Salt Domes: A Geomechanical Model and Its Applications.

Segall, P., & Fitzgerald, S. D. (1998). A note on induced stress changes in hydrocarbon and geothermal reservoirs. *Tectonophysics*, *289*(1–3), 117–128. https://doi.org/10.1016/S0040-1951(97)00311-9

Shahmorad, Z., Salarirad, H., & Molladavoudi, H. (2016). A study on the effect of utilizing different constitutive models in the stability analysis of an underground gas storage within a salt structure. *Journal of Natural Gas Science and Engineering*, *33*, 808–820. https://doi.org/10.1016/j.jngse.2016.06.011

Skrotzki, W., & Haasen, P. (1988). The role of cross slip in the steady state creep of salt. In *The Mechanical Behaviour of Salt: Proceedings of the Second Confk'rence,* (pp. 69–81).

Sriapai, T., Chaowarinwalsri, & Fuenkajorn, K. (2012). Effect of temperature on compressive and tensile strengths of salt. *ScienceAsia*, *38*(2), 166–174. https://doi.org/10.2306/scienceasia1513-1874.2012.38.166

Teas, L. P. (1935). Natural Gas of Gulf Coast Salt Dome Area. *Geology of Natural Gas, AAPG*, 683–740.

Teufel, L. W., Rhett, D. W., & Farrell, H. E. (1991a). Effect of Reservoir Depletion And Pore Pressure Drawdown On In Situ Stress And Deformation In the Ekofisk Field, North Sea. *The 32nd U.S. Symposium on Rock Mechanics (USRMS)*, 63–72. https://doi.org/ARMA-91-063

Teufel, L. W., Rhett, D. W., & Farrell, H. E. (1991b). Effect of Reservoir Depletion And Pore Pressure Drawdown On In Situ Stress And Deformation In the Ekofisk Field, North Sea. *The 32nd U.S. Symposium on Rock Mechanics (USRMS)*.

Trusheim, F. (1960). On the mechanicsm of salt migration in Northern Germany. *AAPG*, *44*, 1519–1540.

Urai, J. L. (1983). Water assisted dynamic recrystallization and weakening in polycrystalline bischofite. *Tectonophysics*. https://doi.org/10.1016/0040-1951(83)90247-0

von Mises, R. (1913). Mechanik der festen Koerper in plastisch deformahlem Zustand. *Goettinger Narchrichten*. https://doi.org/citeulike-article-id:6897288

Warpinski, N. R., Branagan, P. T., & Wilmer, R. (1985). In-situ stress measurements at U. S. DOE's Multiwell Experiment site, Mesaverde Group, Rifle, Colorado. *Journal of Petroleum Technology*, *37*(3), 527–536. https://doi.org/10.2118/12142-PA

Warpinski, N. R., & Teufel, L. W. (1989). In-situ stresses in low-permeability, nonmarine rocks. *Journal of Petroleum Technology*, *41*(4), 405–414. https://doi.org/10.2118/16402-PA

Wawersik, W. R., & Zeuch, D. H. (1984). Creep and creep modeling of three domal salts—a comprehensive update. *Sandia National Laboratories, Albuquerque*.

Wawersik, W. R., & Zeuch, D. H. (1986). Modeling and mechanistic interpretation of creep of rock salt below 200°C. *Tectonophysics*. https://doi.org/10.1016/0040-1951(86)90040-5

Weijermars, R., Jackson, M. P. A., & Vendeville, B. (1993). Rheological and tectonic modeling of salt provinces. *Tectonophysics*, *217*(1–2), 143–174. https://doi.org/10.1016/0040-1951(93)90208-2

Zhang, L. (2006). *Engineering Properties of Rocks*. *Elsevier Geo-Engineering Book Series* (Vol. 4). https://doi.org/10.1016/S1571-9960(06)80002-9

Zimmerman, R. W. (1991). *Compressibility of Sandstones*. (G. V. Chilingarian, Ed.) (DEvelopmen). Amsterdam: Elsevier.